Graduate School ETD Form 9
(Revised 12/07)

# PURDUE UNIVERSITY
## GRADUATE SCHOOL
## Thesis/Dissertation Acceptance

This is to certify that the thesis/dissertation prepared

By Maksud Ismailov

Entitled Modeling of Classical Swirl Injector Dynamics

For the degree of Doctor of Philosophy

Is approved by the final examining committee:

Stephen D. Heister
Chair

Gregory A. Blaisdell

Charles L. Merkle

Paul E. Sojka

To the best of my knowledge and as understood by the student in the *Research Integrity and Copyright Disclaimer (Graduate School Form 20)*, this thesis/dissertation adheres to the provisions of Purdue University's "Policy on Integrity in Research" and the use of copyrighted material.

Approved by Major Professor(s): Stephen D. Heister

Approved by: Anastasios S. Lyrintzis 06/18/2010
Head of the Graduate Program Date

Graduate School Form 20
(Revised 1/10)

# PURDUE UNIVERSITY
## GRADUATE SCHOOL

## Research Integrity and Copyright Disclaimer

Title of Thesis/Dissertation:
Modeling of Classical Swirl Injector Dynamics

For the degree of Doctor of Philosophy

I certify that in the preparation of this thesis, I have observed the provisions of *Purdue University Teaching, Research, and Outreach Policy on Research Misconduct (VIII.3.1)*, October 1, 2008.*

Further, I certify that this work is free of plagiarism and all materials appearing in this thesis/dissertation have been properly quoted and attributed.

I certify that all copyrighted material incorporated into this thesis/dissertation is in compliance with the United States' copyright law and that I have received written permission from the copyright owners for my use of their work, which is beyond the scope of the law. I agree to indemnify and save harmless Purdue University from any and all claims that may be asserted or that may arise from any copyright violation.

Maksud M. Ismailov
Printed Name and Signature of Candidate

06/18/2010
Date (month/day/year)

*Located at http://www.purdue.edu/policies/pages/teach_res_outreach/viii_3_1.html

# MODELING OF CLASSICAL SWIRL INJECTOR DYNAMICS

A Dissertation

Submitted to the Faculty

of

Purdue University

by

Maksud M. Ismailov

In Partial Fulfillment of the

Requirements for the Degree

of

Doctor of Philosophy

August 2010

Purdue University

West Lafayette, Indiana





ProQuest LLC
789 East Eisenhower Parkway
P.O. Box 1346
Ann Arbor, MI 48106-1346

To my wife, Masuda, and daughter, Sabeena.

# ACKNOWLEDGMENTS

First of all, I would like to express my sincere gratitude to my major advisor, Prof. Stephen Heister. Since 2007, when I started working on this research topic, he was the sole person, who guided me in the hard times, when it appeared that some of the ideas in the analysis or the computations do not work. And when they worked, he has wisely pointed the possible directions to proceed further on. He has also helped me to become confident in the professional world through his advices regarding how to better present the research and convey the results of it to the general audience.

I thank my longest and best friend at Purdue, Oscar Garibaldi, for being there. I thank my lunch-mates during the first years of the doctoral program, Tony Tang, John Tsohas, Enrique Portillo, with whom we often had very interesting aerospace and general life related discussions. I also thank George Wurzel, and his company, for the dinner times and the travel adventures that we had together during these first years. I thank Benjamin Ahn for having long conversations concerning the experimental setup and the unsteady flow behavior in the swirl injector, through which we have been able to better understand and characterize the injector dynamics. I thank my office-mate Changjin Yoon for interesting discussions with regard to the general CFD modeling of the injectors. I thank my parents for providing the guidance and support to become a person I am now. Finally, I thank my wife, Masuda, for love, for patience, and for making our home the best place I enjoy to be at.

This research was supported by the Air Force Office of Scientific Research and Dr. Mitat Birkan under contract number FA9550-08-1-0115.

TABLE OF CONTENTS

Page

# LIST OF TABLES

# LIST OF FIGURES

# NOMENCLATURE

| | |
|---|---|
| $A$ | instantaneous core cross-sectional area ($A = \pi(\delta + \eta)^2$) |
| $A_D$ | duct cross-sectional area ($A_D = \pi R^2$) |
| $A_{geom}$ | geometric characteristic $\left(A_{geom} = \dfrac{R_{in} R_n}{N_{in} R_t^2}\right)$ |
| $C$ | angular momentum constant ($C = u_\theta r$) |
| $c$ | disturbance wave speed $\left(c = \dfrac{\omega}{k}\right)$ |
| $c_n$ | disturbance wave speed in uniform nozzle region |
| $c_v$ | disturbance wave speed in uniform vortex chamber region |
| $I_0$ | modified Bessel function of 1st kind of order 0 |
| $I_1$ | modified Bessel function of 1st kind of order 1 |
| $i$ | imaginary unity $\left(i = \sqrt{-1}\right)$ |
| $K_0$ | modified Bessel function of 2nd kind of order 0 |
| $K_1$ | modified Bessel function of 2nd kind of order 1 |
| $k$ | wave number $\left(k = \dfrac{2\pi}{\lambda}\right)$ |
| $k_{he}$ | wave number at head end |
| $k_n$ | wave number in uniform nozzle region |
| $k_v$ | wave number in uniform vortex chamber region |
| $L_c$ | length of conical convergence section |
| $L_n$ | length of nozzle |
| $L_t$ | length of tangential inlet |
| $L_v$ | length of vortex chamber |
| $\dot{m}_{in}$ | inlet mass flow rate |
| $\dot{m}_n$ | nozzle exit mass flow rate |
| $N_{in}$ | number of tangential inlets |
| $R$ | radius of solid boundary |

| | |
|---|---|
| $R_{in}$ | inflow radius ($R_{in} = R_v - R_t$) |
| $R_n$ | radius of nozzle |
| $R_t$ | radius of tangential inlet |
| $R_v$ | radius of vortex chamber |
| $r$ | radial coordinate |
| $r_{he}$ | steady free surface radius at head end, $z = 0$ |
| $r_n$ | steady free surface radius in uniform nozzle region |
| $r_v$ | steady free surface radius in uniform vortex chamber region |
| $t$ | time |
| $u_\theta$ | circumferential velocity |
| $u_r$ | radial velocity |
| $u_z$ | axial velocity |
| $u_{zn}$ | axial velocity in uniform nozzle region |
| $u_{zv}$ | axial velocity in uniform vortex chamber region |
| $W_{in}$ | tangential inlet inflow velocity |
| $z$ | axial coordinate |
| $\alpha$ | angle of solid wall convergence |
| $\Gamma$ | circulation ($\Gamma = 2\pi u_\theta r = 2\pi C$) |
| $\Delta p_{he}$ | pressure drop through liquid body at head end, $z = 0$ |
| $\Delta p_{inj}$ | total injector pressure drop |
| $\Delta p_t$ | pressure drop through tangential inlet |
| $\delta$ | steady free surface radius at any axial position of internal flow |
| $\eta$ | free surface deflection away from $\delta$ |
| $\theta$ | angular coordinate |
| $\lambda$ | wave length |
| $\nu$ | artificial viscosity coefficient in Bazarov's linear theory |
| $\Pi_{inj}$ | total injector response |
| $\phi$ | velocity potential |
| $\rho$ | density |

| | |
|---|---|
| $\sigma$ | surface tension at gas-liquid interface |
| $\Omega$ | angular velocity in gaseous core |
| $\omega$ | angular disturbance frequency |
| *prime* $()'$ | fluctuation value of parameter |
| *bar* $\bar{()}$ | steady state value of parameter |
| *hat* $\hat{()}$ | amplitude of fluctuation of disturbed parameter |
| *star* $()^*$ | dimensional value of parameter |

# ABSTRACT

Ismailov, Maksud M. Ph.D., Purdue University, August 2010. Modeling of Classical Swirl Injector Dynamics . Major Professor: Stephen D. Heister.

The knowledge of the dynamics of a swirl injector is crucial in designing a stable liquid rocket engine. Since the swirl injector is a complex fluid flow device in itself, not much work has been conducted to describe its dynamics either analytically or by using computational fluid dynamics techniques. Even the experimental observation is limited up to date.

Thus far, there exists an analytical linear theory by Bazarov [1], which is based on long-wave disturbances traveling on the free surface of the injector core. This theory does not account for variation of the nozzle reflection coefficient as a function of disturbance frequency, and yields a response function which is strongly dependent on the so called artificial viscosity factor. This causes an uncertainty in designing an injector for the given operational combustion instability frequencies in the rocket engine.

In this work, the author has studied alternative techniques to describe the swirl injector response, both analytically and computationally. In the analytical part, by using the linear small perturbation analysis, the entire phenomenon of unsteady flow in swirl injectors is dissected into fundamental components, which are the phenomena of disturbance wave refraction and reflection, and vortex chamber resonance. This reveals the nature of flow instability and the driving factors leading to maximum injector response. In the computational part, by employing the nonlinear boundary element method (BEM), the author sets the boundary conditions such that they closely simulate those in the analytical part. The simulation results then show distinct peak responses at frequencies that are coincident with those resonant frequencies

predicted in the analytical part. Moreover, a cold flow test of the injector related to this study also shows a clear growth of instability with its maximum amplitude at the first fundamental frequency predicted both by analytical methods and BEM. It shall be noted however that Bazarov's theory does not predict the resonant peaks.

Overall this methodology provides clearer understanding of the injector dynamics compared to Bazarov's. Even though the exact value of response is not possible to obtain at this stage of theoretical, computational, and experimental investigation, this methodology sets the starting point from where the theoretical description of reflection/refraction, resonance, and their interaction between each other may be refined to higher order to obtain its more precise value.

# 1. INTRODUCTION

## 1.1 Steady Operation of Swirl Injector

The swirl injector, also known as simplex pressure atomizer, is a flow device used to break the liquid flowing through it into small drops and ligaments, which is achieved by reshaping the liquid into a thin swirling hollow film in the form of cone at the injector exit. This type of injector is used extensively in liquid rocket and gas turbine engines (Lefebvre [2]) to atomize the propellants. Historically, these injectors were employed more in Russian rocket engines [3], because they require less precision to manufacture and at the same time provide an overall finer spray, when compared to plain orifice designs for impinging element injectors, which were traditionally used in the United States. They are also used in spray drying, cooling, fire suppression, etc.. A schematic of a classical swirl injector is shown in Fig. 1.1. Its major components are: tangential inlets, vortex chamber, conical convergence section, and nozzle. The term classical is used in this study to indicate that the injector has a *single row* of tangential inlets and a distinct conical convergence.

The steady operation of the swirl injector can be described as follows. The propellant enters into the injector through the inlets that are drilled tangentially to the vortex chamber. The vortex chamber has a closed head end on one side and a nozzle through which the propellant issues into the rocket combustion chamber on the other side. The flow behavior in such injector can be ideally described as a superposition of uniform axial and free vortex flows [4, chap. 2.3]. As the flow enters the vortex chamber, it is being pushed by the upper wall of the vortex chamber towards the injector axis and by the head end wall towards the injector exit. This causes a fluid particle to follow a helical trajectory as it flows through the injector. The closer the particle gets to the injector axis, the larger its circumferential velocity due to conservation of

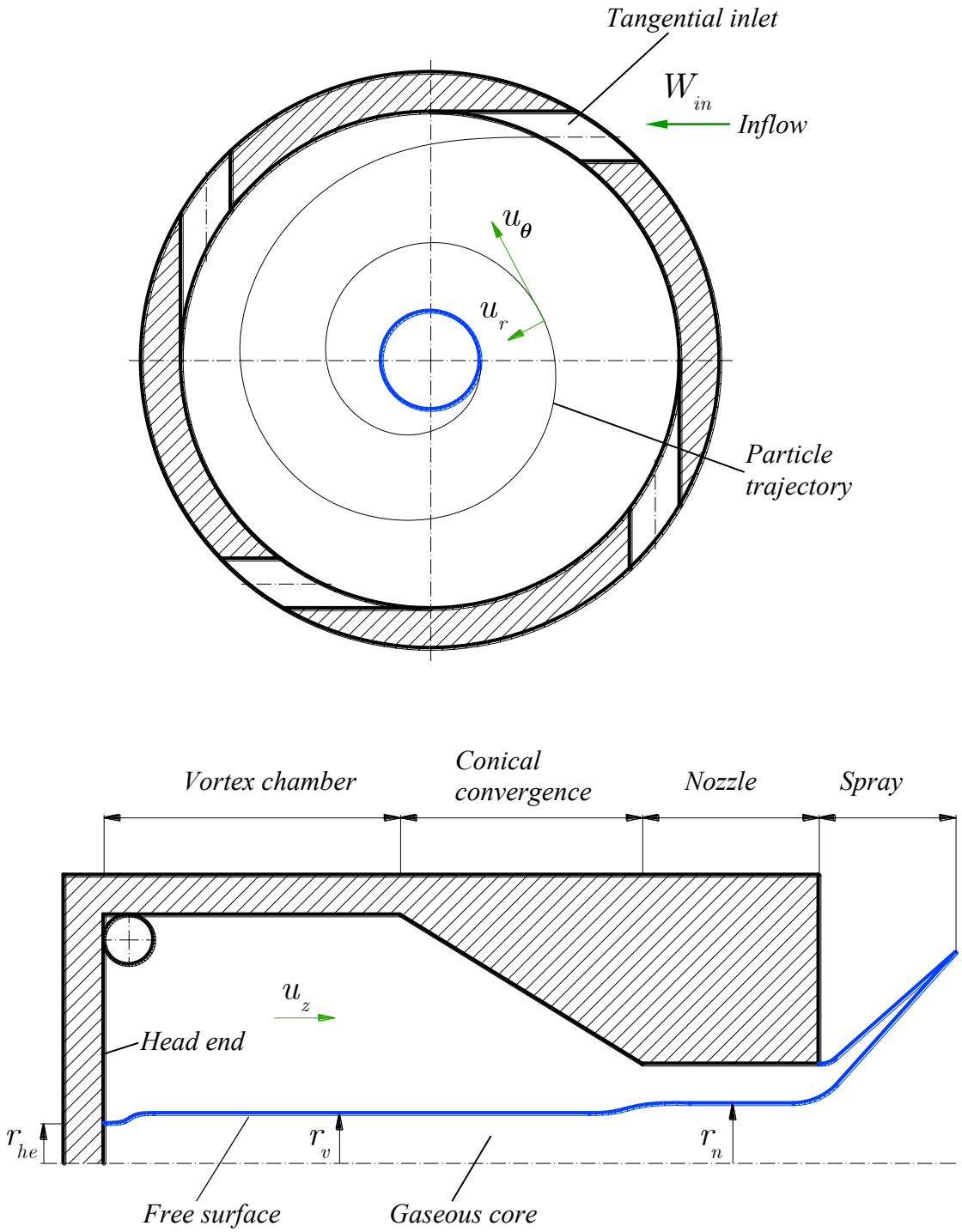


Figure 1.1.: Classical swirl injector schematic

angular momentum, and the smaller its static pressure due to conservation of energy. The flow cannot reach the axis itself, where the circumferential velocity would rise to infinity and static pressure drop to zero, but rather forms a gaseous core [5], in which the static pressure is equal to the ambient gas pressure. Overall, in a steady state operation, the gaseous core is quite stable and the radial distances to the edge of the core at any axial position of the internal flow, do not change over time. Therefore, the radial velocity, $u_r$, at any point in the flow is generally assumed to be negligibly smaller than the circumferential, $u_\theta$, and axial, $u_z$, velocities.

In this study, we will be interested mainly in the *internal flow* of the injector, which is the part of the flow that gives rise to all instabilities visible in the spray. Accordingly, let us notice that the free surface has different radii in different parts inside of the injector. At the head end, the liquid moves mainly in the circumferential direction due to its angular momentum, slowly starting to turn and accelerate in the axial direction. The axial velocity here is close to zero. This causes the free surface to reach the smallest radius, $r_{he}$, over the entire injector. Downstream of the head end, the liquid flows with almost constant uniform axial velocity, also very small but finite, which results in a slightly larger radius of the free surface, $r_v$. Finally, in the nozzle, where the flow area is smallest simply due to converged solid boundary, the liquid moves with the largest axial velocity (almost uniform), which makes the free surface to rise to an even larger radius, $r_n$. In Chapter 2, we will briefly review the standard calculation methodology due to Bazarov [1, Sec. 3.1] of $r_{he}$, $r_v$, and $r_n$, and the flow velocities corresponding to these radii. Other classical references on steady injector calculation are Taylor [6], Giffen and Muraszew [7], Bayvel and Orzechowski [8]. It has to be pointed out that between the said radii, i.e. from $r_{he}$ to $r_v$ and from $r_v$ to $r_n$, the free surface has a continuous smooth *transition*, and the *flow speed in the axial direction is increasing.*

Finally, when the liquid exits the injector, it forms a conical liquid film, because the liquid is still continuing to swirl and move in the axial direction. Eventually, under the forces of aerodynamic drag with the ambient gas, and due to flow disturbances

that were originated inside of the injector, this film disintegrates into ligaments and drops. Until recently, the drop sizes were correlated empirically, such as in [9], Rizk and Lefebvre [10, p. 196], Lefebvre [11], Khavkin [12, p. 107]. However, in the past few years, literature has started to emerge on analytical prediction of drop sizes, and the examples here are [13] and [14].

Because the flow physics in the swirl injectors is complex, historically it was hard to derive analytic theories, describing their behavior in depth. For example, the effect of viscosity in theoretical models is usually presented by including an empirical friction coefficient into the inviscid model as in Doumas and Laster [15] and Yang et al. [16], which reflects how much momentum the liquid will lose because of the friction in flow passages. Or, the effect of flow turning on the angular momentum, when the liquid is entering the vortex chamber and starts to move axially, is also not described theoretically. This usually caused the need for CFD to simulate such effects, Chinn [4, chaps. 8, 9], [17], [18], [19], or an experimental study of swirl injectors, Dombrowski and Hasson [20], [21], [22], [23].

## 1.2 Unsteady or "Dynamic" Operation of Swirl Injector

This study is concerned primarily with the accurate prediction of dynamics of a swirl injector when the flow is unsteady. Physically, there are two sources causing flow instabilities in swirl injector: the propellant delivery line and the rocket combustion chamber. The flow instabilities exhibit themselves in the form of mass flow rate and pressure fluctuations in different parts of the injector. In turn, the combined effect of these fluctuations shows itself in the form of disturbance waves on the free surface of the gaseous core (Kelvin [24], Rayleigh [25], Binnie [26], Maxworthy [27], Feikema [28, Fig. 4]). Correspondingly, this causes variability in the film thickness, spray cone angle, and drop sizes, which are the parameters directly influencing the combustion processes in the rocket engine chamber, such as propellant atomization and vaporization. High amplitude instabilities can arise in the combustion chamber,

should there be a resonance between these spray formation characteristics with the fundamental modes in the chamber. The greater the amplitude of fluctuation of flow parameters inside the injector, the more pronounced the combustion instability in the rocket engine (Bazarov [29], Miller [30], [31]) will be, which is an undesired phenomenon that may potentially lead to engine destruction. This necessitates a thorough study and understanding of swirl injector dynamics, which is performed in this dissertation.

We can see that the free surface disturbance is excited from two fixed locations, either simultaneously or separately, which are: the injector head end and the rocket combustion chamber. Then, from hydrodynamic instability point of view, this problem is a *spatial instability* problem (Criminale et al. [32], Wu et al. [33]), where the disturbance retains its frequency, $\omega$, as it propagates, but its wave number, $k$, may vary. Note that the free surface disturbance, and the corresponding velocity and pressure disturbances, may travel both in positive and negative $z$ directions, however the steady bulk flow moves, becoming faster in transition regions, in positive $z$ direction only. In addition to variable stream velocities, we can see from Fig. 1.1 that the liquid phase disturbances are propagating in the nonuniform flow that has *varying free surface and solid boundaries*. At the same time, the gas phase disturbances experience variation in free surface boundary only, because we may assume that the gaseous core is stagnant due to presence of the head end wall and its small inertia.

Together, the presence of variable stream velocities and flow boundaries leads to the rise of two important phenomena related to propagating disturbance waves: **refraction** and **reflection**. Refraction makes disturbances to change their shape in terms of amplitude and wave length, whereas reflection makes them lose their energy due to partial backward redirection, as they propagate along the injector core. It is known in general, that these *changes in disturbance wave characteristics depend on frequency of the disturbance* itself. Moreover, due to wave reflections, the presence of solid wall at injector head end invokes the occurrence of a standing wave in the vortex

chamber, whose amplitude may maximize at certain frequencies, which happens when the injector is at **resonance**.

The dynamic behavior of the swirl injector is usually characterized by the **response function**, which is the parameter of main interest throughout this work. It is given by

$$\Pi_{inj} = \frac{\dfrac{\dot{m}'_n}{\overline{\dot{m}}_n}}{\dfrac{\Delta p'_{inj}}{\Delta \overline{p}_{inj}}} \tag{1.1}$$

where $\dot{m}_n$ is mass flow rate at the nozzle exit of injector, $\Delta p_{inj}$ is total injector pressure drop, prime means fluctuation, and overbar means steady state value.

According to this definition, the researchers in this field usually pursue to determine the amplitudes and phase shifts of nozzle mass flow rate and pressure drop fluctuations. In the theoretical analysis, this is accomplished by assuming that the disturbances are small, which permits to linearize the flow equations and obtain concise expressions for $\dot{m}'_n$ and $\Delta p'_{inj}$ in terms of free surface disturbance wave amplitude, $\eta$. In the experimental investigation, one usually pursues to artificially pulse the flow to create the flow disturbances.

The important problem then is to make a flow pulsing device (see Bazarov [34] for example) that is capable of generating flow fluctuations clean of noise and close to linear, so that it is possible to compare the results with the theory. Another difficulty lies in measuring the instantaneous mass flow rate at the nozzle exit. This is usually accomplished by inserting conducting electrodes that are some distance apart from each other, somewhere close to the exit of the injector nozzle. These electrodes measure the conductance of the instantaneous body of liquid between them, from which the film thickness, and corresponding mass flow rate, can be computed. But because there is some finite distance between the electrodes, and the lengths of the waves propagating on the core surface may be small, especially at high frequencies, then these electrodes might not capture the instantaneous mass flow rate and its phase shift very accurately.

## 1.3 Previous Works

### 1.3.1 Bazarov's Linear Theory

The most widely recognized analytical work in this field is the 1979 book by Bazarov [1], who developed a linear theory based on small disturbances propagating through the injector flow, which he assumes to be incompressible, inviscid, and to have no surface tension. The concise version of this book is provided in [35]. Under dynamic conditions, the gas pressure or flow rate pulsations lead to the *long* wave development on the free surface of the liquid, as well as striations/waves of liquid with different circumferential velocities, or vorticity waves within the vortex chamber of the injector. Capitalizing on superposition principle valid for linear problems, Bazarov represented the total response as a product of responses of different parts of the swirl injector, among which are the responses of the vortex chamber to the surface waves and vorticity waves. For completeness of this report, a short review of Bazarov's linear theory will be provided in Chapter 2.

Overall, Bazarov's theory [1, Chap. 4] presents itself as a valuable analytical tool that may indicate on which frequencies what strength of injector response one can expect. Before Bazarov's work, there did not exist any theory similar to this one in its level of extensive description of injector dynamics. Bazarov's theory has also disadvantages [36]:

Regarding surface wave treatment:

- The variation of internal flow boundaries is simplified to the case of sudden film thickness change, as the vortex chamber transitions to the nozzle, which permits one to ignore wave refraction and results in a reflection coefficient that does not depend on the disturbance frequency.

- When treating surface waves, that are reflecting back an forth in the vortex chamber, the wave speed taken for both downstream and upstream traveling disturbances is such that it is valid for downstream traveling disturbances only.

Regarding vorticity wave treatment:

- The process of liquid issuing from the injector tangential inlet into the vortex chamber is represented by a conformal mapping of the half-strip into the half-plane, however, no clear theoretical evidence exists justifying this representation.

- To separate vorticity waves from surface waves, the free surface radius at injector head end is assumed to preserve its steady state value, which cannot physically be done because the propagation of vorticity and surface waves happens simultaneously, and the pulsations cause the said radius to be time varying.

- To determine the phase shift in the radial direction, the expression for steady state radial velocity is used which does not obey Laplace's equation describing the potential flow at the steady state.

- To compute the time lag in the radial direction, the radial distance from the cylindrical wall of the vortex chamber to the point of interest at some arbitrary radius is divided by the steady radial velocity corresponding to this point, however, it is not taken into account that this radial velocity actually varies with radius, so that an integral expression for the time lag should be used.

Finally, to model dissipative frictional effects, the response function resulting from Bazarov's theory includes an artificial viscosity coefficient, $\nu$, which turns out to have a strong influence on the value of the response function itself.

Bazarov also conducted cold flow tests [1, Chap. 5] of swirl injectors to justify the dynamic theory at frequencies spanning the largest operating range 500–1200 Hz up to date. In his experiments, Bazarov pioneered the method of flow pulsation where the liquid is flowing through the holes in a rotating disc [34], and the method of measuring

the instantaneous mass flow rate by putting electrodes at the injector nozzle exit. The experimental data points shown in Fig. 54 of his book [1] show reasonable matching with the theory, but indicate that the theoretical prediction starts to deviate from experimental observation starting from 1000 Hz, which may be attributed to the fact that Bazarov's analysis considers long waves only, and at higher frequencies short wave effects start to appear.

### 1.3.2 Other studies of swirl injector dynamics

#### Computational studies

First, we have to note here that there were not many computational studies of the injector dynamics so far. The author believes that this is largely related to the fact that it is generally difficult to set the inflow and free surface boundaries such that they represent the unsteady swirling flow in the swirl injector realistically.

Park [37] investigated the dynamics of swirl injectors by using axisymmetric boundary element method (BEM), which assumes that the flow is incompressible and irrotational. The major advantage of using BEM lies in reducing the number of computational points only to those that lie on the flow boundaries (Brebbia [38], Liggett and Liu [39], [40]), which accordingly reduces the computational time and improves resolution of the processes taking place at the free surface of the flow, such as formation of ligaments and drops, drop pinching events, etc. (Hilbing [41], Yoon [42]). The way Park modeled the flow unsteadiness was by fluctuating sinusoidally the inflow velocity, while the pressure inside the core remained constant. Park did not compute the injector response, but his work was among the first that attempted to model the unsteady dynamics of swirl injector by methods of CFD with the emphasis on high resolution of drops and flow boundaries. His simulations have shown distinct pulsations of spray cone and reduced drop sizes in response to the unsteady upstream flow. The disadvantage of this attempt was in the injector inflow represented by a cylindrical slot in which the liquid moves radially toward the injector axis. This

representation does not truly characterize the three-dimensional inflow in a real swirl injector.

Richardson [43, chap. 4], [44] continued the above work of Park [37] and relaxed the condition of constant gas pressure in the core and allowed it to fluctuate. Now, the inflow velocity was computed based on instantaneous pressure drop and the radius of the core surface at the head end. Richardson presented the comparison of responses from his BEM simulations and Bazarov's linear theory for the same injector geometries and flow conditions, Fig. 1.2. The responses were matching reasonably well at low frequencies up to 2000 Hz and at a narrow section of medium frequencies of about 5000 Hz. However, there was a significant discrepancy at the rest of the frequencies. This may be related to the following drawbacks in his flow setup: (a) the inflow was continued to be modeled as a cylindrical slot after Park [37], (b) the unsteady inflow velocity and injector pressure drop were linked by the steady state Bernoulli equation instead of the unsteady Bernoulli formulation [45, Eq. (6.21)].

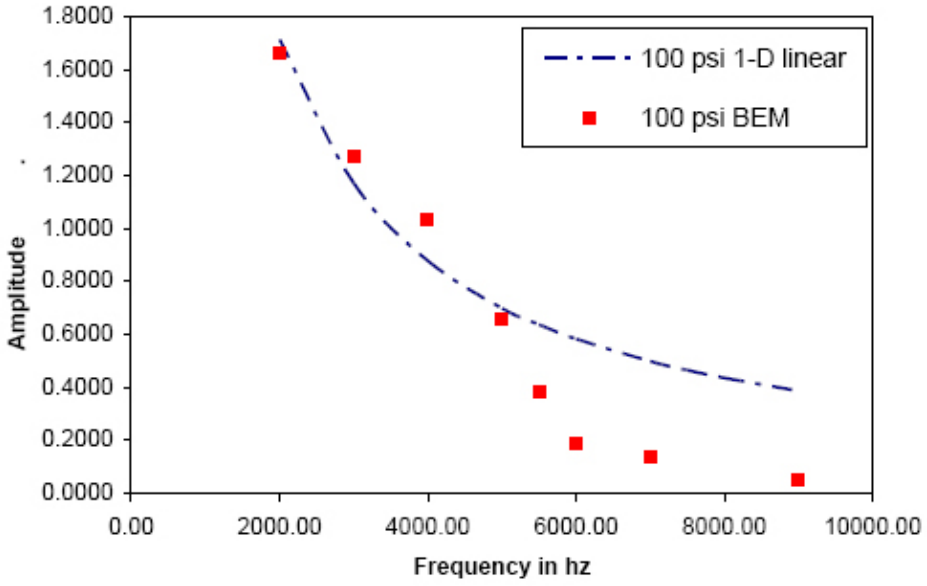


Figure 1.2.: Richardson vs. Bazarov response comparison (Fig. 4.12 in [43, chap. 4])

Fu et al. [46] made an attempt to investigate the dynamics of open swirl injectors, which is the type of injectors where due to the absence of converging solid wall, the reflection is weak, but nevertheless present due to the changes in the film thickness as the jet issues out of the injector nozzle. Basing the analysis largely on Bazarov's [1, chaps. 1–4], they have shown numerous plots [46, Figs. 2–5] describing the nozzle mass flow rate pulsation magnitude and its phase shift at various frequencies. The author assumes that the calculations in [46] were based on their previous paper [47]. Note however, that the latter does not indicate the reasons for choosing a particular value of the artificial viscosity coefficient, which is 0.6 [47, p. 5], and also, as in Bazarov's analysis, all phase shifts are computed with the wave speed valid for downstream propagating waves.

Huo et al. [48] presented an interesting paper describing the open injector dynamics with supercritical oxygen as a working fluid and gaseous oxygen filling the gaseous core. The way they modeled the inflow was very similar to Park [37] and Richardson [43]. Viscous interaction between the gaseous core and supercritical body results in instability patterns analogous to Kelvin-Helmholtz [49, Fig. 1.4] as shown in numerous figures in their work. It can be vividly seen how these patterns propagate downstream into the spray cone. Note however that, in this study, we restrict ourselves only to an *ideal flow*, where viscous effects are absent, so that we leave their work as a reference of what might be expected when the flow is more fully described.

A research team at the University of Alabama in Huntsville is actively investigating the injector dynamics by following the design methodologies outlined by Bazarov. So far, they have presented results of numerical investigation of Bazarov's pulsator in great detail [50], [51].

**Experimental studies**

A small number of experimental works on dynamic modeling of injectors have appeared in the western literature after Bazarov's experiments in the 1970's. Recently, a research group in Korea, Khil et al. [52], [53] pulsed the flow in the range of frequencies of 100–300 Hz. They presented the experimental data for the pressures and mass flow rates, without going further to compute the response.

In the above mentioned paper by Fu et al. [46], the pulsation range was 0–500 Hz. In their Fig. 14, it can be seen that the pressure and flow rate signals are quite nonlinear at lower frequencies of up to 200 Hz. This raises the question of how the experimental injector response and its corresponding phase shift were calculated at lower frequencies. Notice that, in both of these works, [52], [46], the flow pulsator and mass flow measuring technique were very similar to the original Bazarov's [1, Chap. 5].

Continuing numerical investigation of the flow pulsator mentioned above [50], [51], Wilson et al. [54] have conducted its cold flow tests, where a 2% level of pressure pulsation has been achieved. Since this is the initial phase preceeding the studies of the dynamics of the injector itself, the injector response characterization has not been performed yet.

At Purdue University, experimental work is currently being conducted by Ahn [55], [56]. This work is aimed at achieving experimental response data in the broad frequency range, possibly the same as in Bazarov's [1, Chap. 5] experiments. In contrast to previous experimental setups described above, the flow in this case is pulsed *right at the inlets* of the injector. This permits one to achieve a higher magnitude of flow pulsation because the pressure losses between the pulsing device and injector inlet are reduced, up to 12% of injection pressure as shown in [55, Fig. 6.2]. The flow pulsing frequencies so far have reached the level of 300 Hz. This experiment is still in development to reach to even higher frequencies, but provides a good overview of the trends that may be expected for the pulsation of injector pressure drop, gaseous core sizes, and spray cone angle.

## 1.4 Study Objectives

At this point, we can readily conclude that Bazarov's work, both analytical and experimental, is the most complete and detailed piece of information that we can refer to or compare with, when conducting the dynamic analysis of the general swirl injectors (not open ended). However, considering the analytical and experimental shortcomings of Bazarov (Subsection 1.3.1), we can raise the following questions:

1. In the general case, when the injector has a distinct conical convergence and smooth free surface transition at the nozzle entrance, how does the refraction affect its dynamics?

2. How is refraction interrelated with reflection and how does the resulting reflection coefficient depend on the disturbance frequency?

3. When the reflection coefficient is at its extremum values at some particular frequencies, can we expect injector resonance at these frequencies?

4. Is it possible to combine the above effects of items 1 and 2 into the injector response, which at the same time does not bear the sensitivity to artificial viscosity?

5. How does the injector response behave at higher frequencies when the short wave analysis becomes relevant?

6. Can we assess inertial and capillary effects of the gaseous core, which are seen in the experiments [57], [58], on the injector response?

These questions set the stage and motivation for this dissertation. By answering them in this thesis, we will illustrate the important aspects of injector dynamics that were not covered in Bazarov's theory, and clearly identify the areas of analysis that must be developed further, such as the refraction/reflection phenomena. This is the first goal pursued in this thesis.

Also, in our numerical computations, we must be able to see the phenomena that were described analytically. We will continue to use BEM after Richardson [43] as a numerical tool in this study, based on its advantage to resolve the free surface of the flow, where wave refraction/reflection becomes visible, with high precision. But, because Richardson's injector response given above in Fig. 1.2 shows significant discrepancy with the theory, we have to modify the boundary conditions in the BEM code such that they more closely replicate the flow modeled in the theory. Finding the correct BEM boundary conditions is the second goal set in this thesis.

Consequently, this thesis is divided into two major parts: analytical and numerical. Starting with the analytical part, we briefly review the steady and unsteady calculations by Bazarov in Chapter 2. In the unsteady part, we will reiterate in more details on the shortcomings of his analysis outlined above. Also, the baseline injector geometry and nondimensionalization factors will be set. Next, to work with refraction phenomenon in question 1, one needs to know the shape of the free surface in transition regions of the injector. In Chapter 3 this problem is solved by means of potential flow equations. Regarding both questions 1 and 2, we know that refraction and reflection act together at once, which is difficult to model. Therefore, we will consider first the refraction alone in Chapter 4. From this chapter we will learn how the disturbance wave characteristics, wave number and amplitude, change in the environment of nonuniform stream velocity and flow boundaries by using basic small perturbation methods [59], [49]. Proceeding to the reflection problem, which is presented in Chapter 5, we know that it involves the determination of the *lump* reflection and transmission coefficients over the entire region of transition, which describe what portion of the waves from the vortex chamber will propagate further into the nozzle, and what portion will come back into the vortex chamber. Since this problem is hard in itself, we will discretize the flow in transition region into small sections, where we can approximately assume uniformity of flow boundaries and stream velocity. Now the information that we have obtained about the wave characteristics in Chapter 4 becomes handy, as we will use it for *local* stream velocity and flow boundaries in each

of the said small sections. Eventually, this method will provide us with the reflection/transmission characteristics of the swirl injector that depend on the disturbance frequency. From the frequencies where these characteristics exhibit extremum values we will discover the resonance characteristics of the injector in question 3. Moving on to the injector response in question 4, it is clear at this stage that the inclusion of combined effects of variable stream velocity, flow boundaries, and refraction/reflection is not feasible. Therefore, as of now, the author considers only the effect of refraction in injector response calculation, which is presented in Chapter 6, where the refraction materializes itself in different wave numbers in the vortex chamber and the nozzle of the injector. However, both long and short wave response calculations are elaborated, which provides useful knowledge about the injector dynamics in the whole spectrum of frequencies. Also, with regard to question 5, the assessment of inertial and capillary effect of the gaseous core on the response is given. In the numerical part of the thesis, Chapter 7, we will start with setting up the correct boundary conditions based on the information that we have learned in the preceding chapters of the thesis. After that, we will aim to identify the frequencies at which the numerical injector response is maximized, i.e. the injector is at resonance, and compare these frequencies to the analytical ones. The thesis will be concluded with conclusions and recommendations for future work, Chapter 8.

# 2. REVISIONS TO EXISTING THEORY OF SWIRL INJECTOR DYNAMIC RESPONSE

## 2.1 Introduction and General Flow Description

Consider the swirling flow in the swirl injector shown in Fig. 2.1. Notice how this figure schematically shows how the steady axial flow velocity and the disturbance wave characteristics are changing along the injector axis. Let us set definitions for different injector regions according to this figure, Table 2.1. We will explain the origination of additional length $0.5R_n$ in the nozzle entrance transition region in more detail later.

According to the standard flow assumptions (Taylor [6], Bazarov [1, chap. 3], Bayvel and Orzechowski [8], Chinn [4, chap. 3], Niewkamp [60]) that are usually applied in the analysis of the *uniform* regions of the swirl injector, the steady flow is incompressible, inviscid, irrotational, axisymmetric, and the gaseous core is empty. These assumptions lead to the notion of axisymmetric potential flow in the said regions. Note that, since the flow is potential in the uniform regions, it has to be potential in transition regions as well according to Helmholtz theorem of conservation of vorticity.

Now let us go briefly over how exactly the flow disturbances occur inside the injector from the perspective of the terms in the response function, Eq. (1.1).

1. A flow disturbance in propellant delivery line causes a perturbation in the tangential inlets, which results in fluctuation of the incoming mass flow rate, $\dot{m}'_{in}$, and the pressure drop across the inlets, $\Delta p'_t$.

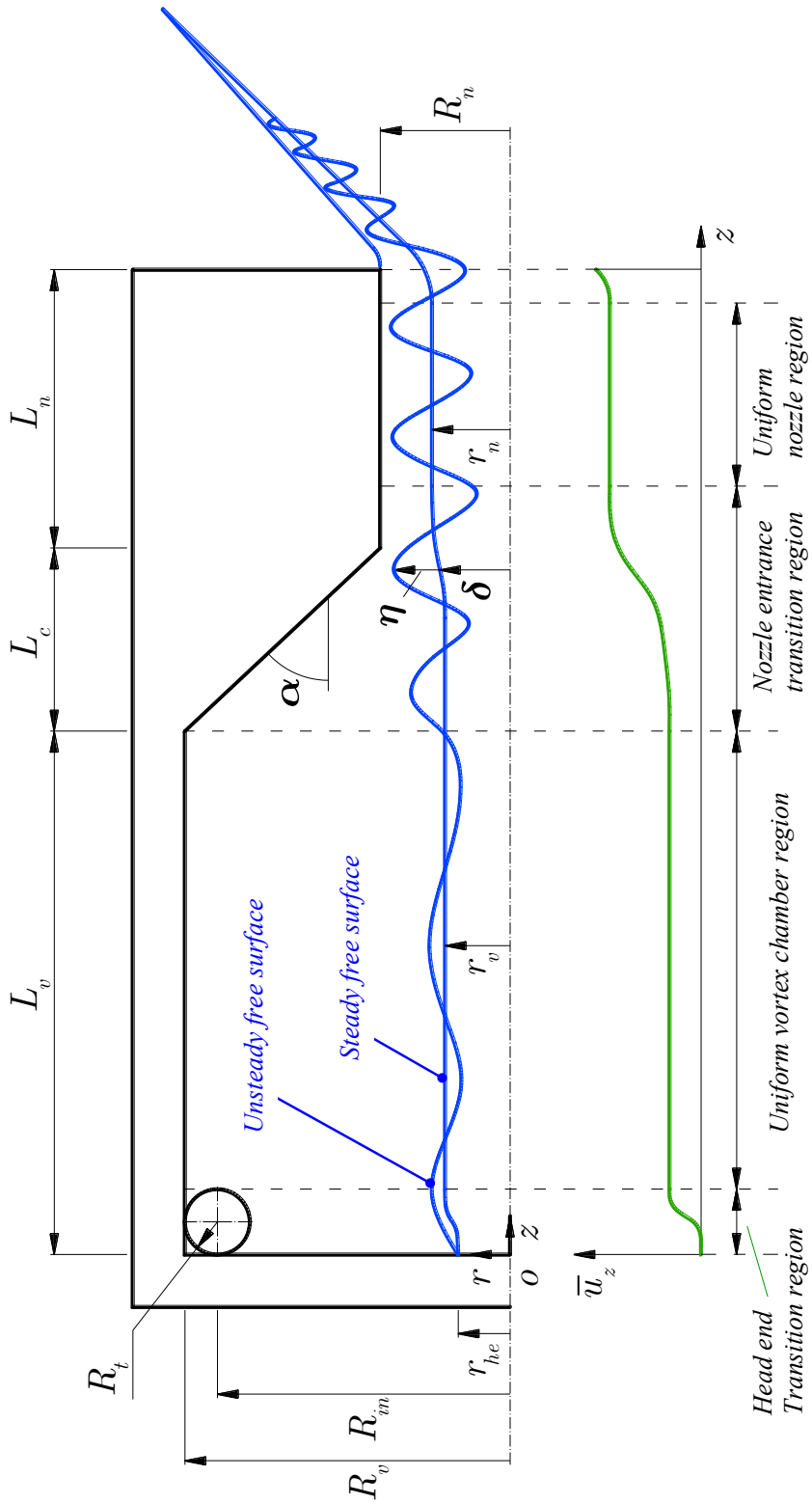


Figure 2.1.: Swirl injector flow schematic

Table 2.1: Definition of swirl injector regions

| **Location** | **Region** |
|---|---|
| z= 0 | head end |
| $0 <$z$\leq 2R_t$ | head end transition |
| $2R_t <$z$\leq L_v$ | uniform vortex chamber |
| $L_v <$z$\leq L_v + L_c + 0.5R_n$ | nozzle entrance transition |
| $L_v + L_c + 0.5R_n <$z$\leq L_v + L_c + L_n$ | uniform nozzle |

2. The fluctuating incoming mass flow rate, $\dot{m}'_{in}$, causes a deflection of the free surface, $\eta$, at the injector head end, which results in fluctuating pressure drop across liquid body at the injector head end, $\Delta p'_{he}$. Sum of $\Delta p'_t$ and $\Delta p'_{he}$ represents the total unsteady pressure drop due to definitions

$$\begin{aligned} \Delta p'_{inj} &= \Delta p'_t + \Delta p'_{he} \\ \Delta \bar{p}_{inj} &= \Delta \bar{p}_t + \Delta \bar{p}_{he} \end{aligned} \tag{2.1}$$

3. A flow disturbance created at the head end propagates downstream, which is viewed by an observer as a surface wave $\eta = \hat{\eta} e^{i(kz-\omega t)}$, where $\hat{\eta}$ is its amplitude, $k$ is the wave number, and $\omega$ is the angular frequency. Eventually, the disturbance reaches the nozzle exit, $z = L_v + L_c + L_n$, which results in corresponding exit mass flow rate fluctuation, $\dot{m}'_n$.

This problem can be also imagined if one starts from the gaseous core:

1. A disturbance, which resulted from combustion instability in the rocket combustion chamber, and is propagating in the gaseous core towards the injector head end, originates the free surface wave, $\eta = \hat{\eta} e^{i(kz-\omega t)}$.

2. The surface wave causes a pressure drop fluctuation at the head end, $p'_{he}$, which means that variable resistance, or static pressure, is applied at the exit of the

tangential inlets/entrance to the vortex chamber. The surface wave also causes variable nozzle exit mass flow rate, $\dot{m}'_n$, at the nozzle exit, $z = L_v + L_c + L_n$.

3. The variable resistance causes fluctuation of the incoming mass flow rate, $\dot{m}'_{in}$, and hence the fluctuation of the pressure drop across the tangential inlets, $\Delta p'_t$.

The important aspect of the potential flow from the circumferential velocity perspective is that it follows the free vortex distribution law given by

$$u_\theta = \frac{C}{r} \tag{2.2}$$

where $C$ is the strength of vortex, or, as we call it in this study, the angular momentum constant. Notice that when the flow is unsteady, we have fluctuations in the tangential inlet velocity, $W_{in} = \bar{W}_{in} + W'_{in}$ (see Fig. 1.1). But this means that the circulation given by $\Gamma = 2\pi R_{in} W_{in}$ is also changing in time, thereby rendering the unsteady flow to be rotational. Then the question arises: will the assumption of potential flow be still valid, if we impose disturbances on the steady flow? We may deal with this problem in two following ways differing in their level of complexity.

The first way, based on the study of infinite swirling hollow columns by Kelvin [24] in 1880 and expanded by Binnie [26] in 1951, is to ignore the fluctuations of circulation induced by unsteady inflow and state that the flow is still potential, so that its instantaneous velocity potential, $\phi = \bar{\phi} + \phi'$, obeys Laplace's equation

$$\frac{\partial^2 \phi}{\partial r^2} + \frac{1}{r}\frac{\partial \phi}{\partial r} + \frac{\partial^2 \phi}{\partial z^2} + \frac{1}{r^2}\frac{\partial^2 \phi}{\partial \theta^2} = 0 \tag{2.3}$$

The free vortex law fits here by stating that

$$\frac{\partial \phi}{\partial \theta} = C = \text{constant} \tag{2.4}$$

so that $\dfrac{1}{r^2}\dfrac{\partial^2 \phi}{\partial \theta^2} = 0$. Then, at some arbitrary point in the flow $(z, r)$ whose say radius fluctuation is given by $r = \bar{r} + r'$, the unsteady parts of the axial and radial flows are linked by the linearized Laplace's equation

$$\frac{\partial^2 \phi'}{\partial r^2} + \frac{1}{r}\frac{\partial \phi'}{\partial r} + \frac{\partial^2 \phi'}{\partial z^2} = 0 \tag{2.5}$$

and the unsteady part of the circumferential velocity comes physically from the equation

$$\frac{1}{r}\frac{\partial \phi}{\partial \theta} = \bar{u}_\theta + u'_\theta = \frac{C}{\bar{r}+r'} = \frac{C}{\bar{r}} - \frac{C}{\bar{r}^2}r' \tag{2.6}$$

where we have used the binomial expansion [61, p. 1196] of the form

$$(\bar{r}+r')^n = \bar{r}^n + n\bar{r}^{n-1}r' + \frac{n\,(n-1)}{2!}\bar{r}^{n-2}(r')^2 + \dots \tag{2.7}$$

up to the first order term. This approach is convenient in its simplicity, however it restricts the flow to be completely irrotational, where the vorticity cannot be generated at any point in the flow. We will see later that this treatment was used by Bazarov [1] when dealing with the surface waves in his dynamic theory. We also will use this approach in this study. More discussion on this subject may be found in [36, Chap. II].

The second alternative, best described in Golubev and Atassi [62] is to split the unsteady part of the velocity vector into rotational and potential parts as

$$\vec{u}' = \vec{u}'^{(R)} + \nabla\phi'$$

where $\vec{u}'^{(R)}$ is the rotational disturbance, and then link them through the mean flow vorticity. This approach describes the flow more realistically, but requires much more effort than Kelvin's approach.

## 2.2 Bazarov's Steady Flow Calculation

This section presents only the key equations needed to compute steady state core radii and velocities at the head end, in the uniform vortex chamber region, and in the uniform nozzle region of the swirl injector (Fig. 2.1, Table 2.1). Complete derivation of these equations can be found in Bazarov [1, sec. 3.1]. Note that Bazarov does not provide steady calculations for the transition regions of the injector.

Provided that one is given the injector parameters $R_v$, $R_t$, $R_n$, $N_{in}$, and $\bar{W}_{in}$, the computation proceeds as follows. First, the geometric characteristic of the injector is computed

$$A_{geom} = \frac{R_{in} R_n}{N_{in} R_t^2} \tag{2.8}$$

Then the coefficient of flow area in the nozzle, $\varphi = 1 - \dfrac{r_n^2}{R_n^2}$, is computed from the implicit relation given by

$$A_{geom} = \frac{(1-\varphi)\sqrt{2}}{\varphi\sqrt{\varphi}} \tag{2.9}$$

which for the core radius in the uniform nozzle region gives

$$r_n = R_n\sqrt{1-\varphi} \tag{2.10}$$

Having $\varphi$, it becomes possible to compute the nondimensional ratio of the head end and nozzle radii

$$a = \frac{2(1-\varphi)^2}{2-\varphi} \tag{2.11}$$

which for the core radius at the head end gives

$$r_{he} = R_n\sqrt{a} \tag{2.12}$$

The injector discharge coefficient is defined as

$$\mu = \frac{\sqrt{a}}{A_{geom}} \tag{2.13}$$

From the implicit relation

$$\mu = \sqrt{1 - \left(\frac{r_{he}}{r_v}\right)^2}\left[\left(\frac{R_v}{R_n}\right)^2 - \frac{\left(\frac{r_{he}}{R_n}\right)^2}{\left(\frac{r_{he}}{r_v}\right)^2}\right] \tag{2.14}$$

we can compute the ratio $r_{he}/r_v$, where $r_{he}$ is already known from Eq. (2.12), and the radius in the uniform vortex chamber region, $r_v$, itself afterwards.

Next, the steady flow velocities (overbar emphasizes steady state) are computed as follows:

- circumferential velocity in any of the above regions from the free vortex law Eq. (2.2), and at the head end radius it is

$$\bar{u}_{\theta he} = \bar{W}_{in}\frac{R_{in}}{r_{he}} \tag{2.15}$$

- axial velocity in the uniform vortex chamber region

$$\bar{u}_{zv} = \frac{\bar{u}_{\theta he}\mu}{R_v^2 - r_v^2} \tag{2.16}$$

- axial velocity in the uniform nozzle region

$$\bar{u}_{zn} = \sqrt{\bar{u}_{zv}^2 + \left(\bar{W}_{in}R_{in}\right)^2\left(\frac{1}{r_v^2} - \frac{1}{r_n^2}\right)} \tag{2.17}$$

The axial velocity at the head end, and the radial velocities in any of the above uniform flow regions, are assumed to be zero.

## 2.3 Nondimensionalization and Baseline Injector

In this study, we use the nozzle radius, $R_n^*$, as the length dimension, and the inflow velocity, $\bar{W}_{in}^*$, as the velocity scaling factor. The dimensional values are denoted by superscript *. Hence, for the parameters that will be often used, we have:

$$\omega^* = \omega\frac{\bar{W}_{in}^*}{R_n^*}, \quad k^* = k\frac{1}{R_n^*}, \quad \phi^* = \phi\bar{W}_{in}^*R_n^*, \quad C^* = C\bar{W}_{in}^*R_n^*$$

Since eventually we will validate theoretical results in this study against Ahn's [55] experimental results, the baseline injector will have the same characteristics as the injector used in his experimental testing [55, App. B] with the sizes outlined in Table 2.2. The baseline steady state pressure drop and convergence angle are: $\Delta\bar{p}_{inj} = 40.3$ psi, $\alpha = 45°$. Applying the methodology described in Section 2.2, we can calculate the steady core radii and velocities, Table 2.3. In conclusion, let us note for future reference that according to the data in Tables 2.2 and 2.3, one unit of nondimensional frequency corresponds to the dimensional frequency equal to

$$\omega^* = 1 \cdot \frac{3.7596 \text{ m/s}}{0.250 \text{ in} \cdot 0.0254 \text{ m/in}} = 592.063 \frac{\text{rad}}{\text{sec}} = 94.230 \text{ Hz}$$

Table 2.2: Baseline injector geometry

| Parameter | Dimensional | Nondimensional |
|---|---|---|
| $R_n$ | 0.250 in | 1.0 |
| $R_{in}$ | 1.125 in | 4.5 |
| $R_t$ | 0.125 in | 0.5 |
| $R_v$ | 1.250 in | 5.0 |
| $L_t$ | 0.450 in | 1.8 |
| $L_n$ | 1.000 in | 4.0 |
| $L_v$ | 5.000 in | 20.0 |
| $N_{in}$ | | 4 |

Table 2.3: Baseline steady core radii and flow velocities

| Parameter | Dimensional | Nondimensional |
|---|---|---|
| $r_{he}$ | 0.17941963 in | 0.71767853 |
| $r_v$ | 0.17942344 in | 0.71769376 |
| $r_n$ | 0.2019 in | 0.8077 |
| $\bar{W}_{in}$ | 3.7596 m/s | 1.0 |
| $\bar{u}_{\theta he}$ | 23.5737 m/s | 6.2702 |
| $\bar{u}_{zv}$ | 0.1535 m/s | 0.0408 |
| $\bar{u}_{zn}$ | 10.8135 m/s | 2.8762 |

## 2.4 Bazarov's Unsteady Flow Calculation

This section presents a brief overview of Bazarov's linear theory describing the dynamics of swirl injectors. A more complete description can be found in the original work of Bazarov [1, Chap. 4], in dissertations by Miller [30] and Richardson [43, Secs. 2.3, 2.4], and in lectures given by Bazarov at Purdue University in spring 2003 [63, Lectures 14–17]. The author has found that the original book of Bazarov and Miller's thesis are more comprehensible in terms of notation. And so, for a more convenient orientation in theoretical equations, the author includes the numbers of corresponding equations in these two references in the form:

- Equations from Bazarov [1, Chap. 4] are written as (Baz No. of Equation)
- Equations from Miller [30] are written as (Mil B. No. of Equation)

Note that there were numerous typographical mistakes in those references, and the author presents his own version of these equation as he deems correct.

Throughout the general revision of Bazarov's equations, the author includes his own remarks with regard to what he thinks may be improved in those equations. These remarks are italicized for distinction from the general text.

Bazarov represents the total injector response in terms of products of the transfer functions of different parts of the injector: the tangential inlet, the vortex chamber, and the nozzle. In the vortex chamber, the response is further divided into two parts that describe effects resulting from propagation of surface waves and vorticity waves. The surface waves are treated by *long wave* approximation. There will be more discussion on this subject further below. Both surface and vorticity waves are formed by the periodic fluctuation of inlet mass flow rate, $\dot{m}'_{in}$, and are defined as follows:

- **Surface waves** are the result of periodic free surface deflection at the injector head end, and they may propagate along the injector axis in both stream wise and counter stream wise directions due to reflections from the nozzle entrance.

- **Vorticity waves** are the result of periodic fluctuation of circumferential velocity at different radial layers of the fluid, and they may propagate only in the radial direction from the upper wall of the vortex chamber to the free surface.

The response analysis systematically proceeds by determining each of the said transfer functions one after another in terms of $\dot{m}'_{in}$. The sequence in this process is schematically shown in Fig. 2.2. In this figure, $\Delta p'_{v2}$ and $\Delta p'_{v3}$ are the fluctuating pressure drops at injector head end due to surface waves and vorticity waves respectively, such that they sum up to $\Delta p'_{v2} + \Delta p'_{v3} = \Delta p'_{he}$ in Eq. (1.1), and $\dot{m}'_{vn}$ is fluctuation of mass flow rate at nozzle entrance ($z = L_v + L_c$). Each of the respective transfer functions will be defined explicitly below.

Bazarov simplifies the internal flow in a swirl injector by dividing it into two ideally cylindrical parts in terms of the flow boundaries: the vortex chamber and the nozzle, as shown in Fig. 2.3. The free surface and solid boundary make a *sudden jump* at the point where the nozzle starts. Except for this discontinuity, both the vortex chamber and the nozzle have axial velocities uniform in $r$, their radial velocities are zero, and the radii of flow boundaries are constant. The length of vortex chamber of this idealized injector is represented as a sum of lengths of vortex chamber and conical convergence section of the general injector. Accordingly, the conical convergence angle is assumed to be 90°.

*The simplified representation of the injector flow with a sudden jump shown in Fig. 2.3 prevents consideration of wave refraction in the nozzle entrance transition region, where the free surface and axial flow velocity vary smoothly and continuously, and the solid boundary has some arbitrary angle of conical convergence different from* 90°. *This would lead to the variation of wave characteristics as the wave propagates over the transition region, and overall represent the flow more realistically. A good introduction on this subject is given in Darmofal [64].*

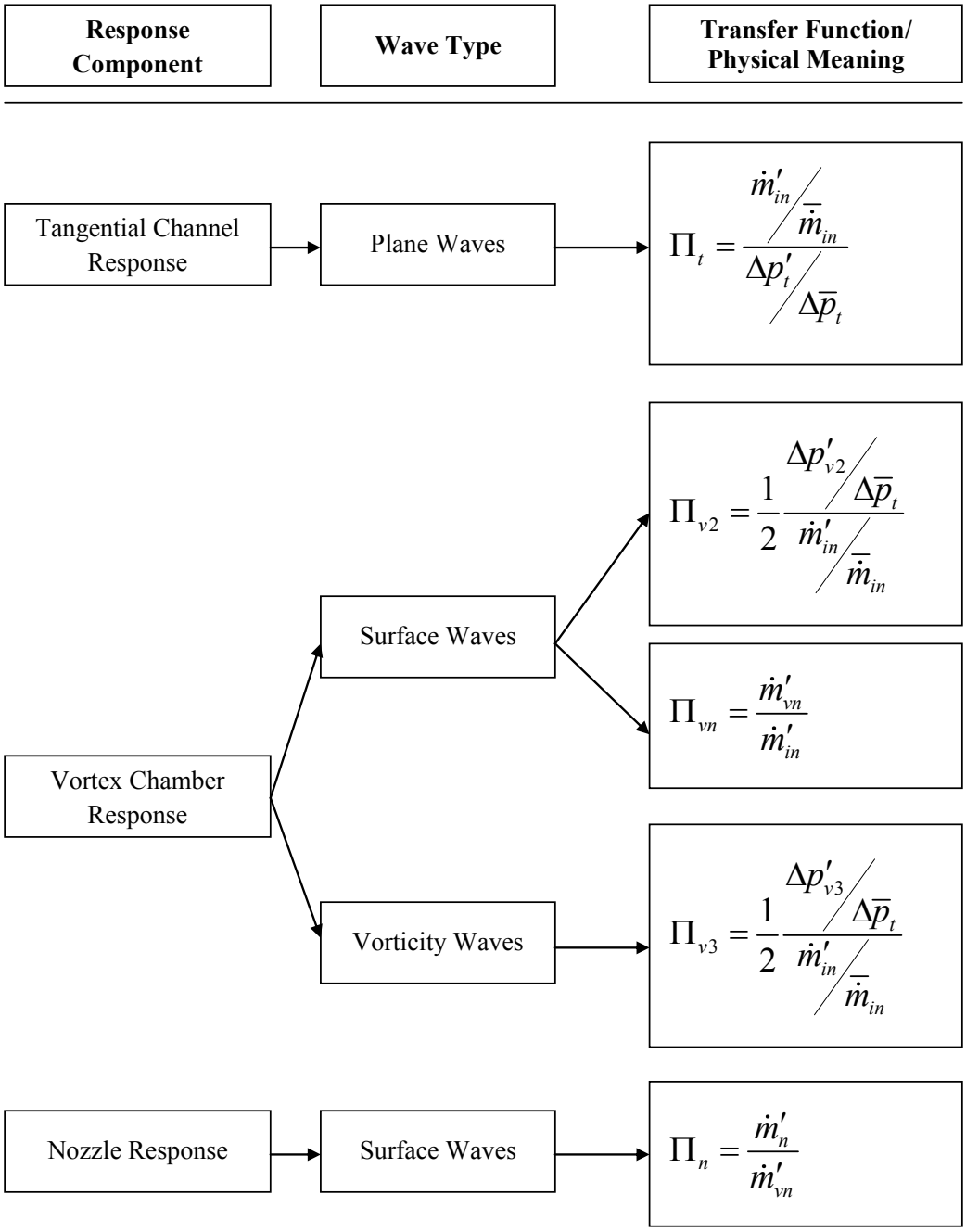


Figure 2.2.: Injector response decomposition by Bazarov

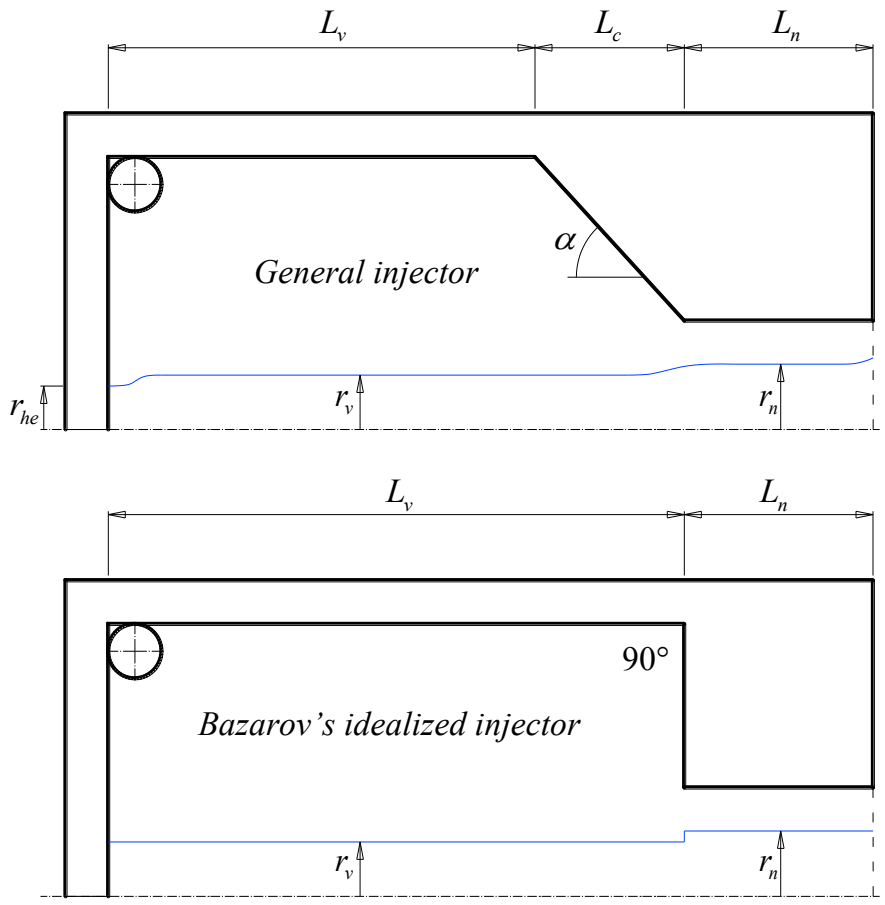


Figure 2.3.: Schematic of Bazarov's idealized injector in unsteady flow calculations

### 2.4.1 Tangential Inlet Response

The unsteady analysis starts with determining the response of the tangential inlet to the input flow velocity disturbance, $W'_{in}$. After defining a Strouhal number [Mil (B.103)] for the tangential inlet as

$$Sh_t = \omega \frac{L_t}{\bar{W}_{in}} \tag{2.18}$$

the **transfer function of the tangential inlet** [Mil (B.105), Baz (3.38)] is given by

$$\Pi_t = \frac{1}{2} \frac{1 - iSh_t}{1 + Sh_t^2} \tag{2.19}$$

### 2.4.2 Vortex Chamber Response to Surface Waves

Next, the surface waves in the vortex chamber are considered. First, a phase shift is defined for the vortex chamber [Mil (B.108), Baz (3.103)]:

$$\Phi_v = \omega \frac{L_v + L_c}{c_v} \tag{2.20}$$

where the wave speed in the uniform vortex chamber region [Baz (3.53)] is given by

$$c_v = \bar{u}_{zv} + \sqrt{C^2 \frac{R_v^2 - r_v^2}{2r_v^4}} \tag{2.21}$$

*The long wave, also known as shallow water, approximation presumes that the radial velocity of a particle anywhere in the flow may be neglected compared to the axial (see analogy with tidal waves in Coulson [65, §41]). This results in a wave speed that does not depend on the disturbance frequency, or is nondispersive, which we see in Eqs. (2.21) and (2.64) for $c_v$ and $c_n$ (below) respectively. This may be realistic for instability processes in the rocket engine, where the combustion instability wave lengths might be several times larger than the injector itself at low frequencies. But what about high frequency instability, when the disturbance wave length may be of the same order as the injector dimension? The dynamic analysis could be more complete and valid at the entire spectrum of frequencies, if one would base the wave speeds on the classical Kelvin's [24] dispersion relation*

$$\frac{\omega}{k} = \bar{u}_z \pm \sqrt{\frac{1}{k} \frac{-I_1(kr_0) + \dfrac{I_1(kR_0)}{K_1(kR_0)} K_1(kr_0)}{I_0(kr_0) + \dfrac{I_1(kR_0)}{K_1(kR_0)} K_0(kr_0)} \frac{C^2}{r_0^3}} \tag{2.22}$$

*where $r_0$ and $R_0$ are the generic free surface and solid boundary radii respectively, and $I$ and $K$ are the modified Bessel functions of orders zero and one. With regard to Bazarov's idealized injector in Fig. 2.3, $r_0$ would take values $r_v$ and $r_n$, and $R_0$ would take values $R_v$ and $R_n$, for the vortex chamber and the nozzle respectively.*

A surface wave traveling from the vortex chamber chamber into the nozzle experiences normal incidence on the straight step discontinuity with subsequent normal

reflection back into the vortex chamber and transmission into the nozzle (see analogy with gravity waves in Mei [66, Sec. 4.2]). The reflected portion would reach the head end wall of the injector, and again have a normal incidence and reflection. This process is assumed to be happening an infinite number of times, with the difference at each new time being that the wave amplitude decays due to viscous damping, which is represented by the artificial viscosity coefficient, $\nu$. The nozzle reflection coefficient [Baz (3.88)] in this process is given by

$$\Pi_{refl} = 1 - 2\frac{\sqrt{\varphi}}{\sqrt{R_v^2 - r_{he}^2}} \tag{2.23}$$

where $\varphi$ is determined from Eq. (2.9).

*From Eq. (2.23) it is clear that Bazarov's nozzle reflection coefficient, $\Pi_{refl}$, is independent of the disturbance frequency. However, from the analogous situation in gravity waves, we know that this dependence should exist. This may be clearly seen if one draws analogy with the classical examples of gravity wave reflections in Miles [67] and Kajiura [68].*

Equations (2.20), (2.21), and (2.23) are then used in the transfer functions describing the above mentioned back and forth reflection in the vortex chamber, which are: the **transfer function of the vortex chamber** [Baz (3.72, 3.110)],

$$\Pi_{v2} = \frac{1}{A_{geom}\sqrt{2\dfrac{(R_v^2 - r_{he}^2)}{R_n^2}}} \sum_{n=0}^{\infty} \Pi_{refl}^n \exp\left(-i \cdot 2n \cdot \Phi_v\right) \exp\left(-2n \cdot \nu \cdot \Phi_v\right) \tag{2.24}$$

and the **transfer function of the nozzle entrance** [Mil (B.119)],

$$\Pi_{vn} = \sum_{n=0}^{\infty} \Pi_{refl}^n \exp\left(-i \cdot (2n+1) \cdot \Phi_v\right) \exp\left(-(2n+1) \cdot \nu \cdot \Phi_v\right) \tag{2.25}$$

*Notice that the wave speed in the vortex chamber, $c_v$ in Eq. (2.21), has a plus sign, which means that the waves described by this equation are traveling strictly downstream. We can also observe that the phase shift $\Phi_v$ in Eq. (2.20), which is based on that wave speed, is used in the surface wave transfer functions, $\Pi_{v2}$ in Eq. (2.24) and $\Pi_{vn}$ in Eq. (2.25), which by definition represent waves traveling in both directions:*

*upstream and downstream. The question is then: should not the waves traveling upstream in these transfer functions be computed with a minus sign? Which would alter the expression for $c_v$ to*

$$c_v = \bar{u}_{zv} - \sqrt{C^2 \frac{R_v^2 - r_v^2}{2r_v^4}} \tag{2.26}$$

*resulting in negative value for $c_v$. Another question to ask is: would the same notion of signs apply if Kelvin's dispersion Eq. (2.22) would be used to calculate the wave speed? And the answer is "yes" to both of these questions if one follows the well known methodology of Peregrine [69, Chap. B]. More discussion on this subject is provided in Appendix B, which clearly resolves these questions, and shows example calculations of the wave characteristics in the long wave limit and in the entire frequency range. Figure 2.4 illustrates the differences between the wave speed used in Bazarov's analysis, Eq. (2.21), and the wave speeds computed computed due to Kelvin' dispersion, Eq. (2.22), for the injector described in Table 2.4 (whose response we will calculate*

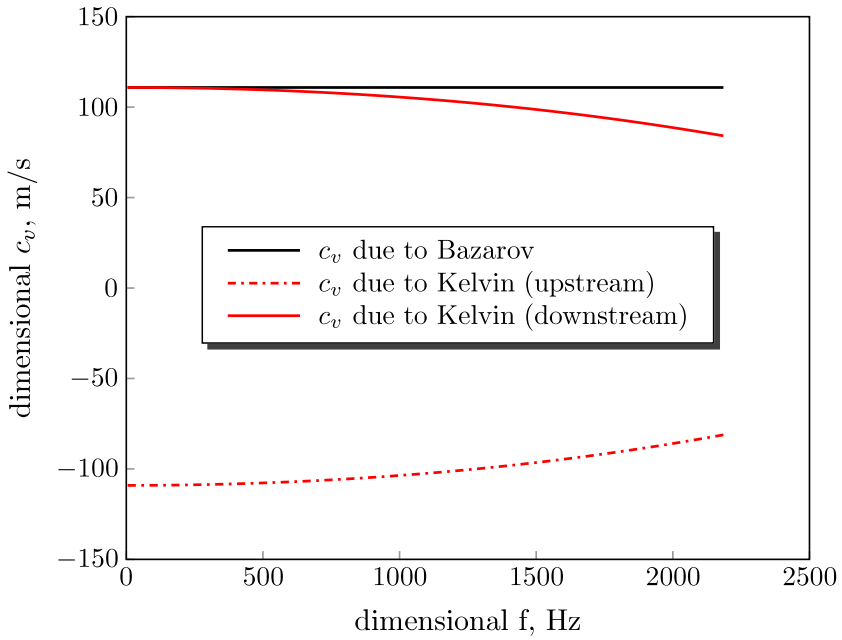


Figure 2.4.: Comparison between wave speeds computed due to Bazarov's Eq. (2.21) and due to Kelvin's Eq. (2.22)

*later on). We can see that the discrepancy grows to a large value at fairly modest frequencies. Also, the negative wave speed for the waves traveling upstream is clearly shown. Overall, this plot represents the ideal case of how the wave speeds should have been calculated in the entire range of disturbance frequencies.*

*In addition, the artificial viscosity, $\nu$, in the transfer functions standing for surface waves in the vortex chamber, $\Pi_{v2}$ in Eq. (2.24) and $\Pi_{vn}$ in Eq. (2.25), may be a heuristic way to damp an infinite number of reflecting waves in the vortex chamber, or otherwise, their sum of amplitudes would grow to infinity. But the steady state calculation of Bazarov shown in Section 2.2 is employing inviscid flow assumption. Then, is it really valid to involve the artificial viscosity?*

In conclusion of this subsection, we shall briefly review the key equations used to derive the infinite sums in transfer functions $\Pi_{v2}$ and $\Pi_{vn}$. We will need this information when we will be examining the overall injector response later on.

**Equations Leading to Infinite Sums in $\Pi_{v2}$ and $\Pi_{vn}$**

Following the discussion on [1, p. 41], the derivation of the infinite sums in $\Pi_{v2}$ and $\Pi_{vn}$ begins with the free surface disturbance at the head end [Baz (3.101)],

$$\eta_{he.1} = \hat{\eta} e^{i\omega t}$$

where the index *he* denotes head end location ($z = 0$) and 1 stands for the original, or first, disturbance. The larger integer numbers will stand for subsequent disturbances respectively. This disturbance propagates downstream with the corresponding phase shift $\Phi_v$ mentioned above in Eq. (2.20) and results in free surface deflection at the nozzle entrance ($z = L_v + L_c$) given by [Baz (3.102)],

$$\eta_{vn.1} = \hat{\eta} e^{i(\omega t - \Phi_v)}$$

where index *vn* indicates the sudden jump location between the vortex chamber and the nozzle (Fig. 2.3). This disturbance reflects back from discontinuity with the

reflection coefficient $\Pi_{refl}$ given by Eq. (2.23) and propagates upstream. Reaching the head end, it deforms the free surface to [Baz (3.105)]

$$\eta_{he.2} = \hat{\eta}\Pi_{refl}e^{i(\omega t-\Phi_v-\Phi_v)} = \hat{\eta}\Pi_{refl}e^{i(\omega t-2\Phi_v)}$$

Notice how Bazarov assumes that the phase shift on the way upstream is exactly same as the original phase shift on the way downstream, and then simply adds them to get $2\Phi_v$. This completes the first cycle of disturbance propagation forth and back. Let us go briefly through one more of such cycles:

- Downstream propagation [Baz (3.106)]

$$\eta_{vn.2} = \hat{\eta}\Pi_{refl}e^{i(\omega t-2\Phi_v-\Phi_v)} = \hat{\eta}\Pi_{refl}e^{i(\omega t-3\Phi_v)}$$

- Upstream propagation

$$\eta_{he.3} = \hat{\eta}\Pi_{refl}\Pi_{refl}e^{i(\omega t-3\Phi_v-\Phi_v)} = \hat{\eta}\Pi^2_{refl}e^{i(\omega t-4\Phi_v)}$$

Notice that on the way back the power of the reflection coefficient has increased by one. In addition, at each step of this process (in both directions), Bazarov adds artificial damping factor in the form $e^{-\nu\Phi_v}$.

Overall, the superposition of the disturbance amplitudes at $z = 0$ and $z = L_v + L_c$ results in infinite sums [Baz (3.108), Baz (3.109)]:

$$\eta_{he} = \hat{\eta}\sum_{n=0}^{\infty}\Pi^n_{refl}e^{i(\omega t-2n\Phi_v)-2\nu n\Phi_v} \tag{2.27}$$

$$\eta_{vn} = \hat{\eta}\sum_{n=0}^{\infty}\Pi^n_{refl}e^{i(\omega t-(2n+1)\Phi_v)-\nu(2n+1)\Phi_v} \tag{2.28}$$

*The difference in* absolute *values of wave speeds computed with either plus or minus signs is small due to small axial stream velocity in the vortex chamber and one might think that the back and forth wave reflection algorithm just shown could be left as it is. However, this may not be done because the negative value of upstream wave speed results in the negative value for the corresponding upstream phase shift. Let us*

*see how exactly this algorithm, and in particular the Eqs. (2.27) and (2.28), would be affected. First note that the vortex chamber phase shift may be rewritten as*

$$\Phi_v = \omega \frac{L_v + L_c}{c_v} = \omega \frac{L_v + L_c}{\omega / k_v} = k_v \left( L_v + L_c \right) \tag{2.29}$$

*Let us denote the wave numbers of downstream and upstream propagating waves by* $k_{v.d}$ *and* $k_{v.u}$ *respectively. It is known that* $k_{v.d}$ *is positive and* $k_{v.u}$ *is negative. Next, let us introduce the corresponding phase shifts:*

$$\Phi_{v.d} = k_{v.d} \left( L_v + L_c \right) \tag{2.30}$$

$$\Phi_{v.u} = \left| k_{v.u} \right| \left( L_v + L_c \right) \tag{2.31}$$

*where we have taken the absolute value of* $k_{v.u}$ *to have a more visual comparison to the always positive phase shift* $\Phi_v$ *given by Eq. (2.20) in Bazarov's analysis. Starting again with the free surface disturbance at the head end,* $\eta_{he.1} = \hat{\eta} e^{i\omega t}$*, we can say that at the nozzle entrance it will be*

$$\eta_{vn.1} = \hat{\eta} e^{i[\omega t - k_{v.d}(L_v + L_c)]} = \hat{\eta} e^{i(\omega t - \Phi_{v.d})}$$

*Reflecting back, it reaches the head end with the value*

$$\eta_{he.2} = \hat{\eta} \Pi_{refl} e^{i[\omega t - k_{v.d}(L_v + L_c) - k_{v.u}(L_v + L_c)]} = \hat{\eta} \Pi_{refl} e^{i(\omega t - \Phi_{v.d} + \Phi_{v.u})}$$

*Accordingly, one more analogous cycle will look like*

$$\begin{aligned}
\eta_{vn.2} &= \hat{\eta} \Pi_{refl} e^{i[\omega t - k_{v.d}(L_v + L_c) - k_{v.u}(L_v + L_c) - k_{v.d}(L_v + L_c)]} \\
&= \hat{\eta} \Pi_{refl} e^{i(\omega t - 2\Phi_{v.d} + \Phi_{v.u})} \\
\eta_{he.3} &= \hat{\eta} \Pi_{refl} \Pi_{refl} e^{i[\omega t - k_{v.d}(L_v + L_c) - k_{v.u}(L_v + L_c) - k_{v.d}(L_v + L_c) - k_{v.u}(L_v + L_c)]} \\
&= \hat{\eta} \Pi_{refl}^2 e^{i(\omega t - 2\Phi_{v.d} + 2\Phi_{v.u})}
\end{aligned}$$

*Notice the alternating sign standing before the upstream and downstream phase shifts,* $\Phi_{v.u}$ *and* $\Phi_{v.d}$*, in these equations. We can summarize then the disturbances at the head end and the nozzle entrance as*

$$\eta_{he} = \hat{\eta} \sum_{n=0}^{\infty} \Pi_{refl}^n e^{i(\omega t - n\Phi_{v.d} + n\Phi_{v.u})} \tag{2.32}$$

$$\eta_{vn} = \hat{\eta} \sum_{n=0}^{\infty} \Pi_{refl}^{n} e^{i(\omega t - (n+1)\Phi_{v.d} + n\Phi_{v.u})} \tag{2.33}$$

*Regarding the viscous damping, by looking at Eqs. (2.24) and (2.25), we can see that, when the wave travels in either direction, upstream or downstream, its amplitude should only decay, and this is why we can include the viscous exponential factor,* $e^{-\nu\Phi_v}$*, in the last two equations in the form:*

$$\eta_{he} = \hat{\eta} \sum_{n=0}^{\infty} \Pi_{refl}^{n} e^{i(\omega t - n\Phi_{v.d} + n\Phi_{v.u}) - \nu n(\Phi_{v.d} + \Phi_{v.u})} \tag{2.34}$$

$$\eta_{vn} = \hat{\eta} \sum_{n=0}^{\infty} \Pi_{refl}^{n} e^{i(\omega t - (n+1)\Phi_{v.d} + n\Phi_{v.u}) - \nu[(n+1)\Phi_{v.d} + n\Phi_{v.u}]} \tag{2.35}$$

### 2.4.3 Vortex Chamber Response to Vorticity Waves

Further, the vorticity waves in the vortex chamber are considered. First, the Strouhal number for the vortex chamber [Mil (B.172)] is defined:

$$Sh_v = \omega \frac{R_v}{\bar{u}_{zv}} \tag{2.36}$$

Second, a new function [Baz (4.57)] and an integration constant are introduced:

$$f(\bar{x}) = \bar{x} Sh_v \tan\left(\frac{\pi}{2}\bar{x}\right) \tag{2.37}$$

$$C_{int} = 1 - \frac{r_{he}}{R_v} \tag{2.38}$$

The last two expressions are then used in the **transfer function of the vortex chamber due to vorticity waves** [Baz (4.59, 4.60), Mil (B.169, B.170)],

$$\Pi_{v3} = \mathrm{Re}(\Pi_{v3}) + i\mathrm{Im}(\Pi_{v3}) \tag{2.39}$$

whose real and imaginary parts are:

$$\mathrm{Re}(\Pi_{v3}) = +2 \int_0^1 \frac{\cos(f(\bar{x}))}{(1 - C_{int}\bar{x})^3} \exp(-\nu f(\bar{x}))\, d\bar{x}$$

$$\mathrm{Im}(\Pi_{v3}) = -2 \int_0^1 \frac{\sin(f(\bar{x}))}{(1 - C_{int}\bar{x})^3} \exp(-\nu f(\bar{x}))\, d\bar{x} \tag{2.40}$$

We can argue with some of the assumptions pertaining to Bazarov's analysis of vorticity waves if we investigate the origin of the integrals in the function $\Pi_{v3}$, Eq. (2.40), which we will do next.

**Equations Leading to Integrals in $\Pi_{v3}$**

Steady Radial Velocity at Injector Head End

Bazarov's treatment of the vorticity starts from the statement that a *steady* process of liquid issuing from the tangential inlet into the vortex chamber is analogous to the process of conformal mapping of a point lying in the complex half-strip of width $\pi$ in plane $Z$ (with coordinates $X$, $Y$) onto its image lying in the complex half-plane in plane $\zeta$ (with coordinates $U$, $V$), Fig. 2.5. The sole purpose of doing this is to obtain the dependence of steady radial velocity at the injector head end, $\bar{u}_r$, on the radius $r$ for further use in the computation of the phase lag in the vorticity waves. Capital letters are introduced to distinguish the complex plane coordinates from the cylindrical coordinates that we have been using so far. In addition, symbol $w$ is introduced to denote the velocity in $Z$ plane. Such mapping is accomplished by

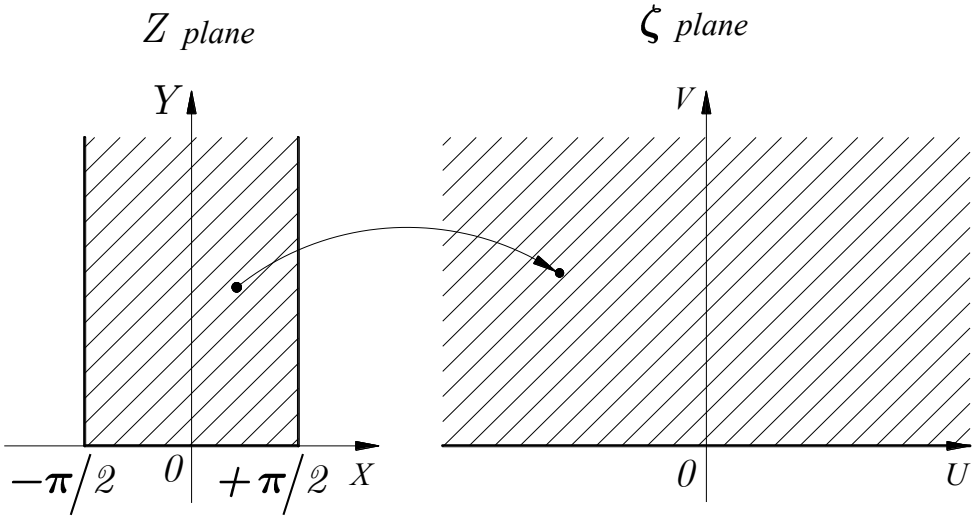


Figure 2.5.: Schematic of conformal mapping of halp-strip into half-plane

a transformation given by [70] and [Baz (4.26)]:

$$\zeta = U + iV = \sin Z = \sin X \cosh Y + i \cos X \sinh Y \tag{2.41}$$

Figure 2.6 shows how the half-strip coordinates ($X$, $Y$) and velocities ($w_X$, $w_Y$) are related to those of the swirl injector ($r$, $z$) and ($\bar{u}_r$, $\bar{u}_z$, $\bar{u}_\theta$). The origin of $Z$ plane is located at the head end ($z = 0$), at the exit of the tangential inlet ($r = R_v$). The real axis $X$ is tangent to the cylindrical vortex chamber wall and lies in plane of the head end ($z = 0$). The imaginary axis $Y$ is parallel to the injector axis $z$.

A point in $Z$ plane is allowed to move from $X = 0$ to $X = \pi/2$ along a straight line coincident with the real axis. While it moves in such way, the real fluid particle travels from the tangential inlet exit toward the injector axis following a spiral path, and reaches the mean free surface radius at the head end, $r_{he}$ (see Fig. 2.6). The radial position $r$ in the fluid particle trajectory is described in terms of $X$ as [Baz (4.35)]

$$\frac{r}{R_v} = 1 - \left[ \left( 1 - \frac{r_{he}}{R_v} \right) \frac{2}{\pi} X \right] \tag{2.42}$$

From this equation $X$ may be written in terms of $r$ as

$$X = \frac{1 - {}^{r}/_{R_v}}{1 - {}^{r_{he}}/_{R_v}} \frac{\pi}{2} \tag{2.43}$$

Note that, when $X = \pi/2$, $r = r_{he}$, and when $X = 0$, $r = R_v$. The axial position $Y$ in this trajectory is exactly equal to cylindrical axial coordinate $z$ without any transformation.

Next, Bazarov states that there exists a velocity potential in plane $\zeta$ that corresponds to a source flow and is given by [Baz (4.46)] as

$$\phi_\zeta = Q \ln |\zeta| \tag{2.44}$$

where $Q$ is its strength. The velocities $w_X$ and $w_Y$, with which the point moves in the $Z$ plane, are found from this velocity potential as

$$w_X = \frac{\partial \phi_\zeta}{\partial X} \qquad \text{and} \qquad w_Y = \frac{\partial \phi_\zeta}{\partial Y} \tag{2.45}$$

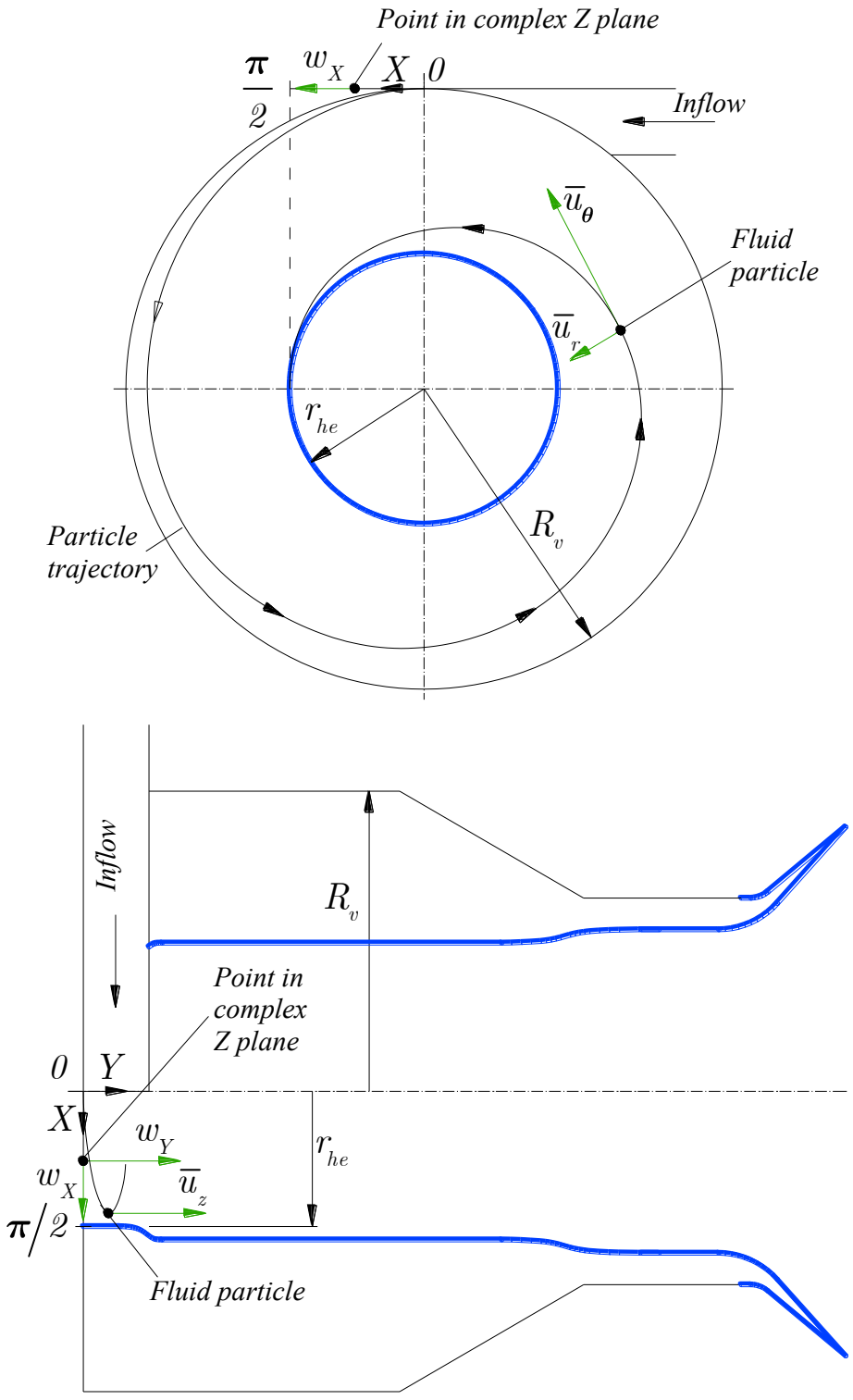


Figure 2.6.: Schematic relating coordinates and velocities of complex halp-strip to those of swirl injector

By combining Eqs. (2.41)–(2.45), the explicit relations for velocities are obtained [Baz (4.48), (4.49)]:

$$w_X = Q\frac{\sin X \cos X}{(\sin X)^2 + (\cosh Y)^2} \tag{2.46}$$

$$w_Y = Q\frac{\sinh Y \cosh Y}{(\sin X)^2 + (\sinh Y)^2} \tag{2.47}$$

These velocities are then presumed to be equal to the steady axial and radial velocities of the real fluid particle,

$$\bar{u}_z = w_Y \qquad \text{and} \qquad \bar{u}_r = w_X \tag{2.48}$$

To find the strength of source, $Q$, Bazarov considers the boundary condition at $Y = \infty$, where $w_Y$ in Eq. (2.47) reduces simply to $Q$, and the axial velocity $\bar{u}_z$ of the real liquid particle is considered to reach the value of finite axial velocity in the vortex chamber, $\bar{u}_{zv}$. Combination of these two limit conditions gives

$$w_Y(Y = \infty) = Q = \bar{u}_{zv} \tag{2.49}$$

Further, the radial velocity of fluid particle in the plane of the head end is considered. At this location, $Y = 0$ and $w_X$ in Eq. (2.46) reduces to $Q \cot X$ [Baz (4.50)], so

$$\bar{u}_r\,(z = 0) = w_X(Y = 0) = Q \cot X \tag{2.50}$$

Combination of Eqs. (2.43), (2.49), and (2.50) gives the final expression for the steady radial velocity at the injector head end [Baz (4.51)]

$$\bar{u}_r = \bar{u}_{zv} \cot\left(\frac{1 - {}^{r}/_{R_v}}{1 - {}^{r_{he}}/_{R_v}}\frac{\pi}{2}\right) \tag{2.51}$$

*Bazarov's method to calculate the steady radial velocity, $\bar{u}_r$, at the injector head ($z = 0$) is based on the analogy of the process of liquid issuing from the tangential inlet into the vortex chamber to the process of conformal mapping of a point lying in the complex infinite half-strip into a point lying in the complex infinite half-plane. We can prove that this analogy does not hold true for the idealized steady swirl injector flow assumed in his theory. In Section 2.1 we have mentioned that, at steady state,*

*the flow has to be potential at all points of the injector to conserve zero vorticity, or in other words, it has to satisfy the Laplace's equation. At the head end, we can write the latter in the form of continuity*

$$\frac{\partial \bar{u}_r}{\partial r} + \frac{\bar{u}_r}{r} + \frac{1}{r}\frac{\partial \bar{u}_\theta}{\partial \theta} + \frac{\partial \bar{u}_z}{\partial z} = 0 \qquad (at\ z = 0)$$

*From Eq. (2.54), which comes later below, since* $\bar{u}_\theta = C/r$, *we know that* $\frac{1}{r}\frac{\partial \bar{u}_\theta}{\partial \theta} = 0$. *Also, we know that* $\bar{u}_z = 0$, *since the wall at the head end is nonpermeable. Then only the radial velocity, given by Eq. (2.51), is left that has to obey continuity. By introducing a constant*

$$\gamma = \frac{1}{1 - {}^{r_{he}}/_{R_v}}\frac{\pi}{2}$$

*we can rewrite the left hand side of continuity equation as*

$$\frac{\partial \bar{u}_r}{\partial r} + \frac{1}{r}\bar{u}_r = \bar{u}_{zv}\frac{-1}{\left[\sin\left(\left(1 - {}^{r}/_{R_v}\right)\gamma\right)\right]^2}\frac{-\gamma}{R_v} + \frac{\bar{u}_{zv}}{r}\frac{\cos\left[\left(1 - {}^{r}/_{R_v}\right)\gamma\right]}{\sin\left[\left(1 - {}^{r}/_{R_v}\right)\gamma\right]}$$

*which is equal to zero only if*

$$\frac{\gamma}{R_v} + \frac{1}{r}\cos\left[\left(1 - {}^{r}/_{R_v}\right)\gamma\right]\sin\left[\left(1 - {}^{r}/_{R_v}\right)\gamma\right] = 0$$

*This equality should hold for all radii. Suppose* $r = R_v$, *then it reduces to* $\gamma/R_v = 0$, *which is not true, since* $\gamma \neq 0$. *Hence, Bazarov's radial velocity* $\bar{u}_r$, *Eq. (2.51), does not satisfy the irrotational flow condition assumed by the problem statement.*

Vorticity Wave Representation

Proceeding next to defining the contribution of vorticity waves to the instantaneous pressure drop through the injector, Bazarov considers again the situation strictly at the head end. He starts from the definition describing part of the pressure drop which is caused by the vorticity waves (see discussion at p. 25, Fig. 2.2, and [Baz (4.18)]),

$$\Delta p_{v3} = \Delta \bar{p}_{v3} + \Delta p'_{v3} = \rho \int_{r_{he}}^{R_v} \frac{u_\theta^2}{r} dr = \rho \int_{r_{he}}^{R_v} \frac{(\bar{u}_\theta)^2 + 2\bar{u}_\theta u'_\theta + (u'_\theta)^2}{r} dr \qquad (2.52)$$

We shall emphasize here that, even though this calculation is unsteady, the free surface at the head end is considered by Bazarov to be steady and described by radius $r_{he}$, which is the lower limit of the integral.

*This serves as a convenient mechanism to separate the vorticity waves from the surface waves. At the same time, because the surface waves are inherently present and the flow is unsteady, the assumption of steady free surface radius at the head becomes inconsistent. In essence, the surface waves cannot be separated from the vorticity waves because both of these processes occur simultaneously.*

*In addition, from Eq. (2.52), we can see that the contribution of the vorticity waves to the pressure drop through the liquid film is based solely on the centrifugal forces*

$$\Delta p_{v3} = \rho \int_{r_{he}}^{R_v} \frac{u_\theta^2}{r} dr$$

*On the other hand, we can say that, because the steady radial velocity $\bar{u}_r$ does exist, as was postulated for the treatment of vorticity waves and calculated by Bazarov in Eq. (2.51), then its fluctuation should also exist. Together, they also should contribute to the unsteady pressure drop. This can be shown, if from the general radial momentum*

$$\frac{\partial u_r}{\partial t} + u_r \frac{\partial u_r}{\partial r} - \frac{u_\theta^2}{r} + u_z \frac{\partial u_r}{\partial z} = -\frac{1}{\rho}\frac{\partial p}{\partial r} \qquad at\ z = 0$$

*the pressure drop is drawn, by noting that $u_z = 0$ at $z = 0$, which results in*

$$\Delta p_{v3} = \rho \int_{r_{he}}^{R_v} \frac{u_\theta^2}{r} dr - \frac{\rho}{2} \int_{r_{he}}^{R_v} \frac{\partial \left(u_r^2\right)}{\partial r} dr - \rho \int_{r_{he}}^{R_v} \frac{\partial u_r}{\partial t} dr$$

Next, neglecting the higher order term, the unsteady part of the pressure drop [Baz (4.19)] from Eq. (2.52) is

$$\Delta p'_{v3} = 2\rho \bar{u}_\theta \int_{r_{he}}^{R_v} \frac{u'_\theta}{r} dr \tag{2.53}$$

The steady part of the circumferential velocity is assumed to obey the *free vortex* distribution [Baz (4.52)],

$$\bar{u}_\theta = \bar{W}_{in} \frac{R_{in}}{r} \tag{2.54}$$

However, its fluctuating part is assumed to have a phase lag, $\Phi_{he}$, and is written as [Baz (4.53)]

$$u'_\theta(r,t) = W'_{in} \cdot \exp\left[i\left(\omega t - \Phi_{he}\right)\right] \cdot \frac{R_{in}}{r} \tag{2.55}$$

This expression represents the essence of the notion of vorticity waves. It shows that the angular momentum is allowed to vary in time and radial direction, which automatically makes the flow in this unsteady problem to be rotational (in an irrotational free vortex, the angular momentum would not be allowed to vary at all [36, Chap. II], Currie [71, Sec. 4.4]).

After that, substitution of Eqs. (2.54) and (2.55) into Eq. (2.53) gives an intermediate expression for the fluctuating pressure drop

$$\Delta p'_{v3} = 2\rho \bar{W}_{in} W'_{in} \cdot R_{in}^2 \cdot \int_{r_{he}}^{R_v} \frac{\exp\left[i\left(\omega t - \Phi_{he}\right)\right]}{r^3} dr \tag{2.56}$$

The phase lag is computed with the radial velocity, Eq. (2.51), that we have obtained previously [Baz (4.53)],

$$\Phi_{he} = \omega \frac{R_v - r}{\bar{u}_r} = \omega \frac{R_v - r}{\bar{u}_{zv}} \tan\left(\frac{1 - {}^{r}/_{R_v}}{1 - {}^{r_{he}}/_{R_v}} \frac{\pi}{2}\right) \tag{2.57}$$

*The corresponding time lag is then* $\Delta t = \dfrac{R_v - r}{\bar{u}_r}$. *Note that it is computed with the current radial velocity and radial position of the particle. However, as the particle travels the from the cylindrical wall of vortex chamber to some particular point on its spiral trajectory, its radial velocity is also changing (see Fig. 2.6). Consider an infinitesimally small distance* $dr$ *travelled by a particle during an infinitesimal time period* $dt$. *With the current radial velocity of the particle, the time elapsed for this travel is* $dt = dr/\bar{u}_r$. *Then, the total time it takes for a particle to travel from* $R_v$ *to* $r$ *is*

$$\Delta t = \int_r^{R_v} dt = \int_r^{R_v} \frac{d\tilde{r}}{\bar{u}_r\left(\tilde{r}\right)}$$

*where $\tilde{r}$ is a dummy radius. Only when $\bar{u}_r$ is not a function of $r$, this expression becomes $(R_v - r)/\bar{u}_r$. This means that the correct expression for the phase lag should be*

$$\Phi_{he} = \omega \int_{r}^{R_v} \frac{d\tilde{r}}{\bar{u}_r\left(\tilde{r}\right)}$$

Finally, proceeding to the response function due to vorticity waves, $\Pi_{v3}$, its definition shown in Fig. 2.2 is rewritten as

$$\Pi_{v3} = \frac{1}{2}\frac{\Delta p'_{v3}}{\Delta \bar{p}_t}\frac{\bar{W}_{in}}{W'_{in}} \tag{2.58}$$

where

$$\Delta \bar{p}_t = \rho\frac{\left(\bar{W}_{in}\right)^2}{2} \tag{2.59}$$

is the Bazarov's state pressure drop through the tangential inlet. Considering this last definition, the response function can be rewritten as

$$\Pi_{v3} = \frac{\Delta p'_{v3}}{\rho \bar{W}_{in} W'_{in}} \tag{2.60}$$

Plugging in the Eqs. (2.56) and (2.57), $\Pi_{v3}$ becomes

$$\Pi_{v3} = 2 \cdot R_{in}^2 \cdot \int_{r_{he}}^{R_v} \exp\left[i\left\{\omega t - \omega\frac{R_v - r}{\bar{u}_{zv}}\tan\left(\frac{1 - {}^{r}/_{R_v}}{1 - {}^{r_{he}}/_{R_v}}\frac{\pi}{2}\right)\right\}\right]\frac{dr}{r^3} \tag{2.61}$$

At this point, Bazarov states that the friction causes different layers of the liquid swirling with uneven angular momentum to exchange energy and thus viscous damping should be introduced to reflect this phenomenon. This alters the last expression for $\Pi_{v3}$ to

$$\Pi_{v3} = 2 \cdot R_{in}^2 \cdot \int_{r_{he}}^{R_v} \exp\left[i\left\{\omega t - \Phi_{he}\right\}\right] \cdot \exp\left(-\nu\Phi_{he}\right) \cdot \frac{dr}{r^3} \tag{2.62}$$

*Nonetheless, similarly to the remark regarding the viscous damping of the surface waves above, it is not completely evident why doing so is possible.*

There are series of manipulations after this step to obtain the final form of $\Pi_{v3}$ as given in Eqs. (2.39) and (2.40), however the equations presented here embody the essential ones needed to understand the vorticity wave treatment and the origination of the integrals in Eq. (2.40).

### 2.4.4 Nozzle Response

Finally, advancing to the nozzle response, first the phase shift for the nozzle [Mil (B.181)] is defined:

$$\Phi_n = \omega \frac{L_n}{c_n} \tag{2.63}$$

where the wave speed in the uniform nozzle region is given by

$$c_n = \bar{u}_{zn} + \sqrt{C^2 \frac{R_n^2 - r_n^2}{2r_n^4}} = 2\bar{u}_{zn} \tag{2.64}$$

Then both of these equations are subsequently used in the **nozzle transfer function** [Mil (B.180)],

$$\Pi_n = (1 - \Pi_{refl}) \exp(-i\Phi_n) \tag{2.65}$$

### 2.4.5 Overall Injector Response

The concluding step in this analysis is to combine all transfer functions above into the **total injector response** [Baz (4.73)]:

$$\Pi_{inj} = \left(\frac{R_v}{r_{he}}\right)^2 \frac{\Pi_t \Pi_{vn} \Pi_n}{1 + 2\Pi_t (\Pi_{v2} + \Pi_{v3})} \tag{2.66}$$

It is of instructional interest to show the application of these equations on the injector provided at Bazarov [1, p. 67], whose parameters given are summarized in Table 2.4. Note that the value of artificial viscocity coefficient, $\nu$, was taken to be 0.1 from [1, p. 130], where he describes a graphical solution for injector response. In order to have a complete description of injector geometry from this table, we need to have the nondimensional radius of the tangential inlet, $R_t$, and the dimensional nozzle radius, $R_n^*$. To find $R_t$ we can employ the definition of the geometric characteristic as follows:

$$A_{geom} = \frac{R_{in} R_n}{N_{in} R_t^2} = \frac{(R_v - R_t) R_n}{N_{in} R_t^2}$$

which gives quadratic equation for $R_t$ in form

$$N_{in} A_{geom} R_t^2 + R_n R_t - R_v R_n = 0$$

Table 2.4: Parameters of swirl injector described in Bazarov [1, p. 67]

| **Parameter** | **Value** | **Units** |
|---|---|---|
| $A_{geom}$ | 3.0 | |
| $R_v$ | 3.0 | |
| $L_v^*$ | 25.0 | mm |
| $R_{in}^*$ | 7.0 | mm |
| $L_n^*$ | 8.0 | mm |
| $L_t^*$ | 2.0 | mm |
| $\alpha$ | 90.0 | degrees |
| $\Delta\bar{p}_{inj}^*$ | 0.6 | MPa |
| $\nu$ | 0.1 | |

where from

$$R_t = \frac{-R_n + \sqrt{R_n^2 + 4N_{in}A_{geom}R_vR_n}}{2N_{in}A_{geom}} \tag{2.67}$$

Note that $R_n = 1$ in this study (see Section 2.3). Then, we can immediately compute

$$R_n^* = \frac{R_{in}^*}{R_v - R_t} \tag{2.68}$$

The above equations from Sections 2.2 and 2.4 are implemented into the MatLab code (Appendix A) that computes the response for the injector in Table 2.4. The response plot produced is shown in Fig. 2.7. Notice that it is very close to the one shown in Bazarov [1, Fig. 23].

*If the wave speeds would be corrected and follow from Kelvin's dispersion Eq. (2.22), then how would that affect the overall injector response (shown in Fig. 2.7)? At this point, we cannot answer this question completely, because the entire calculation of the injector response would have been different to reflect this change. However, just for illustrative purposes, we will calculate the response by using Kelvin's wave speeds shown in Fig. 2.4 and the corrected back-and-forth reflection algorithm shown in the end of Subsection 2.4.2 by leaving everything else unchanged. This produces the response*

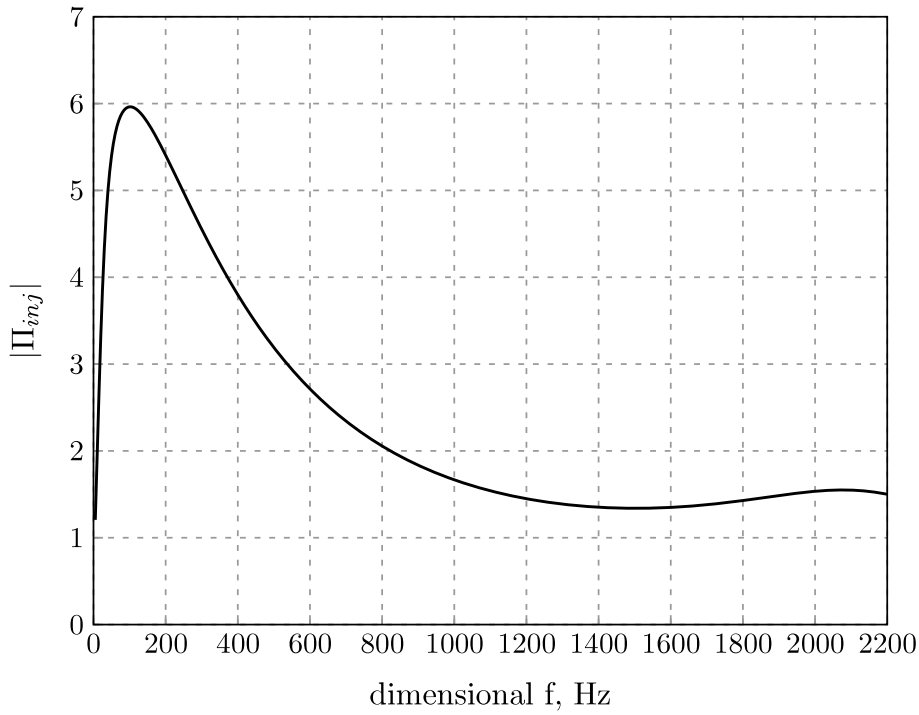


Figure 2.7.: Response of injector in Bazarov [1, Fig. 23], Table 2.4

*curve shown in Fig. 2.8. This plot suggests that at higher frequencies the response will be lower than predicted originally. Which might be expected because the instability waves disturbing the free surface may become so short, that the flow would not "feel" them in terms of the nozzle mass flow rate.*

*What would happen to the injector response (shown in Fig. 2.7) if we would change the value of artificial viscosity coefficient, $\nu$, leaving all equations involved in the response calculation unaltered? Figure 2.9 shows the sensitivity of the response if $\nu$ becomes either smaller or larger relative to baseline value of 0.1. We can see that the response does have a strong sensitivity to the value of $\nu$. This clearly indicates that the choice of $\nu$ is critical. Now, since this coefficient is by definition artificial, which was made up to simulate viscous damping effects, Bazarov does not indicate the ways of how it is chosen or calculated. This causes the need to acquire the knowledge of how to characterize the whole notion of artificial viscosity in future.*

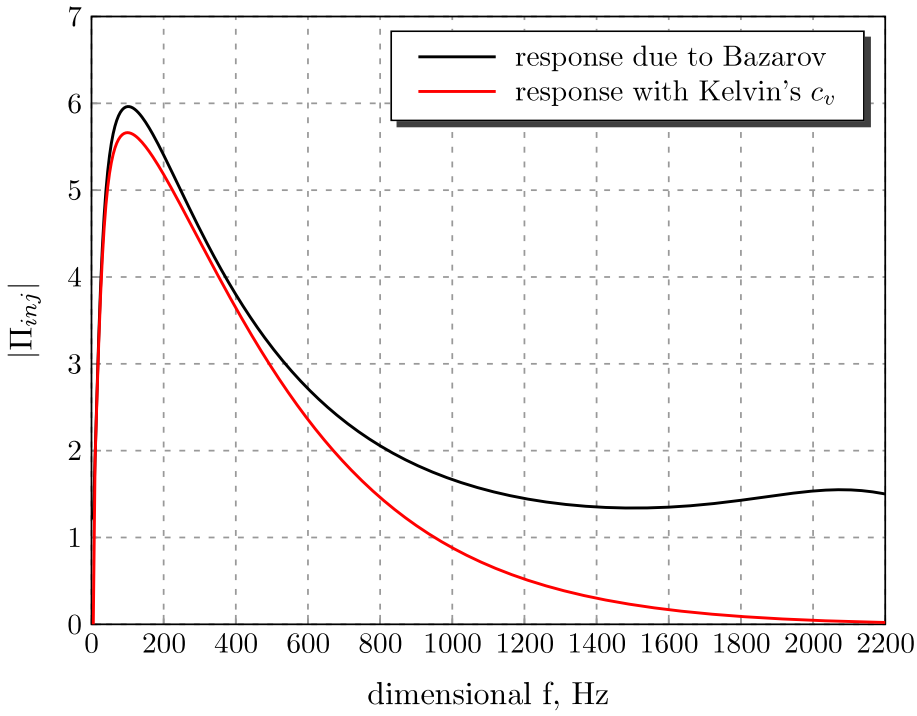


Figure 2.8.: Influence of short wave speeds on Bazarov's injector response

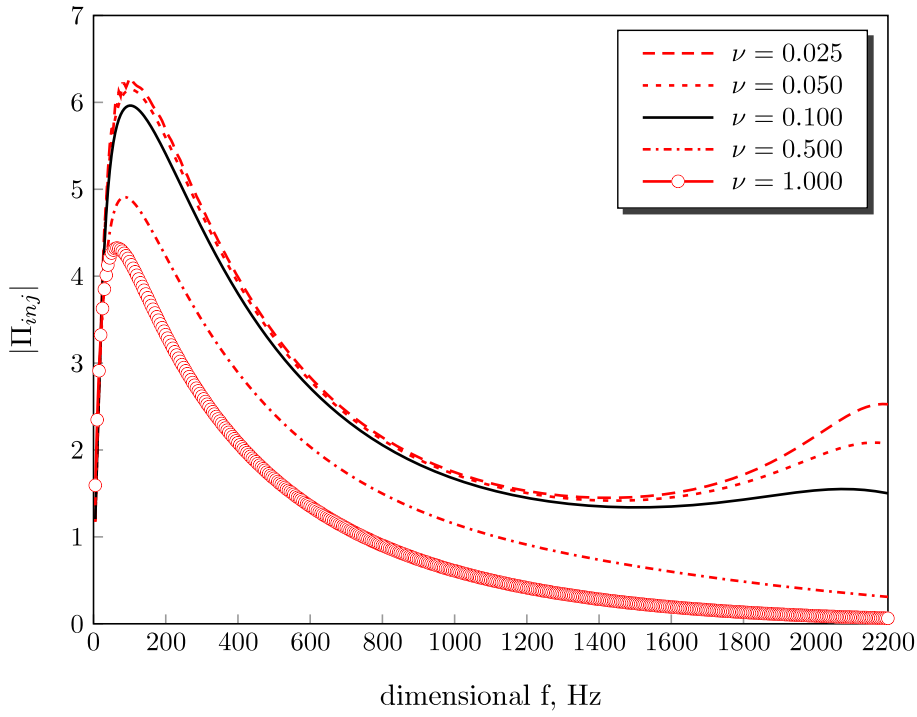


Figure 2.9.: Sensitivity of Bazarov's injector response to artificial viscosity coefficient

*With regard to both sensitivities of the injector response to Kelvin's wave speeds and value of $\nu$, let us discuss Bazarov's experimental data that was summarized in [1, Fig. 54]. Note that his experimental injector had different characteristics than in Table 2.4. To simplify referencing, it is reproduced here by reading the data from it on a point-by-point basis and is shown in Fig. 2.10. It can be observed that the points lie relatively well on theoretical curves, except the region of higher frequencies starting from 1000 Hz. We can also note that there is a relatively larger discrepancy for the point of 700 Hz at 1.2 Mpa. These errors may be attributed to the following possible reasons: (a) at higher frequencies, short wave effects start to appear, and (b) the chosen value of $\nu$ might not be appropriate for all frequencies.*

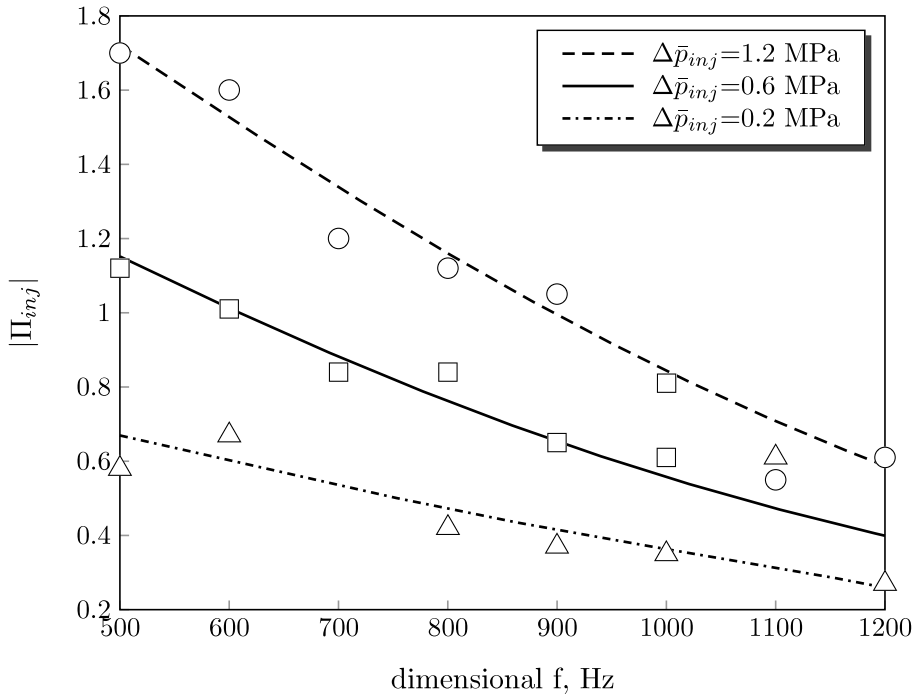


Figure 2.10.: Comparison of Bazarov's experimental data in [1, Fig. 54] vs. Bazarov's linear theory [1, Chap. 4]

## 2.5 Conclusions

In this chapter we have shown the up-to-date treatment of both steady and unsteady flows in swirl injectors based on Bazarov's theory [1]. We have focused on this particular reference, because Bazarov's dynamic analysis is the most known and cited reference on the subject.

Bazarov's steady state calculation follows along the common lines of treating the flow as being potential (see references in Chapter 1). Therefore, we used it in this chapter to calculate the steady flow characteristic of the baseline injector, Table 2.3.

The unsteady calculation by Bazarov, however, has caused many questions in the area of stating and subsequently handling the unsteady flow assumptions. The majority of those questions is related to the calculation of phase shifts involved in the description of traveling surface and vorticity waves, and to the presence of the artificial viscosity coefficient used to simulate viscous damping (Section 2.4). In addition, we have also encountered some fundamental limitations of the analysis, such as the simplified representation of the free surface with a sudden jump at the nozzle entrance, Fig. 2.3, or the independence of the nozzle reflection coefficient from the disturbance frequency, Eq. (2.23). This completely eliminates the possibility to assess the wave refraction effects and indicates that the reflection is not considered in a sufficient manner. The comparison of experimental data to theoretical curves in Fig. 2.10 suggests that the deficiencies of Bazarov's analysis, which we have indicated, might be the leading cause.

Overall, Bazarov's dynamic analysis is pioneering in terms of the depth of description of the unsteady flow in swirl injectors. It gives the big picture of what to look for and what could be done to improve the theory. But due to the shortcomings indicated above, the question arises whether we can use it for further injector dynamics calculations without first correcting it.

# 3. FREE SURFACE SHAPE IN TRANSITION REGIONS OF SWIRL INJECTOR

## 3.1 Introduction

Let us see the images of the free surface in the nozzle transition region taken from BEM simulations and from experimental testing. In Fig. 3.1, the transition region is shown for the baseline injector (Sec. 2.3) with conical convergence angle of 45°, and other identical injectors with the angles 30°, 60°, and 90°. For convenience, all injectors were lined up so that their nozzles start at $z = 0$. Observe that no matter what convergence angle is, the free surface is (a) transitioning smoothly and (b) is approximately same in form. Notice a slight "hump" occurring at $z = 0.5$, and that downstream of it, the radius of the free surface does not change much, which can be seen more evidently in Fig. 3.2, where the axes are scaled equally. Physically, this "hump" reflects how the radial, axial, and circumferential velocities redistribute themselves in the transition region in order for the flow, moving slowly in the vortex chamber, to accelerate to a much higher speed in the nozzle. Note that the steady free surface shapes shown in Figs. 3.1 and 3.2 are the shapes computed with a grid size giving a converged solution, which we will see later in Chapter 7, when we present the grid convergence study. In the same Chapter 7, we will see similar behavior of the free surface when we vary $L_v$, $L_n$, and $W_{in}$, one parameter at a time, while keeping others unaltered. Next, an experimental free surface is shown in Fig. 3.3 [55, Chap. 6]. We can see that the real fluid free surface has a similar shape as in BEM simulations. These figures clearly show that the free surface cannot be simply represented by a sudden jump as was assumed in Bazarov's analysis (Sec. 2.4), and needs to be considered more precisely. As we have mentioned in the study objectives (Sec. 1.4), this will enable us to account for the refraction/reflection phenomena more

realistically and serves as motivation for this chapter of the dissertation. Accordingly, the goal of this chapter is to obtain a simple analytical model which we could use further in the linear first order assessment of the dynamic flow.

Let us now go briefly to the modeling approaches of problems related to this one, which we can find in the literature. Note that BEM operates strictly with potential flow equations, and we want the model describing the free surface to be anchored to BEM solution as close as possible. Therefore, we are *more interested in potential flow models* available in the literature.

At the present time, all analytical models describing directly the steady-state injector core, do represent the flow as potential, however they do not consider the transition region at all, because the engineering design interest lies mainly in finding the core radii in the uniform regions of the injector. Similar conclusions hold for steady-state velocities. Representative examples here are the works by Taylor [6], Bayvel and Orzechowski [8], and Bazarov [1, sec. 3.1].

In the area of finding the steady solution in general non-uniform geometries with swirling flow, the analytical research was advancing quite slowly over the past years because the researchers try to assume the flow to be potential, and it usually leads to calculations that involve infinite series of Bessel and/or Legendre functions. A common difficulty in these types of problems is finding the coefficients of these series based on the given boundary conditions. Moreover, when the series include the modified Bessel functions, $I$ or $K$, which is the case in this study, the analytical solution becomes difficult to obtain, if not impossible at all. This may be seen from the discussion in Gray and Mathews [72], where they show how to integrate the most common Fourier-Bessel series involving the Bessel function of zero kind, $J_0$. Finally, the level of complexity varies depending on whether or not one considers the presence of a hollow core at the flow axis.

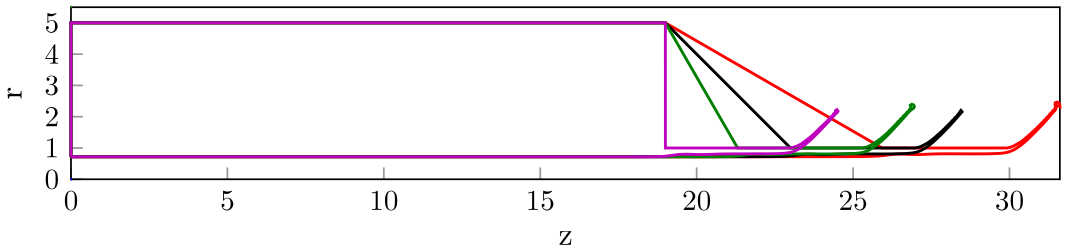


(a) General view of considered cases (legend below)

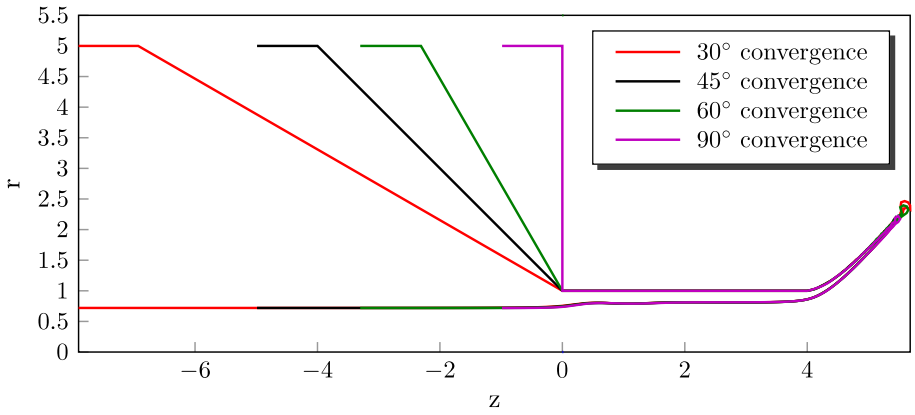


(b) Collapsed view of considered cases at nozzle start

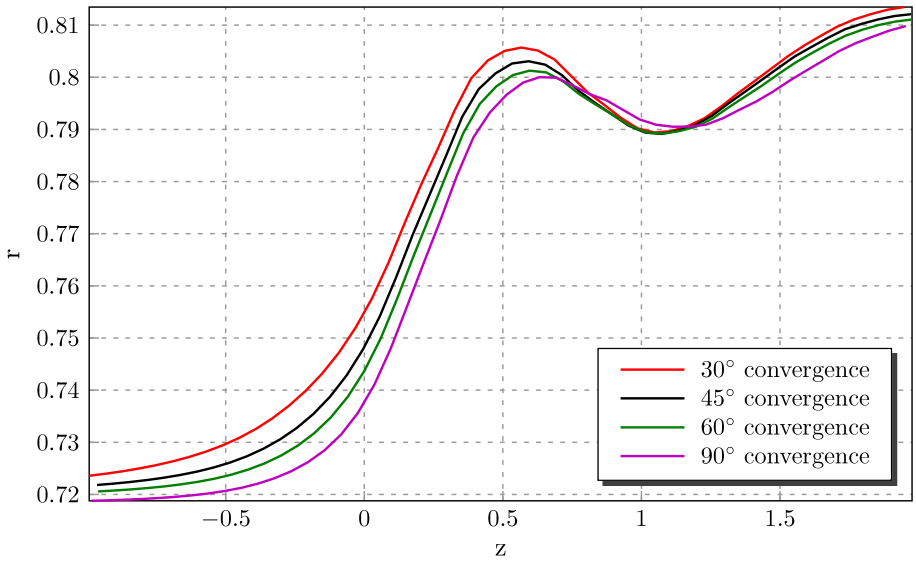


(c) Zoomed in view of free surfaces in nozzle entrance transition region

Figure 3.1.: Steady state BEM flow boundaries at various conical convergence angles

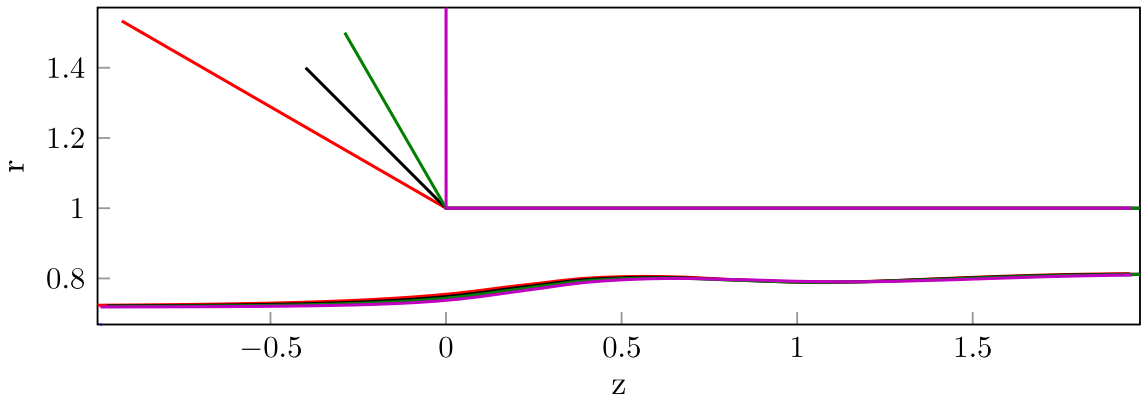


Figure 3.2.: Steady state BEM free surface shapes in nozzle entrance transition region at various conical convergence angles shown when axes $r, z$ are scaled equally

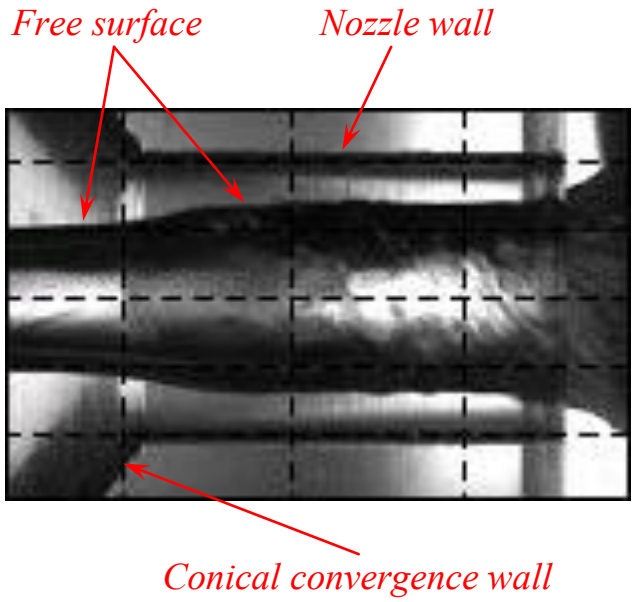


Figure 3.3.: Experimental steady free surface shape in nozzle entrance transition region by Ahn [55]

The following example papers illustrate solutions to problems with filled ducts (without the hollow core). Bostandzhiian [73] models the flow within the conical vortex separator by assuming that the stream function makes sudden jumps at strategic locations of the flow. Miloh [74] considers the flow around bodies of revolution lying at the axis of the conical contraction. Dillmann [75] examines the potential supersonic flow in a variety of ducts by using the velocity potential approach. Lewellen [76] provides a good overview on finding flow solutions for vortices in confined geometries and points out the associated difficulties with finding the Bessel series coefficients.

When the hollow core is present, the nozzle entrance transition followed by the said hump can be imagined as a result of existence of a potential source at the axis of the swirling flow. The classical papers by Barua [77] and Long [78], who analyzed the effects of sources and sinks at the axis of an otherwise uniform swirling fluid would be a good starting point on this subject. On the other hand, switching from the velocity potential to the stream function representation, the solution may be based on Batchelor's [79] approach, from which one can clearly see what trajectory the fluid particle will attain in a general rotational swirling flow that may go through a transition from a larger to smaller duct. Similarly, assuming that the flow is rotational, Darmofal et al. [64] presented a nice simplified quasi-one-dimensional model of the swirling flow (the radial velocities are completely ignored), both steady and unsteady, with or without the hollow core, with the boundaries that may vary.

We start this chapter with a couple of illustrative problems that show what is involved in the computation of the free surface and why we should find another way to compute it in our case. In the first problem, we briefly review Darmofal et al.'s [64] steady state calculation. In the second problem, to show a simple potential flow approach, which combines the ideas of Barua [77], Long [78], and Batchelor [79], we put a source at the nozzle entrance and employ the stream function for particle trajectory tracking. In conclusion, a more detailed potential flow model is shown, that is based on the free surface radii and velocities within the thin layer of the fluid in the transition region.

## 3.2 Illustrative Simple Models

### 3.2.1 Model by Darmofal et al. [64]

Let us start with their one-dimensional equations of continuity (3.7) and momentum (3.8) describing a swirling rotational flow, by omitting the unsteady terms, and by assuming that the gas pressure in the core is zero:

$$\frac{d}{dz}\left[\left(A_D - \bar{A}\right)\bar{u}_z\right] = 0 \tag{3.1}$$

$$\frac{d}{dz}\left[\left(A_D - \bar{A}\right)\bar{u}_z^2\right] = \frac{\Gamma^2}{8\pi\bar{A}^2}\left(A_D - \bar{A}\right)\frac{d\bar{A}}{dz} \tag{3.2}$$

where $A_D = \pi R^2$ is the cross-sectional of the duct, $\bar{A} = \pi\delta^2$ is the cross-sectional of the steady state core, and $\Gamma = 2\pi C$ is the constant circulation, see Fig. 3.4. Then

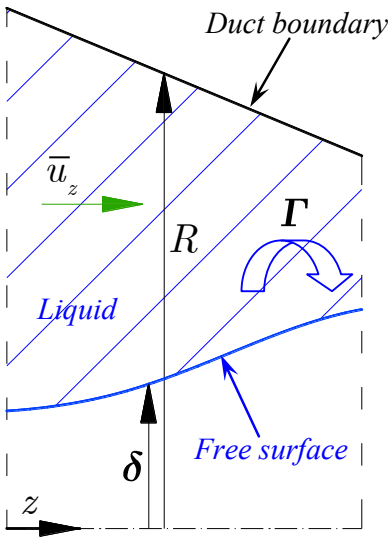


Figure 3.4.: Schematic of steady flow in transition region

continuity may be rewritten as

$$\frac{d}{dz}\left[\pi\left(R^2 - \delta^2\right)\bar{u}_z\right] = 2\pi\left(R\frac{dR}{dz} - \delta\frac{d\delta}{dz}\right)\bar{u}_z + \pi\left(R^2 - \delta^2\right)\frac{d\bar{u}_z}{dz} = 0$$

where from after rearranging, the second term is

$$2\pi\left(R^2 - \delta^2\right)\bar{u}_z\frac{d\bar{u}_z}{dz} = -4\pi\left(R\frac{dR}{dz} - \delta\frac{d\delta}{dz}\right)\bar{u}_z^2 \tag{3.3}$$

Proceeding now to the momentum equation, we can go through the following manipulations:

$$\begin{aligned}
\frac{d}{dz}\left[\pi\left(R^2-\delta^2\right)\bar{u}_z^2\right] &= 2\pi R\frac{dR}{dz}\bar{u}_z^2 - 2\pi\delta\frac{d\delta}{dz}\bar{u}_z^2 + 2\pi\left(R^2-\delta^2\right)\bar{u}_z\frac{d\bar{u}_z}{dz} \\
&\qquad \text{substitute Eq. (3.3) for the last term} \\
&= 2\pi R\frac{dR}{dz}\bar{u}_z^2 - 2\pi\delta\frac{d\delta}{dz}\bar{u}_z^2 - 4\pi R\frac{dR}{dz}\bar{u}_z^2 + 4\pi\delta\frac{d\delta}{dz}\bar{u}_z^2 \\
&= -2\pi R\frac{dR}{dz}\bar{u}_z^2 + 2\pi\delta\frac{d\delta}{dz}\bar{u}_z^2 \\
&= \frac{\Gamma^2}{8\pi\pi^2\delta^4}\pi\left(R^2-\delta^2\right)2\pi\delta\frac{d\delta}{dz} = \frac{\Gamma^2}{8\pi^2\delta^2}\frac{1}{\delta}2\pi\left(R^2-\delta^2\right)\frac{d\delta}{dz}
\end{aligned}$$

which in conclusion gives

$$\delta\frac{d\delta}{dz}\bar{u}_z^2 - R\frac{dR}{dz}\bar{u}_z^2 = \frac{\Gamma^2}{8\pi^2\delta^2}\frac{1}{\delta}\left(R^2-\delta^2\right)\frac{d\delta}{dz}$$

where from we can obtain an implicit relation for the core size variation:

$$\frac{d\delta}{dz} = \frac{R\dfrac{dR}{dz}\bar{u}_z^2}{\delta\bar{u}_z^2 - \dfrac{\Gamma^2}{8\pi^2\delta^2}\dfrac{1}{\delta}\left(R^2-\delta^2\right)} \tag{3.4}$$

Let us now place the origin at a point where the conical convergence section starts, since both the duct radius, $R$, and the flow velocity, $\bar{u}_z$, start to change there, and plot the free surface resulting from this equation in Fig. 3.5. In zoomed in view, we can observe that the free surface ends up with a sharp point right where the nozzle starts and then remains straight in the nozzle where there are no more changes in $R$ and $\bar{u}_z$. But this contradicts to the smooth and continuous BEM and experimental free surface shapes above, which accordingly causes the need to explore other solutions. On the other hand, overall, this model is very elegant and simple in its setup.

### 3.2.2 Model Based on Batchelor's Stream Function Approach

In this section we consider an alternative simple model to that shown above, which is based on irrotational flow. Assume that the entire flow in the injector is considered potential. As such, it may be decomposed into swirling part and *axisymmetric*

axial/radial part, where the latter is responsible for deforming the free surface in the transition region. Since the swirling and axial/radial flows are orthogonal, their streamlines may be considered independent from each other. Hence, following Batchelor [79], we may further consider only this axial/radial part of the flow, as if there was no swirling part at all. But, we shall keep in mind that the swirling component comes into play as a boundary condition stating that the free surface has different

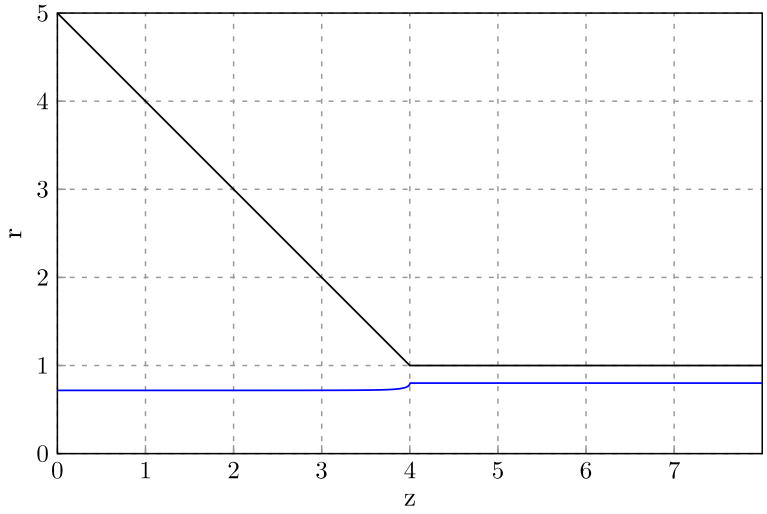


(a) Normal view

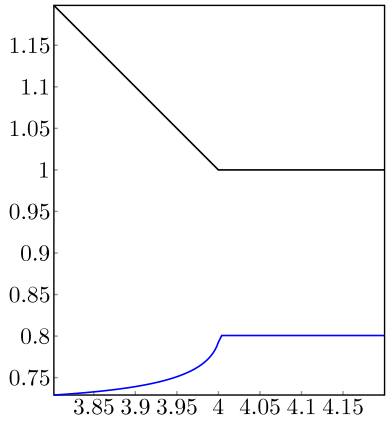


(b) Zoomed in view

Figure 3.5.: Steady free surface shape due to Darmofal et al.

radii at the two ends of the transition region. Finally, motivated by Barua's [77] paper, we will presume this free surface radius adjustment is generated by the presence of a source at the injector axis.

Figure 3.6 shows schematically how we represent the flow in the injector from the potential flow perspective. Notice that the origin is placed at the head end, $z = 0$, and the source is placed where the nozzle starts, $z = L = L_v + L_c$. For simplicity, it is also assumed that the uniform flow in the vortex chamber starts right at the head end, thereby omitting the presence of the head end transition region (see Fig. 2.1).

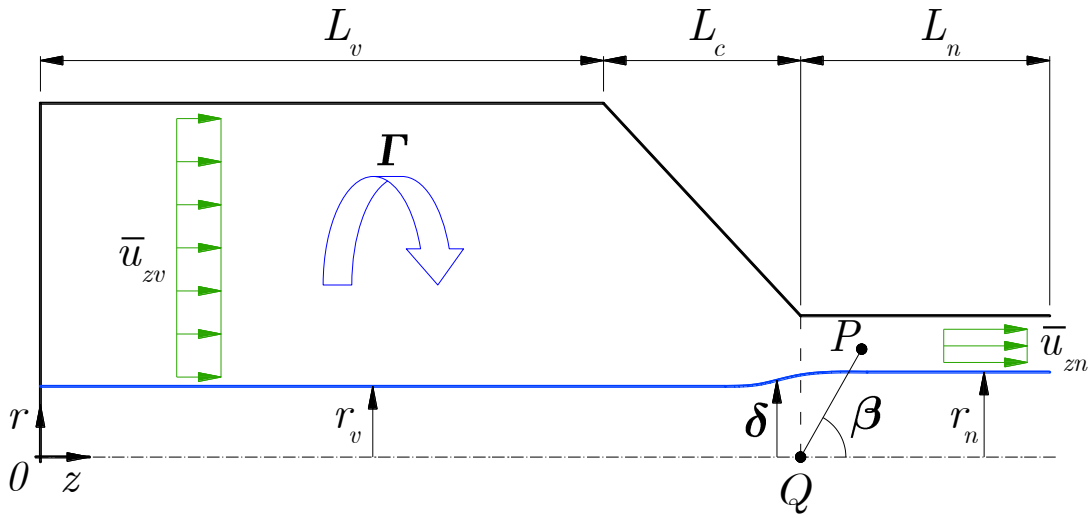


Figure 3.6.: Schematic of uniform and source potential flows in nozzle entrance transition region

The stream function describing the uniform flow in the vortex chamber in cylindrical coordinates is given by (Currie [71, Eq. (5.5b)])

$$\psi = \frac{1}{2}\bar{u}_{zv}r^2$$

Let us follow this uniform flow into the nozzle entrance transition region, where its streamlines start to deviate from the straight lines and represent it following Batchelor [79, Eq. (7.5.15)] in general as

$$\psi = \frac{1}{2}\bar{u}_{zv}r^2 + rF(z,r) \tag{3.5}$$

where the second term is a correction term representing this deviation. Next, let us presume that we can simply think of this correction term as of the source flow placed at $z = L$, which is given by (Currie [71, Eq. (5.6b)])

$$rF(z,r) = -\frac{Q}{4\pi}(1+\cos\beta) \tag{3.6}$$

where $Q$ denotes the strength of source, and $\beta$, which denotes the angle between the injector axis and arbitrary field point $P$ with coordinates $(r,z)$, can be expressed in terms of cylindrical coordinates as

$$\cos\beta = \frac{z-L}{\sqrt{(z-L)^2 + r^2}}$$

Now, let us take a particular streamline in the flow that is coincident with the free surface, which lies at $r = r_v$ in the vortex chamber and at $r = r_n$ in the nozzle. Since the influence of the source is diminishing quickly as the distance between the point of interest and the source itself becomes large, we can think of the uniform nozzle region of the injector as of a limit region where $z = +\infty$ and $\beta = 0$. Then combining Eqs. (3.5) and (3.6), we may write

$$\frac{1}{2}\bar{u}_{zv}r_v^2 = \frac{1}{2}\bar{u}_{zv}r_n^2 - 2\frac{Q}{4\pi}$$

since the stream function is conserved on a streamline. From here the source strength is established,

$$Q = \pi\bar{u}_{zv}\left(r_n^2 - r_v^2\right) \tag{3.7}$$

After combining Eqs. (3.5)–(3.7), for arbitrary $z$ location in transition region we have

$$\frac{1}{2}\bar{u}_{zv}r_v^2 = \frac{1}{2}\bar{u}_{zv}\delta^2 - \frac{\bar{u}_{zv}\left(r_n^2 - r_v^2\right)}{4}\left(1 + \frac{z-L}{\sqrt{(z-L)^2+\delta^2}}\right) \tag{3.8}$$

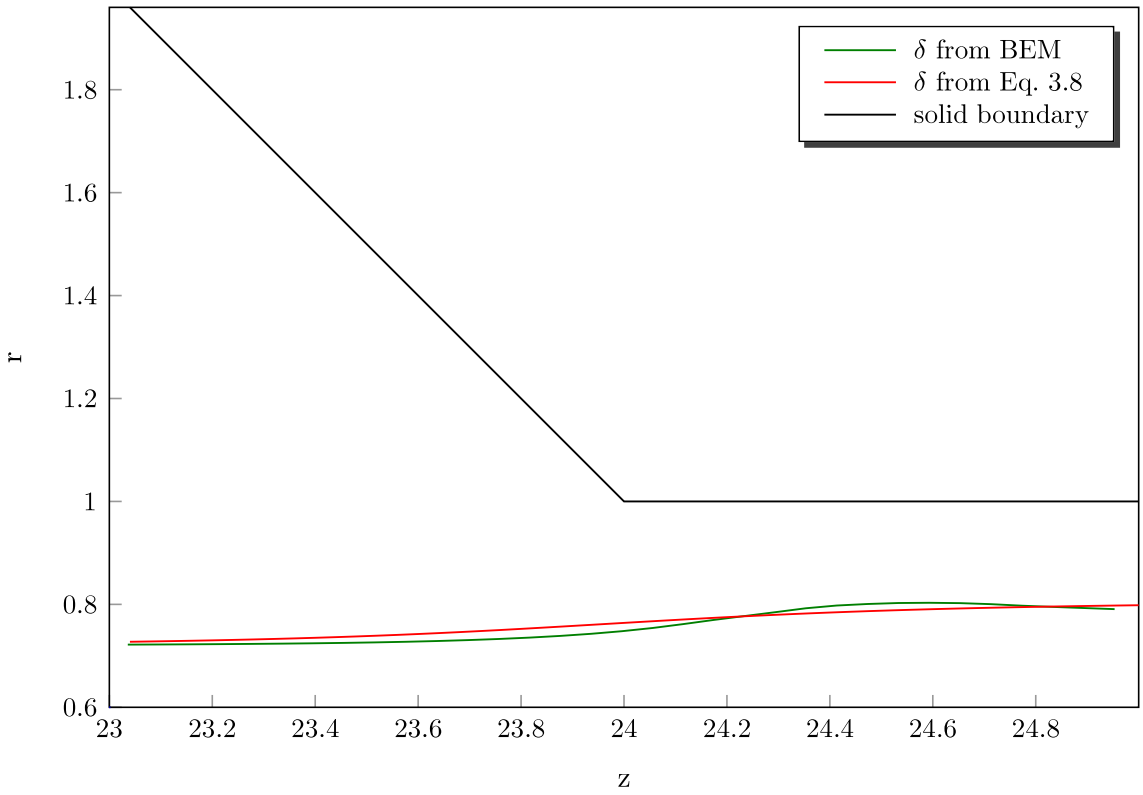


Figure 3.7.: Comparison of solutions for free surface from Eq. (3.8) and BEM in nozzle entrance transition region

This is an implicit relation for finding the radius of free surface in the nozzle entrance transition region, $\delta$. We can compare the resulting solution for $\delta$ to the solution given by BEM that we have seen in Fig. 3.2. In Fig. 3.7, we see that the red line representing the solution produced by added source transitions *too* smoothly, i.e. has smaller $z$ gradients than the BEM solution. And thus we conclude that a finer solution shall be sought. However, this solution is of instructive interest and may serve as a starting point from where this approach may be improved in the future, for example, by adding more types of potential flows at the injector axis, such as a doublet, or by choosing more precisely the locations of each of these flows in terms of the distance $L$.

### 3.3 Current Model Based on Velocity Potential

Let us start with Bowman's [80, Eqs. (3.16)–(3.19)] describing all possible solutions of the Laplace's equation in cylindrical coordinates and rewrite them as the solutions for the steady velocity potential in swirling flow:

$$\bar{\phi} = \left(MI_0\left(\gamma r\right) + NK_0\left(\gamma r\right)\right)\left(D\cos\left(\gamma z\right) + E\sin\left(\gamma z\right)\right) + C\theta \tag{3.9}$$

$$\bar{\phi} = \left(\tilde{M}J_0\left(\gamma r\right) + \tilde{N}Y_0\left(\gamma r\right)\right)\left(\tilde{D}\cosh\left(\gamma z\right) + \tilde{E}\sinh\left(\gamma z\right)\right) + C\theta \tag{3.10}$$

$$\bar{\phi} = \left(\hat{M} + \hat{N}\ln\left(\frac{r}{R_v}\right)\right)\left(\hat{D} + \hat{E}z\right) + C\theta \tag{3.11}$$

In these equations, $I_0$, $K_0$, $J_0$, and $Y_0$ are the modified and ordinary Bessel functions of order zero, $\gamma$, $M$, $N$, $D$, $E$, $\tilde{M}$, $\tilde{N}$, $\tilde{D}$, $\tilde{E}$, $\hat{M}$, $\hat{N}$, $\hat{D}$, $\hat{E}$ are the arbitrary constants, and $C = u_\theta r$ is the angular momentum constant. Then, formally, the complete solution of the potential field can be written in the form of infinite series

$$\begin{aligned}\bar{\phi} = &\sum_{n=1}^{\infty}\left[\left(M_nI_0\left(\gamma_n r\right) + N_nK_0\left(\gamma_n r\right)\right)\left(D_n\cos\left(\gamma_n z\right) + E_n\sin\left(\gamma_n z\right)\right)\right] + \\ &\sum_{n=1}^{\infty}\left[\left(\tilde{M}_nJ_0\left(\gamma_n r\right) + \tilde{N}_nY_0\left(\gamma_n r\right)\right)\left(\tilde{D}_n\cosh\left(\gamma_n z\right) + \tilde{E}_n\sinh\left(\gamma_n z\right)\right)\right] + \\ &\sum_{n=1}^{\infty}\left[\left(\hat{M}_n + \hat{N}_n\ln\left(\frac{r}{R_v}\right)\right)\left(\hat{D}_n + \hat{E}_nz\right)\right] + C\theta\end{aligned} \tag{3.12}$$

where each $n$-th coefficient of the series has to be defined from the corresponding boundary conditions, which are represented by the radii of solid and free surface boundaries, and by the velocities on these boundaries. As was mentioned in Section 3.1, this problem is quite difficult to solve in its completeness.

Alternatively, it is proposed to *focus on the thin region of fluid* bounding the free surface between the radii $r_{he}$ and $r_n$, between which the entire transition of the free surface takes place. This will allow us to obtain a closed analytical solution to this problem without the need to go through integration of the infinite Bessel series. We will consider both head end and nozzle entrance transition regions of swirl injector, where the respective variations of free surface radii and velocities are: $0 \le \bar{u}_z \le \bar{u}_{zv}$, $r_{he} \le r \le r_v$ and $\bar{u}_{zv} \le \bar{u}_z \le \bar{u}_{zn}$, $r_v \le r \le r_n$, see Fig. 2.1 and Table 2.3.

Figure 3.8 depicts the general transition region, where the flow adjusts its axial velocity from $\bar{u}_{z1}$ to $\bar{u}_{z2}$ and the free surface changes its radius from $r_1$ to $r_2$ over the axial distance $L = z_2 - z_1$. Consider the axial/radial flow in this domain that acts together with the swirling flow. Further in this paragraph, we will be referring to this axial/radial flow simply as the flow, and imply that the swirl is present whenever we talk about the former. Based on the traditional steady state theories [1, sec. 3.1], [6], [8], we can say that the flow just before the left boundary, $z = z_1$, is purely axial and has corresponding axial velocity $\bar{u}_z = \bar{u}_{z1}$, uniform in the range $r_1 \leq r \leq r_2$. Similarly, just after the top right point, $z = z_2$, $r = r_2$, we should have a completely axial flow with velocity $\bar{u}_z = \bar{u}_{z2}$. Now, for the radial velocity let us suppose that it should disappear at $r = r_2$ in the entire range $z_1 \leq z \leq z_2$ to enforce the fact that we should approximately have a purely axial flow at the top boundary. At the right boundary, simply because there is no fluid, the radial velocity should be zero in the entire range of radii $r_1 \leq r \leq r_2$. Lastly, we make a forceful assumption that the profile of the axial velocity resulting from this flow adjustment is represented by a periodic function of period $\pi/2$, which makes it possible to choose just one combination of solutions, with $n = 1$ in Eq. (3.12), from all possible solutions of Laplace's equation in cylindrical

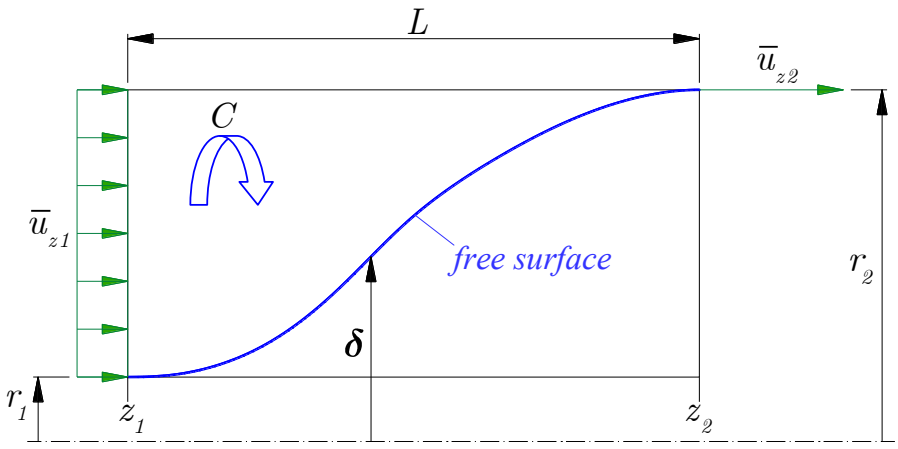


Figure 3.8.: Schematic of steady free surface adjustment in general transition region

coordinates given by Eq. (3.12). This combination of solutions is simply represented by Eqs. (3.9)–(3.11). In summary, the boundary conditions for this domain can be written as follows:

$$\begin{aligned}
&\frac{\partial\bar{\phi}}{\partial z}\left(r_1 \le r \le r_2, z = z_1\right) = \bar{u}_{z1} \\
&\frac{\partial\bar{\phi}}{\partial r}\left(r = r_2, z_1 \le z \le z_2\right) = 0 \\
&\frac{\partial\bar{\phi}}{\partial r}\left(r_1 \le r \le r_2, z = z_2\right) = 0 \\
&\frac{\partial\bar{\phi}}{\partial z}\left(r = r_2, z = z_2\right) = \bar{u}_{z2}
\end{aligned}$$

We can reduce the number of nonhomogeneous boundary conditions to one by applying the following transformation [81, Sec. 7.2]:

$$\begin{aligned}
\tilde{\phi} &= \bar{\phi} - \bar{u}_{z1} z \\
\tilde{z} &= z - z_1 \\
\tilde{r} &= r
\end{aligned}$$

to the above equations. Leaving the constants denoted by the same symbols, we can rewrite the solutions and the boundary conditions as follows:

$$\tilde{\phi} = \left(M I_0\left(\gamma\tilde{r}\right) + N K_0\left(\gamma\tilde{r}\right)\right)\left(D\cos\left(\gamma\tilde{z}\right) + E\sin\left(\gamma\tilde{z}\right)\right) + C\theta \tag{3.13}$$

$$\tilde{\phi} = \left(\tilde{M} J_0\left(\gamma\tilde{r}\right) + \tilde{N} Y_0\left(\gamma\tilde{r}\right)\right)\left(\tilde{D}\cosh\left(\gamma\tilde{z}\right) + \tilde{E}\sinh\left(\gamma\tilde{z}\right)\right) + C\theta \tag{3.14}$$

$$\tilde{\phi} = \left(\hat{M} + \hat{N}\ln\left(\frac{\tilde{r}}{R_v}\right)\right)\left(\hat{D} + \hat{E}\tilde{z}\right) + C\theta \tag{3.15}$$

$$\frac{\partial\tilde{\phi}}{\partial z}\left(r_1 \le \tilde{r} \le r_2, \tilde{z} = 0\right) = 0 \tag{3.16}$$

$$\frac{\partial\tilde{\phi}}{\partial r}\left(\tilde{r} = r_2, 0 \le \tilde{z} \le L\right) = 0 \tag{3.17}$$

$$\frac{\partial\tilde{\phi}}{\partial r}\left(r_1 \le \tilde{r} \le r_2, \tilde{z} = L\right) = 0 \tag{3.18}$$

$$\frac{\partial\tilde{\phi}}{\partial z}\left(\tilde{r} = r_2, \tilde{z} = L\right) = \bar{u}_{z2} - \bar{u}_{z1} \tag{3.19}$$

The derivatives of Eqs. (3.13)–(3.15) in axial direction are given by

$$\frac{\partial\tilde{\phi}}{\partial z} = \left(MI_0\left(\gamma\tilde{r}\right) + NK_0\left(\gamma\tilde{r}\right)\right)\gamma\left(-D\sin\left(\gamma\tilde{z}\right) + E\cos\left(\gamma\tilde{z}\right)\right) \tag{3.20}$$

$$\frac{\partial\tilde{\phi}}{\partial z} = \left(\tilde{M}J_0\left(\gamma\tilde{r}\right) + \tilde{N}Y_0\left(\gamma\tilde{r}\right)\right)\gamma\left(\tilde{D}\sinh\left(\gamma\tilde{z}\right) + \tilde{E}\cosh\left(\gamma\tilde{z}\right)\right) \tag{3.21}$$

$$\frac{\partial\tilde{\phi}}{\partial z} = \left(\hat{M} + \hat{N}\ln\left(\frac{\tilde{r}}{R_v}\right)\right)\hat{E} \tag{3.22}$$

By examining the boundary condition (3.16), we can see that coefficients $E$, $\tilde{E}$, $\hat{E}$ must be zero, because the logarithmic and Bessel functions in Eqs. (3.20)–(3.22) are not zero in general, in the range of radii $r_1 \leq \tilde{r} \leq r_2$, at $z = 0$. Also, by looking at the boundary condition (3.18), we can conclude that $\tilde{D} = 0$, because the hyperbolic cosine function in Eq. (3.14) can never be zero, and that $\hat{D} = 0$ because the radial derivative of logarithm in Eq. (3.15) is not zero in general. Hence, the solutions (3.14) and (3.15) are eliminated, and a single possible solution left is

$$\tilde{\phi} = \left(MI_0\left(\gamma\tilde{r}\right) + NK_0\left(\gamma\tilde{r}\right)\right)\cos\left(\gamma\tilde{z}\right) + C\theta \tag{3.23}$$

where we have incorporated the constant $D$ into the constants $M$ and $N$. Its derivatives in radial and axial directions are:

$$\frac{\partial\tilde{\phi}}{\partial r} = \left(MI_1\left(\gamma\tilde{r}\right) - NK_1\left(\gamma\tilde{r}\right)\right)\gamma\cos\left(\gamma\tilde{z}\right)$$

$$\frac{\partial\tilde{\phi}}{\partial z} = -\left(MI_0\left(\gamma\tilde{r}\right) + NK_0\left(\gamma\tilde{r}\right)\right)\gamma\sin\left(\gamma\tilde{z}\right)$$

The boundary condition (3.18) can be satisfied only if $\gamma L = \dfrac{\pi}{2}$. Also, from boundary condition (3.17) we can conclude that $N = M\dfrac{I_1\left(\gamma r_2\right)}{K_1\left(\gamma r_2\right)}$. By combining this expression with the boundary condition (3.19) we have

$$-\gamma M\left(I_0\left(\gamma r_2\right) + \frac{I_1\left(\gamma r_2\right)}{K_1\left(\gamma r_2\right)}K_0\left(\gamma r_2\right)\right)\sin\left(\gamma L\right) = \bar{u}_{z2} - \bar{u}_{z1}$$

where from $M$ is

$$M = -\frac{\bar{u}_{z2} - \bar{u}_{z1}}{\gamma\left(I_0\left(\gamma r_2\right) + \dfrac{I_1\left(\gamma r_2\right)}{K_1\left(\gamma r_2\right)}K_0\left(\gamma r_2\right)\right)}$$

Then, we can rewrite the solution (3.23) as

$$\tilde{\phi} = -\left(\bar{u}_{z2} - \bar{u}_{z1}\right) \frac{I_0\left(\gamma\tilde{r}\right) + \dfrac{I_1\left(\gamma r_2\right)}{K_1\left(\gamma r_2\right)} K_0\left(\gamma\tilde{r}\right)}{\gamma\left(I_0\left(\gamma r_2\right) + \dfrac{I_1\left(\gamma r_2\right)}{K_1\left(\gamma r_2\right)} K_0\left(\gamma r_2\right)\right)} \cos\left(\gamma\tilde{z}\right) + C\theta \tag{3.24}$$

By transferring back into the original frame of reference, we obtain the final form of solution

$$\bar{\phi}(r,z) = \bar{u}_{z1} z - \left(\bar{u}_{z2} - \bar{u}_{z1}\right) \frac{I_0\left(\gamma r\right) + \dfrac{I_1\left(\gamma r_2\right)}{K_1\left(\gamma r_2\right)} K_0\left(\gamma r\right)}{\gamma\left[I_0\left(\gamma r_2\right) + \dfrac{I_1\left(\gamma r_2\right)}{K_1\left(\gamma r_2\right)} K_0\left(\gamma r_2\right)\right]} \cos\left(\gamma\left(z - z_1\right)\right) + C\theta \tag{3.25}$$

where $\gamma = \dfrac{\pi}{2L}$. The steady state velocities in the thin region bounding the free surface in the transition region are then formally given by:

$$\bar{u}_r = \frac{\partial\bar{\phi}}{\partial r} = -\left(\bar{u}_{z2} - \bar{u}_{z1}\right) \frac{I_1\left(\gamma r\right) - \dfrac{I_1\left(\gamma r_2\right)}{K_1\left(\gamma r_2\right)} K_1\left(\gamma r\right)}{I_0\left(\gamma r_2\right) + \dfrac{I_1\left(\gamma r_2\right)}{K_1\left(\gamma r_2\right)} K_0\left(\gamma r_2\right)} \cos\left(\gamma\left(z - z_1\right)\right) \tag{3.26}$$

$$\bar{u}_z = \frac{\partial\bar{\phi}}{\partial z} = \bar{u}_{z1} + \left(\bar{u}_{z2} - \bar{u}_{z1}\right) \frac{I_0\left(\gamma r\right) + \dfrac{I_1\left(\gamma r_2\right)}{K_1\left(\gamma r_2\right)} K_0\left(\gamma r\right)}{I_0\left(\gamma r_2\right) + \dfrac{I_1\left(\gamma r_2\right)}{K_1\left(\gamma r_2\right)} K_0\left(\gamma r_2\right)} \sin\left(\gamma\left(z - z_1\right)\right) \tag{3.27}$$

Finally, we can determine the sought radius of the free surface, $\delta$, by employing the steady state Bernoulli's equation,

$$\left(\frac{\partial\bar{\phi}}{\partial r}\right)^2 + \left(\frac{\partial\bar{\phi}}{\partial z}\right)^2 + \frac{C^2}{\delta^2} = \frac{C^2}{r_2^2} + \bar{u}_{z2}^2 \tag{3.28}$$

Now we may ask: where exactly does the transition start and end, or what are the values of $z_1$ and $z_2$? For the nozzle entrance transition region, the answer comes from the BEM free surfaces in Figs. 3.1 and 3.2, where we can see that $z_1$ is approximately at $z = -0.5$, and $z_2$ is approximately at $z = +0.5$, in the frame of reference of the latter figure. This converts in terms of nozzle radius, $R_n = 1$, in absolute coordinates starting at injector head end, to: $z_1 = L_v + L_c - 0.5R_n$ and $z_2 = L_v + L_c + 0.5R_n$ (see Fig. 2.1). The transition distance is then $L = z_2 - z_1 = R_n$. As we will see later, these

values of $z_1$ and $z_2$ work well not only when the conical convergence angle is varied as in Fig. 3.2, but also when such parameters as $L_v$, $L_n$, and $\bar{W}_{in}$ are varied. Therefore, further on in this thesis, we will take it as a **rule that the nozzle entrance transition starts at $\mathbf{z_1 = L_v + L_c - 0.5R_n}$ and ends at $\mathbf{z_2 = L_v + L_c + 0.5R_n}$.** This explains the origination of $0.5R_n$ term in Table 2.1. In the head end transition, we simply assume that the transition starts at $z = 0$ and ends at $z = 2R_t$ marking the edge of the tangential channel circular boundary. This completes the definition of the steady free surface radii in all regions of the internal injector flow. The values of $z_1$, $z_2$, $\bar{u}_{z1}$, and $\bar{u}_{z2}$ are summarized in Table 3.1.

Table 3.1: Definition of $r_1$, $r_2$, $z_1$, $z_2$, $\bar{u}_{z1}$, $\bar{u}_{z2}$ in transition regions

| **Transition** | **Parameter** | **Value** |
|---|---|---|
| Head end | $r_1$ | $r_{he}$ |
| | $r_2$ | $r_v$ |
| | $z_1$ | $0$ |
| | $z_2$ | $2R_t$ |
| | $\bar{u}_{z1}$ | $0$ |
| | $\bar{u}_{z2}$ | $\bar{u}_{zv}$ |
| Nozzle entrance | $r_1$ | $r_v$ |
| | $r_2$ | $r_n$ |
| | $z_1$ | $z_1 = L_v + L_c - 0.5R_n$ |
| | $z_2$ | $z_1 = L_v + L_c + 0.5R_n$ |
| | $\bar{u}_{z1}$ | $\bar{u}_{zv}$ |
| | $\bar{u}_{z2}$ | $\bar{u}_{zn}$ |

## 3.4 Results

Based on Eqs. (3.26) and (3.27), Figs. 3.9 and 3.10 show the variation of steady velocities in the head end and nozzle entrance transition regions at the free surface, $r = \delta$. Notice that the radial velocity is four orders of magnitude smaller than the axial velocity in the head end transition, and one order of magnitude smaller – in the the nozzle entrance transition. This fact will enable us to neglect the terms associated with radial velocities in the disturbance refraction/reflection modeling that will come in the next chapters. Note that BEM gives similar results for the velocities. We do not present the BEM velocities here, because it is assumed that if the analytic and numerical free surfaces match well (see below), then so do the velocities.

By solving Eq. (3.28) for the free surface radius in transition regions, $\delta$, we can also compare how well the analytical free surface is matching that of BEM. For this comparison we may take just 45° injector shown in Fig. 3.2, since the free surfaces for all other angles are approximately the same. In Fig. 3.11, the general view of the free surface and zoomed in views of transitions regions are shown. In Fig. 3.11(b) we can see that, in the head end transition region, the free surface radius variation is very small. Note that the BEM boundary starts from $z = 2R_t = 1$, when computing the free surfaces numerically, which will be explained later on, when we will consider how to setup the boundary conditions in BEM simulations in Chapter 7.

The most important comparison, however, which validates the model against BEM, is that for the nozzle entrance transition region. In Fig. 3.11(c) we can see that the matching is satisfactory. This may be seen more clearly if we compare the current free surface to the free surface obtained in the previous simpler potential flow model, which is shown in Fig. 3.12. In this figure, we can see that the blue line representing the current model is lying closer to the BEM free surface than the red line representing the solution obtained by adding source at the injector axis.

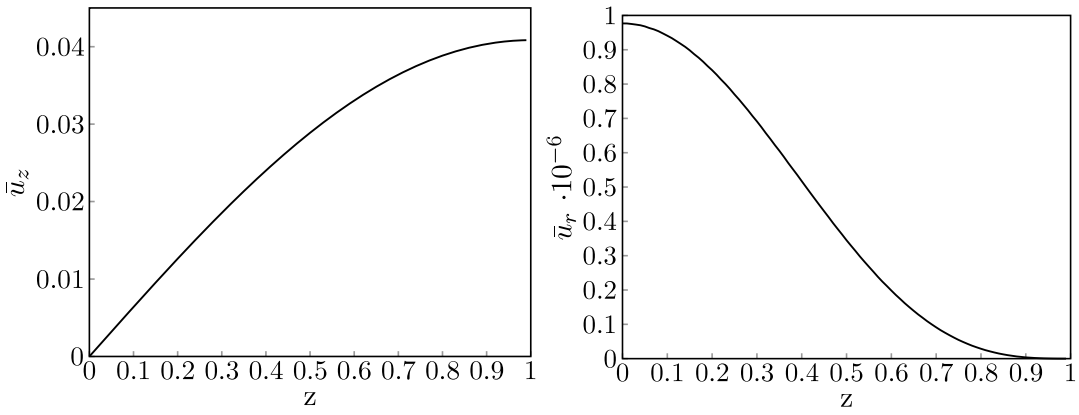


(a) Axial velocity (b) Radial velocity

Figure 3.9.: Variation of steady axial and radial velocities in head end transition region at $r = \delta$

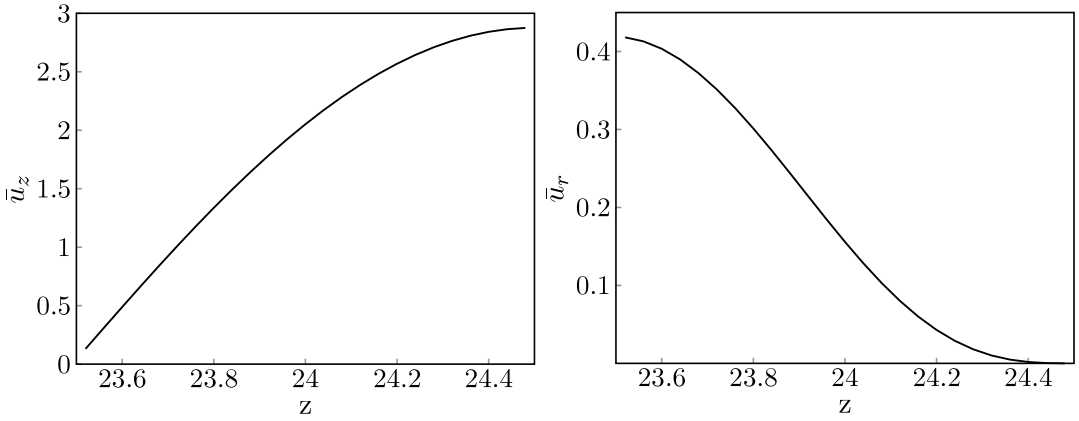


(a) Axial velocity (b) Radial velocity

Figure 3.10.: Variation of steady axial and radial velocities in nozzle entrance transition region at $r = \delta$

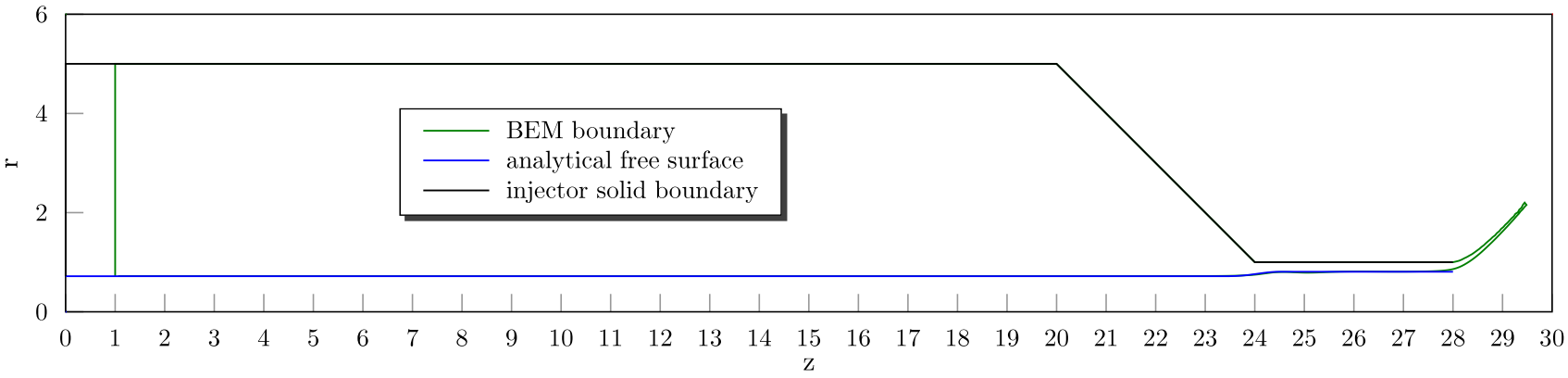


(a) General view of all injector regions

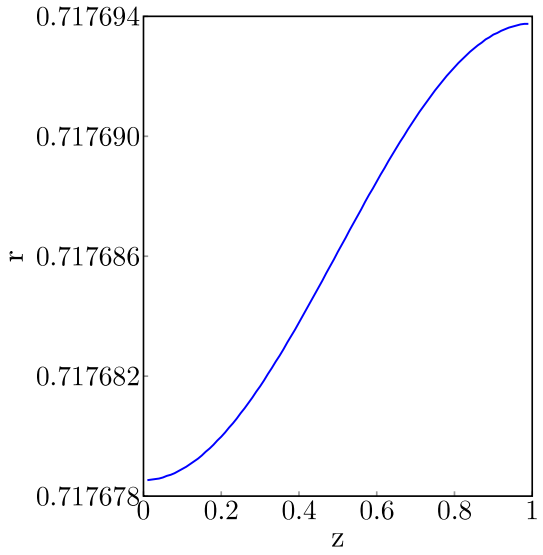


(b) Head end transition

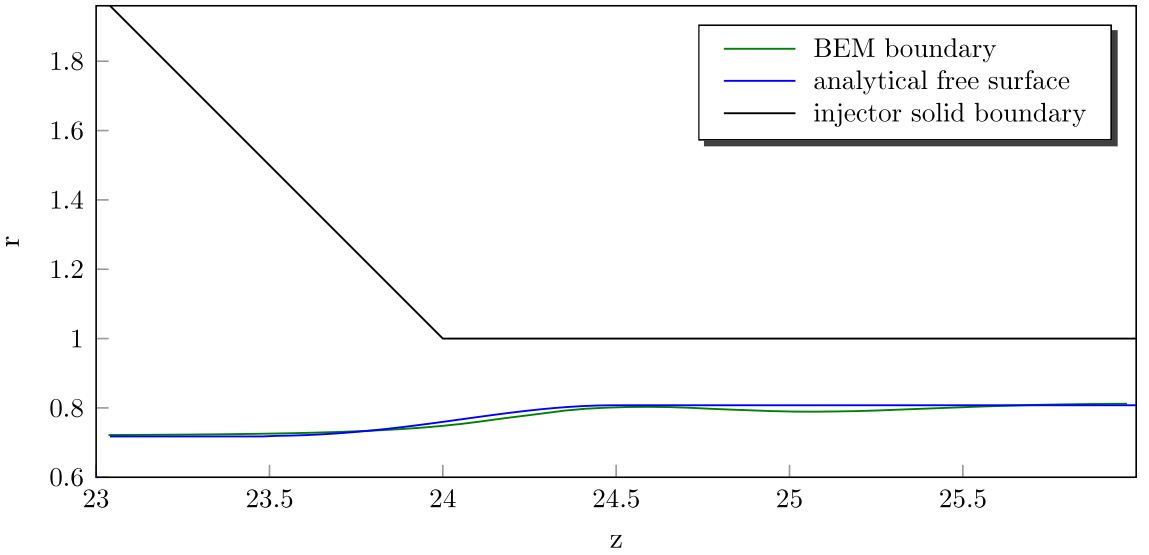


(c) Nozzle entrance transition

Figure 3.11.: Analytic vs. BEM free surface comparison in transition regions

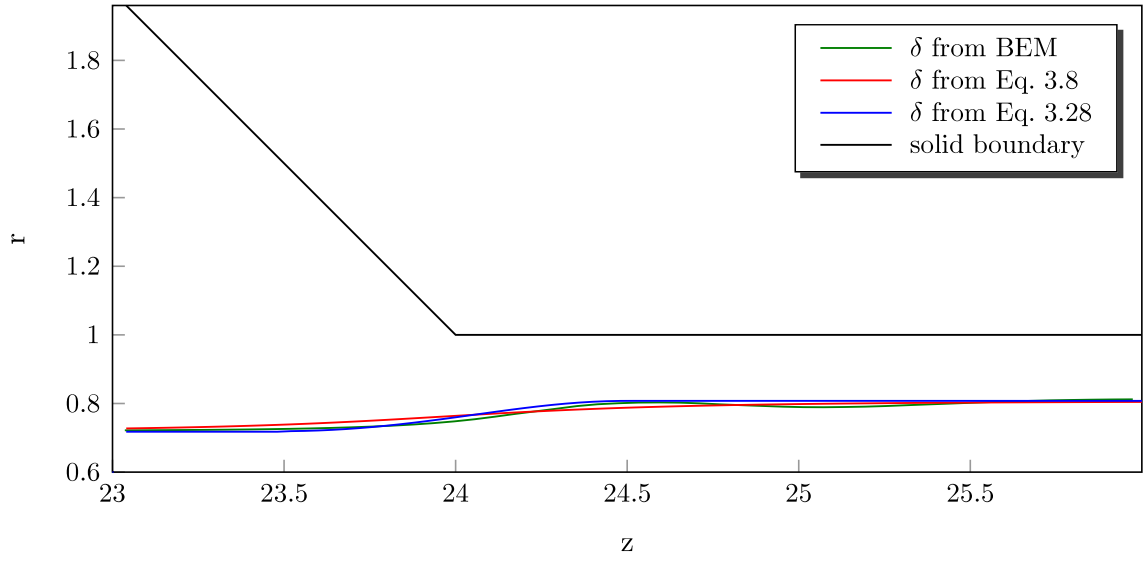


(a) Normal view

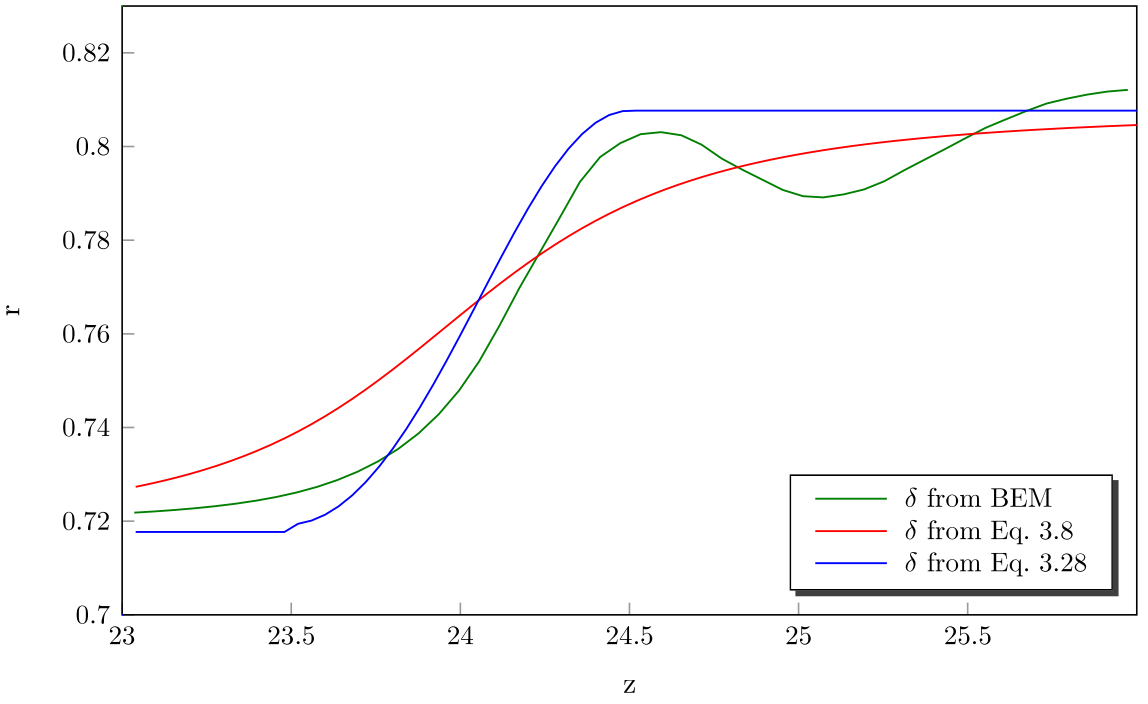


(b) Zoomed in view

Figure 3.12.: Comparison of solutions for free surface resulting from Eqs. (3.8) and (3.28), and BEM, in nozzle entrance transition region

## 3.5 Conclusions

In this chapter we have been seeking a simple analytic model that is capable of describing the free surface in transition regions of swirl injector in a smooth and continuous fashion. We need this information for using in the first order theoretical analysis of wave refraction/reflection in the next chapters. The sought model had to be a potential flow model so that it is possible to compare its results with the BEM simulations. Due to the presence of the infinite Bessel series, all potential flow models are difficult to solve. Therefore, simplifying assumptions are employed that can yield possible analytic solutions.

The most simplistic flow representation is given by Darmofal et al. [64], where the flow is considered one-dimensional. We have briefly reviewed their model in Subsection 3.2.1 and concluded that it results in a sharp discontinuity in the free surface right at the point where the nozzle starts, Fig. 3.5.

Another simplifying approach is to assume that the flow is potential and its free surface is deformed by an axisymmetric source flow at the injector axis. By following Barua [77], Long [78], and Batchelor [79], we have derived Eq. (3.8) in Subsection 3.2.2, which describes the deformation of the free surface due to the source flow located at the nozzle entrance. This equation has yielded a radius of the free surface, $\delta$, that has much smaller axial gradients than the BEM free surface, Fig. 3.7. This has caused the need to find a more precise potential flow model.

In Section 3.3, it has been proposed to focus on a thin layer of fluid bounding the free surface, where all transitions take place, and the boundary conditions are known relatively well. Then, based on the solutions of the Laplace's equation for the velocity potential, we have derived the free surface Eq. (3.28) valid in this thin layer of fluid and satisfying the assumed boundary conditions. The resulting free surface turned out to be closer to the BEM free surface than the previous potential flow model, Fig. 3.12. Accordingly, we have selected this model as the current model for this study.

Finally, we shall point out that both of the potential flow models above are equally important for consideration because they provide the basic ideas for the analytic modeling of the free surface. The first can be improved by adding more types of potential flows at the injector axis, with carefully selecting their respective axial locations and strengths. The second model can be improved by including more solutions of Laplace's equation, and by adding more features in the description of the boundary conditions.

# 4. DISTURBANCE WAVE REFRACTION

## 4.1 Introduction

In this chapter we consider the first fundamental facet of swirl injector dynamics, which is the interaction of varying current (or bulk stream) and flow boundaries with disturbances in transitions regions of the swirl injector. The motivation to do that comes from the fact that we want to obtain the necessary information regarding the variation of the wave characteristics for further using them in the wave reflection/injector resonance analysis, which will be presented in Chapter 5.

The response of propagating disturbance to changes in current can be described as in Peregrine [69, p. 26]:

> *"... if the waves propagate onto a faster or slower flow, the frequency will remain constant, but the wavelength will either increase or decrease."*

Moreover, the changing flow boundaries cause the wave to grow or shrink in amplitude. Overall, this variational behavior of wave characteristics as they propagate is known as wave refraction. We can summarize these facts as in McKee [82, p. 937]:

> *"Water waves are refracted by changes in depth or current."*

The depth in our case being the liquid film thickness, $R - \delta$ (see Fig. 2.1). This can be imagined better from an analogy with sloping beach, where the water wave grows as the depth becomes shallower (Billingham [83, subsection 4.8.2]). Lastly, note that, in this chapter, we are not accounting for the reflection of the waves, which we leave for further consideration in the next chapter.

There are two approximations to this problem in terms of the wave lengths of given disturbances:

- **Long wave** (or shallow water approximation), which assumes that the flow disturbances in the radial direction are much smaller than those acting in the axial direction, and

- **Kelvin's wave**, which assumes that the flow disturbances in both radial and axial directions are of the same order.

Note that the term "Kelvin's wave" is not a standard term accepted in the literature, but the researchers [84], who study topics similar to this here, use it sometimes to indicate that the characteristics of the disturbance wave in consideration may be described by the Kelvin's dispersion relationship [24]. In this dissertation, we will use both the original form and the extended form of that dispersion, where the latter will be derived in this chapter for the swirling flow with variable boundaries and bulk flow axial velocity. Nonetheless, we will use the term "Kelvin's wave" to refer to the waves described by either of these forms.

With regard to the bulk stream velocity, we will assume that it is purely axial in this study. This follows from the fact that the steady radial velocities in transition regions of the injector are much smaller than the steady axial velocities (see Section 3.4). Accordingly, the axial velocity of the bulk stream at any axial position of the flow is estimated based on one-dimensional continuity as

$$\bar{u}_z = \bar{u}_{zv} \frac{R_v^2 - r_v^2}{R^2 - \delta^2} \tag{4.1}$$

where $\delta$ is calculated based on the potential flow model described in Section 3.3.

In the long wave approximation, if we will add to the assumption that we can neglect the radial velocity disturbances, the assumption of one-dimensional steady bulk stream, we can have an overall one-dimensional unsteady problem, which is possible to solve analytically in an *exact* sense. In practice, the long wave approximation is of more importance in rocket engine application because the typical wave length of acoustically driven combustion instability is much greater than any of the injector dimensions, and therefore it is of higher priority in this study.

Most relevant literature sources describing the long wave approach are Darmofal's [64] paper and its derivatives [85], [86]. Their solution elegantly describes the influences of the changing flow boundaries and velocities on the flow disturbances and provides a good introduction on the subject. However, ignoring terms that are products of a disturbance with the derivative of either the flow area or the steady state velocity brings them to the situation that the computed wave speeds at all points of the flow are purely real. This completely eliminates the effects of spatial growth of the disturbances as they propagate, especially in such region of flow convergence as the entrance to the injector nozzle. In other words, the disturbance wave does not change its amplitude as it propagates.

In the Kelvin's wave approach, we must ideally know the steady radial velocity profile and account for radial velocity disturbances based on this known profile. This makes the dynamic problem more difficult, but more fully describes the flow. The solution for the radial velocity profile can be found analytically only in the simplest potential flow cases, and usually requires numerical computation. Alternatively, Dingemans [87, p. 102] states with regard to a similar case in gravity wave propagation,

> *"For the general case matching conditions (for velocity profiles) along the depth transition is difficult and needs the consideration of integral equations."*

On the other hand, as mentioned above, we can approximately assume that the *steady* radial velocities are much smaller than axial, and can be neglected, which makes the Kelvin's wave approach rather *heuristic*, but, at the same time, revealing some of the important physics of the overall dynamic problem that are associated with the presence of radial flow disturbances. This will be the approximation assumed in this study.

There are few examples in the literature, where an attempt has been made to consider the Kelvin's wave approach completely analytically. These works consider only fully filled ducts with swirl, not having the hollow core. Chow [88] analyzed

the flow through the ducts with sinusoidal deformations and converging-diverging nozzles using a stream function approach analogous to Batchelor's [79]. Nan and Xieyuan [89] analyzed the flow in a slowly divergent duct with a very small angle of divergence. By applying the notion of slow and fast variables, they arrived at very complex expressions for the disturbance amplitude variations along the axis of the duct.

In this chapter, we will assume that the gaseous core is empty and is not imposing any second order effects such as capillary or viscous. Moreover, we will consider wave refraction only in the nozzle entrance transition region of the injector, since, as we have seen in the previous chapter, the variation of flow boundaries and velocities in the head end transition is negligibly small.

## 4.2 Long Wave Refraction Model

The paper by Darmofal at al. [64] deals with the swirling flow that has a gaseous core rotating as a solid body. In this case, the core is considered empty, hence not inserting any pressure on the free surface, i.e. in Darmofal et al.'s notation the core pressure $p_\delta = 0$. We start this analysis from their unsteady equations of continuity (3.7) and axial momentum (3.8):

$$\frac{\partial \left(A_D - A\right)}{\partial t} + \frac{\partial}{\partial z}\left[\left(A_D - A\right) u_z\right] = 0 \tag{4.2}$$

$$\frac{\partial}{\partial t}\left[\left(A_D - A\right) u_z\right] + \frac{\partial}{\partial z}\left[\left(A_D - A\right) u_z^2\right] = \frac{\Gamma^2}{8\pi A^2}\left(A_D - A\right)\frac{\partial A}{\partial z} \tag{4.3}$$

where $A_D = \pi R^2$ is the local duct area, $A = \pi(\delta + \eta)^2$ is the local instantaneous gaseous core area, $u_z$ is the local instantaneous axial flow velocity, and $\Gamma = 2\pi C$ is the constant circulation, see Fig. 4.1.

We can linearize these equations by assuming that the local core area and velocity consist of the mean, or steady state, and disturbed components, $A = \bar{A} + A'$, and $u_z = \bar{u}_z + u'_z$, where $\bar{A} = \bar{A}(z)$, $\bar{u}_z = \bar{u}_z(z)$, and $A' = A'(z,t)$, $u'_z = u'_z(z,t)$. Then,

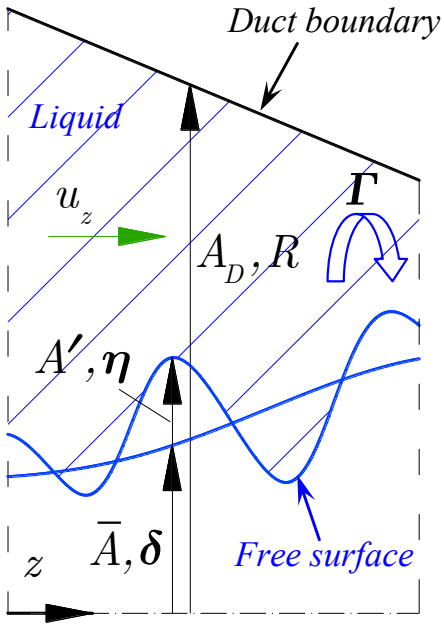


Figure 4.1.: Unsteady flow schematic for long wave refraction analysis

let us scrutinize the equations of continuity and momentum term by term. First, consider the terms in the continuity equation:

$$\frac{\partial \left(A_D - A\right)}{\partial t} = \frac{\partial A_D}{\partial t} - \frac{\partial \bar{A}}{\partial t} - \frac{\partial A'}{\partial t} = -\frac{\partial A'}{\partial t}$$

$$\begin{aligned}\frac{\partial}{\partial z}\left[\left(A_D - A\right)u_z\right] &= \frac{\partial \left(A_D - \bar{A} - A'\right)}{\partial z}\left(\bar{u}_z + u'_z\right) + \left(A_D - \bar{A} - A'\right)\left(\frac{d\bar{u}_z}{dz} + \frac{\partial u'_z}{\partial z}\right) \\ &= -\frac{\partial A'}{\partial z}\bar{u}_z + \frac{d\left(A_D - \bar{A}\right)}{dz}u'_z - A'\frac{d\bar{u}_z}{dz} + \left(A_D - \bar{A}\right)\frac{\partial u'_z}{\partial z}\end{aligned}$$

where we note that

$$\frac{d\left[\left(A_D - \bar{A}\right)\right]}{dz}\bar{u}_z + \left(A_D - \bar{A}\right)\frac{d\bar{u}_z}{dz} = 0$$

due to steady state mass flow conservation. Combination of these results allows us to rewrite the continuity equation as

$$\frac{\partial A'}{\partial t} + \bar{u}_z\frac{\partial A'}{\partial z} = \left(A_D - \bar{A}\right)\frac{\partial u'_z}{\partial z} + u'_z\frac{d\left(A_D - \bar{A}\right)}{dz} - A'\frac{d\bar{u}_z}{dz} \tag{4.4}$$

Compare this reworked continuity Eq. (4.4) to corresponding continuity Eq. (4.3) in Darmofal et al. [64, p. 65], which we quote here for convenience in our notation:

$$\frac{\partial A'}{\partial t} + \bar{u}_z \frac{\partial A'}{\partial z} = \left(A_D - \bar{A}\right) \frac{\partial u'_z}{\partial z}$$

where it can be seen that we have not neglected the terms $u'_z \dfrac{d\left(A_D - \bar{A}\right)}{dz}$ and $-A' \dfrac{d\bar{u}_z}{dz}$.

Proceeding to the terms in the momentum equation, we may write the following:

$$\begin{aligned}
\frac{\partial}{\partial t}\left[\left(A_D - A\right) u_z\right] &= \frac{\partial\left(A_D - \bar{A} - A'\right)}{\partial t}\left(\bar{u}_z + u'_z\right) + \left(A_D - \bar{A} - A'\right)\frac{\partial\left(\bar{u}_z + u'_z\right)}{\partial t} \\
&= -\frac{\partial A'}{\partial t}\bar{u}_z + \left(A_D - \bar{A}\right)\frac{\partial u'_z}{\partial t}
\end{aligned}$$

$$\begin{aligned}
\frac{\partial}{\partial z}\left[\left(A_D - A\right) u_z^2\right] &= \frac{\partial}{\partial z}\left[\left(A_D - A - A'\right)\left(\bar{u}_z^2 + 2\bar{u}_z u'_z + \left(u'_z\right)^2\right)\right] \\
&= \frac{\partial}{\partial z}\left[\left(A_D - \bar{A}\right)\bar{u}_z^2 - A'\bar{u}_z^2 + 2\left(A_D - \bar{A}\right)\bar{u}_z u'_z\right] \\
&= \frac{d\left[\left(A_D - \bar{A}\right)\bar{u}_z^2\right]}{dz} - \frac{\partial A'}{\partial z}\bar{u}_z^2 - 2A'\bar{u}_z\frac{d\bar{u}_z}{dz}\ldots \\
&\ldots + 2\frac{d\left(A_D - \bar{A}\right)}{dz}\bar{u}_z u'_z + 2\left(A_D - \bar{A}\right)\frac{d\bar{u}_z}{dz}u'_z + 2\left(A_D - \bar{A}\right)\bar{u}_z\frac{\partial u'_z}{\partial z}
\end{aligned}$$

Next, we will apply the binomial expansion [61, p. 1196] of the form

$$(s+t)^n = s^n + ns^{n-1}t + \frac{n\left(n-1\right)}{2}s^{n-2}t^2 + \ldots$$

to the $\dfrac{1}{A^2}$ factor in Eq. (4.3), which gives in the first order approximation

$$\frac{1}{A^2} = \left(\bar{A} + A'\right)^{-2} \simeq \frac{1}{\bar{A}^2} - 2\frac{A'}{\bar{A}^3}$$

Accordingly, we rewrite the centrifugal pressure force term as follows:

$$\begin{aligned}
&\frac{\Gamma^2}{8\pi A^2}\left(A_D - A\right)\frac{\partial A}{\partial z} = \frac{\Gamma^2}{8\pi}\left(\frac{1}{\bar{A}^2} - 2\frac{A'}{\bar{A}^3}\right)\left[\left(A_D - \bar{A}\right)\frac{d\bar{A}}{dz} - A'\frac{d\bar{A}}{dz} + \left(A_D - \bar{A}\right)\frac{\partial A'}{\partial z}\right] \\
&= \frac{\Gamma^2}{8\pi\bar{A}^2}\left(A_D - \bar{A}\right)\frac{d\bar{A}}{dz} + \frac{\Gamma^2}{8\pi\bar{A}^2}\left[-A'\frac{d\bar{A}}{dz} + \left(A_D - \bar{A}\right)\frac{\partial A'}{\partial z}\right] - \frac{\Gamma^2}{8\pi}2\frac{A'}{\bar{A}^3}\left(A_D - \bar{A}\right)\frac{d\bar{A}}{dz} \\
&= \frac{\Gamma^2}{8\pi\bar{A}^2}\left(A_D - \bar{A}\right)\frac{d\bar{A}}{dz} + \frac{\Gamma^2}{8\pi\bar{A}^2}\left[\frac{d\bar{A}}{dz}\left(1 - \frac{2A_D}{\bar{A}}\right)A' + \left(A_D - \bar{A}\right)\frac{\partial A'}{\partial z}\right]
\end{aligned}$$

Substitution of these results back into the momentum equation gives

$$\left(A_D - \bar{A}\right)\frac{\partial u'_z}{\partial t} - \bar{u}_z\frac{\partial A'}{\partial t} + 2\left(A_D - \bar{A}\right)\bar{u}_z\frac{\partial u'_z}{\partial z} - \bar{u}_z^2\frac{\partial A'}{\partial z}\ldots$$
$$\ldots + \left[-2A'\bar{u}_z\frac{d\bar{u}_z}{dz} + 2\frac{d\left(A_D - \bar{A}\right)}{dz}\bar{u}_z u'_z + 2\left(A_D - \bar{A}\right)\frac{d\bar{u}_z}{dz}u'_z\right] =$$
$$= \frac{\Gamma^2}{8\pi\bar{A}^2}\left[\frac{d\bar{A}}{dz}\left(1 - \frac{2A_D}{\bar{A}}\right)A' + \left(A_D - \bar{A}\right)\frac{\partial A'}{\partial z}\right] \tag{4.5}$$

where we note that the steady terms $\frac{\Gamma^2}{8\pi\bar{A}^2}\left(A_D - \bar{A}\right)\frac{d\bar{A}}{dz}$ and $\frac{d\left[\left(A_D - \bar{A}\right)\bar{u}_z^2\right]}{dz}$ have cancelled each other. Again, compare this newly obtained momentum Eq. (4.5) to corresponding momentum Eq. (2.25) in Khan [85, p. 24], which we quote here in our notation (without the gas pressure force term):

$$\left(A_D - \bar{A}\right)\frac{\partial u'_z}{\partial t} - \bar{u}_z\frac{\partial A'}{\partial t} + 2\left(A_D - \bar{A}\right)\bar{u}_z\frac{\partial u'_z}{\partial z} + \left[-\bar{u}_z^2 + \frac{\Gamma^2}{4\pi\bar{A}}\left(1 - \frac{A_D}{\bar{A}}\right)\right]\frac{\partial A'}{\partial z} = 0$$

It can be seen that we have kept the terms

$$\left[-2A'\bar{u}_z\frac{d\bar{u}_z}{dz} + 2\frac{d\left(A_D - \bar{A}\right)}{dz}\bar{u}_z u'_z + 2\left(A_D - \bar{A}\right)\frac{d\bar{u}_z}{dz}u'_z\right]$$

$$\frac{\Gamma^2}{8\pi\bar{A}^2}\left[\frac{d\bar{A}}{dz}\left(1 - \frac{2A_D}{\bar{A}}\right)A'\right]$$

whereas they have neglected them. Also, we have to note that there should be $\frac{\Gamma^2}{8\pi\bar{A}}$ instead of $\frac{\Gamma^2}{4\pi\bar{A}}$ in Khan's equation due to the the way the equations are derived above.

The terms that were not omitted in continuity and momentum are the starting point where this model takes on its own path. We will see later that these terms are crucial in amplitude growth when the disturbance propagates through the transition region.

Next, we rearrange continuity Eq. (4.4) and momentum Eq. (4.5) by the order of derivatives, which will be convenient for later use:

$$\frac{\partial A'}{\partial t} + \bar{u}_z\frac{\partial A'}{\partial z} + \frac{d\bar{u}_z}{dz}A' - \left(A_D - \bar{A}\right)\frac{\partial u'_z}{\partial z} - \frac{d\left(A_D - \bar{A}\right)}{dz}u'_z = 0 \tag{4.6}$$

$$
\begin{aligned}
&- \bar{u}_z \frac{\partial A'}{\partial t} - \left[\bar{u}_z^2 + \frac{\Gamma^2}{8\pi \bar{A}^2}\left(A_D - \bar{A}\right)\right]\frac{\partial A'}{\partial z}\ldots \\
&\qquad \ldots - \left[2\bar{u}_z \frac{d\bar{u}_z}{dz} + \frac{\Gamma^2}{8\pi \bar{A}^2}\frac{d\bar{A}}{dz}\left(1 - \frac{2A_D}{\bar{A}}\right)\right] A' + \\
&+ \left(A_D - \bar{A}\right)\frac{\partial u_z'}{\partial t} + 2\left(A_D - \bar{A}\right)\bar{u}_z \frac{\partial u_z'}{\partial z}\ldots \\
&\qquad \ldots + \left[2\frac{d\left(A_D - \bar{A}\right)}{dz}\bar{u}_z + 2\left(A_D - \bar{A}\right)\frac{d\bar{u}_z}{dz}\right] u_z' = 0
\end{aligned} \tag{4.7}
$$

We assume that the gaseous core area and velocity disturbances may be represented in form of the Fourier waves $A' = \hat{A}e^{i(kz-\omega t)}$ and $u_z' = \hat{u}_z e^{i(kz-\omega t)}$, where the small amplitudes, $\hat{A}$ and $\hat{u}_z$, as well as the frequency, $\omega$, are *real*. However, we permit the wave number to be complex, $k = k_r + ik_i$, because we expect spatial growth of the disturbances in the transition region. Analogous reasoning was applied in Wu et al. [33, p. 1547], where they considered spatially growing waves on a swirling jet after it is injected into the ambient.

By substituting the Fourier waves into the continuity Eq. (4.6), we can rewrite it in the form

$$
-i\omega\hat{A} + \bar{u}_z\left(ik_r - k_i\right)\hat{A} + \frac{d\bar{u}_z}{dz}\hat{A} - \left(A_D - \bar{A}\right)\left(ik_r - k_i\right)\hat{u}_z - \frac{d\left(A_D - \bar{A}\right)}{dz}\hat{u}_z = 0 \tag{4.8}
$$

Now, because the amplitudes and the frequency are real in this expression, both its imaginary and real parts should be zero, that is:

$$
\left[k_r\bar{u}_z - \omega\right]\hat{A} - \left(A_D - \bar{A}\right)k_r\hat{u}_z = 0 \tag{4.9}
$$

$$
\left(\frac{d\bar{u}_z}{dz} - k_i\bar{u}_z\right)\hat{A} + \left[k_i\left(A_D - \bar{A}\right) - \frac{d\left(A_D - \bar{A}\right)}{dz}\right]\hat{u}_z = 0 \tag{4.10}
$$

We can do the same with the momentum Eq. (4.7) and transform it to

$$
\begin{aligned}
&+ \bar{u}_z i\omega\hat{A} - \left[\bar{u}_z^2 + \frac{\Gamma^2}{8\pi \bar{A}^2}\left(A_D - \bar{A}\right)\right]\left(ik_r - k_i\right)\hat{A}\ldots \\
&\qquad \ldots - \left[2\bar{u}_z \frac{d\bar{u}_z}{dz} + \frac{\Gamma^2}{8\pi \bar{A}^2}\frac{d\bar{A}}{dz}\left(1 - \frac{2A_D}{\bar{A}}\right)\right]\hat{A}\ldots \\
&- \left(A_D - \bar{A}\right)i\omega\hat{u}_z + 2\left(A_D - \bar{A}\right)\bar{u}_z\left(ik_r - k_i\right)\hat{u}_z\ldots \\
&\qquad \ldots + \left[2\frac{d\left(A_D - \bar{A}\right)}{dz}\bar{u}_z + 2\left(A_D - \bar{A}\right)\frac{d\bar{u}_z}{dz}\right]\hat{u}_z = 0
\end{aligned} \tag{4.11}
$$

with its imaginary and real parts given by

$$\left\{\omega\bar{u}_z - k_r\left[\bar{u}_z^2 + \frac{\Gamma^2}{8\pi\bar{A}^2}\left(A_D - \bar{A}\right)\right]\right\}\hat{A} + \left(A_D - \bar{A}\right)\left(-\omega + 2k_r\bar{u}_z\right)\hat{u}_z = 0 \tag{4.12}$$

$$\begin{aligned}\left\{k_i\left[\bar{u}_z^2 + \frac{\Gamma^2}{8\pi\bar{A}^2}\left(A_D - \bar{A}\right)\right] - \left[2\bar{u}_z\frac{d\bar{u}_z}{dz} + \frac{\Gamma^2}{8\pi\bar{A}^2}\frac{d\bar{A}}{dz}\left(1 - \frac{2A_D}{\bar{A}}\right)\right]\right\}\hat{A}\ldots \\ \ldots + \left[-k_i 2\left(A_D - \bar{A}\right)\bar{u}_z + 2\frac{d\left(A_D - \bar{A}\right)}{dz}\bar{u}_z + 2\left(A_D - \bar{A}\right)\frac{d\bar{u}_z}{dz}\right]\hat{u}_z = 0\end{aligned} \tag{4.13}$$

Next, we will assemble the imaginary and real parts of continuity and momentum separately from each other in two different matrices with the aim to produce solutions for real and imaginary wave numbers. Overall, this technique is similar to the methodology applied in gravity waves and can be seen in Didenkulova [90, p. 5].

The imaginary parts of the continuity Eq. (4.9) and the momentum Eq. (4.12) brought together in a matrix form look like

$$\begin{pmatrix} k_r\bar{u}_z - \omega & -\left(A_D - \bar{A}\right)k_r \\ \omega\bar{u}_z - k_r\left[\bar{u}_z^2 + \frac{\Gamma^2}{8\pi\bar{A}^2}\left(A_D - \bar{A}\right)\right] & \left(A_D - \bar{A}\right)\left(-\omega + 2k_r\bar{u}_z\right) \end{pmatrix}\begin{pmatrix}\hat{A}\\ \hat{u}_z\end{pmatrix} = \begin{pmatrix}0\\0\end{pmatrix} \tag{4.14}$$

This system of homogeneous equations can have a nontrivial solution for $\hat{A}$ and $\hat{u}_z$ only if the determinant of the matrix is zero (Kreyszig [91, p. 312, Theorem 4]), which we may write as

$$\begin{aligned}\left(k_r\bar{u}_z - \omega\right)\left(A_D - \bar{A}\right)\left(-\omega + 2k_r\bar{u}_z\right) + \ldots \\ \ldots\left(A_D - \bar{A}\right)k_r\left\{\omega\bar{u}_z - k_r\left[\bar{u}_z^2 + \frac{\Gamma^2}{8\pi\bar{A}^2}\left(A_D - \bar{A}\right)\right]\right\} = 0\end{aligned}$$

This equation may be simplified to a quadratic

$$\omega^2 - 2k_r\bar{u}_z\omega + k_r^2\left[\bar{u}_z^2 - \frac{\Gamma^2}{8\pi\bar{A}^2}\left(A_D - \bar{A}\right)\right] = 0$$

where from the solution follows as

$$\omega = k_r\bar{u}_z \pm k_r\sqrt{\frac{\Gamma^2}{8\pi\bar{A}^2}\left(A_D - \bar{A}\right)}$$

which is same as

$$\frac{\omega}{k_r} = \bar{u}_z \pm \sqrt{\frac{\Gamma^2}{8\pi\bar{A}^2}\left(A_D - \bar{A}\right)} \tag{4.15}$$

Now, this is the familiar equation of the phase speed of disturbance on a free surface, which propagates in swirling flow moving in the axial direction with a constant bulk velocity, and whose free surface and solid boundary have constant radii, or, in other words, are cylindrical. Recall from Chapter 2 that it was used with only a plus sign in Bazarov's [1] dynamic analysis. Thus, we can make an important conclusion here that in order to compute a *local* real wave number at some particular point in the transition region, we can simply use the "constant radii – constant velocity relation" between the angular frequency and the wave number. Lastly, it has to be pointed out that the plus sign in this equation corresponds to downstream propagating disturbances, and the minus sign – to upstream propagating disturbances (see Appendix B for more discussion).

Proceeding next to the real part of the continuity Eq. (4.10) and the momentum Eq. (4.13), we can gather them in a matrix form as

$$\begin{pmatrix} \dfrac{d\bar{u}_z}{dz} - k_i\bar{u}_z & k_i\left(A_D - \bar{A}\right) - \dfrac{d\left(A_D - \bar{A}\right)}{dz} \\ k_i S - P & -k_i 2\left(A_D - \bar{A}\right)\bar{u}_z + Q \end{pmatrix} \begin{pmatrix} \hat{A} \\ \hat{u}_z \end{pmatrix} = \begin{pmatrix} 0 \\ 0 \end{pmatrix} \tag{4.16}$$

where

$$\begin{aligned} S &= \bar{u}_z^2 + \frac{\Gamma^2}{8\pi\bar{A}^2}\left(A_D - \bar{A}\right) \\ P &= 2\bar{u}_z\frac{d\bar{u}_z}{dz} + \frac{\Gamma^2}{8\pi\bar{A}^2}\frac{d\bar{A}}{dz}\left(1 - \frac{2A_D}{\bar{A}}\right) \\ Q &= 2\frac{d\left(A_D - \bar{A}\right)}{dz}\bar{u}_z + 2\left(A_D - \bar{A}\right)\frac{d\bar{u}_z}{dz} \end{aligned}$$

The condition of zero determinant applies again and is given by

$$\begin{aligned} \left(\frac{d\bar{u}_z}{dz} - k_i\bar{u}_z\right)\left[-k_i 2\left(A_D - \bar{A}\right)\bar{u}_z + Q\right] - \ldots \\ \ldots (k_i S - P)\left[k_i\left(A_D - \bar{A}\right) - \frac{d\left(A_D - \bar{A}\right)}{dz}\right] = 0 \end{aligned}$$

This may be converted to the quadratic equation for $k_i$ as

$$\begin{aligned}
&\left(A_D - \bar{A}\right)\left(2\bar{u}_z^2 - S\right)k_i^2 + \ldots \\
&\ldots + \left[-2\left(A_D - \bar{A}\right)\bar{u}_z\frac{d\bar{u}_z}{dz} - \bar{u}_z Q + \left(A_D - \bar{A}\right)P + \frac{d\left(A_D - \bar{A}\right)}{dz}S\right]k_i \\
&\ldots + \frac{d\bar{u}_z}{dz}Q - \frac{d\left(A_D - \bar{A}\right)}{dz}P = 0
\end{aligned}$$

Then, the solution for $k_i$ is

$$k_i = \frac{-b_q \pm \sqrt{b_q^2 - 4a_q c_q}}{2a_q} \tag{4.17}$$

where the quadratic coefficients are given by

$$\begin{aligned}
a_q &= \left(A_D - \bar{A}\right)\left(2\bar{u}_z^2 - S\right) \\
b_q &= -2\left(A_D - \bar{A}\right)\bar{u}_z\frac{d\bar{u}_z}{dz} - \bar{u}_z Q + \left(A_D - \bar{A}\right)P + \frac{d\left(A_D - \bar{A}\right)}{dz}S \\
c_q &= \frac{d\bar{u}_z}{dz}Q - \frac{d\left(A_D - \bar{A}\right)}{dz}P
\end{aligned}$$

where $S$, $P$, and $Q$ are defined on page 81.

Now the questions are: which root of the two in Eq. (4.17) represents a wave traveling downstream, and which represents a wave traveling upstream. Intuitively, we should expect that the downstream traveling wave should grow in amplitude as it sees contraction of flow boundaries, and decay to the original amplitude when it finally enters the nozzle, where the stream velocity and flow boundaries are constant. Hence, the imaginary wave number corresponding to this wave should first grow more and more negative and then less and less negative. On the other hand, with regard to the upstream traveling wave, we know that it cannot exist in the uniform nozzle region (see Appendix B for more discussion), but it does exist in the uniform vortex chamber region. Hence, for this wave to disappear in the uniform nozzle region, its wave speed should decay to zero at a point where the uniform nozzle region starts. Accordingly, its real wave number should decay to negative infinity at this point, or, in other words, its length should become infinitesimally small. But in order

to conserve energy, this means that its amplitude should grow to positive infinity. Implying that, its imaginary wave number should decay to negative infinity. Based on this physical reasoning, we can make a clear selection which of the imaginary wave numbers corresponds to the upstream and downstream traveling waves.

## 4.3 Kelvin's Wave Refraction Model

The aim of this section is to derive a dispersion relation for Kelvin's waves propagating along the injector core in the nozzle entrance transition region of the swirl injector. The model approximations are set as follows:

1. The entire flow in the transition region is presumed to consist of infinitesimally short sections (axial direction wise) that are bounded by two truncated cones, of which the larger one is the solid boundary surface, and the smaller is the liquid free surface, Fig. 4.2. The slope of the larger cone is equal to the constant angle of conical convergence, $\alpha$, upstream of the nozzle entrance, and to zero, downstream of the nozzle entrance. The slope of the smaller cone is treated as being approximately constant within the boundaries of the section, with the slope given by the local derivative of the free surface radius, $\frac{d\delta}{dz}$.

2. Based on the fact that at any point of the swirl injector, the radial velocities of the steady bulk flow are much smaller than the axial ones (see Chapter 3), we presume that the steady axial velocity in each section is uniform in $r$, its value is equal to the local value computed from the one-dimensional continuity Eq. (4.1), and there is no bulk flow acceleration within the boundaries of the sections, or $\frac{d\bar{u}_z}{dz} = \frac{d\bar{\phi}^2}{dz^2} = 0$.

3. In each section, the unsteady fluctuations of the radial and axial velocities are assumed to be irrotational.

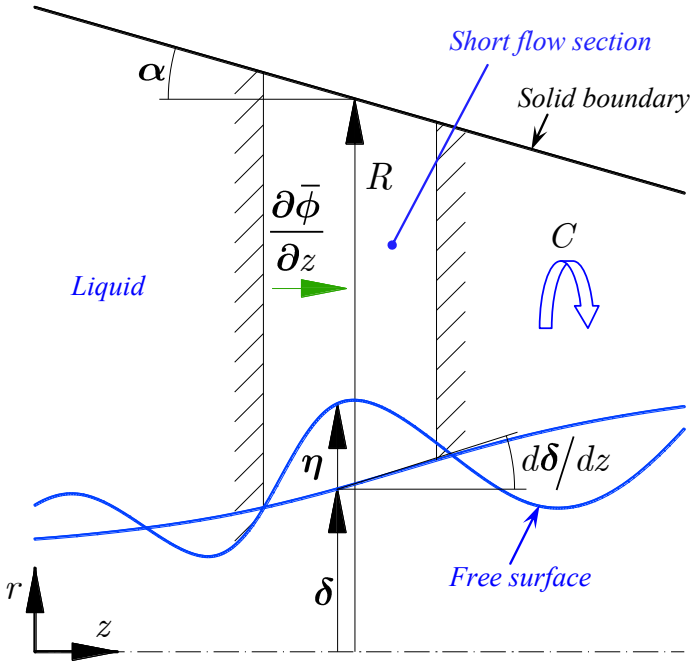


Figure 4.2.: Unsteady flow schematic for Kelvin's wave refraction analysis

4. At any point of the swirl injector, the unsteady fluctuations of circulation are ignored and the instantaneous circumferential velocity is presumed to follow the free vortex law (see Section 2.1 for more discussion on this treatment).

5. Based on presumptions 1–4, the unsteady flow in each section is potential.

The solution based on these assumptions will be rather *heuristic*, because ideally, one would not ignore the steady radial velocities and flow accelerations in the axial direction. However, this usually requires a higher (than first) order of small perturbation analysis, which drastically increases the mathematical effort to solve the unsteady problem. An analogous gravity wave problem was considered in the classical paper by Longuet-Higgins and Stewart [92], where they have shown that a second order analysis involving an interaction potential between the wave and the accelerating current is needed to treat the unsteady flow more precisely. On the other hand, the first order approximation that will be considered here helps to reveal the

intrinsic physics associated with the presence of radial velocity fluctuations, which were absent in the long wave analysis above.

In contrast with the analysis of Kelvin [24], who started from the equations of momentum and continuity, the analysis here is based on the existence of the velocity potential similarly to Binnie [26]. Accordingly, the governing equations describing the flow are [71, sec. 6.1]: the Laplace's equation,

$$\frac{\partial^2\phi}{\partial r^2}+\frac{1}{r}\frac{\partial\phi}{\partial r}+\frac{\partial^2\phi}{\partial z^2}=0 \qquad (\text{any } r) \tag{4.18}$$

the kinematic condition stating that the point moving on the free surface remains on it at all times,

$$\frac{D}{Dt}\left(r-(\delta+\eta)\right)=0 \qquad (r=\delta+\eta) \tag{4.19}$$

and the dynamic boundary condition, which is the unsteady Bernoulli's equation,

$$\frac{\partial\phi}{\partial t}+\frac{1}{2}\left[\left(\frac{\partial\phi}{\partial r}\right)^2+\left(\frac{\partial\phi}{\partial z}\right)^2+\frac{C^2}{(\delta+\eta)^2}\right]=\frac{1}{2}\left[\bar{u}_z^2+\bar{u}_r^2+\frac{C^2}{\delta^2}\right] \tag{4.20}$$

The linearization of these equations is obtained by applying flow splitting of the form $\phi=\bar{\phi}+\phi'$, where $\bar{\phi}$ is the steady part, and $\phi'$ is the unsteady part of the velocity potential. The Laplace's equation is then modified to

$$\frac{\partial^2\phi'}{\partial r^2}+\frac{1}{r}\frac{\partial\phi'}{\partial r}+\frac{\partial^2\phi'}{\partial z^2}=0 \qquad (\text{any } r) \tag{4.21}$$

Note that the steady part of Laplace's equation is identically zero because of zero radial velocities and axial accelerations stated above. To linearize the kinematic condition, we take the following steps:

$$\begin{aligned}
\frac{D}{Dt}\left(r-(\delta+\eta)\right) &= \frac{\partial\left(r-\delta-\eta\right)}{\partial t}+\frac{\partial\phi}{\partial r}\frac{\partial\left(r-\delta-\eta\right)}{\partial r}+\frac{\partial\phi}{\partial z}\frac{\partial\left(r-\delta-\eta\right)}{\partial z}\\
&= -\frac{\partial\eta}{\partial t}+\frac{\partial\phi}{\partial r}-\frac{\partial\phi}{\partial r}\frac{\partial\delta}{\partial r}-\frac{\partial\phi}{\partial r}\frac{\partial\eta}{\partial r}-\frac{\partial\phi}{\partial z}\frac{\partial\delta}{\partial z}-\frac{\partial\phi}{\partial z}\frac{\partial\eta}{\partial z}\\
&\qquad \left(\text{assume } \left|-\frac{\partial\phi}{\partial r}\frac{\partial\delta}{\partial r}-\frac{\partial\phi}{\partial r}\frac{\partial\eta}{\partial r}\right| \ll \left|-\frac{\partial\phi}{\partial z}\frac{\partial\delta}{\partial z}-\frac{\partial\phi}{\partial z}\frac{\partial\eta}{\partial z}\right|\right)\\
&= -\frac{\partial\eta}{\partial t}+\frac{\partial\bar{\phi}}{\partial r}+\frac{\partial\phi'}{\partial r}-\frac{\partial\bar{\phi}}{\partial z}\frac{\partial\delta}{\partial z}-\frac{\partial\phi'}{\partial z}\frac{\partial\delta}{\partial z}-\frac{\partial\bar{\phi}}{\partial z}\frac{\partial\eta}{\partial z}-\frac{\partial\phi'}{\partial z}\frac{\partial\eta}{\partial z}=0
\end{aligned}$$

In the last expression we note that the steady free surface slope is given by

$$\frac{\partial \delta}{\partial z} = \frac{\dfrac{\partial \bar{\phi}}{\partial r}}{\dfrac{\partial \bar{\phi}}{\partial z}}$$

and that $\dfrac{\partial \phi'}{\partial z}\dfrac{\partial \eta}{\partial z}$ term is negligibly small due to its second order, which permits us to rewrite the kinematic condition in its final form as

$$-\frac{\partial \eta}{\partial t} + \frac{\partial \phi'}{\partial r} - \frac{\partial \phi'}{\partial z}\frac{d\delta}{dz} - \frac{\partial \bar{\phi}}{\partial z}\frac{\partial \eta}{\partial z} = 0 \qquad (r = \delta) \tag{4.22}$$

Note that we have switched from $r = \delta + \eta$ to $r = \delta$ because of the following Taylor series approximations:

$$\begin{aligned}
\frac{\partial \phi'}{\partial r}(\delta + \eta) &= \frac{\partial \phi'}{\partial r}(\delta) + \eta\frac{\partial^2 \phi'}{\partial r^2}(\delta) + \ldots \simeq \frac{\partial \phi'}{\partial r}(\delta) \\
\frac{\partial \phi'}{\partial z}(\delta + \eta) &= \frac{\partial \phi'}{\partial z}(\delta) + \eta\frac{\partial^2 \phi'}{\partial z \partial r}(\delta) + \ldots \simeq \frac{\partial \phi'}{\partial z}(\delta) \\
\frac{\partial \eta}{\partial z}(\delta + \eta) &= \frac{\partial \eta}{\partial z}(\delta) + \eta\frac{\partial^2 \eta}{\partial z \partial r}(\delta) + \ldots \simeq \frac{\partial \eta}{\partial z}(\delta)
\end{aligned}$$

Next, we linearize Bernoulli's equation by first noting that

$$\frac{1}{(\delta + \eta)^2} \simeq \frac{1}{\delta^2} - \frac{2}{\delta^3}\eta$$

due to binomial expansion [61, p. 1196] shown on page 77 above. Then, we may write

$$\frac{\partial \phi'}{\partial t} + \frac{1}{2}\left[\left(\frac{\partial \bar{\phi}}{\partial z}\right)^2 + 2\frac{\partial \bar{\phi}}{\partial z}\frac{\partial \phi'}{\partial z} + \left(\frac{\partial \bar{\phi}}{\partial r}\right)^2 + 2\frac{\partial \bar{\phi}}{\partial r}\frac{\partial \phi'}{\partial r} + \frac{C^2}{\delta^2} - 2\frac{C^2}{\delta^3}\eta\right] = \frac{1}{2}\left[\bar{u}_z^2 + \bar{u}_r^2 + \frac{C^2}{\delta^2}\right]$$

where we have omitted higher order terms. After canceling the steady terms due to the steady state Bernoulli's equality,

$$\left(\frac{\partial \bar{\phi}}{\partial z}\right)^2 + \left(\frac{\partial \bar{\phi}}{\partial r}\right)^2 + \frac{C^2}{\delta^2} = \bar{u}_z^2 + \bar{u}_r^2 + \frac{C^2}{\delta^2}$$

and noting that

$$\left|\frac{\partial \bar{\phi}}{\partial r}\frac{\partial \phi'}{\partial r}\right| \ll \left|\frac{\partial \bar{\phi}}{\partial z}\frac{\partial \phi'}{\partial z}\right|$$

we obtain the final form of linearized Bernoulli's equation

$$\frac{\partial \phi'}{\partial t} + \frac{\partial \bar{\phi}}{\partial z}\frac{\partial \phi'}{\partial z} - \frac{C^2}{\delta^3}\eta = 0 \qquad (r = \delta) \tag{4.23}$$

where we again have switched to $r = \delta$ due to the reasoning above.

We now proceed to the Fourier analysis of disturbances by assuming that they may be represented by a sinusoidal form given by $\phi' = \hat{\phi}(r)\, e^{i(kz-\omega t)}$ and $\eta = \hat{\eta} e^{i(kz-\omega t)}$, where the amplitude $\hat{\phi}(r)$ is some unknown function of $r$. Also, as in the previous section, we allow the wave number to be complex, thereby indicating possible growth and/or decay of the disturbances in the transition region.

Laplace's equation (4.21) is then transformed into the modified Bessel's equation

$$\frac{\partial^2 \hat{\phi}}{\partial r^2} + \frac{1}{r}\frac{\partial \hat{\phi}}{\partial r} - k^2 \hat{\phi} = 0 \qquad (\text{any } r)$$

which has a solution given by

$$\hat{\phi}(r) = AI_0(kr) + BK_0(kr) \qquad (\text{any } r) \tag{4.24}$$

where $A$ and $B$ are unknown coefficients, that we will seek from the *local* boundary conditions depending on the axial position $z$ of the short section in consideration.

At the surface of the larger cone, the velocity disturbances have to obey the no-slip condition given by

$$\frac{\dfrac{\partial \phi'}{\partial r}}{\dfrac{\partial \phi'}{\partial z}} = -\tan(\alpha) \qquad (r = R)$$

This links the disturbance amplitudes by

$$\frac{\partial \hat{\phi}}{\partial r} = -ik\hat{\phi}\tan(\alpha) \qquad (r = R)$$

Substitution of the general expression for $\hat{\phi}$, Eq. (4.24), then gives

$$k\left[AI_1(kR) - BK_1(kR)\right] = -ik\left[AI_0(kR) + BK_0(kR)\right]\tan(\alpha)$$

which yields the dependence between $A$ and $B$

$$B = A\frac{I_1(kR) + iI_0(kR)\tan(\alpha)}{K_1(kR) - iK_0(kR)\tan(\alpha)} \tag{4.25}$$

For further calculations, it is convenient to have a variable

$$\beta = \frac{I_1(kR) + iI_0(kR)\tan(\alpha)}{K_1(kR) - iK_0(kR)\tan(\alpha)}$$

so that from Eq. (4.24) we have

$$\hat{\phi} = A\left[I_0(kr) + \beta K_0(kr)\right] \qquad (\text{any } r) \tag{4.26}$$

$$\frac{\partial \hat{\phi}}{\partial r} = Ak\left[I_1(kr) - \beta K_1(kr)\right] \qquad (\text{any } r) \tag{4.27}$$

At the surface of the smaller cone, the kinematic boundary condition (4.22) applies, which can be manipulated as

$$-i\omega(-\hat{\eta}) + \frac{\partial \hat{\phi}}{\partial r} - ik\hat{\phi}\frac{d\delta}{dz} - \frac{\partial \bar{\phi}}{\partial z}ik\hat{\eta} = 0 \qquad (r = \delta)$$

$$\frac{\partial \hat{\phi}}{\partial r} - ik\hat{\phi}\frac{d\delta}{dz} = \hat{\eta}i\left(k\frac{\partial \bar{\phi}}{\partial z} - \omega\right) \qquad (r = \delta)$$

Substitution of $\hat{\phi}$ and its derivative from Eqs. (4.26) and (4.27) into the last equation gives

$$Ak\left[I_1(k\delta) - \beta K_1(k\delta)\right] - ikA\left[I_0(k\delta) + \beta K_0(k\delta)\right]\frac{d\delta}{dz} = \hat{\eta}i\left(k\frac{\partial \bar{\phi}}{\partial z} - \omega\right)$$

From here we can obtain the expression for $A$:

$$A = \frac{i\left(k\dfrac{\partial \bar{\phi}}{\partial z} - \omega\right)}{k\left\{\left[I_1(k\delta) - \beta K_1(k\delta)\right] - i\left[I_0(k\delta) + \beta K_0(k\delta)\right]\dfrac{d\delta}{dz}\right\}}\hat{\eta} \tag{4.28}$$

This completes the definition of the unknown amplitude function $\hat{\phi}$. For further development, it is convenient to name the denominator in this equation as

$$\gamma = k\left\{\left[I_1(k\delta) - \beta K_1(k\delta)\right] - i\left[I_0(k\delta) + \beta K_0(k\delta)\right]\frac{d\delta}{dz}\right\}$$

Next, we proceed to find the dispersion relation between the wave number $k$ and the frequency $\omega$. By substituting $\hat{\phi}$ into the linearized Bernoulli's equation (4.23), we have

$$\hat{\phi}(-i\omega) + \frac{\partial \bar{\phi}}{\partial z}ik\hat{\phi} - \frac{C^2}{\delta^3}\hat{\eta} = 0 \qquad (r = \delta)$$

which is same as

$$\hat{\phi} = \frac{\dfrac{C^2}{\delta^3}}{i\left(k\dfrac{\partial\bar{\phi}}{\partial z} - \omega\right)}\hat{\eta} \qquad (r = \delta)$$

Now, we combine Eqs. (4.26) and (4.28) in $\hat{\phi}$, and rewrite the last equation as

$$\frac{i\left(k\dfrac{\partial\bar{\phi}}{\partial z} - \omega\right)\hat{\eta}}{\gamma}\left[I_0\left(k\delta\right) + \beta K_0\left(k\delta\right)\right] = \frac{\dfrac{C^2}{\delta^3}}{i\left(k\dfrac{\partial\bar{\phi}}{\partial z} - \omega\right)}\hat{\eta}$$

This then given the quadratic equation

$$\left(k\frac{\partial\bar{\phi}}{\partial z} - \omega\right)^2 = -\frac{\gamma}{\left[I_0\left(k\delta\right) + \beta K_0\left(k\delta\right)\right]}\frac{C^2}{\delta^3}$$

By performing the following manipulations

$$\frac{\omega}{k} = \frac{\partial\bar{\phi}}{\partial z} \pm \sqrt{-\frac{1}{k^2}\frac{\gamma}{\left[I_0\left(k\delta\right) + \beta K_0\left(k\delta\right)\right]}\frac{C^2}{\delta^3}}$$

(substitute $\gamma$ from its definition on page 88)

$$= \frac{\partial\bar{\phi}}{\partial z} \pm \sqrt{-\frac{1}{k^2}\frac{k\left\{\left[I_1\left(k\delta\right) - \beta K_1\left(k\delta\right)\right] - i\left[I_0\left(k\delta\right) + \beta K_0\left(k\delta\right)\right]\dfrac{d\delta}{dz}\right\}}{\left[I_0\left(k\delta\right) + \beta K_0\left(k\delta\right)\right]}\frac{C^2}{\delta^3}}$$

we obtain the final form of the dispersion relation after substituting $\beta$ from its definition on page 88

$$\frac{\omega}{k} = \frac{\partial\bar{\phi}}{\partial z} \pm \sqrt{\frac{1}{k}\left[\frac{-I_1\left(k\delta\right) + \dfrac{I_1\left(kR\right) + iI_0\left(kR\right)\tan\left(\alpha\right)}{K_1\left(kR\right) - iK_0\left(kR\right)\tan\left(\alpha\right)}K_1\left(k\delta\right)}{I_0\left(k\delta\right) + \dfrac{I_1\left(kR\right) + iI_0\left(kR\right)\tan\left(\alpha\right)}{K_1\left(kR\right) - iK_0\left(kR\right)\tan\left(\alpha\right)}K_0\left(k\delta\right)} + i\frac{d\delta}{dz}\right]\frac{C^2}{\delta^3}} \tag{4.29}$$

Note that this dispersion reduces to the classical result of Kelvin [24] when the flow boundaries do not change, or $\alpha = 0$ and $\dfrac{d\delta}{dz} = 0$. If say $R = R_0$ and $\delta = r_0$ in such case, then the dispersion takes the form

$$\frac{\omega}{k} = \bar{u}_z \pm \sqrt{\frac{1}{k}\frac{-I_1\left(kr_0\right) + \dfrac{I_1\left(kR_0\right)}{K_1\left(kR_0\right)}K_1\left(kr_0\right)}{I_0\left(kr_0\right) + \dfrac{I_1\left(kR_0\right)}{K_1\left(kR_0\right)}K_0\left(kr_0\right)}\frac{C^2}{r_0^3}} \tag{4.30}$$

which we have mentioned in Chapter 2 and rewritten here for convenience.

## 4.4 Results

In this section we will present the wave refraction patterns resulting from the long and Kelvin's wave models. From the previous two sections above, we can see that, in order to compute the variation of the real and imaginary wave numbers, we need to have the axial derivatives of $\bar{u}_z$, $\delta$, and $R$. For variation of $\delta$ we will use the results of Chapter 3, where a solution closely matching that of BEM has been obtained. The injector considered is the baseline injector described in Section 2.3, and the flow region considered is shown in Fig. 4.3. Notice that we have placed the origin at the entrance to the conical transition.

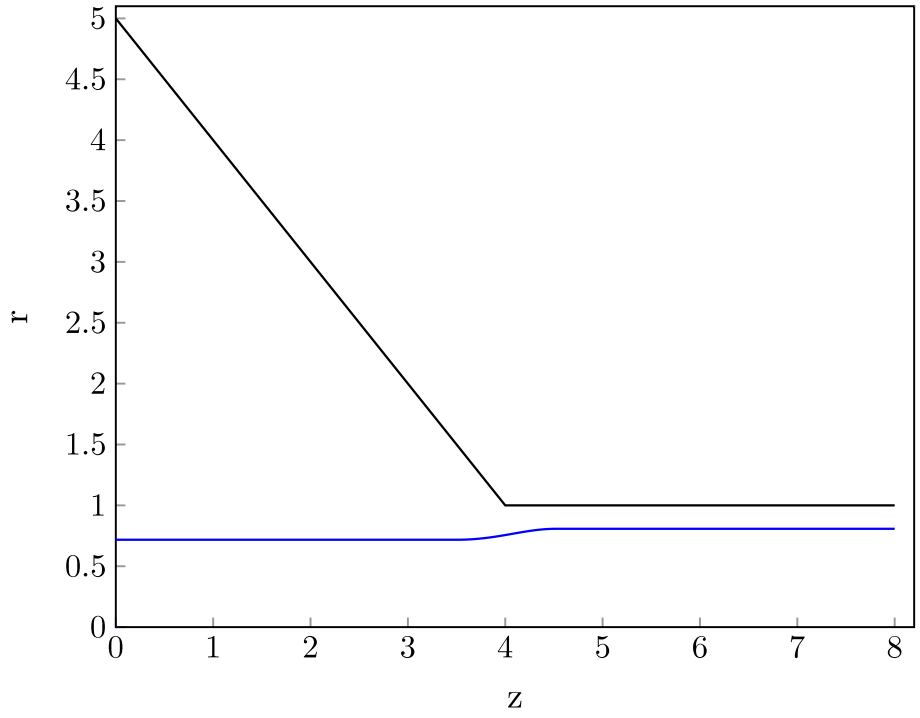


Figure 4.3.: Flow region considered for wave refraction

We have to point out here that, although the matching between the calculated $\delta$ and BEM was satisfactory in Chapter 2, it is still only approximate. One of the nuisances of that matching lies in the fact that, just downstream of the point where the free surface starts to deviate from $r_v$, the free surface radius makes a slight jump.

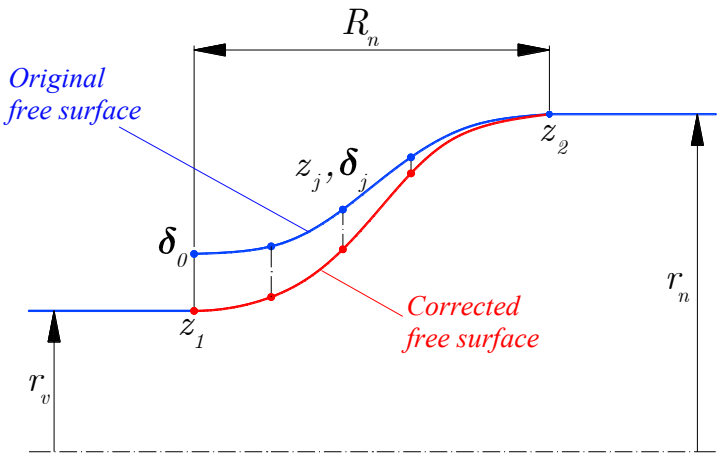


Figure 4.4.: Exaggerated view of free surface discontinuity at beginning of free surface transition

Let us denote the free surface radius at this point as $\delta_0$. Fig. 4.4 illustrates this situation in an exaggerated manner. Calculation shows that $\delta_0 = 0.7193$, whereas from Table 2.3 we know that $r_v = 0.7177$, which gives about 0.2% difference between them. We need to overcome this problem because, even though this discontinuity is almost unnoticeable, it will show up as a sharp peak in the refraction wave patterns produced. To do this, we will artificially stretch the originally calculated free surface radii in the transition region as shown in Fig. 4.4. This linear transformation is given by

$$\delta_j^{new} = \delta_j^{old} - \frac{z_2 - z_j}{z_2 - z_1}(\delta_0 - r_v)$$

where $z_1 = L_v + L_c - 0.5R_n$ and $z_2 = L_v + L_c + 0.5R_n$ are defined as was explained in Section 3.3.

With this correction, the variations of some of the key parameters involved in long and Kelvin's wave refraction equations are shown in Fig. 4.5. Notice the sharp changes in these parameters at a point where the nozzle starts, $z = 4$. Also, there are slight discontinuities in derivatives (see Fig. 4.5(c)) at the points where the free surface just starts to curve in the transition, $z = 3.5$, and where the free surface ends

transitioning, $z = 4.5$. All of these discontinuities will have repercussions in the wave refraction patterns that we will see below.

The results that will follow are presented for the baseline injector (Tables 2.2, 2.3) disturbed at an example dimensionless frequency $\omega = 10$. For this frequency, the calculations of wave numbers and speeds for the cylindrical sections of the flow are provided in Appendix B. The wave development will be shown for times $1.00 < t < 1.32$ with $\Delta t = 0.08$ intervals.

Figures 4.6 and 4.8 show the long wave results. From both Figs. 4.6(a) and 4.6(b) we can see the discontinuities at locations $z = 3.5$ and $z = 4$, which follow from the sudden changes in flow parameters shown in Fig. 4.5. Note that the imaginary wave number peaks out at $z = 4$, being most positive for downstream traveling waves and most negative for upstream traveling waves. This means that, close to this location, we should see a node in downstream traveling waves and maximum growth of upstream traveling waves as they travel through the transition. In Fig. 4.6(a), we can see that, for the downstream traveling waves, the imaginary wave number has two negative zones before and after that peak, meaning that we should see them growing in these areas. Beyond these areas, since the imaginary wave number is zero, their amplitude should be the same as the original one, with which they have entered the transition. Also, because the real wave number is greater in the nozzle region than in the transition, we should see shorter downstream traveling waves in the nozzle than in the vortex chamber. In Fig. 4.6(b), we can observe that, for upstream traveling waves, both real and imaginary wave numbers grow to negative infinity in the nozzle, indicating that their length should shrink to zero and their amplitude grow infinite. Physically, this means that, in the nozzle, the upstream traveling waves should disappear. We can observe all of these effects in Fig. 4.8 depicting the temporal and spatial development of the long waves.

Figures 4.7 and 4.9 show the results for the Kelvin's waves. Again, we can notice the sharp discontinuities at $z = 4$ and $z = 4.5$. For the downstream traveling waves, in Fig. 4.7(a), we can see that the imaginary wave number grows more and more negative

before $z = 4$, then jumps to less negative values in the area from $4 < z < 4.5$, and finally becomes zero at $z > 4.5$. This means that we can expect growth of downstream traveling waves up until $z = 4.5$. After that, the amplitude should be same as the original one. For the upstream traveling waves, in Fig. 4.7(b), we can see that their imaginary wave number grows to a large negative value at $z = 4$, which physically indicates that, after this location, the upstream traveling waves may be considered to be absent, and, accordingly, the resulting wave pattern can be ignored as non-physical. Another indication supporting this thought is the value of the wave number for the upstream traveling waves in the nozzle region, after $z = 4.5$. In this region, it is exactly equal to the value that corresponds to the downstream traveling waves, $k = 1.76$ (compare Figs. 4.7(a) and 4.7(b)), which is positive, meaning that the upstream traveling waves, which must have a negative wave number, do not exist, and are just replaced by the downstream traveling waves. All of these effects can be seen in Fig. 4.9 that shows how the waves develop in time and space due to Kelvin's approximation.

Finally, we can compare the resulting wave patterns for downstream traveling waves, which follow from both the long wave and Kelvin's wave analyses, Fig. 4.10. We can see that the long wave analysis produces larger wave length in the transition region. Accordingly, since Kelvin's waves are shorter, they should grow to a larger amplitude compared to the long waves, which we see at $z = 4$ location. Finally, notice that, in the nozzle, the lengths and amplitudes of both of these waves are almost the same.

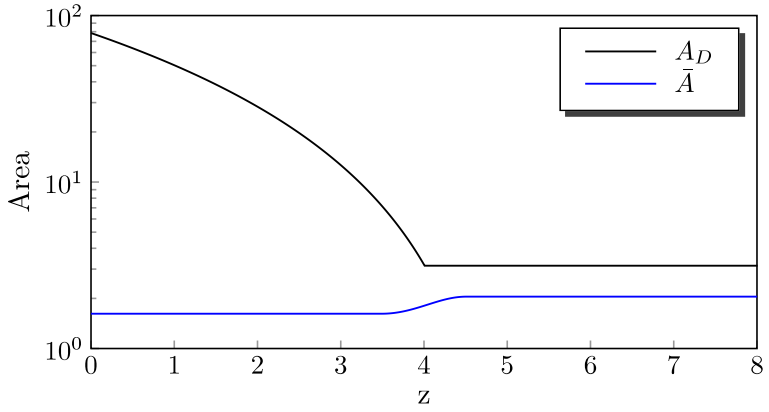


(a) Variation of duct and core areas in transition region

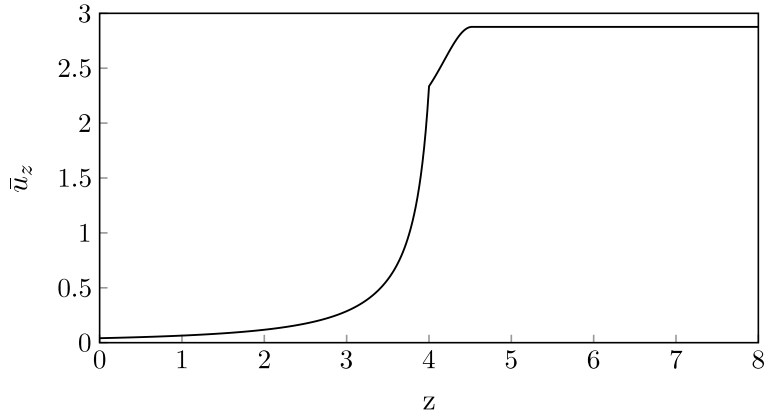


(b) Variation of bulk flow axial velocity in transition region

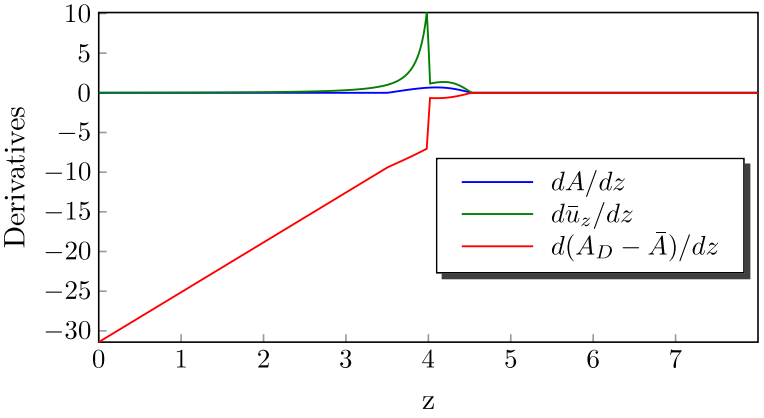


(c) Area and velocity derivatives in transition region

Figure 4.5.: Variation of flow parameters in transition region involved in disturbance wave refraction analysis (baseline injector, Tables 2.2, 2.3)

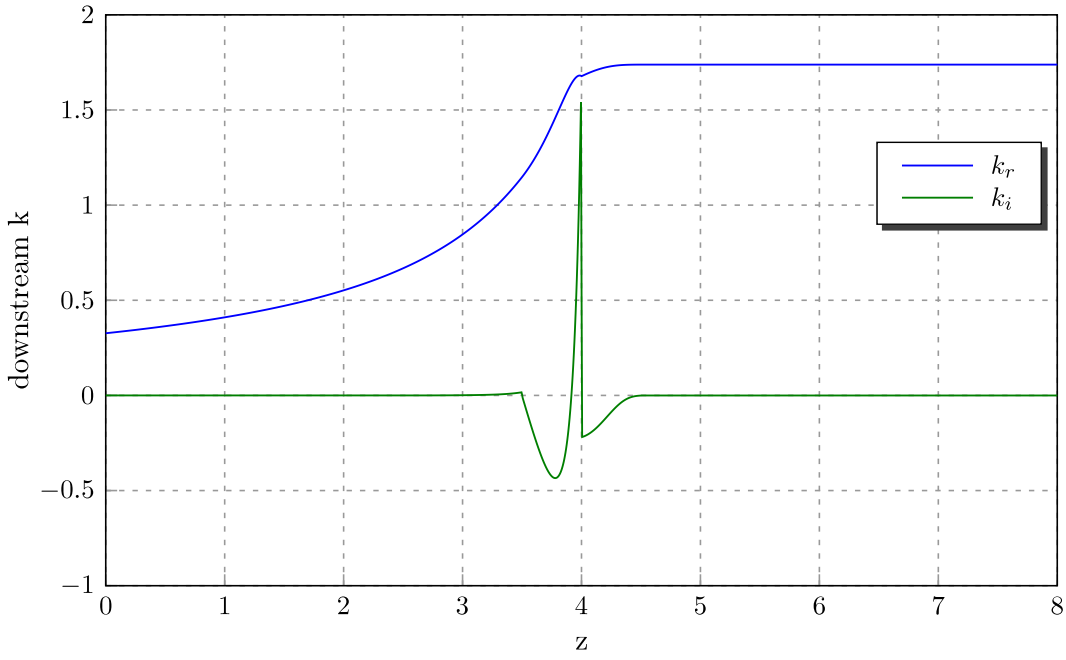


(a) Wave numbers of long waves traveling downstream

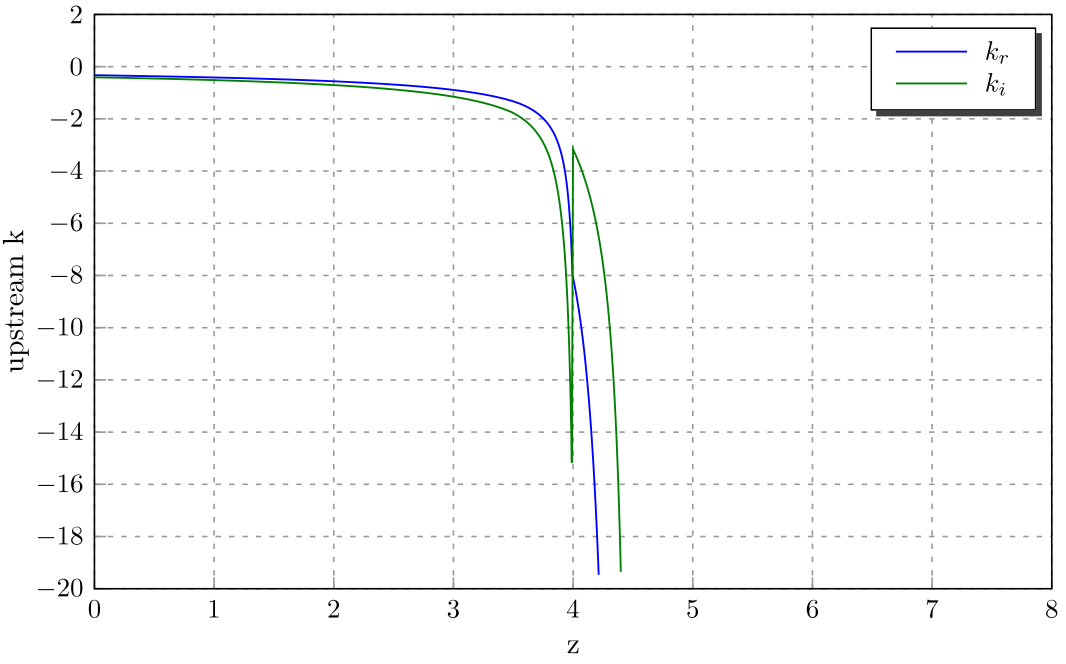


(b) Wave numbers of long waves traveling upstream

Figure 4.6.: Variation of real and imaginary wave numbers of long waves traveling downstream and upstream in nozzle entrance transition region ($\omega = 10$)

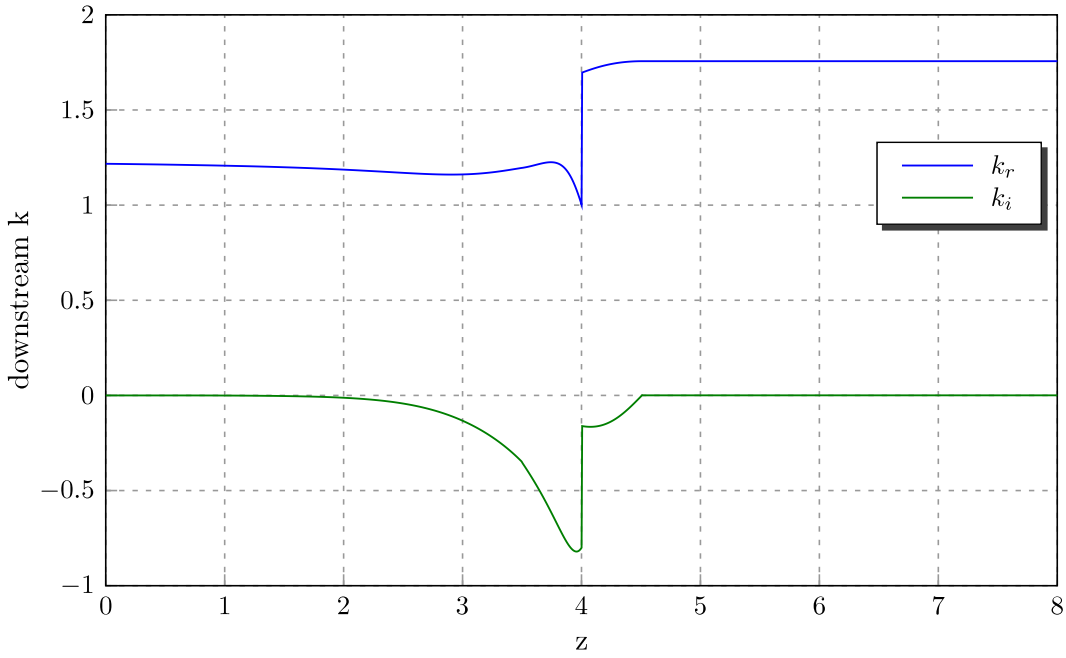


(a) Wave numbers of Kelvin's waves traveling downstream

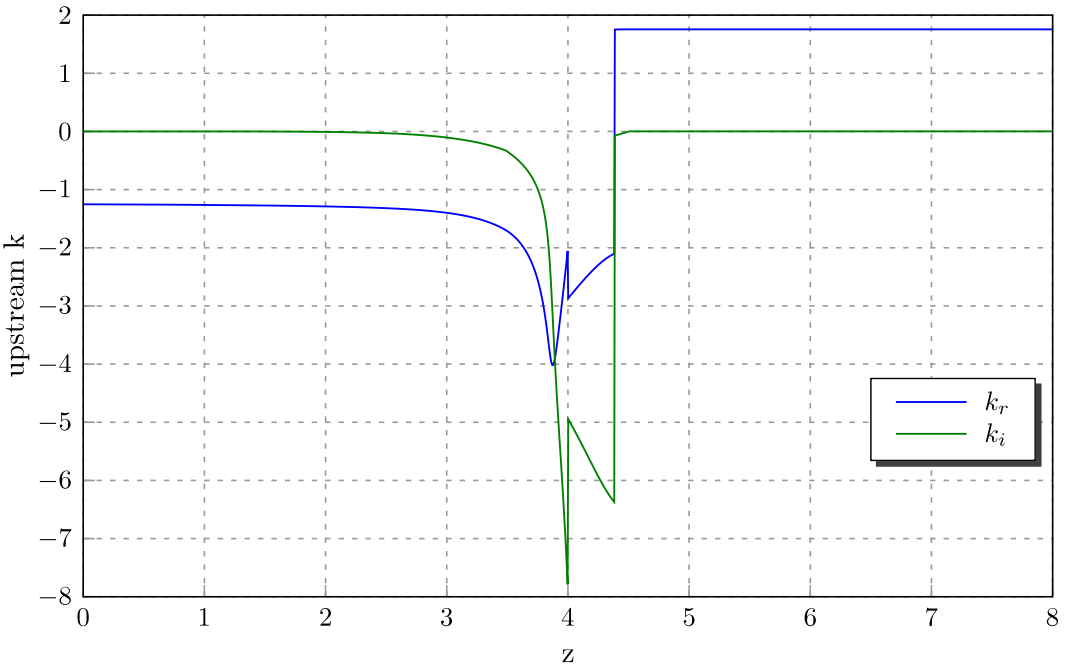


(b) Wave numbers of Kelvin's waves traveling upstream

Figure 4.7.: Variation of real and imaginary wave numbers of Kelvin's waves traveling downstream and upstream in nozzle entrance transition region ($\omega = 10$)

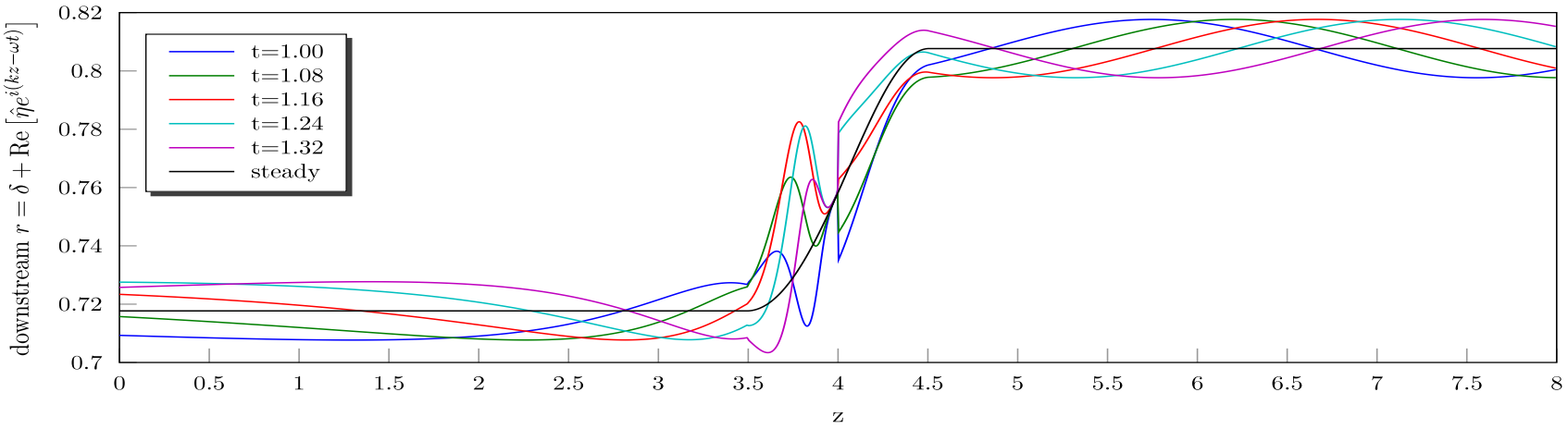


(a) Long waves traveling downstream

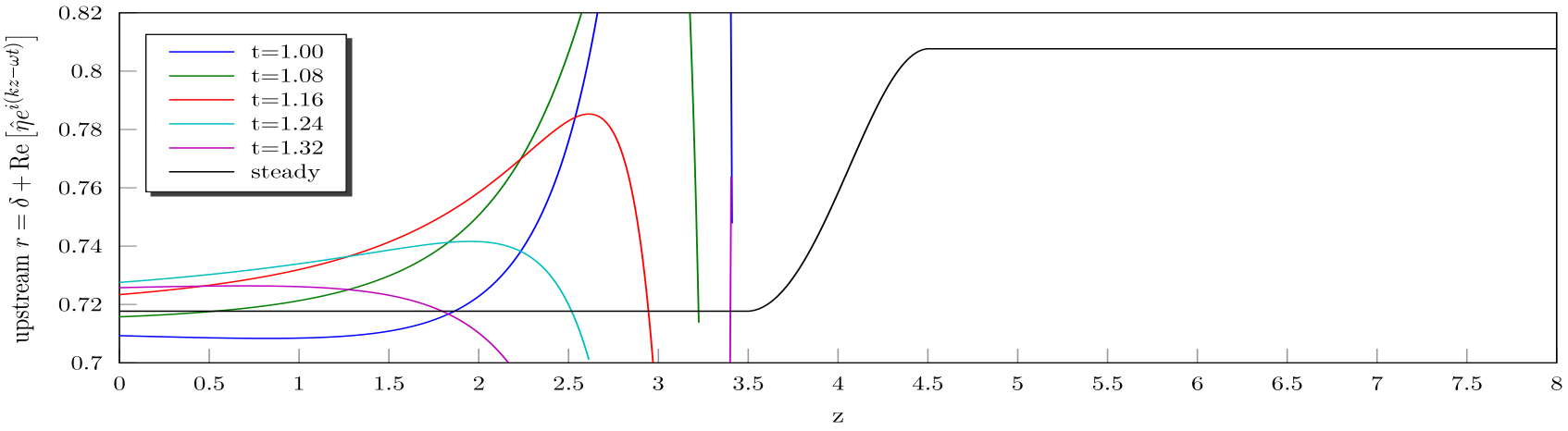


(b) Long waves traveling upstream

Figure 4.8.: Refraction pattern of long waves traveling downstream and upstream in nozzle entrance transition region

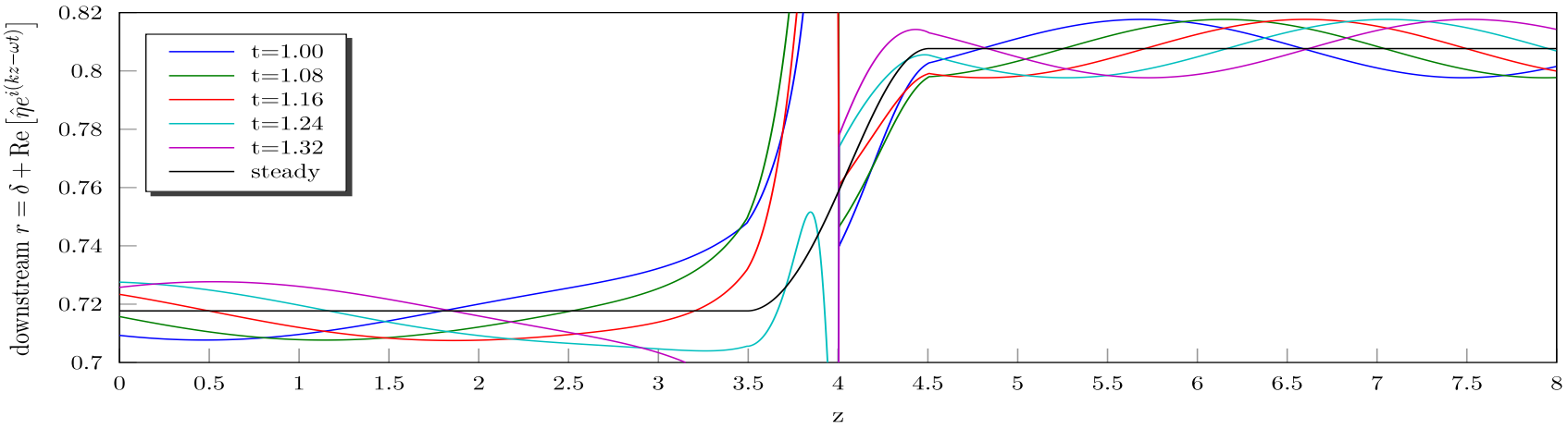


(a) Kelvin's waves traveling downstream

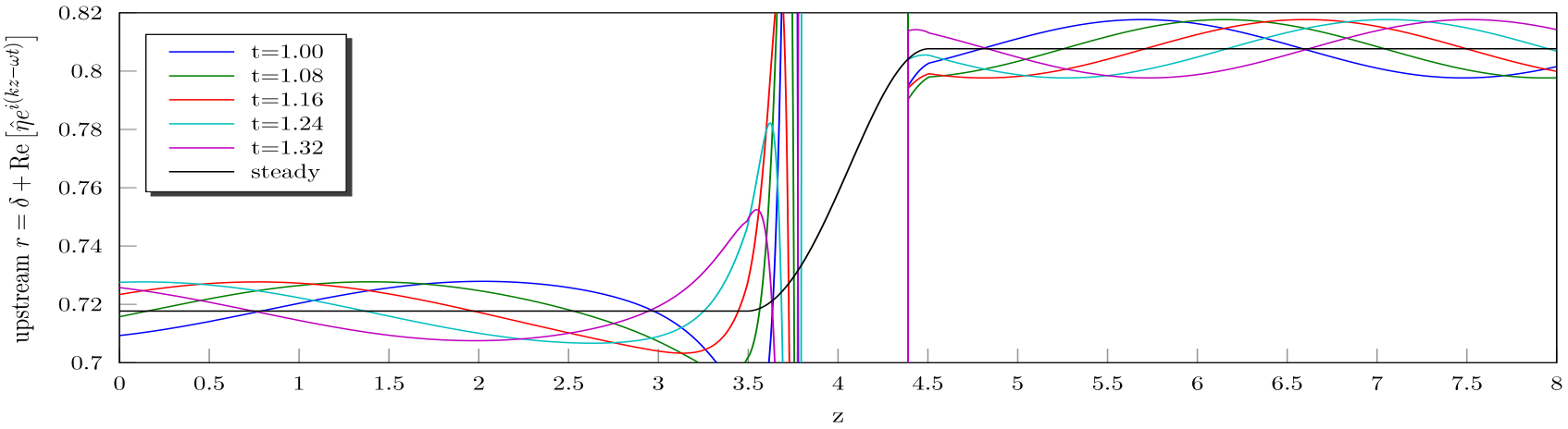


(b) Kelvin's waves traveling upstream

Figure 4.9.: Refraction pattern of Kelvin's waves traveling downstream and upstream in nozzle entrance transition region

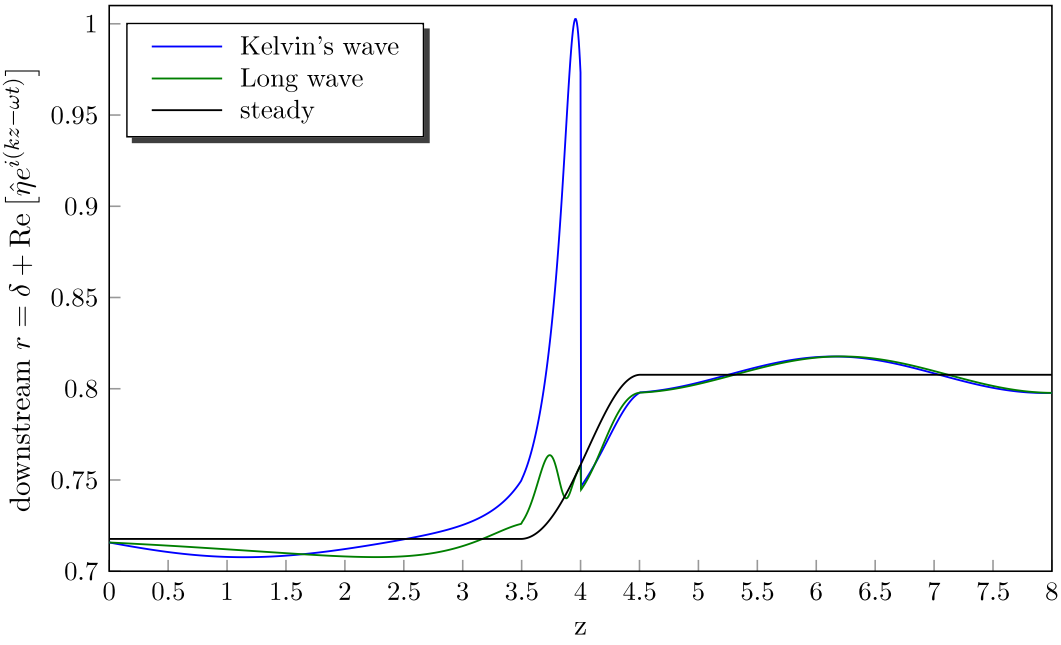


Figure 4.10.: Comparison between Kelvin's and long wave refraction patterns for waves traveling downstream in nozzle entrance transition region

## 4.5 Conclusions and Discussion

In this chapter, we have illustrated an application of the first order small perturbation analysis to the problem of disturbance wave refraction in the nozzle entrance transition region of a swirl injector. Two approximations have been studied: the long wave, which took its origin in Darmofal et al. [64], and the Kelvin's wave, which was an extension of classical Kelvin's [24] work on swirling cylindrical flows to the swirling flows where the bulk flow velocity and boundaries may vary. The solution for long waves can be considered exact because the whole flow has been assumed one-dimensional, and the radial velocity component was completely ignored. The Kelvin's wave analysis, however, is rather heuristic, because we have ignored the steady radial velocity component of the flow. Nonetheless, we have derived it to see the differences in the resulting refractive wave patterns relative to the long wave patterns.

The wave refraction has been achieved by allowing the wave number to be complex, thereby setting the possibility for the wave to grow in nonuniform regions of the flow. We have learned that, if the long wave approximation is assumed, then the wave speeds may be computed just as in purely cylindrical flows, with the difference that the local bulk flow velocity and bounding radii should be used. This information will become handy in the next chapter, where we will study wave reflection.

Based on the wave numbers that follow from the long wave and the Kelvin's wave approximations, we were able to produce the corresponding wave patterns in the transition, Fig. 4.8–4.10. These wave patterns reveal that the main region where the disturbance wave experiences variations in its length and amplitude is the nozzle entrance transition region of the swirl injector. Outside this region, the wave characteristics may be considered constant. Also, they show that there is distinctive difference between the long waves and Kelvin's waves: Kelvin's waves are shorter, and they grow to larger amplitudes, while traveling through the transition.

Of course, by looking at those wave patterns, one can argue that the discontinuities in the wave patterns are not physically possible, and the wave amplitudes would not grow to such large values at the nozzle entrance in proportion to the original amplitude, otherwise these waves may be considered as finite amplitude waves (Maxworthy [27]). However, the author believes that these discontinuities would be smoothed out if a higher order analysis is applied. Even then, the wave amplitudes might be growing to quite large values.

To conclude, the intention of this chapter is not to show the last word in the refraction analysis of the dynamic flow in swirl injectors, but rather to illustrate the first order linear assessment of it. Both the short and long wave refraction models described here may be developed further in the future, by refining the respective flow assumptions and boundary conditions.

# 5. DISTURBANCE WAVE REFLECTION AND SWIRL INJECTOR RESONANCE

## 5.1 Introduction

In this chapter, we will consider the second fundamental facet of the swirl injector dynamics: the disturbance wave reflections and the resonance caused by them. There is no indication in the existing literature that this topic has been investigated to date. On the other hand, there are such natural phenomena as the resonance in sea harbors (Miles [93], [94], [95]) or in a Helmholtz resonator (Miles [96], Ingard [97], Chanaud [98], Tang [99]), that have been widely studied. Accordingly, in this chapter, the author will attempt to setup the analytical models describing the wave reflections and resonance in the swirl injector by drawing an analogy to these known phenomena.

A general wave reflection problem is usually characterized by the reflection and transmission coefficients. If there is an incident disturbance wave in an oscillating system, these coefficients respectively describe what portion of the incident wave is reflected back into the system and what portion transmits out of the system. These coefficients depend on the sizes of the oscillating system and on the oscillation frequency itself.

In our case, the oscillating system is given by a swirl injector, where the wave reflections may occur in its vortex chamber and the nozzle entrance transition region. Imagine that an incident wave has been induced in the vortex chamber and is moving in the positive axial direction towards the nozzle. At the plane where the straight cylindrical solid boundary bends to become conical, an abrupt change in the bulk flow velocity and the liquid film thickness takes place. Then, as Mei [66, p. 123] states:

> *"When a propagating wave enters a region where the fractional change of depth within a wavelength is significant, the phenomenon of scattering occurs in which* reflection *becomes appreciable."*

Thus, when an incident wave arrives at that discontinuity plane, one portion of it reflects back into the vortex chamber, in the negative axial direction, and another portion transmits further into the transition region. Now, let us track the reflected portion of it in the vortex chamber. When the reflected wave comes to the head end solid wall, it is reflected once again, in the positive axial direction. Thus, we see two planes generating a wave reflection, suggesting that a *standing wave* pattern may be arranged in the vortex chamber, or as Kinsler and Frey [100, p. 134] write:

> *"The formation of a reflected wave at any plane boundary of a fluid medium will, of course, generate a pattern of standing waves in the fluid."*

The amplitude of the resulting standing wave depends on the reflection and transmission coefficients quantifying the events of reflections just described. Because these coefficients depend on the disturbance frequency, then, there may be frequencies, at which this amplitude is maximized. These frequencies are the natural frequencies of the swirl injector. Since the swirl injector is coupled to the combustion chamber of the rocket engine, then a resonance may occur when the combustion instability frequency coincides with one of the natural frequencies of the injector. We can draw an analogy to this situation by citing Gupta et al. [101], who investigated the conditions for resonance in the gaseous swirling flows:

> *"At the points where the natural resonant frequency of the enclosure and the frequency of PVC (precessing vortex core) coincide, high intensity of oscillations are expected."*

Accordingly, further on, we will refer to the natural frequencies of the swirl injector as the resonant frequencies.

Based on the discussion above, the aim of this chapter is to find the answers to the following questions:

- How are the amplitudes of the reflected and transmitted waves in the swirl injector defined in terms of its dimensions and the disturbance frequency?
- Is there a distinct set of resonant frequencies relevant for the swirl injector?

We can deal with this problem by presuming three different levels of approximation, depending on what parts of the injector are included in the analysis. In the first approximation, we consider only the vortex chamber as the main element causing the resonance and ignore the presence of the conical section and the nozzle, Section 5.2. In the second approximation, Section 5.4, we consider both the vortex chamber and the nozzle by assuming that they are connected by a sudden step, similar to Bazarov's idealized representation shown in Chapter 2, and look for the nozzle effect on the wave reflection and resonance characteristics. In the third approximation, Section 5.5, we consider all three elements of the swirl injector, the vortex chamber, the conical section, and the nozzle, and look for their collective influence on the wave reflection and resonance. We will respectively call these approximating models as:

- Abrupt Convergence Resonance Model 1 (ACRM-1)
- Abrupt Convergence Resonance Model 2 (ACRM-2)
- Conical Convergence Resonance Model (CCRM)

In the second and the third approximations we approach this problem by matching the instantaneous mass flow rate and momentum fluctuations at locations where the flow has discontinuities. For this purpose, in Section 5.3, the expressions for the instantaneous mass flow rate and momentum fluctuation in terms of the disturbance frequency will be derived.

All of these approximations are equally important, because each one of them may be used for the assessment of the swirl injector in terms of its resonant characteristics, depending on the level of detail required in the assessment. Also, all three of them may serve as a cross check between each other, since this topic is new and the results have to be anchored to one another when possible.

Finally, we shall emphasize that, in this chapter, we will deal with the *long* waves only, as the same analysis for Kelvin's waves is much more complicated and is out of the scope of this study. Moreover, there is more interest in the long wave resonance, as it is closer to real rocket engine conditions, as was mentioned in Section 4.1.

## 5.2 Abrupt Convergence Resonance Model 1 (ACRM-1): Vortex Chamber Wave Reflections and Resonance from Analogy With Sea Harbor

It is known that, when a harbor connected to the sea through a narrow channel is in resonance with say a tidal wave incident from the sea, the oscillations at the far end (relative to the entrance) of the harbor are the largest, while the oscillations at the channel entrance are negligibly smaller, Fig. 5.1. This is due to the standing gravity wave that establishes in the harbor, whose antinodes and nodes are located at the far end harbor wall and the channel entrance respectively. This situation is well described in Sorensen [102, Sec. 4.6], where the author shows the fundamental and harmonic

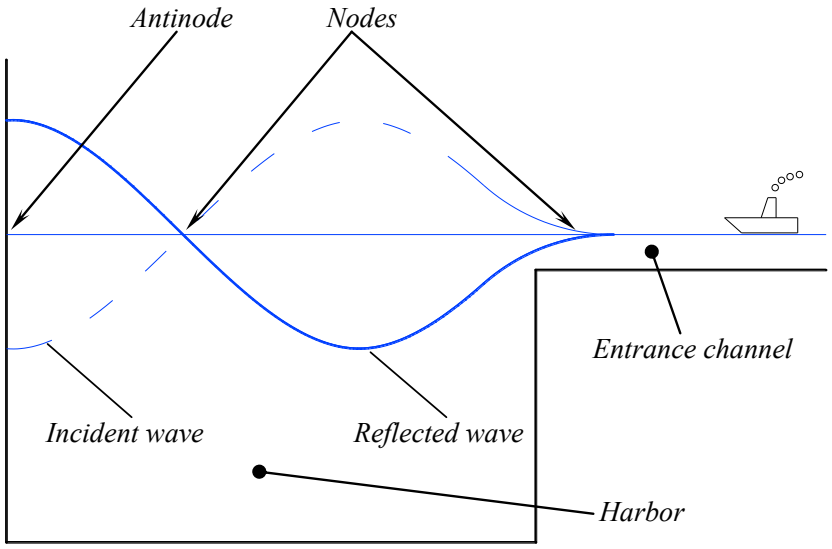


Figure 5.1.: Schematic of resonant standing wave formation in sea harbor with narrow entrance channel

modes of an open basin, and in Carrier et al. [103, App. I] and Mei [66, Sec. 5.7] who show how the channel couples to the harbor and causes the resonance.

It may be noticed that the swirl injector with the nozzle as a dynamic system bears a resemblance to the harbor with a narrow channel, where, in swirl injector, the vortex chamber plays the role of the harbor, and the nozzle plays the role of the narrow (and shallow) channel. From this perspective, we are looking for a simple qualitative description of the standing wave in the vortex chamber, and of the resonant frequencies that it produces.

We know that a general swirl injector with an arbitrary angle of conical convergence generates an oblique reflection at the point where the vortex chamber connects to the conical section. For simplicity, let us imagine that we have placed a straight step discontinuity at that point, so that all reflections in the vortex chamber become normal, which is similar to the harbor wall at the channel entrance that is perpendicular to the sea bed above in Fig. 5.1. Further, let us completely disregard the part of the injector downstream of that step discontinuity. Figure 5.2 then shows the assumed injector representation for this problem.

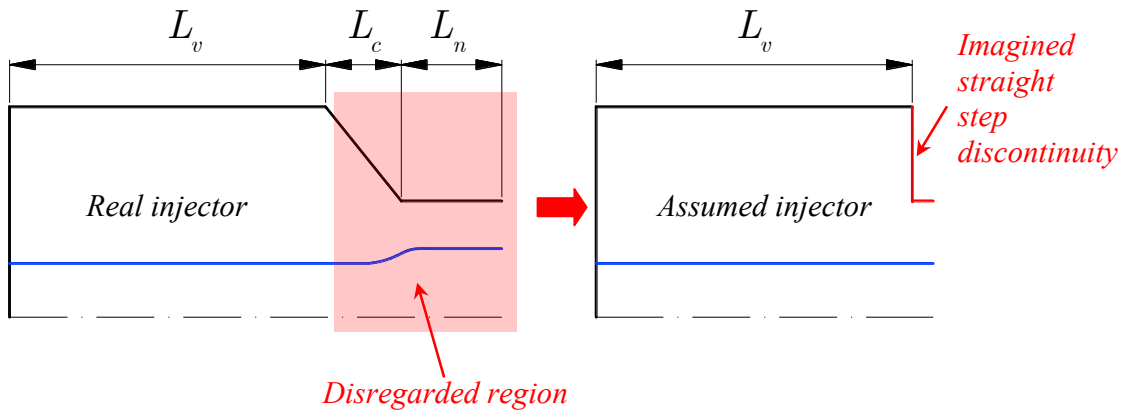


Figure 5.2.: Schematic of injector representation for Abrupt Convergence Resonance Model 1 (ACRM-1)

Now, let us imagine what would the standing wave pattern look like when the injector resonates with the combustion chamber of the rocket engine. Consider vortex chamber resonance from the injector response perspective. First, we expect that at resonance, the injector response should be at its maximum. Second, from its definition Eq. (1.1), which we rewrite here for convenience,

$$\Pi_{inj} = \frac{\dfrac{\dot{m}'_n}{\bar{\dot{m}}_n}}{\dfrac{\Delta p'_{inj}}{\Delta \bar{p}_{inj}}}$$

we see that the injector response is maximized when the magnitude of the nozzle mass flow rate fluctuation, $\dot{m}'_n$, is at its maximum, and the magnitude of the injector pressure drop fluctuation, $\Delta p'_{inj}$, is at its minimum. This is true, if and only if we have a node at the head end and an antinode at the nozzle entrance. Notice that this is very similar to the description of the standing wave in the harbor, with the locations of the node and the antinode reversed. Figure 5.3 shows schematically different possible modes of the wave patten that we may anticipate when the injector resonates.

In addition to the imagined straight step discontinuity, let us add another couple of simplifying assumptions as follows:

1. The disturbance wave speed is much larger than the axial bulk flow velocity in the vortex chamber (compare $c_v = +30.6089$ and $c_v = -30.5273$ from Table B.1 with $\bar{u}_{zv} = 0.0408$ from Table 2.3), so that we can think of the fluid in the vortex chamber as being quiescent with zero axial velocity, or $\bar{u}_{zv} = 0$ and $\dfrac{d\bar{u}_{zv}}{dz} = 0$.

2. Since the variation of the free surface radius at the head end is small, based on the results of Chapter 3, we can overall assume that there are no changes in steady flow boundaries in the vortex chamber, i.e $\dfrac{dA_D}{dz} = 0$ and $\dfrac{d\bar{A}}{dz} = 0$ (see Fig. 4.1).

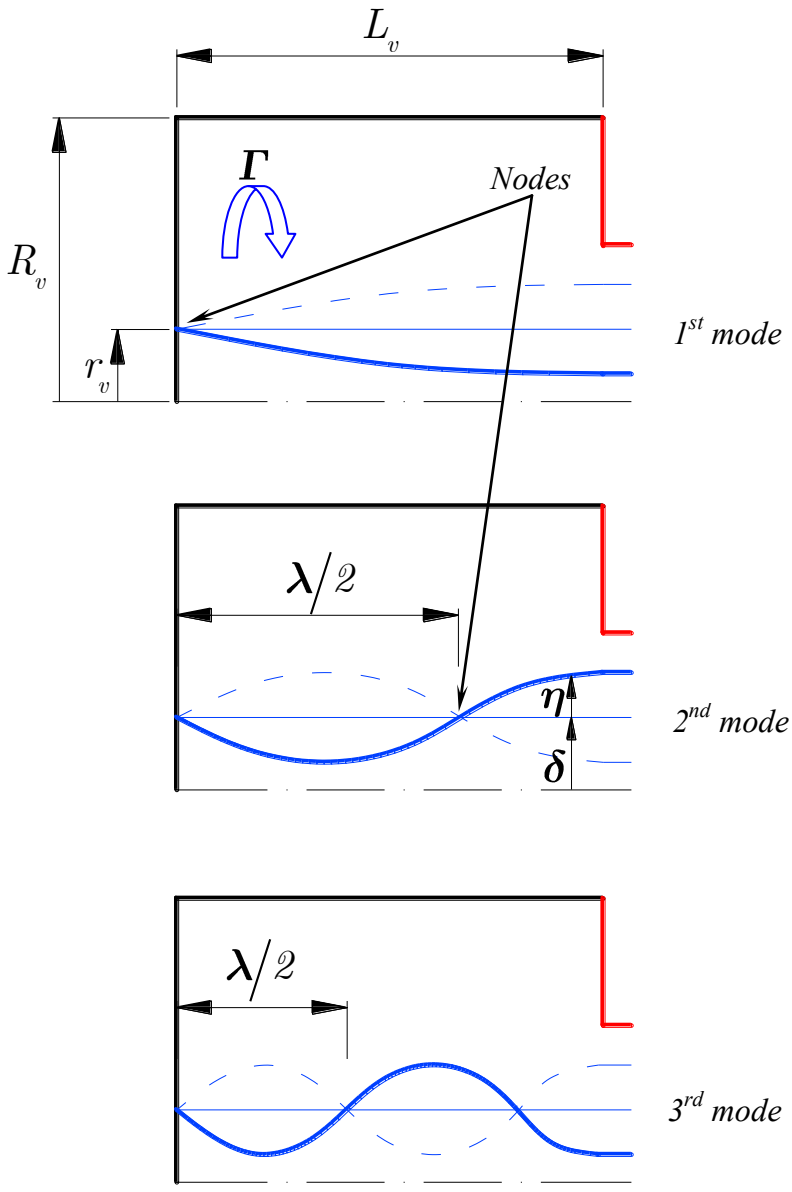


Figure 5.3.: Schematic of standing wave pattern when swirl injector is at resonance

This flow representation permits us to rewrite the long wave linearized Eqs. (4.4), (4.5) of continuity and momentum from Section 4.2 as follows:

$$\frac{\partial A'}{\partial t} = \left(A_D - \bar{A}\right) \frac{\partial u'_z}{\partial z} \tag{5.1}$$

$$\frac{\partial u'_z}{\partial t} = \frac{\Gamma^2}{8\pi \bar{A}^2} \frac{\partial A'_z}{\partial z} \tag{5.2}$$

From these equations, it is not difficult to construct the wave equation if we take the time derivative of Eq. (5.1),

$$\frac{\partial^2 A'}{\partial t^2} = \left(A_D - \bar{A}\right) \frac{\partial}{\partial t}\left(\frac{\partial u_z'}{\partial z}\right) = \left(A_D - \bar{A}\right) \frac{\partial}{\partial z}\left(\frac{\partial u_z'}{\partial t}\right)$$

and substitute Eq. (5.2) for the derivative of the velocity disturbance

$$\frac{\partial^2 A'}{\partial t^2} = \left(A_D - \bar{A}\right) \frac{\Gamma^2}{8\pi \bar{A}^2} \frac{\partial^2 A'}{\partial z^2} \tag{5.3}$$

We can rewrite this equation in terms of $\eta$, and radii $R$ and $\delta$. First we note that from

$$A = \bar{A} + A' = \pi(\delta + \eta)^2 \simeq \pi\delta^2 + 2\pi\delta\eta$$

we can define

$$A' = 2\pi\delta\eta \tag{5.4}$$

Also, by definition: $\Gamma = 2\pi C$, $A_D = \pi R^2$, and $\bar{A} = \pi\delta^2$. Substituting these definitions into the wave equation (5.3) gives

$$\frac{\partial^2 \eta}{\partial t^2} = C^2 \frac{R^2 - \delta^2}{2\delta^4} \frac{\partial^2 \eta}{\partial z^2} \tag{5.5}$$

which is a standard result for the long waves traveling on the core of swirling fluid that does not move axially. This is discussed in a different fashion from the kinematic approach perspective in Chinn [4, Subsec. 3.4.1], and in Bazarov [1, Eq. (3.44)] as an equation analogous to the gravity wave equation in a quiescent pool of water. In terms of the actual vortex chamber dimensions (see Fig. 5.3), this equation looks like

$$\frac{\partial^2 \eta}{\partial t^2} = C^2 \frac{R_v^2 - r_v^2}{2r_v^4} \frac{\partial^2 \eta}{\partial z^2} \tag{5.6}$$

It may be solved by representing $\eta$ as a product of the functions of time and space that are independent of each other, $\eta = F(t)G(z)$. For convenience, let us introduce a new variable

$$\gamma^2 = C^2 \frac{R_v^2 - r_v^2}{2r_v^4}$$

which represents the wave speed of the swirling flow in the vortex chamber, not moving in axial direction. Then, we can separate the variables as

$$\frac{1}{\gamma^2 F}\frac{d^2F}{dt^2} = \frac{1}{G}\frac{d^2G}{dz^2} = -k^2$$

where we have chosen the negative wave number squared as a separation constant to obtain a bounded solution. Then, the general solution is a periodic function given by

$$\eta = [P\cos(k\gamma t) + Q\sin(k\gamma t)]\,[A\cos(kz) + B\sin(kz)]$$

where $P$, $Q$, $A$, and $B$ are the unknown constants.

The positions of nodes and antinodes in Fig. 5.3 indicate two boundary conditions for $\eta$ valid at all times:

(a) $|\eta|$ should be zero at the head end, $z = 0$.

(b) $|\eta|$ should be maximum at the end of the vortex chamber, $z = L_v$.

From (a), we conclude that $A = 0$, which reduces the general solution to

$$\eta = [P\cos(k\gamma t) + Q\sin(k\gamma t)]\sin(kz)$$

where we have absorbed $B$ into $P$ and $Q$. Now the standing wave pattern is clearly seen. From (b), we deduce that $\sin(kL_v) = \pm 1$, which yields the resonant wave numbers:

$$k = n\frac{\pi}{2L_v}, \qquad n = 1, 3, 5, \ldots \tag{5.7}$$

The resonant frequencies, $\omega_0 = k\gamma$, are respectively

$$\omega_0 = n\frac{\pi}{2L_v}\sqrt{C^2\frac{R_v^2 - r_v^2}{2r_v^4}}, \qquad n = 1, 3, 5, \ldots \tag{5.8}$$

where by subscript zero we emphasize the notion of resonance.

## 5.3 Long Wave Fluctuations of Mass Flow Rate and Momentum in Cylindrical Flow Sections

In this section, based on the definitions of instantaneous mass flow rate and momentum, we will derive the expressions for the fluctuating parts of each of them, that are valid in a purely cylindrical section of the swirling flow, in which the radii of steady flow boundaries and bulk stream velocity are considered constant, and which is experiencing long wave perturbations. We need to know this information for use in the more precise wave reflection/resonance models (ACRM-2 and CCRM) of the swirl injector that will come later in the next two sections.

The cylindrical constant velocity flow setup assumed here in permits us to use the results of Chapter 4 with the omission of steady flow derivatives and the imaginary wave numbers which account for refraction, i.e $\frac{dA_D}{dz},\ \frac{d\bar{A}}{dz},\ \frac{d\bar{u}_z}{dz},\ k_i = 0.$

In both mass flow rate and momentum, we will need to know the value of the axial velocity fluctuation magnitude, which we can immediately obtain from Eq. (4.8) in Section 4.2,

$$\hat{u}_z = \frac{k_r \bar{u}_z - \omega}{\left(A_D - \bar{A}\right) k_r} \hat{A}$$

After substituting the magnitude of core area fluctuation based on Eq. (5.4), $\hat{A} = 2\pi\delta\hat{\eta}$, the definitions $A_D = \pi R^2$, and $A = \pi\delta^2$, and switching back to the whole disturbance values instead of the magnitude values, we can rewrite this equation as

$$u'_z = 2\delta \frac{k\bar{u}_z - \omega}{k\left(R^2 - \delta^2\right)} \eta \tag{5.9}$$

where $\delta$ is the steady free surface radius, and $R$ is the solid boundary radius. Note that, from here on, for simplicity, we will omit the subscript $r$ under the wave number, which denotes the real value, because, due to the absence of refraction, the wave number is purely real.

### 5.3.1 Long Wave Fluctuation of Mass Flow Rate

By definition, the instantaneous mass flow rate at any flow cross-section can be written as

$$\dot{m} = \bar{\dot{m}} + \dot{m}' = \rho \int_{\delta+\eta}^{R} (\bar{u}_z + u'_z) 2\pi r dr$$

$$= \rho \left[ \int_{\delta}^{R} \bar{u}_z 2\pi r dr - \int_{\delta}^{\delta+\eta} \bar{u}_z 2\pi r dr + \int_{\delta}^{R} u'_z 2\pi r dr - \int_{\delta}^{\delta+\eta} u'_z 2\pi r dr \right]$$

The first integral here is just the steady state mass flow rate,

$$\bar{\dot{m}} = \rho \int_{\delta}^{R} \bar{u}_z 2\pi r dr$$

and the last integral vanishes due to Taylor series expansion of $u'_z$,

$$u'_z(\delta + \eta) = u'_z(\delta) + \eta \frac{\partial u'_z}{\partial r}(\delta) \simeq u'_z(\delta)$$

Then we can rewrite the mass flow rate equation as

$$\dot{m} = \bar{\dot{m}} - \rho \bar{u}_z \pi \left[ (\delta + \eta)^2 - \delta^2 \right] + \rho u'_z \pi \left( R^2 - \delta^2 \right)$$

$$= \bar{\dot{m}} - \rho \bar{u}_z \pi 2\delta\eta + \rho u'_z \pi \left( R^2 - \delta^2 \right)$$

Which means that the unsteady part of the mass flow rate is

$$\dot{m}' = -2\pi\rho\delta\bar{u}_z\eta + \rho\pi \left( R^2 - \delta^2 \right) u'_z$$

We can modify further this equation by substituting the velocity fluctuation from Eq. (5.9)

$$\dot{m}' = -2\pi\rho\delta\bar{u}_z\eta + \rho\pi \left( R^2 - \delta^2 \right) 2\delta \frac{k\bar{u}_z - \omega}{k\left( R^2 - \delta^2 \right)} \eta$$

$$= -2\pi\rho\delta\bar{u}_z\eta + \rho\pi 2\delta\bar{u}_z\eta - \rho\pi 2\delta \frac{\omega}{k}\eta$$

Then, after canceling the first two terms, we have the final expression for the unsteady mass flow rate fluctuation:

$$\dot{m}' = -2\pi\rho\delta\frac{\omega}{k}\eta \tag{5.10}$$

### 5.3.2 Long Wave Fluctuation of Momentum

Assuming there are no external body or friction forces acting on the flow, we can define the total momentum of the flow, $M_\Sigma = \bar{M}_\Sigma + M'_\Sigma$, as being consistent of the kinetic part, $M_u = \bar{M}_u + M'_u$, and the pressure part, $M_p = \bar{M}_p + M'_p$, which we may write as

$$M_\Sigma = M_u + M_p = \rho \int_{\delta+\eta}^{R} \left(\bar{u}_z + u'_z\right)^2 2\pi r dr + \int_{\delta+\eta}^{R} p\left(r\right) 2\pi r dr \tag{5.11}$$

Let us investigate both of these integrals separately. Starting from the kinetic part, we may write

$$\begin{aligned} M_u = \bar{M}_u + M'_u &= \rho \int_{\delta+\eta}^{R} \left(\bar{u}_z + u'_z\right)^2 2\pi r dr = \rho \int_{\delta+\eta}^{R} \left(\bar{u}_z^2 + 2\bar{u}_z u'_z\right) 2\pi r dr \\ &= \rho\left(\bar{u}_z^2 + 2\bar{u}_z u'_z\right)\pi\left[R^2 - \left(\delta+\eta\right)^2\right] = \rho\left(\bar{u}_z^2 + 2\bar{u}_z u'_z\right)\pi\left(R^2 - \delta^2 - 2\delta\eta\right) \\ &= \rho\bar{u}_z^2\pi\left(R^2 - \delta^2\right) - \rho\bar{u}_z^2\pi 2\delta\eta + \rho 2\bar{u}_z u'_z\pi\left(R^2 - \delta^2\right) \end{aligned}$$

From here we can extract the unsteady part, and then substitute the velocity fluctuation from Eq. (5.9) as follows:

$$\begin{aligned} M'_u &= -\rho 2\pi\delta\bar{u}_z^2\eta + \rho 2\pi\left(R^2 - \delta^2\right)\bar{u}_z u'_z \\ &= -\rho 2\pi\delta\bar{u}_z^2\eta + \rho 2\pi\left(R^2 - \delta^2\right)\bar{u}_z 2\delta\frac{k\bar{u}_z - \omega}{k\left(R^2 - \delta^2\right)}\eta \\ &= \rho\pi\left(-2\delta\bar{u}_z^2 + 4\bar{u}_z\delta\frac{k\bar{u}_z - \omega}{k}\right)\eta \end{aligned} \tag{5.12}$$

Next, since the flow is purely axial and we do not have the radial velocity fluctuations in the long wave treatment, the pressure at some radius in the flow may be written as

$$p\left(r\right) = \rho \int_{\delta+\eta}^{r} \frac{C^2}{\tilde{r}^3} d\tilde{r} = \rho\frac{1}{2}C^2\left[\frac{1}{\left(\delta+\eta\right)^2} - \frac{1}{r^2}\right]$$

where $\tilde{r}$ is a dummy radius. Now, we can insert this expression into the pressure part of momentum Eq. (5.11) to get

$$\begin{aligned} M_p = \bar{M}_p + M_p' &= \int_{\delta+\eta}^{R} p\,(r)\,2\pi r dr = \rho \int_{\delta+\eta}^{R} \frac{1}{2} C^2 \left[\frac{1}{(\delta+\eta)^2} - \frac{1}{r^2}\right] 2\pi r dr \\ &= \rho\pi C^2 \left[\frac{1}{(\delta+\eta)^2} \int_{\delta+\eta}^{R} r dr - \int_{\delta+\eta}^{R} \frac{1}{r} dr\right] \\ &= \rho\pi C^2 \left\{\frac{1}{2}\frac{1}{(\delta+\eta)^2}\left[R^2 - (\delta+\eta)^2\right] - \ln\frac{R}{\delta+\eta}\right\} \end{aligned} \tag{5.13}$$

To work on the first term in this expression, we will use the binomial expansion shown in Section 4.3, which we rewrite here for convenience

$$\frac{1}{(\delta+\eta)^2} \simeq \frac{1}{\delta^2} - \frac{2}{\delta^3}\eta$$

By substituting into previous equation, we can write

$$\begin{aligned} \frac{1}{2}\frac{1}{(\delta+\eta)^2}\left[R^2 - (\delta+\eta)^2\right] &= \frac{1}{2}\left(\frac{1}{\delta^2} - \frac{2}{\delta^3}\eta\right)\left(R^2 - \delta^2 - 2\delta\eta - \eta^2\right) \\ &= \frac{1}{2}\left(\frac{R^2-\delta^2}{\delta^2} - 2\frac{R^2-\delta^2}{\delta^3}\eta - 2\frac{\delta}{\delta^2}\eta + 4\frac{\delta}{\delta^3}\eta^2\right) \\ &= \frac{R^2-\delta^2}{2\delta^2} - \frac{R^2-\delta^2}{\delta^3}\eta - \frac{1}{\delta}\eta \end{aligned} \tag{5.14}$$

To modify the logarithm term in Eq. (5.13), we will use the binomial expansion

$$\frac{1}{\delta+\eta} \simeq \frac{1}{\delta} - \frac{1}{\delta^2}\eta$$

written up to the first order in $\eta$, and the series expansion [104, p. 111]

$$\ln x \simeq (x-1) - \frac{(x-1)^2}{2} + \frac{(x-1)^3}{3}$$

which we write up to the third term in this study. Note that this expansion is formally valid for $|x-1| \leq 1$, or $0 < x \leq 2$. In this study, for simplicity, we will assume that this series expansion is valid for the whole range of the argument, or for $x > 0$. Ideally,

one would write as many terms in this expansion as possible to make the end result more precise. The logarithmic term may be manipulated as follows:

$$\ln\frac{R}{\delta+\eta}=\ln\left(\frac{R}{\delta}-\frac{R}{\delta^2}\eta\right)=$$

$$=\left(\frac{R}{\delta}-\frac{R}{\delta^2}\eta-1\right)-\frac{\left(\frac{R}{\delta}-\frac{R}{\delta^2}\eta-1\right)^2}{2}+\frac{\left(\frac{R}{\delta}-\frac{R}{\delta^2}\eta-1\right)^3}{3}=$$

$$=\left(\frac{R}{\delta}-\frac{R}{\delta^2}\eta-1\right)-\frac{1}{2}\left[\left(\frac{R}{\delta}-1\right)^2-2\left(\frac{R}{\delta}-1\right)\frac{R}{\delta^2}\eta+\left(\frac{R}{\delta^2}\eta\right)^2\right]+\ldots$$

$$\ldots+\frac{1}{3}\left[\left(\frac{R}{\delta}-1\right)^3-3\left(\frac{R}{\delta}-1\right)^2\frac{R}{\delta^2}\eta+3\left(\frac{R}{\delta}-1\right)\left(\frac{R}{\delta^2}\eta\right)^2-\left(\frac{R}{\delta^2}\eta\right)^3\right]=$$

(neglect all higher order terms)

$$=\left(\frac{R}{\delta}-1\right)-\frac{1}{2}\left(\frac{R}{\delta}-1\right)^2+\frac{1}{3}\left(\frac{R}{\delta}-1\right)^3+\frac{R}{\delta^2}\left[-1+\left(\frac{R}{\delta}-1\right)-\left(\frac{R}{\delta}-1\right)^2\right]\eta$$

The last expression in square brackets can be rearranged as

$$-1+\left(\frac{R}{\delta}-1\right)-\left(\frac{R}{\delta}-1\right)^2=-2+\frac{R}{\delta}-\frac{R^2}{\delta^2}+2\frac{R}{\delta}-1=-\frac{R^2}{\delta^2}+3\frac{R}{\delta}-3$$

Then, the final expression for the logarithmic term can be written as

$$\ln\frac{R}{\delta+\eta}=\left(\frac{R}{\delta}-1\right)-\frac{1}{2}\left(\frac{R}{\delta}-1\right)^2+\frac{1}{3}\left(\frac{R}{\delta}-1\right)^3+\frac{R}{\delta^2}\left(-\frac{R^2}{\delta^2}+3\frac{R}{\delta}-3\right)\eta \quad (5.15)$$

Plugging Eqs. (5.14) and (5.15) back into the pressure part of momentum, Eq. (5.13), we have

$$M_p=\rho\pi C^2\left(\frac{R^2-\delta^2}{2\delta^2}-\frac{R^2-\delta^2}{\delta^3}\eta-\frac{1}{\delta}\eta\right)\ldots$$

$$\ldots-\rho\pi C^2\left[\left(\frac{R}{\delta}-1\right)-\frac{1}{2}\left(\frac{R}{\delta}-1\right)^2+\frac{1}{3}\left(\frac{R}{\delta}-1\right)^3+\frac{R}{\delta^2}\left(-\frac{R^2}{\delta^2}+3\frac{R}{\delta}-3\right)\eta\right]$$

$$=\rho\pi C^2\left[\frac{R^2-\delta^2}{2\delta^2}-\left(\frac{R}{\delta}-1\right)+\frac{1}{2}\left(\frac{R}{\delta}-1\right)^2-\frac{1}{3}\left(\frac{R}{\delta}-1\right)^3\right]\ldots$$

$$\ldots+\rho\pi C^2\left[-\frac{R^2-\delta^2}{\delta^3}-\frac{1}{\delta}-\frac{R}{\delta^2}\left(-\frac{R^2}{\delta^2}+3\frac{R}{\delta}-3\right)\right]\eta$$

From here, we conclude that the unsteady part of the pressure momentum is given by

$$\begin{aligned} M'_p &= \rho\pi C^2 \left[ -\frac{R^2-\delta^2}{\delta^3} - \frac{1}{\delta} - \frac{R}{\delta^2}\left( -\frac{R^2}{\delta^2} + 3\frac{R}{\delta} - 3 \right) \right] \eta \\ &= \rho\pi C^2 \frac{1}{\delta^4} \left( -R^2\delta + \delta^3 - \delta^3 + R^3 - 3R^2\delta + 3R\delta^2 \right) \eta \\ &= \rho\pi C^2 \frac{1}{\delta^4} \left( R^3 - 4R^2\delta + 3R\delta^2 \right) \eta \end{aligned} \tag{5.16}$$

Adding the unsteady kinetic and pressure parts given by Eqs. (5.12) and (5.16), we obtain the total unsteady momentum

$$M'_\Sigma = M'_u + M'_p = \rho\pi \left( -2\delta\bar{u}_z^2 + 4\bar{u}_z\delta\frac{k\bar{u}_z - \omega}{k} \right) \eta + \rho\pi C^2 \frac{1}{\delta^4} \left( R^3 - 4R^2\delta + 3R\delta^2 \right) \eta$$

Rearranging, we arrive at the final expression for the unsteady momentum fluctuation:

$$M'_\Sigma = \rho\pi \left[ -2\delta\bar{u}_z^2 + 4\bar{u}_z\delta\frac{k\bar{u}_z - \omega}{k} + C^2 \frac{1}{\delta^4} \left( R^3 - 4R^2\delta + 3R\delta^2 \right) \right] \eta \tag{5.17}$$

## 5.4 Abrupt Convergence Resonance Model 2 (ACRM-2): Wave Reflections and Resonance when Vortex Chamber and Nozzle are Connected with an Abrupt Step Discontinuity

In this section, let us build upon the above mentioned idea that we have an abrupt step change at the end of the vortex chamber, and connect the nozzle just downstream of that step, with its own solid boundary and free surface radii, $R_n$ and $r_n$ respectively, Fig. 5.4. Consider an incident downstream traveling wave $D\exp\left[i\left(k_2 z - \omega t\right)\right]$ in the vortex chamber. When it comes to the step discontinuity, a part of it reflects back as an upstream traveling wave $B\exp\left[i\left(k_1 z - \omega t\right)\right]$, and another part of it propagates further into the nozzle as a transmitted downstream traveling wave $A\exp\left[i\left(k_n z - \omega t\right)\right]$. The arrows indicate the respective directions in which all of these waves travel, and $k_1$, $k_2$, and $k_n$ denote the corresponding wave numbers. Here and further on, the upstream traveling waves will be indicated by odd numbers, and the downstream traveling waves – by even numbers. Note that, as we have discussed in Chapter 4, there may not exist an upstream traveling wave in the nozzle. Finally, similarly to

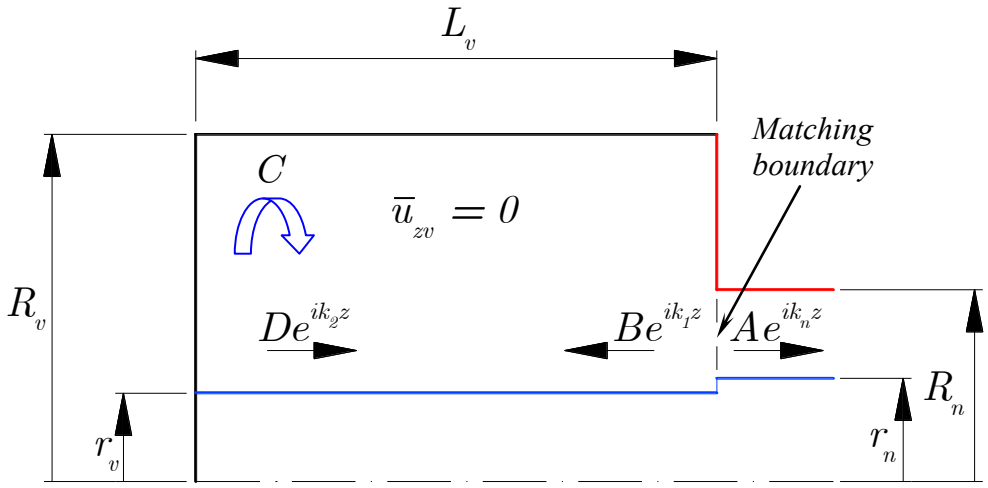


Figure 5.4.: Schematic of wave reflection and transmission for Abrupt Convergence Resonance Model 2 (ACRM-2)

Section 5.2, we will assume again that the bulk flow axial velocity in the vortex chamber is negligibly smaller in comparison with the disturbance wave speed, and may be set to zero, $\bar{u}_{zv} = 0$.

Based on Eq. (5.9), at any point in the vortex chamber, we may write the collective velocity fluctuation of the waves $B$ and $D$, that are superposed on each other, as

$$u'_z = 2r_v \left[ \frac{k_1 \bar{u}_{zv} - \omega}{k_1 \left(R_v^2 - r_v^2\right)} B e^{i(k_1 z - \omega t)} + \frac{k_2 \bar{u}_{zv} - \omega}{k_2 \left(R_v^2 - r_v^2\right)} D e^{i(k_2 z - \omega t)} \right]$$

At the head end solid wall, $z = 0$, we know that the axial velocity fluctuation should be zero at all times. Then, noting that $\bar{u}_{zv} = 0$, we can reduce this equation to

$$u'_z(0,t) = \frac{B}{k_1} + \frac{D}{k_2} = 0$$

Again, since $\bar{u}_{zv} = 0$, then the wave numbers $k_1$ and $k_2$ are symmetrical, $k_1 = -k_2$ (see Appendix B for more discussion on this subject). But, based on the last equation, this means that $D = B$. Conclusively, we can say that we have a purely standing wave in the vortex chamber, which excites an outgoing wave $A$ in the nozzle.

To relate the amplitude of the outgoing wave in the nozzle, $A$, to the amplitude of the standing wave in the vortex chamber, $D$, consider the balance of the mass

flow rate fluctuation at the matching boundary, $z = L_v$ (see Fig. 5.4). Based on the derived Eq. (5.10) for the mass flow rate fluctuation, we may write

$$-2\pi\rho r_v \left[\frac{\omega}{k_1} B e^{i(k_1 L_v - \omega t)} + \frac{\omega}{k_2} D e^{i(k_2 L_v - \omega t)}\right] = -2\pi\rho r_n \frac{\omega}{k_n} A e^{i(k_n L_v - \omega t)}$$

By substituting the equalities $D = B$ and $k_1 = -k_2$, we can reduce this equation to

$$r_v \left[\frac{\omega}{k_2} e^{-ik_2 L_v} - \frac{\omega}{k_2} e^{ik_2 L_v}\right] D = -r_n \frac{\omega}{k_n} A e^{ik_n L_v}$$

which gives the sought expression for $A$ in terms of $D$:

$$A = \frac{\frac{r_v}{k_2}\left(e^{-ik_2 L_v} - e^{ik_2 L_v}\right)}{-\frac{r_n}{k_n} e^{ik_n L_v}} D \tag{5.18}$$

What does this equation mean from the injector resonance point of view? In this equation, $k_2$ and $k_n$ depend on the disturbance frequency through the long wave speed relationship (see Section 4.2 and Appendix B), which we rewrite here for convenience

$$\omega - k\bar{u}_z = \pm k\sqrt{C^2 \frac{R^2 - \delta^2}{2\delta^4}} \tag{5.19}$$

which for the vortex chamber and the nozzle is given by

$$\omega = +k_2 \sqrt{C^2 \frac{R_v^2 - r_v^2}{2r_v^4}}$$

$$\omega - k_n \bar{u}_{zn} = +k_n \sqrt{C^2 \frac{R_n^2 - r_n^2}{2r_n^4}}$$

These equations take into account the respective film thicknesses in the vortex chamber, $R_v - r_v$, and the nozzle, $R_n - r_n$. Hence, if $D$ is fixed in Eq. (5.18), the magnitude of $A$ should vary with regard to $\omega$. Then, there may be frequencies, where $|A|$ is maximized, thereby causing the most pronounced mass flow rate pulsation in the nozzle. Theoretically, these frequencies should coincide with the resonant frequencies, Eq. (5.8), which we have derived in the simplest ACRM-1 above (Section 5.2).

## 5.5 Conical Convergence Resonance Model (CCRM): Wave Reflections and Resonance in Injector with a Conical Convergence Section

Let us add some of the more realistic features to the previous model by considering that there are the following additional components of the injector flow:

1. A distinct head end region, $0 < z < 2R_t$, where the bulk flow velocity is zero, and the free surface radius is equal to $r_v$.

2. A nonzero bulk flow velocity in the vortex chamber, in the region $2R_t < z < L_v$.

3. A distinct conical convergence section connecting the vortex chamber to the nozzle, spanning the region $L_v < z < L_v + L_c$.

What changes will we see after adding these components? Item 1 tells us that, now, we can have a purely standing wave only in the head end region of the flow. Item 2 will result in the fact that, because there is now a finite bulk flow velocity in the vortex chamber, the lengths of the waves propagating in stream wise and counter stream wise directions will differ from each other, which leads to the phenomenon of *partial* standing waves, which is well described in Dean and Dalrymple [105, Sec. 4.6]. Lastly, item 3 invokes the notion of a smooth variation of bulk flow velocity and boundaries in the conical convergence region up to the point where the free surface radius reaches the value of $r_n$ in the nozzle, as we have seen in Chapter 3. The nonuniform flow causes the disturbance waves to both refract and reflect as they travel through the flow transition.

Such compound problem of wave refraction and reflection is difficult to attack at once. However, there is a simplifying way to deal with it by saying that we can discretize the entire transition region into the short cylindrical sections, in which the radii of solid and free surface boundaries do not change, thereby eliminating refraction. This technique is very similar to that used in gravity waves, where the classic example is the paper by O'Hare and Davies [106]. But, in each of these short sections we need to know the *local* disturbance wave characteristics such as the wave

number. Here comes the point where the information that we have learned about the wave refraction in the transition region, Chapter 4, becomes useful. From that chapter we know how to compute the real wave numbers based on the local bulk flow velocity, see Eq. (5.19) above. In turn, the local bulk flow velocity follows simply from the steady state continuity in each of these sections. And we do not have to worry about imaginary wave numbers because refraction is eliminated. Lastly, as the disturbance wave progresses through each of the short cylinders, some part of it is reflected, and some is transmitted into the next cylinder.

We will start the analysis first by considering that there is just one cylindrical section connecting the vortex chamber to the nozzle. This will serve as a good platform to show the main features of the problem. Then, we will generalize the equations used in this simple problem for further using in geometries where more transition sections are considered. The analysis will be concluded with an algorithm that produces solutions for such general geometries.

### 5.5.1 CCRM with One Cylindrical Section in Transition

For now, let us represent the transition region by just one cylindrical section as shown in Fig. 5.5. The flow parameters corresponding to this cylindrical section will be denoted by subscript 2 to indicate that it is located next to the nozzle section. Further, let the radii of this cylindrical section be given as the average between the corresponding solid boundary and free surface radii of the vortex chamber and the nozzle: $R_2 = (R_v + R_n)/2$ and $r_2 = (r_v + r_n)/2$. We have four sections of the flow connected at their respective discontinuity boundaries: the head end region, the uniform vortex chamber region, the cylindrical section, and the nozzle. Note that we consider the nozzle up to the point where we assume the transition ends, which, based on the results of Chapter 3 is located at $z = L_v + L_c + 0.5R_n$, see Fig. 5.5.

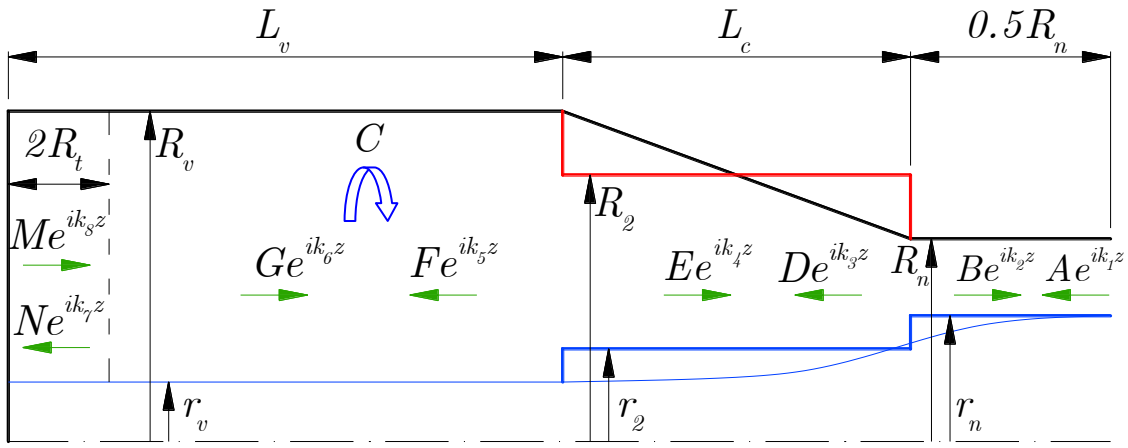


Figure 5.5.: Schematic of wave reflection and transmission for Conical Convergence Resonance Model (CCRM) with one cylindrical section in transition

Similarly to the previous model ACRM-2, if an incident wave $M \exp[i(k_8 z - \omega t)]$ has originated say at the head, it will generate a series of reflected and transmitted waves in all of these four flow sections. Fig. 5.5 shows their respective directions of propagation and wave numbers. In each section, we have two waves traveling in opposite directions. We can calculate their wave numbers, but their amplitudes are unknown.

Note that, if we set the radii of the very first section (sections are counted from right to left) to be exactly equal to $R_n$ and $r_n$, as shown in Fig. 5.5, that will mean that the bulk flow velocity for this section from one-dimensional continuity is exactly equal to $\bar{u}_{zn}$, which formally eliminates the upstream traveling wave in this section, $A \exp[i(k_1 z - \omega t)]$ (see Appendix B for more discussion). In reality, the free surface is still transitioning in this section, and we should have upstream traveling waves. To overcome this problem, we will assume that, in the first section, the bulk flow velocity is a little less than $\bar{u}_{zn}$ and takes the value of $\bar{u}_{zn} \cdot (1 - 10^{-9})$. But, if we do that, as we have seen in Chapter 4, the wave number $k_1$ will become a very large negative number. Without the loss of generality, we can restrict it to be -20, as the magnitude of this number is much larger than any wave number in the frequency range of up

to 2000 Hz. This will be the approach for the first cylindrical section taken here and further on in this study.

Let us say that we know the amplitude of the original incident wave, $M$. Since there is a purely standing wave at the head end, then we also know that $N = M$ and $k_7 = -k_8$ (see ACRM-2 for more discussion). This leaves us with six unknown amplitudes, $A$ through $G$. There are three matching discontinuity boundaries that can relate them together, with locations at: $z = 2R_t$, $z = L_v$, and $z = L_v + L_c$. In contrast with the previous ACRM-2, at each of these boundaries, in addition to the matching of the fluctuating mass flow rate, we will also assure the matching of the fluctuating momentum. This will accordingly provide six equations to solve for the unknown wave amplitudes.

Let us start with the matching of the fluctuating mass flow rate given by Eq. (5.10) at $z = 2R_t$, $z = L_v$, and $z = L_v + L_c$. For simplicity, we will omit the $2\pi\rho$ and $exp(-i\omega t)$ factors since they eventually cancel out. Then we can write the following equations:

$$-r_v\frac{\omega}{k_8}Me^{ik_8 2R_t} - r_v\frac{\omega}{k_7}Ne^{ik_7 2R_t} = -r_v\frac{\omega}{k_6}Ge^{ik_6 2R_t} - r_v\frac{\omega}{k_5}Fe^{ik_5 2R_t} \tag{5.20}$$

$$-r_v\frac{\omega}{k_6}Ge^{ik_6 L_v} - r_v\frac{\omega}{k_5}Fe^{ik_5 L_v} = -r_2\frac{\omega}{k_4}Ee^{ik_4 L_v} - r_2\frac{\omega}{k_3}De^{ik_3 L_v} \tag{5.21}$$

$$-r_2\frac{\omega}{k_4}Ee^{ik_4(L_v+L_c)} - r_2\frac{\omega}{k_3}De^{ik_3(L_v+L_c)} = -r_n\frac{\omega}{k_2}Be^{ik_2(L_v+L_c)} - r_n\frac{\omega}{k_1}Ae^{ik_1(L_v+L_c)} \tag{5.22}$$

After noting that $N = M$ and $k_7 = -k_8$, we can respectively rearrange Eqs. (5.20)–(5.22) as follows:

$$-\frac{\omega}{k_5}Fe^{ik_5 2R_t} - \frac{\omega}{k_6}Ge^{ik_6 2R_t} = \frac{\omega}{k_8}\left(e^{-ik_8 2R_t} - e^{ik_8 2R_t}\right)M \tag{5.23}$$

$$-r_2\frac{\omega}{k_3}De^{ik_3 L_v} - r_2\frac{\omega}{k_4}Ee^{ik_4 L_v} + r_v\frac{\omega}{k_5}Fe^{ik_5 L_v} + r_v\frac{\omega}{k_6}Ge^{ik_6 L_v} = 0 \tag{5.24}$$

$$-r_n\frac{\omega}{k_1}Ae^{ik_1(L_v+L_c)} - r_n\frac{\omega}{k_2}Be^{ik_2(L_v+L_c)} + r_2\frac{\omega}{k_3}De^{ik_3(L_v+L_c)} + r_2\frac{\omega}{k_4}Ee^{ik_4(L_v+L_c)} = 0 \tag{5.25}$$

Before we consider the matching of the fluctuating momentum, let us introduce the following coefficients:

$$K_A = -2r_n\bar{u}_{zn}^2 + 4\bar{u}_{zn}r_n\frac{k_1\bar{u}_{zn}-\omega}{k_1} + C^2\frac{1}{r_n^4}\left(R_n^3 - 4R_n^2r_n + 3R_nr_n^2\right)$$
$$K_B = -2r_n\bar{u}_{zn}^2 + 4\bar{u}_{zn}r_n\frac{k_2\bar{u}_{zn}-\omega}{k_2} + C^2\frac{1}{r_n^4}\left(R_n^3 - 4R_n^2r_n + 3R_nr_n^2\right)$$
$$K_D = -2r_2\bar{u}_{z2}^2 + 4\bar{u}_{z2}r_2\frac{k_3\bar{u}_{z2}-\omega}{k_3} + C^2\frac{1}{r_2^4}\left(R_2^3 - 4R_2^2r_2 + 3R_2r_2^2\right)$$
$$K_E = -2r_2\bar{u}_{z2}^2 + 4\bar{u}_{z2}r_2\frac{k_4\bar{u}_{z2}-\omega}{k_4} + C^2\frac{1}{r_2^4}\left(R_2^3 - 4R_2^2r_2 + 3R_2r_2^2\right)$$
$$K_F = -2r_v\bar{u}_{zv}^2 + 4\bar{u}_{zv}r_v\frac{k_5\bar{u}_{zv}-\omega}{k_5} + C^2\frac{1}{r_v^4}\left(R_v^3 - 4R_v^2r_v + 3R_vr_v^2\right)$$
$$K_G = -2r_v\bar{u}_{zv}^2 + 4\bar{u}_{zv}r_v\frac{k_6\bar{u}_{zv}-\omega}{k_6} + C^2\frac{1}{r_v^4}\left(R_v^3 - 4R_v^2r_v + 3R_vr_v^2\right)$$

Then, based on Eq. (5.17), the matching equations for the fluctuating momentum at $z = 2R_t$, $z = L_v$, and $z = L_v + L_c$ are given by:

$$C^2\frac{1}{r_v^4}\left(R_v^3 - 4R_v^2r_v + 3R_vr_v^2\right)\left(Me^{ik_8 2R_t} + Ne^{ik_7 2R_t}\right) = \ldots$$
$$\ldots = K_GGe^{ik_6 2R_t} + K_FFe^{ik_5 2R_t} \tag{5.26}$$

$$K_GGe^{ik_6L_v} + K_FFe^{ik_5L_v} = K_EEe^{ik_4L_v} + K_DDe^{ik_3L_v} \tag{5.27}$$
$$K_EEe^{ik_4(L_v+L_c)} + K_DDe^{ik_3(L_v+L_c)} = K_BBe^{ik_2(L_v+L_c)} + K_AAe^{ik_1(L_v+L_c)} \tag{5.28}$$

Note that in Eq. (5.26) we have employed the fact that $\bar{u}_z(0 \le z < 2R_t) = 0$. Once again, using the relations $N = M$ and $k_7 = -k_8$, we can rearrange Eqs. (5.26)–(5.28) to get:

$$K_FFe^{ik_5 2R_t} + K_GGe^{ik_6 2R_t} = C^2\frac{1}{r_v^4}\left(R_v^3 - 4R_v^2r_v + 3R_vr_v^2\right)\left(e^{-ik_8 2R_t} + e^{ik_8 2R_t}\right)M \tag{5.29}$$

$$K_DDe^{ik_3L_v} + K_EEe^{ik_4L_v} - K_FFe^{ik_5L_v} - K_GGe^{ik_6L_v} = 0 \tag{5.30}$$
$$K_AAe^{ik_1(L_v+L_c)} + K_BBe^{ik_2(L_v+L_c)} - K_DDe^{ik_3(L_v+L_c)} - K_EEe^{ik_4(L_v+L_c)} = 0 \tag{5.31}$$

$$
\begin{pmatrix}
-r_n\frac{\omega}{k_1}e^{ik_1(L_v+L_c)} & -r_n\frac{\omega}{k_2}e^{ik_2(L_v+L_c)} & r_2\frac{\omega}{k_3}e^{ik_3(L_v+L_c)} & r_2\frac{\omega}{k_4}e^{ik_4(L_v+L_c)} & 0 & 0 \\
0 & 0 & -r_2\frac{\omega}{k_3}e^{ik_3L_v} & -r_2\frac{\omega}{k_4}e^{ik_4L_v} & r_v\frac{\omega}{k_5}e^{ik_5L_v} & r_v\frac{\omega}{k_6}e^{ik_6L_v} \\
0 & 0 & 0 & 0 & -\frac{\omega}{k_5}e^{ik_52R_t} & -\frac{\omega}{k_6}e^{ik_62R_t} \\
K_Ae^{ik_1(L_v+L_c)} & K_Be^{ik_2(L_v+L_c)} & -K_De^{ik_3(L_v+L_c)} & -K_Ee^{ik_4(L_v+L_c)} & 0 & 0 \\
0 & 0 & K_De^{ik_3L_v} & K_Ee^{ik_4L_v} & -K_Fe^{ik_5L_v} & -K_Ge^{ik_6L_v} \\
0 & 0 & 0 & 0 & K_Fe^{ik_52R_t} & K_Ge^{ik_62R_t}
\end{pmatrix}
\begin{pmatrix} A \\ B \\ D \\ E \\ F \\ G \end{pmatrix} =
$$

$$
\begin{pmatrix}
0 \\
0 \\
\frac{\omega}{k_8}\left(e^{-ik_82R_t} - e^{ik_82R_t}\right) \\
0 \\
0 \\
C^2\frac{1}{r_v^4}\left(R_v^3 - 4R_v^2r_v + 3R_vr_v^2\right)\left(e^{-ik_82R_t} + e^{ik_82R_t}\right)
\end{pmatrix} M
$$

Figure 5.6.: Representation of Eqs. (5.23)–(5.25) and (5.29)–(5.31) in matrix form for CCRM with one cylindrical section

Conclusively, we can rewrite Eqs. (5.23)–(5.25) and (5.29)–(5.31) in a matrix form as shown in Fig. 5.6. Solution of this matrix equation then gives the dependence of the wave amplitudes $A$ through $G$ on the wave amplitude of the original incident wave, $M$.

What information can we extract from this solution with regard to the injector resonance? As before, all wave numbers in the matrix equation, Fig. 5.6, depend on the disturbance frequency, $\omega$. Therefore, all amplitudes $A$ through $G$ in the solution depend on $\omega$ as well. At injector resonance, because the film thickness fluctuation in the injector nozzle should be maximum, we should see the greatest magnitude of the disturbance wave transmitted into the nozzle, which is represented by the amplitude $B$, and vice versa, we should see the smallest magnitude of the disturbance wave traveling back into the vortex chamber, which is represented by the amplitude $A$. Accordingly, the frequency at which $|B|$ is maximum, indicates a resonant frequency.

### 5.5.2 Generalization of CCRM to Multiple Cylindrical Sections in Transition

We are interested in having more than one cylindrical sections in the transition region. This will generate a bigger matrix than that shown in Fig. 5.6 for finding all wave amplitudes involved in the solution. Let the solution in this case be represented by a matrix equation $X \cdot a = Y$, where $X$ and $Y$ are the generic matrices similar to the left hand side (LHS) and the right hand side (RHS) matrices in Fig. 5.6, and $a$ are the generic wave amplitudes. To illustrate how to construct the matrices $X$ and $Y$, let us consider again the flow setup that has just one cylindrical section in conical transition as a reference, Fig. 5.7. This will serve as a starting platform, from where the solution may be extended further on to more transition sections.

Let us represent each flow section by an index $q$, and their total number by $N$. Let the head end section be denoted by the index $q = N + 1$. In this particular case, $N = 3$ and $q = 1 \ldots 4$. Let the first index under the wave number correspond to the

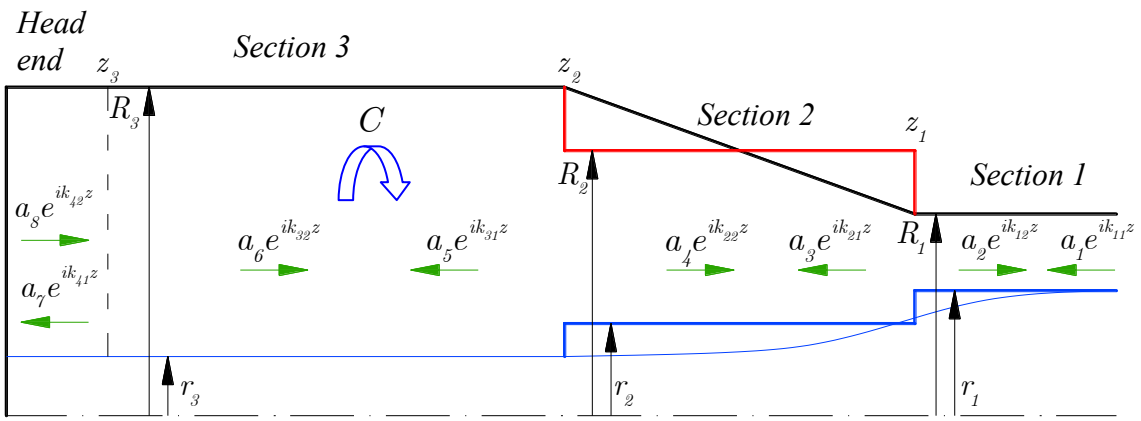


Figure 5.7.: Schematic of wave reflection and transmission for generic Conical Convergence Resonance Model (CCRM) with one cylindrical section in transition

flow section number, and the second index – to the direction of wave propagation: 1 – for upstream traveling waves, and 2 – for downstream traveling waves. Moreover, let us define the radial boundaries of each section by $r_q$ and $R_q$, and the discontinuity boundaries, at which the flow sections connect to each other, by $z_q$. Finally, note that the wave amplitudes $a$ are counted simply in a sequence 1, 2, 3, ....

By comparing Fig. 5.7 to Fig. 5.5 it is easy to determine $r_q$, $R_q$, and $z_q$, they are summarized in Table 5.1. Based on $r_q$, $R_q$, we can determine the bulk flow velocity, $\bar{u}_{zq}$, the wave numbers, $k_q$, and coefficients $K_q$ (that are needed for the momentum

Table 5.1: Values of $r_q$, $R_q$, and $z_q$ in generic CCRM with one cylindrical section

| | | |
|---|---|---|
| $r_1 = r_n$ | $R_1 = R_n$ | $z_1 = L_v + L_c$ |
| $r_2 = (r_v + r_n)/2$ | $R_2 = (R_v + R_n)/2$ | $z_2 = L_v$ |
| $r_3 = r_v$ | $R_3 = R_v$ | $z_3 = 2R_t$ |
| $r_4 = r_v$ | $R_4 = R_v$ | $z_4 = 0$ |

balance, see page 122) for each section of the flow. The bulk flow velocity follows from the one-dimensional continuity as

$$\bar{u}_{zq} = \bar{u}_{zv}\frac{R_v^2 - r_v^2}{R_q^2 - r_q^2} \tag{5.32}$$

The wave numbers for both upstream and downstream traveling waves can be found based on Eq. (5.19) as

$$k_{q,1} = \omega\frac{\bar{u}_{zq} + \sqrt{C^2\frac{R_q^2 - r_q^2}{2r_q^4}}}{\bar{u}_{zq}^2 - C^2\frac{R_q^2 - r_q^2}{2r_q^4}} \tag{5.33}$$

$$k_{q,2} = \omega\frac{\bar{u}_{zq} - \sqrt{C^2\frac{R_q^2 - r_q^2}{2r_q^4}}}{\bar{u}_{zq}^2 - C^2\frac{R_q^2 - r_q^2}{2r_q^4}} \tag{5.34}$$

And, by using Eqs. (5.32)–(5.34), we can determine the coefficients $K$ as

$$K_{q,1} = -2r_q\bar{u}_{zq}^2 + 4\bar{u}_{zq}r_q\frac{k_{q,1}\bar{u}_{zq} - \omega}{k_{q,1}} + C^2\frac{1}{r_q^4}\left(R_q^3 - 4R_q^2r_q + 3R_qr_q^2\right) \tag{5.35}$$

$$K_{q,2} = -2r_q\bar{u}_{zq}^2 + 4\bar{u}_{zq}r_q\frac{k_{q,2}\bar{u}_{zq} - \omega}{k_{q,2}} + C^2\frac{1}{r_q^4}\left(R_q^3 - 4R_q^2r_q + 3R_qr_q^2\right) \tag{5.36}$$

Now we can rewrite the matrix equation shown in Fig. 5.6 in terms $r_q$, $z_q$, $k_q$, and $K_q$ as given in Fig. 5.8. Similarly to the previous matrix solution, the resonance will follow from this solution at frequencies where $|a_2|$ is at its maximum.

$$\begin{pmatrix}
-r_1\frac{\omega}{k_{1,1}}e^{ik_{1,1}z_1} & -r_1\frac{\omega}{k_{1,2}}e^{ik_{1,2}z_1} & r_2\frac{\omega}{k_{2,1}}e^{ik_{2,1}z_1} & r_2\frac{\omega}{k_{2,2}}e^{ik_{2,2}z_1} & 0 & 0 \\
0 & 0 & -r_2\frac{\omega}{k_{2,1}}e^{ik_{2,1}z_2} & -r_2\frac{\omega}{k_{2,2}}e^{ik_{2,2}z_2} & r_3\frac{\omega}{k_{3,1}}e^{ik_{3,1}z_2} & r_3\frac{\omega}{k_{3,2}}e^{ik_{3,2}z_2} \\
0 & 0 & 0 & 0 & -\frac{\omega}{k_{3,1}}e^{ik_{3,1}z_3} & -\frac{\omega}{k_{3,2}}e^{ik_{3,2}z_3} \\
K_{1,1}e^{ik_{1,1}z_1} & K_{1,2}e^{ik_{1,2}z_1} & -K_{2,1}e^{ik_{2,1}z_1} & -K_{2,2}e^{ik_{2,2}z_1} & 0 & 0 \\
0 & 0 & K_{2,1}e^{ik_{2,1}z_2} & K_{2,2}e^{ik_{2,2}z_2} & -K_{3,1}e^{ik_{3,1}z_2} & -K_{3,2}e^{ik_{3,2}z_2} \\
0 & 0 & 0 & 0 & K_{3,1}e^{ik_{3,1}z_3} & K_{3,2}e^{ik_{3,2}z_3}
\end{pmatrix}
\begin{pmatrix} a_1 \\ a_2 \\ a_3 \\ a_4 \\ a_5 \\ a_6 \end{pmatrix} =$$

$$\begin{pmatrix}
0 \\
0 \\
\frac{\omega}{k_{4,2}}\left(e^{-ik_{4,2}z_3} - e^{ik_{4,2}z_3}\right) \\
0 \\
0 \\
C^2\frac{1}{r_4^4}\left(R_4^3 - 4R_4^2r_4 + 3R_4r_4^2\right)\left(e^{-ik_{4,2}z_3} + e^{ik_{4,2}z_3}\right)
\end{pmatrix} a_8$$

Figure 5.8.: Matrix form of solution for generic CCRM with one cylindrical section

### 5.5.3 Generic Solution Algorithm for CCRM with Multiple Cylindrical Sections in Transition

Let us now create an algorithm that will produce the matrix form of solution $X \cdot a = Y$ like that in Fig. 5.8. This algorithm then can be employed to generate a solution for any number of cylindrical sections in the conical transition.

By looking at the LHS matrix in Fig. 5.8, we can notice that it consists of two halves: the upper half corresponding to the mass flow rate balance, and the lower half corresponding to the momentum balance. We can respectively number these halves by an index $p = 1, 2$. We can also notice that the rows $1 \ldots N-1$ and $N+1 \ldots 2N-1$ of the LHS matrix consist of four elements, whereas the rows $N$ and $2N$ consist of only two elements. Let us name the elements of the LHS matrix as $b$. Then, a generic algorithm for determining each one of these elements may be written as follows:

do $p = 1, 2$

if $p = 1$ then *(upper half of LHS matrix)*

do $q = 1 \ldots N$

if $q \leq N - 1$ then

$$b_{q,1} = -r_q \frac{\omega}{k_{q,1}} e^{ik_{q,1}z_q}$$

$$b_{q,2} = -r_q \frac{\omega}{k_{q,2}} e^{ik_{q,2}z_q}$$

$$b_{q,3} = +r_{q+1} \frac{\omega}{k_{q+1,1}} e^{ik_{q+1,1}z_q}$$

$$b_{q,4} = +r_{q+1} \frac{\omega}{k_{q+1,2}} e^{ik_{q+1,2}z_q}$$

else if $q = N$ then

$$b_{q,1} = -\frac{\omega}{k_{q,1}} e^{ik_{q,1}z_q}$$

$$b_{q,2} = -\frac{\omega}{k_{q,2}} e^{ik_{q,2}z_q}$$

$$b_{q,3} = 0$$

$$b_{q,4} = 0$$

end if

end do

else if $p = 2$ then *(lower half of LHS matrix)*

do $q = 1 \ldots N$

if $q \leq N - 1$ then

$b_{N+q,1} = +K_{q,1} e^{ik_{q,1} z_q}$

$b_{N+q,2} = +K_{q,2} e^{ik_{q,2} z_q}$

$b_{N+q,3} = -K_{q+1,1} e^{ik_{q+1,1} z_q}$

$b_{N+q,4} = -K_{q+1,2} e^{ik_{q+1,2} z_q}$

else if $q = N$ then

$b_{N+q,1} = +K_{q,1} e^{ik_{q,1} z_q}$

$b_{N+q,2} = +K_{q,2} e^{ik_{q,2} z_q}$

$b_{N+q,3} = 0$

$b_{N+q,4} = 0$

end if

end do

end if

end do

Let us introduce the dummy integers $s$ and $t$, and initialize the LHS matrix, $X = 0$. Then, we can construct the LHS matrix out of the elements $b$ that we have just produced with the following generic algorithm:

do $p = 1, 2$

if $p = 1$ then *(upper half of LHS matrix)*

do $q = 1 \ldots N$

if $q < N$ then $t = 4$

elseif $q = N$ then $t = 2$

end if

do $s = 1 \ldots t$

$X_{q,2(q-1)+s} = b_{q,s}$

end do

end do

elseif $p = 2$ then *(lower half of LHS matrix)*

do $q = 1 \ldots N$

if $q < N$ then $t = 4$

elseif $q = N$ then $t = 2$

end if

do $s = 1 \ldots t$

$X_{N+q,2(q-1)+s} = b_{N+q,s}$

end do

end do

end if

end do

Finally, the RHS matrix is easy to construct, if it is first initialized as $Y(1:2N,1) = 0$, and thereafter, the following elements are added:

$$Y_{N,1} = \frac{\omega}{k_{N+1,2}} \left( e^{-ik_{N+1,2}2R_t} - e^{+ik_{N+1,2}2R_t} \right)$$

$$Y_{2N,1} = C^2 \frac{1}{r_v^4} \left( R_v^3 - 4R_v^2 r_v + 3R_v r_v^2 \right) \left( e^{-ik_{N+1,2}2R_t} + e^{ik_{N+1,2}2R_t} \right)$$

This completes the procedure for finding the solution for the wave reflection and resonance in the injector with a distinct conical section between the vortex chamber and the nozzle. In the next section, we will show the implementation of the solution algorithm just shown to the situation when we have eight and more cylindrical sections in the transition region of the injector.

## 5.6 Results

In this section, the results will be presented for each of the above derived models of the wave reflection and resonance. We will start with ACRM-1, as it is the basic reference point with which the ACRM-2 and CCRM should be comparable in terms of the resonant frequencies. All results presented here are valid for the baseline injector described in Tables 2.2 and 2.3.

### 5.6.1 ACRM-1 Results

From Eq. (5.8) we can immediately determine the resonant frequencies. For the baseline injector, we have summarized them in Table 5.2 for the first five modes. Notice that due to this calculation the first resonant frequency is 226.2 Hz.

Table 5.2: Resonant frequencies due to ACRM-1 (first 5 modes, baseline injector, Tables 2.2, 2.3)

| Mode, n | $\omega_0$ | $\omega_0^*$ (rad/sec) | $f_0^*$ (Hz) |
|---|---|---|---|
| 1 | 2.4 | 1421.4 | 226.2 |
| 3 | 7.2 | 4264.3 | 678.7 |
| 5 | 12.0 | 7107.2 | 1131.1 |
| 7 | 16.8 | 9950.1 | 1583.6 |
| 9 | 21.6 | 12793.0 | 2036.1 |

### 5.6.2 ACRM-2 Results

In ACRM-2, we can set the amplitude of the incident wave at the head end to unity, $D = 1$. Then, based on Eq. (5.18), we can plot the amplitude (absolute value) of the outgoing wave, $|A|$ versus the disturbance frequency, Fig. 5.9. Notice that the

peaks of $|A|$ are located exactly at the same frequencies as was predicted in ACRM-1 (see Table 5.2). As was assumed in ACRM-2, these peaks indicate the frequencies, at which the mass flow rate pulsation in the nozzle becomes maximum, and hence are the resonant peaks.

Also, this calculation shows that the value of $|A|$ varies from zero to 9.45. The fact that $|A|$ shrinks to zero at some frequencies tells us that, at these frequencies, we can potentially expect damping of flow pulsations in the injector. And the fact that $|A|$ may reach to values as large as 9.45 compared to the value of $D = 1$ signifies that the amplitudes of the outgoing waves may be much larger than the amplitudes of the original incident waves in the vortex chamber. This situation is natural, because we know that the wave length in the nozzle is shorter than in the vortex chamber, and thus the wave amplitude has to be larger to conserve energy.

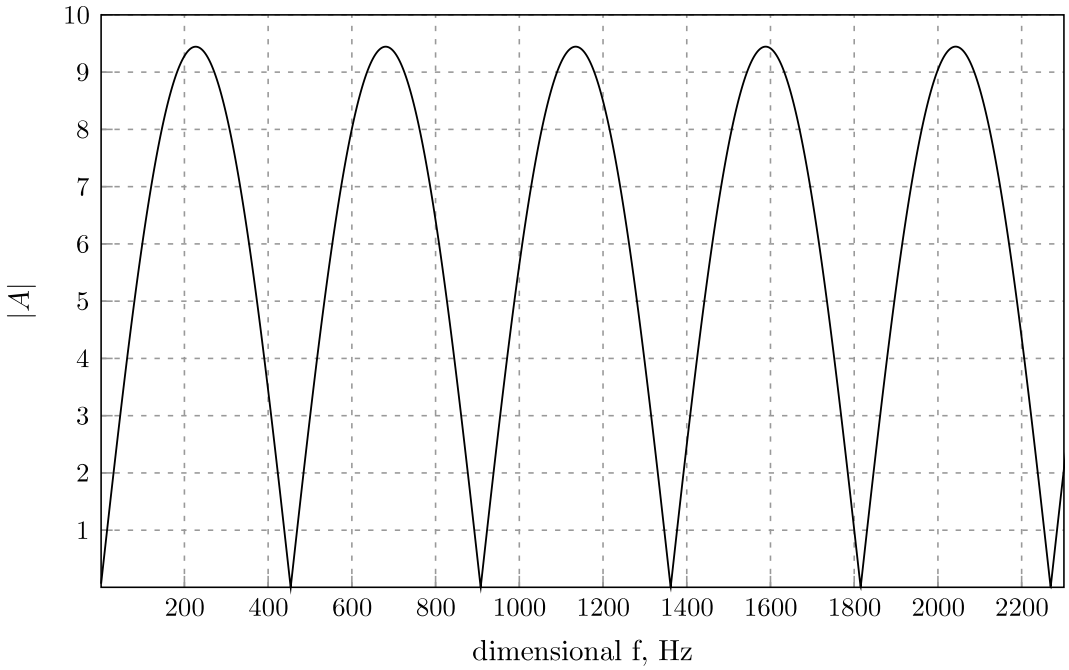


Figure 5.9.: Amplitude of the outgoing wave vs. disturbance frequency in ACRM-2 (baseline injector, Tables 2.2, 2.3)

### 5.6.3 CCRM Results

In this subsection, we will present the results in the range of frequencies from zero to 600 Hz, as this is the range where we can validate the resonant frequencies against those predicted by BEM simulations (Chapter 7). As was explained in Subsection 5.5.1, in the first cylindrical section, we assume that the value of bulk flow velocity is equal to $\bar{u}_{zn} \cdot (1 - 10^{-9})$ and $k_{11} = -20$, at all disturbance frequencies considered.

From the way the CCRM is derived, we can raise a question of how many short cylindrical sections there should be in the transition region. Or, in other words, what does "short" mean in relation to the axial dimension of the transition? We can deal with this problem as follows. We will investigate several different setups, with a different number of cylindrical sections in the transition in each case, in terms of the resonant peaks that each of them produces. Note that increasing the number of cylindrical sections leads to larger solution matrices, which increases the computational time. If there is a large variation in the answer from case to case, we should be looking for a converged solution. If the answer does not change much, then we can choose the setup, that is the fastest.

Let us first consider eight cylindrical sections in the transition, Fig. 5.10. This corresponds to the length of each of these sections equal to $0.5R_n$. The amplitude of the original incident wave at the head end, is set to 1 as before. For this setup, the amplitude of the outgoing wave, $a_2$ (see Fig. 5.7) versus the disturbance frequency is shown in Fig. 5.11. Notice that the resonant peaks, now located at 118 Hz and 470 Hz, are different from the first two resonant peaks, 226 Hz and 679 Hz, predicted by ACRM-1 and ACRM-2 (see Table 5.2 and Fig. 5.9). This immediately indicates that the resonant characteristics of an injector with a distinct conical convergence section do differ from those of an injector with a 90° step transition. Also, by looking at the magnitude of $|a_2|$ at different frequencies (that reaches the value of 1263 at the second peak) in relation to the magnitude of the original incident wave, which is 1,

one may wonder why the former is so much larger. The answer follows from Chapter 4, where we have seen that the amplitude of the upstream traveling waves rises to infinity as we move closer to the point where the transition ends and the uniform nozzle region starts. This fact causes the large difference between the amplitudes of the original incident waves and the outgoing waves. Since, after all, this analysis is a first order small disturbance analysis, the wave amplitudes are not as much important as the frequencies where they peak out.

Now, let us move on to the larger number of cylindrical sections by decreasing their width down to 5% of the previous width $0.5R_n$. The width is denoted as $w$ in this investigation. Fig. 5.12 shows the new locations of the resonant peaks and Table 5.3 summarizes the respective resonant frequencies along with the sizes of the solution matrices in each of the cases considered. The former case with $w = 0.5R_n$ is shown in black for distinction.

In Table 5.3 we can see that the resonant peaks are moving within 3% of the baseline values as we vary $w$. The solution matrices however, grow roughly two times bigger each time we decrease the width to the half of the previous. This means that we can choose the baseline case, with $w = 0.5R_n$, for further calculations, because it requires the least computational time.

Table 5.3: Sensitivity of resonant peaks in CCRM to cylindrical section width

| Width, w | 1st peak, Hz | 2nd peak, Hz | Solution matrix size |
|---|---|---|---|
| $0.500R_n$ | 118 | 470 | 10x10 |
| $0.250R_n$ | 119 | 463 | 19x19 |
| $0.100R_n$ | 121 | 484 | 46x46 |
| $0.050R_n$ | 110 | 462 | 91x91 |
| $0.025R_n$ | 120 | 455 | 181x181 |

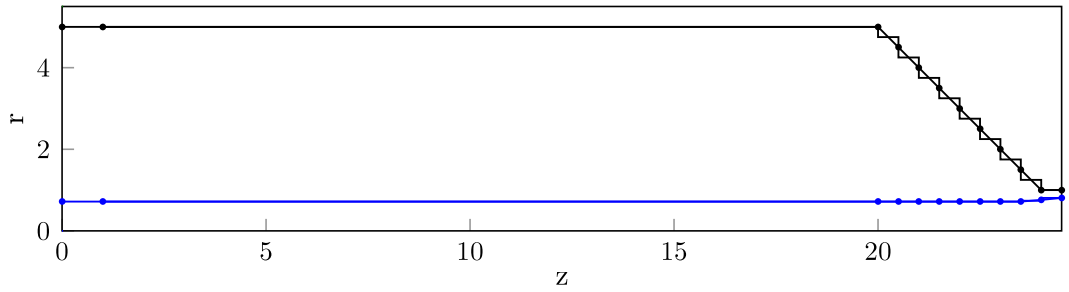


(a) Normal view

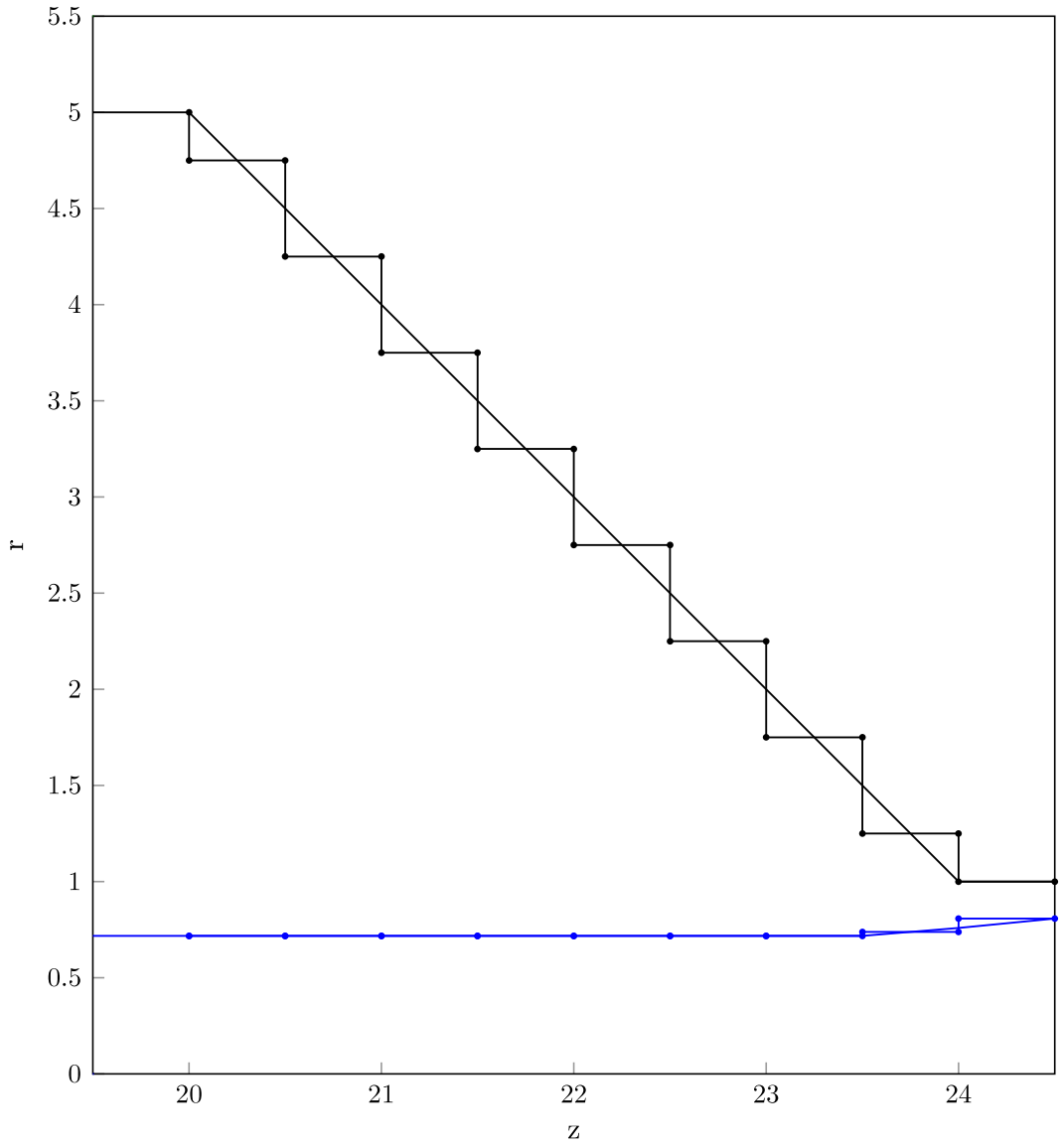


(b) Zoomed in view

Figure 5.10.: Example of eight cylindrical sections in transition considered for wave reflections in CCRM (baseline injector, Tables 2.2, 2.3)

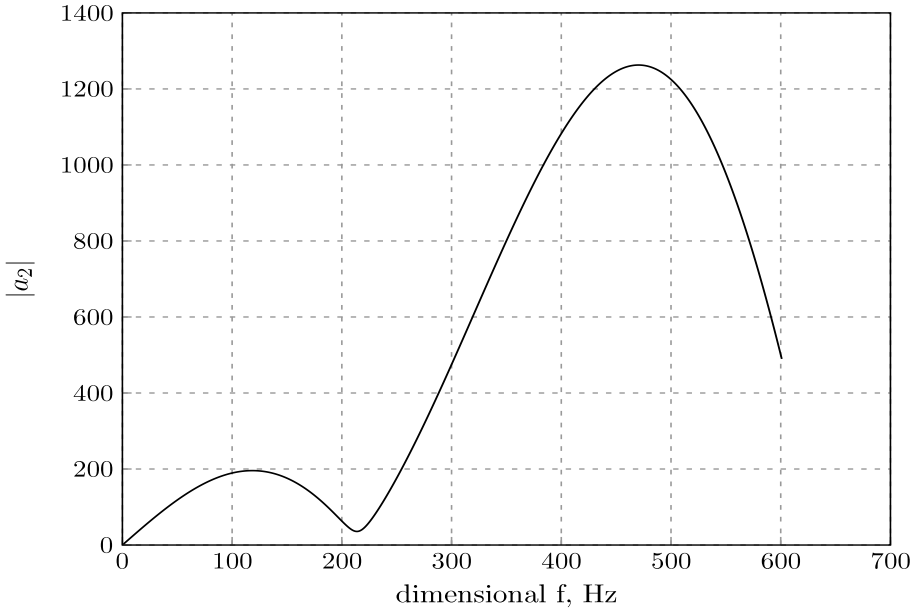


Figure 5.11.: Outgoing wave amplitude vs. disturbance frequency for CCRM with eight cylindrical sections in transition (peaks at 118 and 470 Hz)

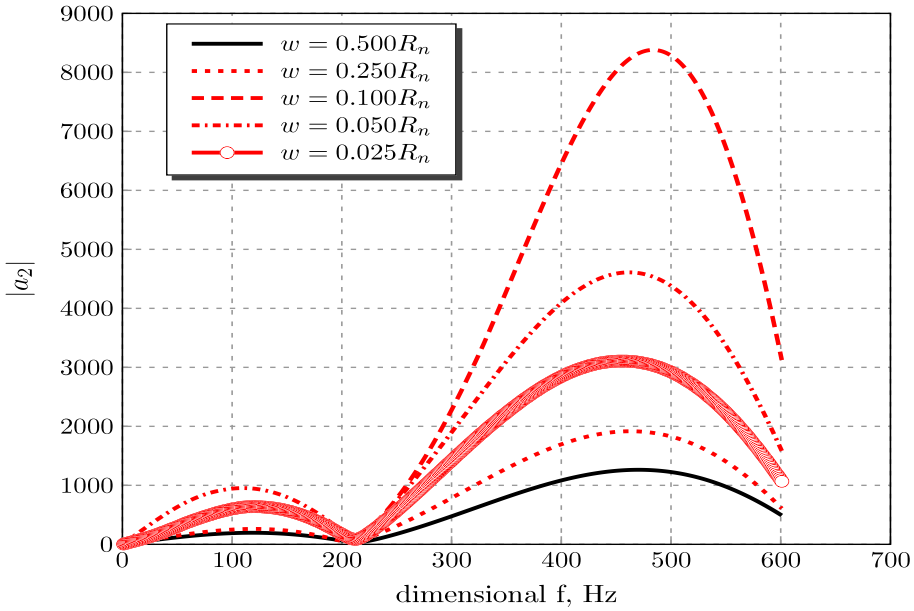


Figure 5.12.: Sensitivity of outgoing wave amplitude to cylindrical section width in CCRM (resonant peaks are summarized in Table 5.3)

## 5.7 Conclusions and Discussion

In this chapter we have presented possible methods for accounting for the disturbance wave reflections and the resonance caused by them in the rocket swirl injector. We have considered three models differing in their levels of complexity depending on such factors as: whether or not we consider the presence of the nozzle, and, if we do, then how exactly do we treat the connection of the nozzle to the vortex chamber, either through a sudden step discontinuity, or through the conical convergence section.

In ACRM-1, we have drawn an analogy to the standing waves in the harbor having a narrow channel entrance connecting it with the sea, and concluded that we should have a node at the head end, and an antinode at the end of the vortex chamber to have resonance in the swirl injector. Based on this fact, and the knowledge of the wave characteristics in the vortex chamber, we have derived the general expression for the resonant modes of the swirl injector.

In ACRM-2, we have connected the nozzle to the vortex chamber through a sudden step discontinuity and assumed that the flows at both sides of that discontinuity are simply cylindrical. By setting the amplitude of an incident wave in the vortex chamber, which originates flow pulsations in the injector, we have calculated the amplitudes of the reflected and transmitted waves that it generates as it passes through the step discontinuity, based on balancing the mass flow rates at both sides of the discontinuity. The frequencies, at which the transmitted wave amplitude is maximized, thereby creating the maximum mass flow pulsation in the nozzle, have been postulated to be the resonant frequencies.

In CCRM, we have accounted for the conical convergence section between the vortex chamber and the nozzle. We have approximated the solid boundary and the free surface in that region by a series of short cylindrical sections. This way, we were able to disregard the refraction, and compute the wave characteristics based on the local bulk flow velocities and boundaries in each of these sections, which followed

from the results of Chapter 4. To find the amplitudes of the reflected and transmitted waves, as the incident wave progresses through the transition, we have balanced both the mass flow rate and the momentum.

The results following from the first two models have shown that ACRM-2 produces the same resonant frequencies as ACRM-1, which tells us that the assumptions employed in both of these models were correct. Because both of them take into account only a sudden step discontinuity, we can potentially expect that both of them can be used for the resonance analysis of the injectors having 90° sudden convergence. Also, ACRM-2 clearly shows that the amplitude of the transmitted wave does depend on the frequency, which consequently proves that the nozzle reflection in Bazarov's theory (see Section 2.4) should depend on the frequency as well.

From the results of CCRM, we have seen that the amplitude of the outgoing wave can be much larger than the amplitude of the incident wave. This is attributed to the fact that the amplitude of the upstream traveling wave, at the point where the nozzle entrance transition region ends and the uniform nozzle region begins (see Fig. 2.1), grows to infinity, as follows from Chapter 4. Also, we have seen that the resonant frequencies following from the CCRM are different from those in ACRM-1 and ACRM-2. This clearly shows that, when the injector has a distinct conical convergence between the vortex chamber and the nozzle, its wave reflection and resonance characteristics are different from the injector having the 90° sudden step convergence. In turn, this illustrates why the idealized injector in Bazarov's dynamic theory (see Section 2.4) cannot accurately represent the flow dynamics in a general swirl injector.

The question is now: can we trust these models to predict the injector resonance? Our approach to answer this question will be through setting up a computational BEM model (Chapter 7) that closely replicates the boundary conditions used in the models here, and going through the parametric study, in which we can investigate the influences of such parameters as $L_v$, $L_n$, $R_v$, etc. on the injector response. The comparison of the frequencies where the response is maximized with the resonant frequencies predicted by the analytic models in this chapter will provide an indication

of how adequate they are. Following this logic, in Chapter 7, we will be presenting both theoretical and computational results in parallel. Ultimately, we shall compare the theoretical and computational results to the experimental. This will be done in Chapter 7 as well.

To conclude, it has to be noted that, in such reflection–refraction problems, where the transition is approximated by the cylindrical sections, in addition to the regular linear reflected and transmitted waves, we would expect another type of waves to form, which would damp out as they propagate far away from their respective step discontinuities, or as Dingemans [87, p. 102] states:

> *"In the case of abrupt bottom transitions like those with a step in the depth, so-called* evanescent *modes are of importance locally."*

But usually, the required analysis applies a variational approach, a classic gravity wave demonstration of which is provided in Miles [67]. In this study, we have ignored these waves, as the application of variational analysis to the swirling flow is difficult. But their inclusion could potentially make the reflection/resonance analysis presented here to be more precise.

# 6. LINEAR ASSESSMENT OF KELVIN'S WAVES AND GAS-LIQUID INTERACTION ON INJECTOR RESPONSE

## 6.1 Introduction

Recall from Chapter 2 that Bazarov's [1, Chap. 4] linear injector response was based on a long wave limit, when considering the disturbance waves traveling on the gaseous core. Also recall that Bazarov did account for wave reflections in the vortex chamber when considering the injector response due to the surface waves.

In this chapter, we are wondering how the injector response will behave, if we relax the long wave assumption. Now, in Chapter 5, we have investigated only the long wave reflections in the vortex chamber and in the transition region of the swirl injector. We do not have the information how to analyze the wave reflections in terms of the Kelvin's waves, which cover the entire wave length spectrum. Therefore, in this chapter, which serves rather as a preliminary assessment of Kelvin's waves on the injector response, we will make an assumption that there are no wave reflections at all, as the disturbance wave propagates along the injector core. Also, we will consider the hypothetical situation when the disturbance originates at the tangential inlet and travels thereafter downstream to the nozzle exit. Accordingly, we will derive the expressions for the pressure drops and mass flow rates of the parts of the injector that lie in the path of the propagation of that disturbance and are involved in the injector response calculation. After deriving these expressions valid for Kelvin's waves, we will take them to the long wave limit to see the corresponding difference that is produced in the injector response. In the end of this chapter, we will compare both Kelvin's wave and long wave results for the injector response against the injector response shown in Bazarov [1, Fig. 23] and in Fig. 2.7 of this dissertation. These goals can be viewed as a first task of this chapter.

From Chapter 2, we can also see that Bazarov's dynamic analysis does not account for the effects following from the interaction of the liquid body with the gaseous core, such as: the effect of density difference between them, or the effect of the gas-liquid surface tension. However, it is possible to address these effects in terms of the first order small perturbation analysis, as is demonstrated in Ponstein [107]. And this will be the second task pursued in this chapter, as we are interested in knowing how the inertial and capillary effects influence the injector response.

## 6.2 Assessment of Kelvin's Waves on Injector Response

Let us rewrite the definition of the injector response from Chapter 1 here for convenience

$$\Pi_{inj} = \frac{\dfrac{\dot{m}'_n}{\bar{\dot{m}}_n}}{\dfrac{\Delta p'_{inj}}{\Delta \bar{p}_{inj}}} \tag{6.1}$$

$$\Delta p'_{inj} = \Delta p'_t + \Delta p'_{he} \tag{6.2}$$

$$\Delta \bar{p}_{inj} = \Delta \bar{p}_t + \Delta \bar{p}_{he} \tag{6.3}$$

where $\dot{m}_n$ is the mass flow rate at the nozzle exit of injector, $\Delta p_{inj}$ is the total injector pressure drop, prime means fluctuation, and overbar means steady state value. In turn, the total injector pressure drop, $\Delta p_{inj}$, consists of the pressure drop across the tangential inlets, $\Delta p_t$, and the pressure drop across the liquid body at the head end of the vortex chamber, $\Delta p_{he}$ (see Chapter 2). Equations (6.2) and (6.3) show the respective decomposition of the pressure drop into its steady and unsteady parts.

In this section, we will sequentially find the expressions for the instantaneous $\Delta p_t$, $\Delta p_{he}$, and $\dot{m}_n$, in terms of the traveling disturbance wave amplitude, $\eta$. Having these expressions in place, we will be able to compute the injector response, Eq. (6.1), itself.

### 6.2.1 Pressure Drop Across Tangential Inlets

In this study, we will model the tangential inlet as a constant area cylinder of length $L_t$, Fig. 6.1. We assume that the flow inside the cylinder is axisymmetric and does not move in the radial direction. The axial velocity is denoted here as $u_z$, as was the case for the fluid flow inside of the swirl injector after it has been injected into the vortex chamber. According to these assumptions, due to the mass flow rate conservation, we have a uniform flow in the axial direction, $\partial u_z/\partial z = 0$.

From the momentum equation

$$\frac{\partial u_z}{\partial t} + u_z \frac{\partial u_z}{\partial z} = -\frac{1}{\rho}\frac{dp}{dz}$$

it follows that

$$L_t \frac{du_z}{dt} = -\frac{1}{\rho}\int_0^{L_t} dp = \frac{p\,(0) - p\,(L_t)}{\rho} = \frac{\Delta p_t}{\rho} \tag{6.4}$$

considering that the origin is located at the left end of the inlet as seen in Fig. 6.1. When the flow is steady, on the RHS of this equation, we have $\Delta\bar{p}_t/\rho$, and, on the LHS, we have $L_t d\bar{u}_z/dt = 0$, which means that the steady part of the pressure drop across the tangential inlets is zero at all times in this model,

$$\Delta\bar{p}_t = 0 \tag{6.5}$$

The instantaneous pressure drop is then simply equal to the unsteady part of it, $\Delta p_t = \Delta p'_t$.

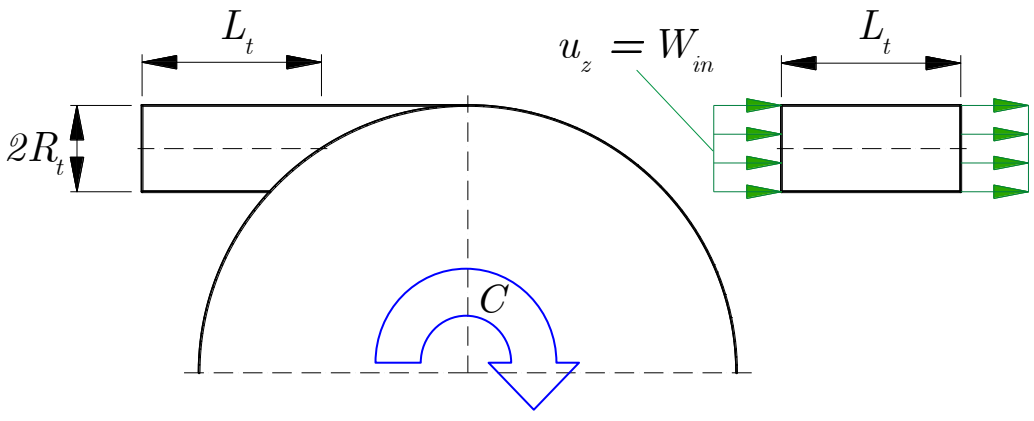


Figure 6.1.: Schematic of tangential inlet

The velocity is linked to the unsteady inflow mass flow rate as

$$\frac{d\dot{m}_{in}}{dt} = \frac{d\dot{m}'_{in}}{dt} = \rho \frac{du_z}{dt} A \tag{6.6}$$

where $A$ is the total inflow cross-sectional area, given by $A = N_{in}\pi R_t^2$, where, in turn, $N_{in}$ is the number of tangential inlets and $R_t$ is the tangential inlet radius. By combining Eqs. (6.4)–(6.6), we arrive at the expression for the the fluctuation of the unsteady pressure drop through the tangential inlets in terms of the fluctuation of the unsteady inflow mass flow rate:

$$\Delta p'_t = \frac{L_t}{N_{in}\pi R_t^2} \frac{d\dot{m}'_{in}}{dt} \tag{6.7}$$

From this equation, to obtain an explicit dependence of $\Delta p'_t$ on $\eta$, we need to have an expression relating the inflow mass flow rate fluctuation, $\dot{m}'_{in}$, to $\eta$, which we seek next.

### 6.2.2 Mass Balance at Head End

Recall from Chapters 2 and 3 that the head end transition region is assumed to be located within the boundaries $0 < z < 2R_t$. Consider a control volume with the boundaries depicted by the dashed lines in Fig. 6.2. Notice that it includes the tangential inlets on the left side of Fig. 6.2. The only surfaces of this control volume that let the flow in and out are the left boundary surface of the tangential inlet and the right boundary surface of the head end region, they are shown by the green arrows. The other surfaces are non-permeable. The unsteady mass balance [45] for this control volume is given by

$$\frac{\partial}{\partial t} \int_{CV} \rho dV + \int_{CS} \rho \vec{u} \cdot d\vec{S} = 0 \tag{6.8}$$

where CV and CS denote integration over the entire control volume and control surface, and $d\vec{S}$ is the elementary part of the control surface.

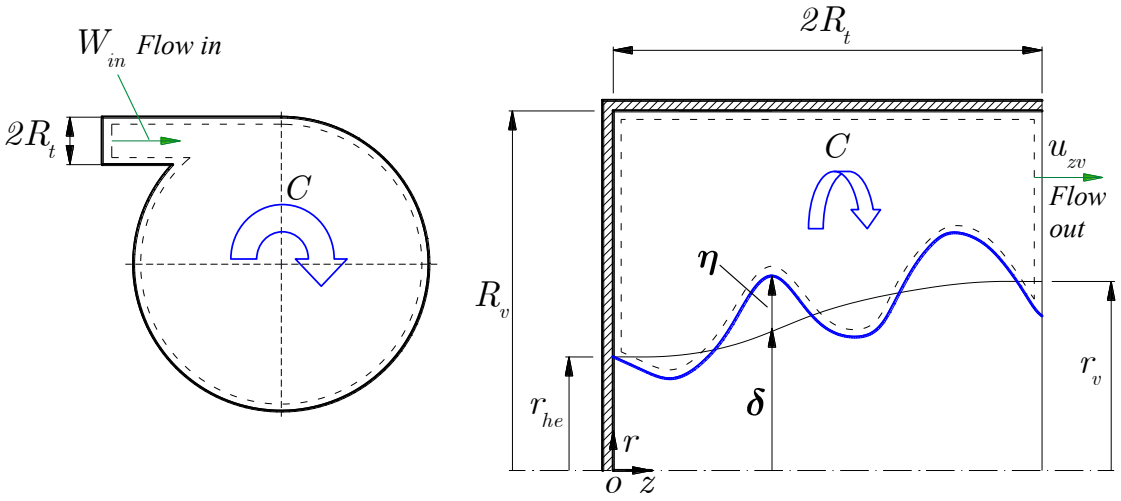


Figure 6.2.: Schematic of head end control volume for mass balance analysis

In terms of the free surface disturbance, the first integral in Eq. (6.8) can be written as

$$\int_{CV} \rho dV = \rho \int_0^{2R_t} \left( \int_{\delta+\eta}^{R_v} 2\pi r dr \right) dz = \rho\pi \int_0^{2R_t} \left( R_v^2 - (\delta+\eta)^2 \right) dz = \dots$$
$$= \rho\pi \int_0^{2R_t} \left( R_v^2 - \delta^2 - 2\delta\eta \right) dz = \rho\pi \int_0^{2R_t} \left( R_v^2 - \delta^2 \right) dz - 2\rho\pi \int_0^{2R_t} \delta\eta dz$$

where from it follows that

$$\frac{\partial}{\partial t} \int_{CV} \rho dV = -2\rho\pi \int_0^{2R_t} \delta \frac{\partial \eta}{\partial t} dz \tag{6.9}$$

For the second integral in Eq. (6.8) we have

$$\int_{CS} \rho \vec{u} \cdot d\vec{S} = -\rho \left( \bar{W}_{in} + W'_{in} \right) N_{in} \pi R_t^2 + \rho \int_{r_v+\eta}^{R_v} \left( \bar{u}_{zv} + \frac{\partial \phi'}{\partial z} \right) \Big|_{z=2R_t} 2\pi r dr =$$
$$= -\rho \bar{W}_{in} N_{in} \pi R_t^2 - \rho W'_{in} N_{in} \pi R_t^2 + \rho \int_{r_v}^{R_v} \bar{u}_{zv} 2\pi r dr \dots$$
$$\dots - \rho \int_{r_v}^{r_v+\eta|_{z=2R_t}} \bar{u}_{zv} 2\pi r dr + \rho \int_{r_v+\eta}^{R_v} \frac{\partial \phi'}{\partial z} \Big|_{z=2R_t} 2\pi r dr =$$
$$= -\dot{m}'_{in} + 2\rho\pi \left[ - \int_{r_v}^{r_v+\eta|_{z=2R_t}} \bar{u}_{zv} r dr + \int_{r_v+\eta}^{R_v} \frac{\partial \phi'}{\partial z} \Big|_{z=2R_t} r dr \right] \tag{6.10}$$

where we have canceled the mass flow rates at steady state given by

$$\rho \bar{W}_{in} N_{in} \pi R_t^2 = \rho \int_{r_v}^{R_v} \bar{u}_{zv} 2\pi r dr$$

Next, we can approximate the axial velocity disturbance in Eq. (6.10) as

$$\left.\frac{\partial\phi'}{\partial z}\right|_{r=r_v+\eta} = \left.\frac{\partial\phi'}{\partial z}\right|_{r=r_v} + \eta|_{z=2R_t}\left.\frac{\partial^2\phi'}{\partial z\partial r}\right|_{r=r_v} + \ldots \simeq \left.\frac{\partial\phi'}{\partial z}\right|_{r=r_v} \tag{6.11}$$

Combining Eqs. (6.8)–(6.11), we obtain an intermediate expression for the unsteady inflow mass flow rate in terms of $\eta = \hat{\eta}e^{i(kz-\omega t)}$ and $\phi' = \hat{\phi}\,(r)\,e^{i(kz-\omega t)}$:

$$\dot{m}'_{in} = 2\rho\pi\left[-\int_0^{2R_t}\delta\frac{\partial\eta}{\partial t}dz - \int_{r_v}^{r_v+\eta|_{z=2R_t}}\bar{u}_{zv}rdr + \int_{r_v}^{R_v}\left.\frac{\partial\phi'}{\partial z}\right|_{z=2R_t}rdr\right] \tag{6.12}$$

Following the discussion in Section 3.3, we know that, right at the head end, $z = 0$, and at the end of the head end transition region, $z = 2R_t$, the gradient of the steady free surface radius shrinks to zero, $d\delta/dz = 0$. We also know that the solid boundary radius is constant and equal to $R_v$ at all points $0 < z < 2R_t$, meaning that the corresponding angle of solid wall convergence is zero, $\alpha = 0$. Then, continuing the discussion in Section 4.3, we can say that, with these simplified conditions, the refractive terms can be eliminated, which results in the reduced expressions for the velocity potential disturbance, $\phi'$, and the dispersion relation:

$$\phi'\,(z,r,t) = i\left(k\frac{\partial\bar{\phi}}{\partial z} - \omega\right)\frac{I_0\,(kr) + \dfrac{I_1\,(kR)}{K_1\,(kR)}K_0\,(kr)}{k\left[I_1\,(k\delta) - \dfrac{I_1\,(kR)}{K_1\,(kR)}K_1\,(k\delta)\right]}\hat{\eta}e^{i(kz-\omega t)} \tag{6.13}$$

$$\frac{\omega}{k} = \frac{\partial\bar{\phi}}{\partial z} + \sqrt{\frac{1}{k}\left[\frac{-I_1\,(k\delta) + \dfrac{I_1\,(kR)}{K_1\,(kR)}K_1\,(k\delta)}{I_0\,(k\delta) + \dfrac{I_1\,(kR)}{K_1\,(kR)}K_0\,(k\delta)}\right]\frac{C^2}{\delta^3}} \tag{6.14}$$

Note that only downstream traveling wave solution, with a positive radical, is considered here.

Let us name the wave numbers at $z = 0$ and $z = 2R_t$ as $k_{he}$ and $k_v$ respectively, so that their indices correspond to the steady state radii $r_{he}$ and $r_v$ (see Table 2.3). Then based on Eq. (6.14) we can immediately obtain their values from the equations

$$\frac{\omega}{k_{he}} = \sqrt{\frac{1}{k_{he}}\frac{-I_1\,(k_{he}r_{he}) + \dfrac{I_1\,(k_{he}R_v)}{K_1\,(k_{he}R_v)}K_1\,(k_{he}r_{he})}{I_0\,(k_{he}r_{he}) + \dfrac{I_1\,(k_{he}R_v)}{K_1\,(k_{he}R_v)}K_0\,(k_{he}r_{he})}\frac{C^2}{r_{he}^3}} \tag{6.15}$$

$$\frac{\omega}{k_v} = \bar{u}_{zv} + \sqrt{\frac{1}{k_v}\frac{-I_1(k_v R_v) + \frac{I_1(k_v R_v)}{K_1(k_v R_v)} K_1(k_v r_v)}{I_0(k_v r_v) + \frac{I_1(k_v R_v)}{K_1(k_v R_v)} K_0(k_v r_v)} \frac{C^2}{r_v^3}} \tag{6.16}$$

Going back to the mass flow rate fluctuation Eq. (6.12), we can rewrite the first integral in it as

$$\int_0^{2R_t} \delta \frac{\partial \eta}{\partial t} dz = \hat{\eta}(-i\omega) e^{-i\omega t} \int_0^{2R_t} \delta e^{ikz} dz \tag{6.17}$$

As we have discussed in Chapters 3 and 4, because the variation of the steady free surface radius and the wave numbers in the head end transition region is small, we can make the following approximations:

$$\delta(z) = r_{he} + \frac{d\delta}{dz} z + \frac{1}{2}\frac{d^2\delta}{dz^2} z^2 + \ldots \simeq r_{he}$$
$$k(z) = k_{he} + \frac{dk}{dz} z + \frac{1}{2}\frac{d^2 k}{dz^2} z^2 + \ldots \simeq k_{he}$$

These approximations allow us to rewrite the part of the integral (6.17) that comes after the integral sign in the form

$$\int_0^{2R_t} \delta e^{ikz} dz = \int_0^{2R_t} r_{he} e^{ik_{he} z} dz = \frac{r_{he}}{ik_{he}} \left( e^{ik_{he} 2R_t} - 1 \right) \tag{6.18}$$

The second integral in Eq. (6.12) can be rewritten as

$$\int_{r_v}^{r_v + \eta|_{z=2R_t}} \bar{u}_{zv} r dr = \frac{\bar{u}_{zv}}{2} \left[ r_v^2 + 2 r_v \eta + \eta^2 - r_v^2 \right]_{z=2R_t} =$$
$$= \bar{u}_{zv} r_v \eta|_{z=2R_t} = \bar{u}_{zv} r_v \hat{\eta} e^{ik_v 2R_t} e^{-i\omega t} \tag{6.19}$$

By substituting $\phi'$ from Eq. (6.13) into the third integral in Eq. (6.12), we can rewrite the latter as

$$\int_{r_v}^{R_v} \left. \frac{\partial \phi'}{\partial z} \right|_{z=2R_t} r dr = e^{ik_v 2R_t} e^{-i\omega t} \hat{\eta} (k_v \bar{u}_{zv} - \omega) \int_{r_v}^{R_v} \frac{I_0(k_v r) + \frac{I_1(k_v R_v)}{K_1(k_v R_v)} K_0(k_v r)}{-I_1(k r_v) + \frac{I_1(k_v R_v)}{K_1(k_v R_v)} K_1(k_v r_v)} r dr \tag{6.20}$$

Lastly, by combining Eqs. (6.17)–(6.20) with Eq. (6.12), we obtain the final expression for the fluctuation of the unsteady inflow mass flow rate as a function of $\eta$:

$$\dot{m}'_{in} = 2\rho\pi\hat{\eta}e^{-i\omega t}\left[+\omega\frac{r_{he}}{k_{he}}\left(e^{ik_{he}2R_t}-1\right)-\bar{u}_{zv}r_v e^{ik_v 2R_t}+\ldots\right.$$
$$\left.\ldots+e^{ik_v 2R_t}\left(k_v\bar{u}_{zv}-\omega\right)\int_{r_v}^{R_v}\frac{I_0\left(k_v r\right)+\dfrac{I_1\left(k_v R_v\right)}{K_1\left(k_v R_v\right)}K_0\left(k_v r\right)}{-I_1\left(kr_v\right)+\dfrac{I_1\left(k_v R_v\right)}{K_1\left(k_v R_v\right)}K_1\left(k_v r_v\right)}rdr\right] \tag{6.21}$$

where: $R_t$, $R_v$, $r_{he}$, $r_v$, and $\bar{u}_{zv}$ are given in Tables 2.2 and 2.3; $k_{he}$ and $k_v$ follow from Eqs. (6.15) and (6.16). This expression can be substituted into Eq. (6.7) in order to calculate the unsteady part of the pressure drop through the tangential inlets, $\Delta p'_t$.

### 6.2.3 Pressure Drop Through Liquid Body at Head End

In this analysis, we are considering the instantaneous pressure drop through the liquid body at location $z = 0$ (Fig. 6.2). We start from the axisymmetric radial momentum

$$\frac{\partial u_r}{\partial t}+u_r\frac{\partial u_r}{\partial r}-\frac{u_\theta^2}{r}+u_z\frac{\partial u_r}{\partial z}=-\frac{1}{\rho}\frac{\partial p}{\partial r} \tag{6.22}$$

The disturbed form of it, at any $r$ of the liquid body, can be written as

$$\frac{\partial}{\partial t}\left(\bar{u}_r+u'_r\right)+\left(\bar{u}_r+u'_r\right)\frac{\partial}{\partial r}\left(\bar{u}_r+u'_r\right)-\frac{C^2}{r^3}+\left(\bar{u}_z+u'_z\right)\frac{\partial}{\partial z}\left(\bar{u}_r+u'_r\right)=-\frac{1}{\rho}\frac{\partial}{\partial r}\left(\bar{p}+p'\right) \tag{6.23}$$

where, as before, the assumption is made that the the circumferential velocity follows the potential free vortex distribution (see Section 2.1 for more discussion on this treatment). In this equation, we neglect all terms that involve $\bar{u}_r$ because, from Section 3.4, we know that the steady state radial velocities at the head are very small. Also, we note that, at $z = 0$, $\bar{u}_z = 0$. These considerations reduce Eq. (6.23) to

$$\frac{\partial u'_r}{\partial t}-\frac{C^2}{r^3}=-\frac{1}{\rho}\frac{\partial\bar{p}}{\partial r}-\frac{1}{\rho}\frac{\partial p'}{\partial r} \tag{6.24}$$

where from we can deduce that the steady and the unsteady parts of the radial pressure gradient are given by:

$$\begin{aligned} \frac{\partial \bar{p}}{\partial r} &= \rho \frac{C^2}{r^3} \\ \frac{\partial p'}{\partial r} &= -\rho \frac{\partial u'_r}{\partial t}\bigg|_{z=0} \end{aligned} \tag{6.25}$$

The instantaneous pressure drop through the liquid body at the head end is formally given as an integral of the radial pressure gradient as

$$\begin{aligned} \Delta p_{he} = \Delta \bar{p}_{he} + \Delta p'_{he} = \int_{r_{he}+\eta}^{R_v} \left( \frac{\partial \bar{p}}{\partial r} + \frac{\partial p'}{\partial r} \right)\bigg|_{z=0} dr = \\ = \int_{r_{he}}^{R_v} \frac{\partial \bar{p}}{\partial r} dr - \int_{r_{he}}^{r_{he}+\eta|_{z=0}} \frac{\partial \bar{p}}{\partial r} dr + \int_{r_{he}}^{R_v} \frac{\partial p'}{\partial r} dr - \int_{r_{he}}^{r_{he}+\eta|_{z=0}} \frac{\partial p'}{\partial r} dr \end{aligned} \tag{6.26}$$

In this equation, the last term can be neglected due to

$$\frac{\partial p'}{\partial r}\bigg|_{r_{he}+\eta|_{z=0}} = \frac{\partial p'}{\partial r}\bigg|_{r_{he}} + \eta|_{z=0} \frac{\partial^2 p'}{\partial r^2}\bigg|_{r_{he}} + \ldots \simeq \frac{\partial p'}{\partial r}\bigg|_{r_{he}}$$

Then, by using expressions (6.25), from Eq. (6.26), we can conclude that the steady state part of the pressure drop is given by

$$\Delta \bar{p}_{he} = \int_{r_{he}}^{R_v} \frac{\partial \bar{p}}{\partial r} dr = \int_{r_{he}}^{R_v} \rho \frac{C^2}{r^3} dr = \rho \frac{C^2}{2} \left[ \frac{1}{r_{he}^2} - \frac{1}{R_v^2} \right] \tag{6.27}$$

and the unsteady part of the pressure drop is given by

$$\Delta p'_{he} = -\int_{r_{he}}^{r_{he}+\eta|_{z=0}} \frac{\partial \bar{p}}{\partial r} dr + \int_{r_{he}}^{R_v} \frac{\partial p'}{\partial r} dr = -\int_{r_{he}}^{r_{he}+\eta|_{z=0}} \rho \frac{C^2}{r^3} dr - \int_{r_{he}}^{R_v} \rho \frac{\partial u'_r}{\partial t}\bigg|_{z=0} dr \tag{6.28}$$

The first integral in Eq. (6.28) results in

$$\int_{r_{he}}^{r_{he}+\eta|_{z=0}} \rho \frac{C^2}{r^3} dr = -\rho \frac{C^2}{2} \left[ \frac{1}{\left(r_{he} + \eta|_{z=0}\right)^2} - \frac{1}{r_{he}^2} \right] = \rho \frac{C^2}{r_{he}^3} \eta|_{z=0} = \rho \frac{C^2}{r_{he}^3} \hat{\eta} e^{-i\omega t} \tag{6.29}$$

where we have used the binomial expansion [61, p. 1196]

$$\frac{1}{\left(r_{he} + \eta|_{z=0}\right)^2} = \frac{1}{r_{he}^2} - \frac{2}{r_{he}^3} \eta|_{z=0} + \frac{3}{r_{he}^4} \left(\eta|_{z=0}\right)^2 - \ldots \simeq \frac{1}{r_{he}^2} - \frac{2}{r_{he}^3} \eta|_{z=0}$$

to cancel the $1/r_{he}^2$ term. By using the expression for the velocity potential (6.13), the last integral in Eq. (6.28) can be written as

$$\int_{r_{he}}^{R_v} \left.\frac{\partial u_r'}{\partial t}\right|_{z=0} dr = \int_{r_{he}}^{R_v} \frac{\partial}{\partial t}\left(\left.\frac{\partial \phi'}{\partial r}\right|_{z=0}\right) dr = \\ = \hat{\eta}\omega^2 e^{-i\omega t} \int_{r_{he}}^{R_v} \frac{I_1(k_{he}r) - \dfrac{I_1(k_{he}R_v)}{K_1(k_{he}R_v)} K_1(k_{he}r)}{-I_1(k_{he}r_{he}) + \dfrac{I_1(k_{he}R_v)}{K_1(k_{he}R_v)} K_1(k_{he}r_{he})} dr \qquad (6.30)$$

Finally, by combining Eqs. (6.28)–(6.30), we can obtain the expression for the fluctuation of the unsteady pressure drop at the head end in terms of $\eta$:

$$\Delta p_{he}' = -\rho\hat{\eta} e^{-i\omega t}\left[\frac{C^2}{r_{he}^3} + \omega^2 \int_{r_{he}}^{R_v} \frac{I_1(k_{he}r) - \dfrac{I_1(k_{he}R_v)}{K_1(k_{he}R_v)} K_1(k_{he}r)}{-I_1(k_{he}r_{he}) + \dfrac{I_1(k_{he}R_v)}{K_1(k_{he}R_v)} K_1(k_{he}r_{he})} dr\right] \qquad (6.31)$$

where: $r_{he}$, $R_v$, and $C = \bar{W}_{in}R_{in} = 4.5$ are given in Tables 2.2 and 2.3; and $k_{he}$ follows from Eq. (6.15).

### 6.2.4 Mass Flow Rate at Nozzle Exit

In this study, we will assume that the free surface at the nozzle exit, is simply cylindrical and ignore the effect of flow bending at the end of the nozzle, Fig. 6.3. Let us denote the end of the nozzle by $z_n = L_v + L_c + L_n$. Then, for the instantaneous mass flow rate at the nozzle exit we have

$$\dot{m}_n = \bar{\dot{m}}_n + \dot{m}_n' = \rho \int_{r_n+\eta|_{z=z_n}}^{R_n} (\bar{u}_{zn} + u_{zn}')2\pi r dr = \\ = \rho\left[\int_{r_n}^{R_n} \bar{u}_{zn} 2\pi r dr - \int_{r_n}^{r_n+\eta|_{z=z_n}} \bar{u}_{zn} 2\pi r dr\right] + \ldots \\ \ldots + \rho\left[\int_{r_n}^{R_n} u_{zn}' 2\pi r dr - \int_{r_n}^{r_n+\eta|_{z=z_n}} u_{zn}' 2\pi r dr\right] \qquad (6.32)$$

The last integral here can be neglected due to

$$u_{zn}'|_{r_n+\eta|_{z=z_n}} = u_{zn}'|_{r_n} + \eta|_{z=z_n} \left.\frac{\partial u_{zn}'}{\partial r}\right|_{r_n} + \ldots \simeq u_{zn}'|_{r_n}$$

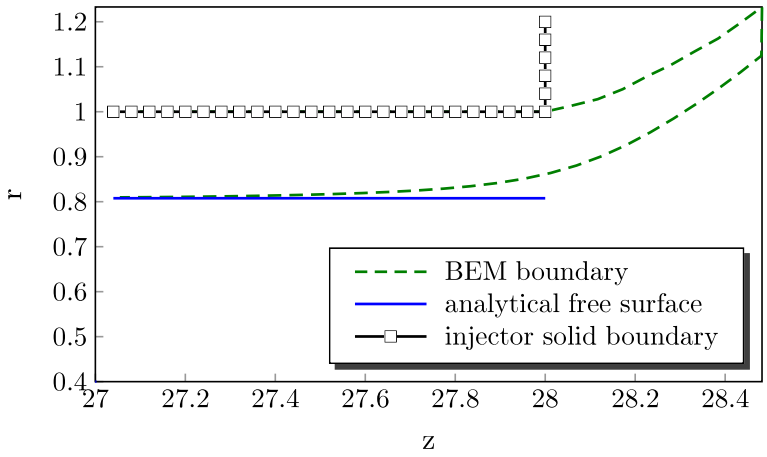


Figure 6.3.: Analytical vs. BEM free surface comparison at nozzle exit

We can equate the steady part of the exit mass flow rate in Eq. (6.32) to the steady part of the inflow mass flow rate as

$$\bar{\dot{m}}_n = \rho \int_{r_n}^{R_n} \bar{u}_{zn} 2\pi r dr = \rho \frac{C}{R_{in}} N_{in} \pi R_t^2 \tag{6.33}$$

The unsteady part of the exit mass flow rate, on the other hand, from Eq. (6.32) is given by

$$\dot{m}'_n = \rho \left[ - \int_{r_n}^{r_n + \eta|_{z=z_n}} \bar{u}_{zn} 2\pi r dr + \int_{r_n}^{R_n} u'_{zn} 2\pi r dr \right] \tag{6.34}$$

As in Subsection 6.2.2, the fact that the steady radii of the flow boundaries in this model, $R_n$ and $r_n$, do not change in $z$ direction, allows us to use the simplified equations for the velocity potential disturbance, Eq. (6.13), and the dispersion relation, Eq. (6.14). Let us denote the wave number at the nozzle exit as $k(z_n) = k_n$. Then, based on Eq. (6.14), we can calculate it implicitly from the expression

$$\frac{\omega}{k_n} = \bar{u}_{zn} + \sqrt{\frac{1}{k_n} \frac{-I_1(k_n r_n) + \dfrac{I_1(k_n R_n)}{K_1(k_n R_n)} K_1(k_n r_n)}{I_0(k_n r_n) + \dfrac{I_1(k_n R_n)}{K_1(k_n R_n)} K_0(k_n r_n)} \frac{C^2}{r_n^3}} \tag{6.35}$$

Consequently, for the first integral in Eq. (6.34) we can write

$$\int_{r_n}^{r_n+\eta|_{z=z_n}} \bar{u}_{zn} 2\pi r dr = \pi \bar{u}_{zn} \left[ r_n^2 + 2r_n \eta|_{z=z_n} + \left(\eta|_{z=z_n}\right)^2 - r_n^2 \right] =$$

$$= 2\pi \bar{u}_{zn} r_n \eta|_{z=z_n} = 2\pi \bar{u}_{zn} r_n \hat{\eta} e^{ik_n z_n} e^{-i\omega t} \tag{6.36}$$

For the second integral in Eq. (6.34) we can write

$$\int_{r_n}^{R_n} u'_{zn} 2\pi r dr = \int_{r_n}^{R_n} \left. \frac{\partial \phi'}{\partial z} \right|_{z=z_n} 2\pi r dr =$$

$$= 2\pi \hat{\eta} \left(k_n \bar{u}_{zn} - \omega\right) e^{ik_n z_n} e^{-i\omega t} \int_{r_n}^{R_n} \frac{I_0(k_n r) + \dfrac{I_1(k_n R_n)}{K_1(k_n R_n)} K_0(k_n r)}{-I_1(k_n r_n) + \dfrac{I_1(k_n R_n)}{K_1(k_n R_n)} K_1(k_n r_n)} r dr \tag{6.37}$$

Conclusively, by putting together Eqs. (6.34)–(6.37), we obtain the expression for the fluctuation of the nozzle exit mass flow rate in terms of $\eta$:

$$\dot{m}'_n = 2\pi \hat{\eta} e^{ik_n z_n} e^{-i\omega t} \rho \times \ldots$$

$$\ldots \times \left[ -\bar{u}_{zn} r_n + \left(k_n \bar{u}_{zn} - \omega\right) \int_{r_n}^{R_n} \frac{I_0(k_n r) + \dfrac{I_1(k_n R_n)}{K_1(k_n R_n)} K_0(k_n r)}{-I_1(k_n r_n) + \dfrac{I_1(k_n R_n)}{K_1(k_n R_n)} K_1(k_n r_n)} r dr \right] \tag{6.38}$$

where: $z_n = L_v + L_c + L_n$; $\bar{u}_{zn}$, $R_n$, and $r_n$ are given in Tables 2.2 and 2.3; and $k_n$ follows from Eq. (6.35).

### 6.2.5 Injector Response at Long Wave Limit

At the limit, when the wave length becomes large, or the wave number tends to zero, $k \to 0$, we can write the following approximations [108, p. 156] for the Bessel functions:

$$I_0(x) \to 1, \qquad I_1(x) \to \frac{1}{2}x, \qquad K_0(x) \to \ln\frac{1}{x}, \qquad K_1(x) \to \frac{1}{x} \tag{6.39}$$

Let us investigate how these approximations will change the components of the injector response due to Kelvin's waves in the previous subsections. The steady state

mass flow rates and pressure drops will stay same as they do not depend on the wave number. The unsteady parts will however simplify such that the integrals involving the Bessel functions will reduce to much simpler expressions. This will affect the equations for $\dot{m}'_n$, $\dot{m}'_{in}$, and $\Delta p'_{he}$.

Let us investigate the integrals in the expressions for $\dot{m}'_n$ and $\dot{m}'_{in}$, Eqs. (6.38) and (6.21). Let us write the wave numbers contained in these equations, in general, as $k_0$, and the flow bounding radii as $R_0$ and $r_0$. Then, at the limit $k_0 \to 0$, due to Eqs. (6.39), we have

$$\lim_{k_0\to 0} \frac{I_0(k_0 r) + \dfrac{I_1(k_0 R_0)}{K_1(k_0 R_0)} K_0(k_0 r)}{-I_1(k_0 r_0) + \dfrac{I_1(k_0 R_0)}{K_1(k_0 R_0)} K_1(k_0 r_0)} = \frac{1 + \dfrac{\frac{1}{2}k_0 R_0}{\dfrac{1}{k_0 R_0}} \ln\left(\dfrac{1}{k_0 r}\right)}{-\frac{1}{2}k_0 r_0 + \dfrac{\frac{1}{2}k_0 R_0}{\dfrac{1}{k_0 R_0}} \dfrac{1}{k_0 r_0}} =$$

$$= \frac{1 + \frac{1}{2}(k_0 R_0)^2 \ln\left(\dfrac{1}{k_0 r}\right)}{\frac{1}{2}k_0\left(\dfrac{R_0^2}{r_0} - r_0\right)} = \frac{1}{\frac{1}{2}k_0\left(\dfrac{R_0^2}{r_0} - r_0\right)} \tag{6.40}$$

where the last equality comes from the fact that the square function grows much faster than the logarithmic function for positive arguments. This reduces the integral with the Bessel functions to the following simple fraction

$$\lim_{k_0\to 0} \int_{r_0}^{R_0} \frac{I_0(k_0 r) + \dfrac{I_1(k_0 R_0)}{K_1(k_0 R_0)} K_0(k_0 r)}{-I_1(k_0 r_0) + \dfrac{I_1(k_0 R_0)}{K_1(k_0 R_0)} K_1(k_0 r_0)} r dr = \int_{r_0}^{R_0} \frac{1}{\frac{1}{2}k_0\left(\dfrac{R_0^2}{r_0} - r_0\right)} r dr =$$

$$= \frac{2r_0}{k_0\left(R_0^2 - r_0^2\right)} \frac{\left(R_0^2 - r_0^2\right)}{2} = \frac{r_0}{k_0} \tag{6.41}$$

Consequently, due to Eq. (6.41), the mass flow rate fluctuations, Eqs. (6.38) and (6.21), can be rewritten as

$$\dot{m}'_n = 2\pi\hat{\eta} e^{ik_n z_n} e^{-i\omega t} \rho \left[-\bar{u}_{zn} r_n + \frac{r_n}{k_n}\left(k_n \bar{u}_{zn} - \omega\right)\right] \tag{6.42}$$

$$\dot{m}'_{in} = 2\rho\pi\hat{\eta} e^{-i\omega t} \left[+\omega \frac{r_{he}}{k_{he}}\left(e^{ik_{he}2R_t} - 1\right) - \bar{u}_{zv} r_v e^{ik_v 2R_t} + e^{ik_v 2R_t} \frac{r_v}{k_v}\left(k\bar{u}_{zv} - \omega\right)\right] \tag{6.43}$$

To find the wave numbers, $k_{he}$, $k_v$ and $k_n$, we first use Eq. (6.40) to reduce the radical in the Kelvin's dispersion relationship as follows:

$$\lim_{k_0\to 0}\sqrt{\frac{1}{k_0}\frac{-I_1(k_0r_0)+\dfrac{I_1(k_0R_0)}{K_1(k_0R_0)}K_1(k_0r_0)}{I_0(k_0r_0)+\dfrac{I_1(k_0R_0)}{K_1(k_0R_0)}K_0(k_0r_0)}\frac{C^2}{r_0^3}}=\sqrt{\frac{1}{k_0}\frac{1}{2}k_0\left(\frac{R_0^2}{r_0}-r_0\right)\frac{C^2}{r_0^3}}=$$

$$=\sqrt{C^2\frac{R_0^2-r_0^2}{2r_0^4}} \tag{6.44}$$

which allows to reduce Eqs. (6.15), (6.16), and (6.35) to

$$\frac{\omega}{k_{he}}=\sqrt{C^2\frac{R_v^2-r_{he}^2}{2r_{he}^4}} \tag{6.45}$$

$$\frac{\omega}{k_v}=\bar{u}_{zv}+\sqrt{C^2\frac{R_v^2-r_v^2}{2r_v^4}} \tag{6.46}$$

$$\frac{\omega}{k_n}=\bar{u}_{zn}+\sqrt{C^2\frac{R_n^2-r_n^2}{2r_n^4}} \tag{6.47}$$

These are the familiar long wave relations between the wave number and the disturbance frequency (see Appendix B).

Proceeding further to the pressure drops, note that the Eq. (6.7) relating the fluctuation of the pressure drop through tangential inlets, $\Delta p_t'$, to the inflow mass flow fluctuation, $\dot{m}_{in}'$, is still valid in the long wave limit. However, the fluctuation of the pressure drop through the liquid body at the head end, $\Delta p_{he}'$, Eq. (6.31), is now different due to the following. As we know, in the long wave limit, the radial velocity fluctuations are neglected. This assumption reduces Eq. (6.28) to

$$\Delta p_{he}'=-\int_{r_{he}}^{r_{he}+\eta|_{z=0}}\rho\frac{C^2}{r^3}dr$$

and subsequently simplifies Eq. (6.31) to the first term

$$\Delta p_{he}'=-\rho\hat{\eta}e^{-i\omega t}\frac{C^2}{r_{he}^3} \tag{6.48}$$

This completes the set of equations needed to compute the injector response at the long wave limit.

## 6.3 Influence of Inertial and Capillary Effects on Injector Response

To make a first order assessment of the inertial and capillary effects imposed by the gaseous core on the injector response, first, we will obtain the dispersion equation relating the disturbance wave number to the disturbance frequency in the general unsteady swirling flow with variable flow boundaries and bulk axial velocity, which, at the same time, explicitly includes the gas-liquid density ratio and the surface tension terms. Then, as was shown in Section 6.2, we will use this information to derive the injector response components at the points of the flow where it can be considered cylindrical. All parameters relevant to the gaseous core will be denoted by subscript $g$ further on. Figure 6.4 shows the flow schematic considered for this analysis, where the liquid density is denoted by $\rho_l$, and the gas density – by $\rho_g$.

With regard to the liquid phase, in this section, we will make the same assumptions as in Section 4.3, where the attempt was to characterize the dispersion of Kelvin's

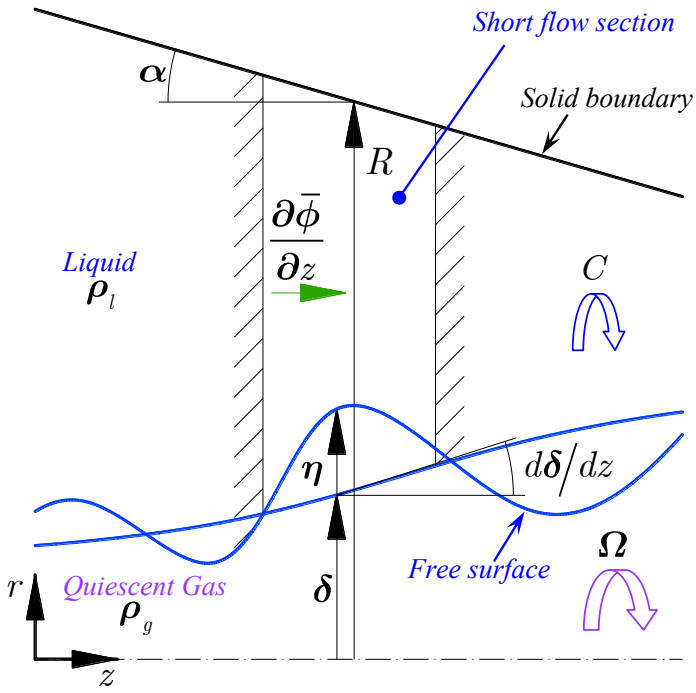


Figure 6.4.: Combined gas-liquid unsteady flow schematic

waves in general nonuniform flows with an empty hollow core. Thus, the analysis of the liquid phase will closely follow the potential flow analysis in Section 4.3.

Regarding the gaseous phase, for simplicity, it is assumed that it is incompressible, inviscid, and axisymmetric. Concerning its circumferential velocity, Chinn [4, p. 22] states:

> *"... it is likely that the air-core experiences solid-body rotation, although this has not been measured ..."*

Accordingly, we assume that the *steady* circumferential velocity in the gaseous core follows the solid body rotation profile given by $\Omega r$, where $\Omega$ is a constant angular velocity. Hence, the gaseous core is rotational. Consequently, a discontinuity in vorticity occurs at the free surface $r = \delta$ (Fig. 6.4), where the rotational flow transitions to irrotational, and, as Lessen [109, p. 461] states, is:

> *"... regarded as a cylindrical vortex sheet of infinite vorticity."*

Overall, this results in circumferential velocity profile known as Rankine. Lastly, we assume that the gaseous core does not move in the axial direction based on the facts that the gas meets a stagnant wall at the injector head end, and its inertia is small.

There are a couple of papers in the literature related to this problem. Ponstein [107, §5] investigated a case when the liquid phase does not move axially, and the inertia of the gaseous core is neglected. Lessen [109] investigated the Rankine profile problem, but his outer fluid did not have the solid boundary and extended to infinity in the direction perpendicular to the axis. Also, both the outer and the inner fluids were assumed to have the same density. Richardson [43, chap. 3], in his hydrodynamic instability analysis, considered that, at steady state, the liquid phase has the solid body rotation profile, and the gaseous core is moving with some uniform axial velocity, but does not rotate at all. As one can see, all of these three problems are different in their setup from the one considered here. Therefore, they may only serve as a good starting point from where we can develop the analysis relevant particularly to our flow setup.

### 6.3.1 Dispersion Relation in Variable Flow Geometry Considering Inertial and Capillary Effects of Gaseous Core

To characterize the refractive interaction between the gas and the liquid in variable flow geometry, we will first derive the expression for the instantaneous surface curvature in terms of the free surface disturbance $\eta$. Then, we will separately consider the gaseous core and the liquid phase equations, which will be connected through the pressure drop across the free surface. Finally, we will combine the above obtained information to derive the dispersion relation which describes that gas-liquid interaction. Later, the results of this hydrodynamic stability analysis will be used to calculate the injector response that accounts for the inertia and capillary effects of the gaseous core.

#### Unsteady Surface Curvature

Let us start with the general expression for the unsteady curvature, K, of the axisymmetric free surface, $r = \delta + \eta$, shown in Fig. 6.4 (see Smirnov [110], [111]):

$$\mathrm{K} = \frac{1}{(\delta+\eta)\left\{1+\left[\dfrac{\partial(\delta+\eta)}{\partial z}\right]^2\right\}^{\frac{1}{2}}} + \frac{-\dfrac{\partial^2(\delta+\eta)}{\partial z^2}}{\left\{1+\left[\dfrac{\partial(\delta+\eta)}{\partial z}\right]^2\right\}^{\frac{3}{2}}} = \bar{\mathrm{K}} + \mathrm{K}' \tag{6.49}$$

where by the sum $\bar{\mathrm{K}} + \mathrm{K}'$ we are showing its decomposition into the steady and unsteady parts. For the steady part, when $\eta = 0$, we can write

$$\bar{\mathrm{K}} = \frac{1}{\delta\left\{1+\left[\dfrac{\partial\delta}{\partial z}\right]^2\right\}^{\frac{1}{2}}} + \frac{-\dfrac{\partial^2\delta}{\partial z^2}}{\left\{1+\left[\dfrac{\partial\delta}{\partial z}\right]^2\right\}^{\frac{3}{2}}} \tag{6.50}$$

Let us anchor the instantaneous curvature, Eq. (6.49), to the terms contained in the steady curvature, Eq. (6.50), by writing

$$\mathrm{K} = \frac{1}{\delta\left\{1+\left[\dfrac{\partial\delta}{\partial z}\right]^2\right\}^{\frac{1}{2}}}\left(1+x_1\right) + \frac{-\dfrac{\partial^2\delta}{\partial z^2}}{\left\{1+\left[\dfrac{\partial\delta}{\partial z}\right]^2\right\}^{\frac{3}{2}}}\left(1+x_2\right) \tag{6.51}$$

where $x_1$ and $x_2$ are the unknown coefficients which we will determine next.

By comparing Eq. (6.49) with Eq. (6.51), we can see that

$$\frac{1}{\delta\left\{1+\left[\dfrac{\partial\delta}{\partial z}\right]^2\right\}^{\frac{1}{2}}}\left(1+x_1\right) = \frac{1}{(\delta+\eta)\left\{1+\left[\dfrac{\partial\left(\delta+\eta\right)}{\partial z}\right]^2\right\}^{\frac{1}{2}}}$$

from where it follows that

$$\begin{aligned} 1+x_1 &= \frac{\delta}{\delta+\eta}\left\{\frac{1+\left[\dfrac{\partial\delta}{\partial z}\right]^2}{1+\left[\dfrac{\partial\left(\delta+\eta\right)}{\partial z}\right]^2}\right\}^{\frac{1}{2}} = \\ &= \frac{1}{1+\dfrac{\eta}{\delta}}\left\{\frac{1+\left[\dfrac{\partial\delta}{\partial z}\right]^2}{1+\left[\dfrac{\partial\delta}{\partial z}\right]^2+2\dfrac{\partial\delta}{\partial z}\dfrac{\partial\eta}{\partial z}}\right\}^{\frac{1}{2}} = \left(1+\frac{\eta}{\delta}\right)^{-1}\left\{1+\frac{2\dfrac{\partial\delta}{\partial z}\dfrac{\partial\eta}{\partial z}}{1+\left[\dfrac{\partial\delta}{\partial z}\right]^2}\right\}^{-\frac{1}{2}} \end{aligned} \tag{6.52}$$

Next we will use the binomial expansion [61, p. 1196] of the form

$$(s+t)^n = s^n + ns^{n-1}t + \frac{n\left(n-1\right)}{2!}s^{n-2}t^2 + \ldots \tag{6.53}$$

for both terms in the last expression, up to the first order. Then, the first and the second terms respectively can be expanded to

$$\left(1+\frac{\eta}{\delta}\right)^{-1} = 1-\frac{\eta}{\delta} \tag{6.54}$$

$$\left\{1+\frac{2\dfrac{\partial\delta}{\partial z}\dfrac{\partial\eta}{\partial z}}{1+\left[\dfrac{\partial\delta}{\partial z}\right]^2}\right\}^{-\frac{1}{2}} = 1-\frac{\dfrac{\partial\delta}{\partial z}\dfrac{\partial\eta}{\partial z}}{1+\left[\dfrac{\partial\delta}{\partial z}\right]^2} \tag{6.55}$$

Substituting Eqs. (6.54) and (6.55) back into Eq. (6.52), we obtain the expression for $x_1$:

$$1 + x_1 = \left(1 - \frac{\eta}{\delta}\right)\left(1 - \frac{\dfrac{\partial\delta}{\partial z}\dfrac{\partial\eta}{\partial z}}{1 + \left[\dfrac{\partial\delta}{\partial z}\right]^2}\right) = 1 - \frac{\eta}{\delta} - \frac{\dfrac{\partial\delta}{\partial z}\dfrac{\partial\eta}{\partial z}}{1 + \left[\dfrac{\partial\delta}{\partial z}\right]^2} \tag{6.56}$$

Further, we proceed to determination of $x_2$ starting again from the comparison of Eq. (6.49) with Eq. (6.51), from where we see that

$$\frac{-\dfrac{\partial^2\delta}{\partial z^2}}{\left\{1 + \left[\dfrac{\partial\delta}{\partial z}\right]^2\right\}^{\frac{3}{2}}}(1 + x_2) = \frac{-\dfrac{\partial^2(\delta+\eta)}{\partial z^2}}{\left\{1 + \left[\dfrac{\partial(\delta+\eta)}{\partial z}\right]^2\right\}^{\frac{3}{2}}}$$

which we can rearrange to

$$\begin{aligned} 1 + x_2 &= \frac{-\dfrac{\partial^2(\delta+\eta)}{\partial z^2}}{-\dfrac{\partial^2\delta}{\partial z^2}}\left\{\frac{1 + \left[\dfrac{\partial\delta}{\partial z}\right]^2}{1 + \left[\dfrac{\partial(\delta+\eta)}{\partial z}\right]^2}\right\}^{\frac{3}{2}} = \\ &= \frac{-\dfrac{\partial^2\delta}{\partial z^2} - \dfrac{\partial^2\eta}{\partial z^2}}{-\dfrac{\partial^2\delta}{\partial z^2}}\left\{\frac{1 + \left[\dfrac{\partial\delta}{\partial z}\right]^2}{1 + \left[\dfrac{\partial\delta}{\partial z}\right]^2 + 2\dfrac{\partial\delta}{\partial z}\dfrac{\partial\eta}{\partial z}}\right\}^{\frac{3}{2}} = \left(1 + \frac{\dfrac{\partial^2\eta}{\partial z^2}}{\dfrac{\partial^2\delta}{\partial z^2}}\right)\left\{1 + \frac{2\dfrac{\partial\delta}{\partial z}\dfrac{\partial\eta}{\partial z}}{1 + \left[\dfrac{\partial\delta}{\partial z}\right]^2}\right\}^{-\frac{3}{2}} \end{aligned} \tag{6.57}$$

Using the binomial expansion of the form (6.53), we can make a first order approximation of the second term in the last expression as

$$\left\{1 + \frac{2\dfrac{\partial\delta}{\partial z}\dfrac{\partial\eta}{\partial z}}{1 + \left[\dfrac{\partial\delta}{\partial z}\right]^2}\right\}^{-\frac{3}{2}} = 1 - 3\frac{\dfrac{\partial\delta}{\partial z}\dfrac{\partial\eta}{\partial z}}{1 + \left[\dfrac{\partial\delta}{\partial z}\right]^2} \tag{6.58}$$

Plugging this back into Eq. (6.57), we obtain the expression for $x_2$:

$$1 + x_2 = \left(1 + \frac{\dfrac{\partial^2\eta}{\partial z^2}}{\dfrac{\partial^2\delta}{\partial z^2}}\right)\left(1 - 3\frac{\dfrac{\partial\delta}{\partial z}\dfrac{\partial\eta}{\partial z}}{1 + \left[\dfrac{\partial\delta}{\partial z}\right]^2}\right) = 1 + \frac{\dfrac{\partial^2\eta}{\partial z^2}}{\dfrac{\partial^2\delta}{\partial z^2}} - 3\frac{\dfrac{\partial\delta}{\partial z}\dfrac{\partial\eta}{\partial z}}{1 + \left[\dfrac{\partial\delta}{\partial z}\right]^2} \tag{6.59}$$

Let us now rewrite the instantaneous curvature, Eq. (6.51), with the newly obtained expression for $x_1$ and $x_2$, Eqs. (6.56) and (6.59), as

$$\mathrm{K} = \frac{1}{\delta\left\{1+\left[\frac{\partial\delta}{\partial z}\right]^2\right\}^{\frac{1}{2}}}\left(1-\frac{\eta}{\delta}-\frac{\frac{\partial\delta}{\partial z}\frac{\partial\eta}{\partial z}}{1+\left[\frac{\partial\delta}{\partial z}\right]^2}\right)+\ldots \\ \ldots+\frac{-\frac{\partial^2\delta}{\partial z^2}}{\left\{1+\left[\frac{\partial\delta}{\partial z}\right]^2\right\}^{\frac{3}{2}}}\left(1+\frac{\frac{\partial^2\eta}{\partial z^2}}{\frac{\partial^2\delta}{\partial z^2}}-3\frac{\frac{\partial\delta}{\partial z}\frac{\partial\eta}{\partial z}}{1+\left[\frac{\partial\delta}{\partial z}\right]^2}\right) \tag{6.60}$$

This equation shows the dependence of the surface curvature on $\eta$ in an axisymmetric flow whose steady free radius, $\delta$, is variable. We can rewrite this equation as

$$\mathrm{K} = \frac{1}{\delta\left\{1+\left[\frac{\partial\delta}{\partial z}\right]^2\right\}^{\frac{1}{2}}}-\frac{\eta}{\delta^2\left\{1+\left[\frac{\partial\delta}{\partial z}\right]^2\right\}^{\frac{1}{2}}}-\frac{\frac{\partial\delta}{\partial z}\frac{\partial\eta}{\partial z}}{\delta\left\{1+\left[\frac{\partial\delta}{\partial z}\right]^2\right\}^{\frac{3}{2}}}+\ldots \\ \ldots+\frac{-\frac{\partial^2\delta}{\partial z^2}}{\left\{1+\left[\frac{\partial\delta}{\partial z}\right]^2\right\}^{\frac{3}{2}}}-\frac{\frac{\partial^2\eta}{\partial z^2}}{\left\{1+\left[\frac{\partial\delta}{\partial z}\right]^2\right\}^{\frac{3}{2}}}+\frac{3\frac{\partial^2\delta}{\partial z^2}\frac{\partial\delta}{\partial z}\frac{\partial\eta}{\partial z}}{\left\{1+\left[\frac{\partial\delta}{\partial z}\right]^2\right\}^{\frac{5}{2}}} \tag{6.61}$$

After taking out the steady part given by Eq. (6.50), the unsteady part left is

$$\mathrm{K}' = -\frac{\eta}{\delta^2\left\{1+\left[\frac{\partial\delta}{\partial z}\right]^2\right\}^{\frac{1}{2}}}-\frac{\frac{\partial\delta}{\partial z}\frac{\partial\eta}{\partial z}}{\delta\left\{1+\left[\frac{\partial\delta}{\partial z}\right]^2\right\}^{\frac{3}{2}}}-\frac{\frac{\partial^2\eta}{\partial z^2}}{\left\{1+\left[\frac{\partial\delta}{\partial z}\right]^2\right\}^{\frac{3}{2}}}+\frac{3\frac{\partial^2\delta}{\partial z^2}\frac{\partial\delta}{\partial z}\frac{\partial\eta}{\partial z}}{\left\{1+\left[\frac{\partial\delta}{\partial z}\right]^2\right\}^{\frac{5}{2}}} \tag{6.62}$$

Expressing the free surface and the curvature disturbances in terms of the traveling Fourier waves, $\eta = \hat{\eta}e^{i(kz-\omega t)}$ and $\mathrm{K}' = \hat{\mathrm{K}}e^{i(kz-\omega t)}$, we can rewrite Eq. (6.62) as

$$\hat{\mathrm{K}} = -\frac{\hat{\eta}}{\delta^2\left\{1+\left[\frac{\partial\delta}{\partial z}\right]^2\right\}^{\frac{1}{2}}}-\frac{\frac{\partial\delta}{\partial z}ik\hat{\eta}}{\delta\left\{1+\left[\frac{\partial\delta}{\partial z}\right]^2\right\}^{\frac{3}{2}}}+\frac{k^2\hat{\eta}}{\left\{1+\left[\frac{\partial\delta}{\partial z}\right]^2\right\}^{\frac{3}{2}}}+\frac{3\frac{\partial^2\delta}{\partial z^2}\frac{\partial\delta}{\partial z}ik\hat{\eta}}{\left\{1+\left[\frac{\partial\delta}{\partial z}\right]^2\right\}^{\frac{5}{2}}}$$

and further rearrange to

$$\hat{\mathrm{K}} = \left[ -\frac{1}{\delta^2 \left\{ 1 + \left[ \frac{\partial \delta}{\partial z} \right]^2 \right\}^{\frac{1}{2}}} + \frac{-i\frac{k}{\delta}\frac{\partial \delta}{\partial z} + k^2}{\left\{ 1 + \left[ \frac{\partial \delta}{\partial z} \right]^2 \right\}^{\frac{3}{2}}} + \frac{3\frac{\partial^2 \delta}{\partial z^2}\frac{\partial \delta}{\partial z} ik}{\left\{ 1 + \left[ \frac{\partial \delta}{\partial z} \right]^2 \right\}^{\frac{5}{2}}} \right] \hat{\eta} \tag{6.63}$$

which shows the magnitude of the curvature disturbance in terms of the free surface disturbance amplitude $\hat{\eta}$. We will use this expression later on when defining the pressure balance at the gas-liquid interface due to the presence of surface tension.

### Gaseous Core Fluctuation

To derive the equations characterizing the unsteady axisymmetric gas core fluctuation, let us start with the axisymmetric Euler's equations:

$$\frac{u_{rg}}{r} + \frac{\partial u_{rg}}{\partial r} + \frac{\partial u_{zg}}{\partial z} = 0 \tag{6.64}$$

$$\frac{\partial u_{rg}}{\partial t} + u_{rg}\frac{\partial u_{rg}}{\partial r} - \frac{u_{\theta g}^2}{r} + u_{zg}\frac{\partial u_{rg}}{\partial z} = -\frac{1}{\rho_g}\frac{\partial p_g}{\partial r} \tag{6.65}$$

$$\frac{\partial u_{\theta g}}{\partial t} + u_{rg}\frac{\partial u_{\theta g}}{\partial r} + \frac{u_{rg}u_{\theta g}}{r} + u_{zg}\frac{\partial u_{\theta g}}{\partial z} = 0 \tag{6.66}$$

$$\frac{\partial u_{zg}}{\partial t} + u_{rg}\frac{\partial u_{zg}}{\partial r} + u_{zg}\frac{\partial u_{zg}}{\partial z} = -\frac{1}{\rho_g}\frac{\partial p_g}{\partial z} \tag{6.67}$$

where index $g$ denotes the gas core parameters, and $u_{rg}$, $u_{zg}$, and $u_{\theta g}$ are the velocity components in $r$, $z$, and $\theta$ directions respectively.

As we have mentioned above, at the steady state, the gaseous core does not move in the axial direction, $\bar{u}_{zg} = 0$, and its circumferential velocity is given by $\bar{u}_{\theta g} = \Omega r$, which implies that $\frac{\partial \bar{p}_g}{\partial z} = 0$ and $\frac{\partial \bar{u}_{\theta g}}{\partial z} = 0$. Consequently, from Eq. (6.64) we see that $\bar{u}_{rg} = 0$, and from Eq. (6.65) – that $\Omega^2 r = \frac{1}{\rho_g}\frac{\partial \bar{p}_g}{\partial r}$.

Considering these steady state relations, at the disturbed state, we can rewrite Eqs. (6.64)–(6.67) as follows. The instantaneous continuity Eq. (6.64) becomes

$$\frac{u'_{rg}}{r} + \frac{\partial u'_{rg}}{\partial r} + \frac{\partial u'_{zg}}{\partial z} = 0 \tag{6.68}$$

The radial momentum Eq. (6.65) becomes

$$\frac{\partial u'_{rg}}{\partial t} + u'_{rg}\frac{\partial u'_{rg}}{\partial r} - \frac{\left(\Omega r + u'_{\theta g}\right)^2}{r} + u'_{zg}\frac{\partial u'_{rg}}{\partial z} = -\frac{1}{\rho_g}\frac{\partial \bar{p}_g}{\partial r} - \frac{1}{\rho_g}\frac{\partial p'_g}{\partial r}$$

Which after cancellation of the higher order and the steady state terms can be rewritten as

$$\frac{\partial u'_{rg}}{\partial t} - 2\Omega u'_{\theta g} = -\frac{1}{\rho_g}\frac{\partial p'_g}{\partial r} \tag{6.69}$$

The angular momentum Eq. (6.66) turns into

$$\frac{\partial u'_{\theta g}}{\partial t} + u'_{rg}\frac{\partial \left(\Omega r + u'_{\theta g}\right)}{\partial r} + \frac{u'_{rg}\left(\Omega r + u'_{\theta g}\right)}{r} + u'_{zg}\frac{\partial u'_{\theta g}}{\partial z} = 0$$

which, if we neglect the higher order terms, gives

$$\frac{\partial u'_{\theta g}}{\partial t} + 2\Omega u'_{rg} = 0 \tag{6.70}$$

Finally, the axial momentum Eq. (6.67) at the disturbed state is

$$\frac{\partial u'_{zg}}{\partial t} + u'_{rg}\frac{\partial u'_{zg}}{\partial r} + u'_{zg}\frac{\partial u'_{zg}}{\partial z} = -\frac{1}{\rho_g}\frac{\partial p'_g}{\partial z}$$

which can be rewritten in the first order approximation as

$$\frac{\partial u'_{zg}}{\partial t} = -\frac{1}{\rho_g}\frac{\partial p'_g}{\partial z} \tag{6.71}$$

Assuming the following Fourier form of the disturbances of the velocity components and the pressure,

$$u'_{rg} = \hat{u}_{rg}e^{i(kz-\omega t)},\ u'_{zg} = \hat{u}_{zg}e^{i(kz-\omega t)},\ u'_{\theta g} = \hat{u}_{\theta g}e^{i(kz-\omega t)},\ p'_g = \hat{p}_g e^{i(kz-\omega t)}$$

we can rewrite Eqs. (6.68)–(6.71) as

$$\frac{\hat{u}_{rg}}{r} + \frac{\partial \hat{u}_{rg}}{\partial r} + ik\hat{u}_{zg} = 0 \tag{6.72}$$

$$-i\omega\hat{u}_{rg} - 2\Omega\hat{u}_{\theta g} = -\frac{1}{\rho_g}\frac{\partial \hat{p}_g}{\partial r} \tag{6.73}$$

$$-i\omega\hat{u}_{\theta g} + 2\Omega\hat{u}_{rg} = 0 \tag{6.74}$$

$$-i\omega\hat{u}_{zg} = -\frac{1}{\rho_g}ik\hat{p}_g \tag{6.75}$$

Note that it is assumed that the amplitudes of disturbances, $\hat{u}_{rg}$, $\hat{u}_{zg}$, $\hat{u}_{\theta g}$, and $\hat{p}_g$, are some unknown functions of $r$. To find a solution for these functions, let us first express $\hat{u}_{\theta g}$ through $\hat{u}_{rg}$ from Eq. (6.74)

$$\hat{u}_{\theta g} = 2\frac{\Omega}{i\omega}\hat{u}_{rg} = -2i\frac{\Omega}{\omega}\hat{u}_{rg}$$

Plugging this into Eq. (6.73), we have

$$-\frac{1}{\rho_g}\frac{\partial \hat{p}_g}{\partial r} = -i\omega\hat{u}_{rg} + 4i\frac{\Omega^2}{\omega}\hat{u}_{rg} = i\omega\hat{u}_{rg}\left(\frac{4\Omega^2}{\omega^2} - 1\right)$$

Now let us use this expression in the radial derivative of Eq. (6.75) as

$$-i\omega\frac{\partial \hat{u}_{zg}}{\partial r} = ik\left(-\frac{1}{\rho_g}\frac{\partial \hat{p}_g}{\partial r}\right) = -k\omega\hat{u}_{rg}\left(\frac{4\Omega^2}{\omega^2} - 1\right)$$

where from $\hat{u}_{rg}$ is given by

$$\hat{u}_{rg} = i\frac{1}{k\left(\frac{4\Omega^2}{\omega^2} - 1\right)}\frac{\partial \hat{u}_{zg}}{\partial r} \tag{6.76}$$

Lastly, we can insert this result into Eq. (6.72) to have

$$i\frac{1}{k\left(\frac{4\Omega^2}{\omega^2} - 1\right)}\frac{\partial^2 \hat{u}_{zg}}{\partial r^2} + i\frac{1}{k\left(\frac{4\Omega^2}{\omega^2} - 1\right)}\frac{1}{r}\frac{\partial \hat{u}_{zg}}{\partial r} + ik\hat{u}_{zg} = 0$$

which can be rearranged to become the standard Bessel's equation

$$\frac{\partial^2 \hat{u}_{zg}}{\partial r^2} + \frac{1}{r}\frac{\partial \hat{u}_{zg}}{\partial r} - k^2\left(1 - \frac{4\Omega^2}{\omega^2}\right)\hat{u}_{zg} = 0 \tag{6.77}$$

Introducing a new variable

$$\mu = k\sqrt{1 - \frac{4\Omega^2}{\omega^2}} \tag{6.78}$$

we can write the general solution to the Bessel's Eq. (6.77) in the form

$$\hat{u}_{zg}(r) = MI_0(\mu r) + NK_0(\mu r)$$

where $M$ and $N$ are arbitrary constants. Since the solution has to be bounded at $r = 0$, $N$ has to be zero, hence

$$\hat{u}_{zg}(r) = MI_0(\mu r) \tag{6.79}$$

And, based on Eq. (6.75), we also have

$$\hat{p}_g(r) = \frac{\omega}{k}\rho_g \hat{u}_{zg} = \frac{\omega}{k}\rho_g M I_0(\mu r) \tag{6.80}$$

We can find $M$ in Eqs. (6.79) and (6.80), if we recall that the kinematic boundary condition [71, Sec. 6.1] applies at the gas-liquid interface, $r = \delta$,

$$\begin{aligned}\frac{D[r-(\delta+\eta)]}{Dt} &= \frac{\partial(r-\delta-\eta)}{\partial t} + \dots \\ &\quad \dots + \left(u'_{rg}, \Omega\delta + u'_{\theta g}, u'_{zg}\right) \cdot \left(\frac{\partial(r-\delta-\eta)}{\partial r}, 0, \frac{\partial(r-\delta-\eta)}{\partial z}\right) = \\ &= -\frac{\partial\eta}{\partial t} + u'_{rg}\left(1 - \frac{\partial\delta}{\partial r}\right) + u'_{zg}\left(-\frac{\partial\delta}{\partial z} - \frac{\partial\eta}{\partial z}\right) = \\ &= -\frac{\partial\eta}{\partial t} + u'_{rg} - u'_{rg}\frac{\partial\delta}{\partial r} - u'_{zg}\frac{\partial\delta}{\partial z} = 0\end{aligned}$$

From Chapter 3, we know that the radial gradient of the steady free surface radius is much smaller than the axial, and, therefore, we can assume that

$$\left|u'_{rg}\frac{\partial\delta}{\partial r}\right| \ll \left|u'_{zg}\frac{\partial\delta}{\partial z}\right|$$

which allows us to reduce the last expression above to

$$-\frac{\partial\eta}{\partial t} + u'_{rg} - u'_{zg}\frac{\partial\delta}{\partial z} = 0$$

In the wave amplitude form, this equation looks like

$$+i\omega\hat{\eta} + \hat{u}_{rg} - \hat{u}_{zg}\frac{\partial\delta}{\partial z} = 0$$

We can substitute the dependence of $\hat{u}_{rg}$ on $\hat{u}_{zg}$ from Eq. (6.76) in here to get

$$i\omega\hat{\eta} + i\frac{1}{k\left(\frac{4\Omega^2}{\omega^2} - 1\right)}\frac{\partial\hat{u}_{zg}}{\partial r} - \hat{u}_{zg}\frac{\partial\delta}{\partial z} = 0$$

and further substitute the solution for $\hat{u}_{zg}$ from Eq. (6.79),

$$i\omega\hat{\eta} + i\frac{1}{k\left(\frac{4\Omega^2}{\omega^2} - 1\right)}M\mu I_1(\mu\delta) - M I_0(\mu\delta)\frac{\partial\delta}{\partial z} = 0$$

By substituting the value of $\mu$ from Eq. (6.78), and rearranging, we can rewrite this equation as

$$M\left[-i\frac{k\sqrt{1-\frac{4\Omega^2}{\omega^2}}I_1\left(\mu\delta\right)}{k\left(1-\frac{4\Omega^2}{\omega^2}\right)}-I_0\left(\mu\delta\right)\frac{\partial\delta}{\partial z}\right]=-i\omega\hat{\eta}$$

which yields the sought expression for $M$:

$$M=\frac{i\omega\hat{\eta}}{i\frac{I_1\left(\mu\delta\right)}{\sqrt{1-\frac{4\Omega^2}{\omega^2}}}+I_0\left(\mu\delta\right)\frac{\partial\delta}{\partial z}} \tag{6.81}$$

**Liquid Body Fluctuation**

For the liquid flow setup considered in this problem, we can apply the same Laplace's equation and kinematic boundary condition as in Section 4.3, which are given by

$$\frac{\partial^2\phi}{\partial r^2}+\frac{1}{r}\frac{\partial\phi}{\partial r}+\frac{\partial^2\phi}{\partial z^2}=0$$

$$\frac{D}{Dt}\left(r-\left(\delta+\eta\right)\right)=0$$

If the velocity potential disturbance is assumed to have the form $\phi'=\hat{\phi}\left(r\right)e^{i(kz-\omega t)}$, then, following the derivation in Section 4.3, we know that these equations lead to the solution given by

$$\hat{\phi}=A\left[I_0\left(kr\right)+\beta K_0\left(kr\right)\right] \tag{6.82}$$

where

$$A=\frac{i\left(k\frac{\partial\bar{\phi}}{\partial z}-\omega\right)}{\gamma}\hat{\eta} \tag{6.83}$$

$$\gamma=k\left\{\left[I_1\left(k\delta\right)-\beta K_1\left(k\delta\right)\right]-i\left[I_0\left(k\delta\right)+\beta K_0\left(k\delta\right)\right]\frac{d\delta}{dz}\right\} \tag{6.84}$$

$$\beta=\frac{I_1\left(kR\right)+iI_0\left(kR\right)\tan\left(\alpha\right)}{K_1\left(kR\right)-iK_0\left(kR\right)\tan\left(\alpha\right)} \tag{6.85}$$

and $R$ and $\alpha$ are respectively the solid boundary radius and its slope as shown in Fig. 6.4.

The unsteady Bernoulli's equation at the free surface, $r = \delta$, however, is now different, because we have the additional pressure term at the liquid side of the interface, $p_l$, created by the presence of the gaseous core,

$$\frac{\partial \phi}{\partial t} + \frac{p_l}{\rho_l} + \frac{1}{2}\left[\left(\frac{\partial \phi}{\partial r}\right)^2 + \left(\frac{\partial \phi}{\partial z}\right)^2 + \frac{C^2}{(\delta+\eta)^2}\right] = \frac{1}{2}\left[\bar{u}_z^2 + \bar{u}_r^2 + \frac{C^2}{\delta^2}\right] + \frac{\bar{p}_l}{\rho_l}$$

Similarly to Section 4.3, this equation can be decomposed into the steady and unsteady parts as

$$\frac{\partial \phi'}{\partial t} + \frac{\bar{p}_l}{\rho_l} + \frac{p_l'}{\rho_l} + \frac{1}{2}\left[\left(\frac{\partial \bar{\phi}}{\partial z}\right)^2 + 2\frac{\partial \bar{\phi}}{\partial z}\frac{\partial \phi'}{\partial z} + \left(\frac{\partial \bar{\phi}}{\partial r}\right)^2 + 2\frac{\partial \bar{\phi}}{\partial r}\frac{\partial \phi'}{\partial r} + \frac{C^2}{\delta^2} - 2\frac{C^2}{\delta^3}\eta\right] = \\ = \frac{1}{2}\left[\bar{u}_z^2 + \bar{u}_r^2 + \frac{C^2}{\delta^2}\right] + \frac{\bar{p}_l}{\rho_l}$$

As in the gaseous core analysis above, since the radial gradients of the steady velocity potential are assumed to be much smaller than the axial, we have the condition

$$\left|\frac{\partial \bar{\phi}}{\partial r}\frac{\partial \phi'}{\partial r}\right| \ll \left|\frac{\partial \bar{\phi}}{\partial z}\frac{\partial \phi'}{\partial z}\right|$$

After applying this condition to the last equation and canceling the steady state terms, we arrive at

$$\frac{\partial \phi'}{\partial t} + \frac{p_l'}{\rho_l} + \frac{\partial \bar{\phi}}{\partial z}\frac{\partial \phi'}{\partial z} - \frac{C^2}{\delta^3}\eta = 0$$

which in the traveling Fourier wave form can be written as

$$\hat{\phi}\,(-i\omega) + \frac{\hat{p}_l}{\rho_l} + \frac{\partial \bar{\phi}}{\partial z} ik\hat{\phi} - \frac{C^2}{\delta^3}\hat{\eta} = 0$$

This equation yields the dependence of the velocity potential, $\phi$, on the free surface disturbance, $\eta$, and the pressure at the liquid side of the gas-liquid interface, $p_l$:

$$\hat{\phi} = \frac{\dfrac{C^2}{\delta^3}\hat{\eta} - \dfrac{\hat{p}_l}{\rho_l}}{i\left(k\dfrac{\partial \bar{\phi}}{\partial z} - \omega\right)}$$

Equating this equation to Eq. (6.82), we have

$$\frac{i\left(k\dfrac{\partial \bar{\phi}}{\partial z} - \omega\right)\hat{\eta}}{\gamma}\left[I_0(k\delta) + \beta K_0(k\delta)\right] = \frac{\dfrac{C^2}{\delta^3}\hat{\eta} - \dfrac{\hat{p}_l}{\rho_l}}{i\left(k\dfrac{\partial \bar{\phi}}{\partial z} - \omega\right)} \tag{6.86}$$

**Dispersion Relation**

The pressure fluctuations at the gas-liquid interface are related through the surface tension as

$$\hat{p}_l = \hat{p}_g - \sigma\hat{\mathrm{K}} \tag{6.87}$$

where the amplitude of the surface curvature fluctuation, $\hat{\mathrm{K}}$, is given by Eq. (6.63), and $\sigma$ is the surface tension coefficient. Also, at the interface, we should have a continuity of the circumferential velocity, $u_\theta$, meaning that $C/\delta = \Omega\delta$, where from $\Omega = C/\delta^2$. Formally then, $\Omega$ has to be variable to track the changes in $\delta$. However, in this study, since the overall variation of the steady free surface radius is not large, we will simply assume that it is constant and given by $C/r_v^2$.

Substituting for $\hat{p}_g$ from Eq. (6.80), and considering Eq. (6.87), we can rewrite Eq. (6.86) as

$$\frac{i\left(k\dfrac{\partial\bar{\phi}}{\partial z}-\omega\right)\hat{\eta}}{\gamma}\left[I_0\left(k\delta\right)+\beta K_0\left(k\delta\right)\right] = \frac{\dfrac{C^2}{\delta^3}\hat{\eta}-\dfrac{1}{\rho_l}\left(\dfrac{\omega}{k}\rho_g M I_0\left(\mu\delta\right)-\sigma\hat{\mathrm{K}}\right)}{i\left(k\dfrac{\partial\bar{\phi}}{\partial z}-\omega\right)}$$

which we can rearrange as

$$\left(k\frac{\partial\bar{\phi}}{\partial z}-\omega\right)^2 = \frac{\dfrac{C^2}{\delta^3}\hat{\eta}-\dfrac{1}{\rho_l}\left(\dfrac{\omega}{k}\rho_g M I_0\left(\mu\delta\right)-\sigma\hat{\mathrm{K}}\right)}{\hat{\eta}\left[I_0\left(k\delta\right)+\beta K_0\left(k\delta\right)\right]}\frac{\gamma}{i^2}$$

This yields the sought dispersion equation in its preliminary form:

$$\frac{\omega}{k} = \frac{\partial\bar{\phi}}{\partial z} \pm \sqrt{\frac{\gamma}{k^2}\frac{\dfrac{1}{\rho_l}\left(\dfrac{\omega}{k}\rho_g M I_0\left(\mu\delta\right)-\sigma\hat{\mathrm{K}}\right)-\dfrac{C^2}{\delta^3}\hat{\eta}}{\hat{\eta}\left[I_0\left(k\delta\right)+\beta K_0\left(k\delta\right)\right]}} \tag{6.88}$$

Notice how this equation explicitly includes the densities of the gaseous and liquid phases along with the surface tension coefficient.

Let us bring this equation to its final form by plugging in the coefficients $\gamma$ and $\beta$ from Eqs. (6.84) and (6.85), the coefficient $M$ from Eq. (6.81), and the amplitude

of the surface curvature fluctuation, $\hat{\mathrm{K}}$, from Eq. (6.63). Substituting first for $\gamma$ and then for $M$, we have

$$\frac{\omega}{k} = \frac{\partial\bar{\phi}}{\partial z} \pm \left[ \frac{k\left\{ \left[ I_1(k\delta) - \beta K_1(k\delta) \right] - i\left[ I_0(k\delta) + \beta K_0(k\delta) \right] \frac{d\delta}{dz} \right\}}{k^2 \left[ I_0(k\delta) + \beta K_0(k\delta) \right]} \times \right.$$
$$\left. \times \frac{1}{\hat{\eta}} \left( \frac{1}{\rho_l} \left( \frac{\omega}{k} \rho_g M I_0(\mu\delta) - \sigma\hat{\mathrm{K}} \right) - \frac{C^2}{\delta^3}\hat{\eta} \right) \right]^{\frac{1}{2}}$$

$$\frac{\omega}{k} = \frac{\partial\bar{\phi}}{\partial z} \pm \left[ \frac{1}{k} \left\{ \frac{I_1(k\delta) - \beta K_1(k\delta)}{I_0(k\delta) + \beta K_0(k\delta)} - i\frac{d\delta}{dz} \right\} \times \right.$$
$$\left. \times \frac{1}{\hat{\eta}} \left\{ \frac{1}{\rho_l} \left( \frac{\omega}{k} \rho_g \frac{i\omega\hat{\eta}}{i\dfrac{I_1(\mu\delta)}{\sqrt{1 - \dfrac{4\Omega^2}{\omega^2}}} + I_0(\mu\delta)\dfrac{\partial\delta}{\partial z}} I_0(\mu\delta) - \sigma\hat{\mathrm{K}} \right) - \frac{C^2}{\delta^3}\hat{\eta} \right\} \right]^{\frac{1}{2}}$$

Substituting next for $\beta$ and $\hat{\mathrm{K}}$, we obtain

$$\frac{\omega}{k} = \frac{\partial\bar{\phi}}{\partial z} \pm \ldots$$
$$\ldots \pm \left[ \frac{1}{k} \left( \frac{I_1(k\delta) - \dfrac{I_1(kR) + iI_0(kR)\tan(\alpha)}{K_1(kR) - iK_0(kR)\tan(\alpha)} K_1(k\delta)}{I_0(k\delta) + \dfrac{I_1(kR) + iI_0(kR)\tan(\alpha)}{K_1(kR) - iK_0(kR)\tan(\alpha)} K_0(k\delta)} - i\frac{d\delta}{dz} \right) \left( K_{\rho\sigma} - \frac{C^2}{\delta^3} \right) \right]^{\frac{1}{2}} \tag{6.89}$$

where we have represented the terms due to the inertial and capillary effects by a single correction term $K_{\rho\sigma}$ given by

$$K_{\rho\sigma} = \frac{\rho_g}{\rho_l} \frac{\omega^2}{k} \frac{iI_0(\mu\delta)}{i\dfrac{I_1(\mu\delta)}{\sqrt{1 - \dfrac{4\Omega^2}{\omega^2}}} + I_0(\mu\delta)\dfrac{\partial\delta}{\partial z}} - \ldots$$
$$\ldots - \frac{\sigma}{\rho_l} \left[ -\frac{1}{\delta^2 \left\{ 1 + \left[ \dfrac{\partial\delta}{\partial z} \right]^2 \right\}^{\frac{1}{2}}} + \frac{-i\dfrac{k}{\delta}\dfrac{\partial\delta}{\partial z} + k^2}{\left\{ 1 + \left[ \dfrac{\partial\delta}{\partial z} \right]^2 \right\}^{\frac{3}{2}}} + \frac{3\dfrac{\partial^2\delta}{\partial z^2}\dfrac{\partial\delta}{\partial z} ik}{\left\{ 1 + \left[ \dfrac{\partial\delta}{\partial z} \right]^2 \right\}^{\frac{5}{2}}} \right] \tag{6.90}$$

Notice that, if we neglect the gas density, then the first term in this expression will disappear. Similarly, if the surface tension is neglected, then the second term goes away. Lastly, if both the inertia of gas and the surface tension at the gas-liquid interface are neglected, then the whole correction term $K_{\rho\sigma}$ shrinks to zero.

To conclude, let us change the signs in Eq. (6.89) so that it becomes comparable to the previous dispersion Eq. (6.14), which did not account for the inertial and capillary effects of the gaseous core. Then, the final form of the dispersion relation can be written as

$$\frac{\omega}{k} = \frac{\partial \bar{\phi}}{\partial z} \pm \ldots \\ \ldots \left[ \frac{1}{k} \left( \frac{-I_1(k\delta) + \dfrac{I_1(kR) + iI_0(kR)\tan(\alpha)}{K_1(kR) - iK_0(kR)\tan(\alpha)} K_1(k\delta)}{I_0(k\delta) + \dfrac{I_1(kR) + iI_0(kR)\tan(\alpha)}{K_1(kR) - iK_0(kR)\tan(\alpha)} K_0(k\delta)} + i\frac{d\delta}{dz} \right) \left( \frac{C^2}{\delta^3} - K_{\rho\sigma} \right) \right]^{\frac{1}{2}} \tag{6.91}$$

where $\mu$ is defined in Eq. (6.78), which we rewrite here for convenience

$$\mu = k\sqrt{1 - \frac{4\Omega^2}{\omega^2}}$$

### 6.3.2 Injector Response due to Kelvin's Waves Considering Inertial and Capillary Effects of Gaseous Core

If we follow the derivation of the injector response in Section 6.2, we can conclude that, when we do account for the inertial and capillary effects of the gaseous core, we can use the same equations that were outlined in Subsections 6.2.1–6.2.4, with the only difference that, now, the wave numbers at the head end, $k_{he}$, at the end of the head end region, $k_v$, and at the nozzle exit, $k_n$, have to be calculated by employing the modified dispersion relation given by Eq. (6.91).

Continuing the logic of Section 6.2, we need first to reduce the complete dispersion Eq. (6.91) to the form valid in the case when the solid boundary and the free surface

radii are constant, i.e. $\alpha = 0$ and $d\delta/dz = 0$, and when there are only downstream traveling waves. This simplifies Eq. (6.91) to

$$\frac{\omega}{k} = \frac{\partial\bar{\phi}}{\partial z} + \left[\frac{1}{k}\left(\frac{-I_1(k\delta) + \dfrac{I_1(kR)}{K_1(kR)}K_1(k\delta)}{I_0(k\delta) + \dfrac{I_1(kR)}{K_1(kR)}K_0(k\delta)}\right)\left(\frac{C^2}{\delta^3} - K_{\rho\sigma}\right)\right]^{\frac{1}{2}} \tag{6.92}$$

where the correction term due to the gas-liquid density difference and the surface tension between them is now given by

$$K_{\rho\sigma} = \frac{\rho_g}{\rho_l}\frac{\omega^2}{k}\frac{I_0(\mu\delta)}{\dfrac{I_1(\mu\delta)}{\sqrt{1-\dfrac{4\Omega^2}{\omega^2}}}} - \frac{\sigma}{\rho_l}\left[-\frac{1}{\delta^2} + k^2\right] \tag{6.93}$$

The $\mu$ coefficient in Eq. (6.93) remains the same as given in Eq. (6.78).

Note that both Eqs. (6.92) and (6.93) are nondimensional. The dimensional form of them would be written as

$$\frac{\omega\dfrac{W_{in}^*}{R_n^*}}{\dfrac{k}{R_n^*}} = \frac{\partial\bar{\phi}}{\partial z}W_{in}^* + \ldots$$

$$\ldots + \left[\frac{R_n^*}{k}\left(\frac{-I_1(k\delta)\dfrac{I_1(kR)}{K_1(kR)}K_1(k\delta)}{I_0(k\delta) + \dfrac{I_1(kR)}{K_1(kR)}K_0(k\delta)}\right)\left(\frac{C^2(W_{in}^*R_n^*)^2}{\delta^3(R_n^*)^3} - K_{\rho\sigma}K_{\rho\sigma}^*\right)\right]^{\frac{1}{2}}$$

where

$$K_{\rho\sigma}K_{\rho\sigma}^* = \frac{\rho_g\rho_l^*}{1\cdot\rho_l^*}\frac{\omega^2\left(\dfrac{W_{in}^*}{R_n^*}\right)^2}{\dfrac{k}{R_n^*}}\frac{I_0(\mu\delta)}{\dfrac{I_1(\mu\delta)}{\sqrt{1-\dfrac{4\Omega^2}{\omega^2}}}} - \frac{1\cdot\sigma^*}{1\cdot\rho_l^*}\frac{1}{(R_n^*)^2}\left[-\frac{1}{\delta^2} + k^2\right]$$

where we have assumed that the nondimensional liquid density, $\rho_l$, and surface coefficient, $\sigma$, are both simply equal to 1. Then the last equation can be rewritten in the more familiar nondimensional form than in Eq. (6.93), through the Weber number:

$$K_{\rho\sigma} = \rho_g\frac{\omega^2}{k}\frac{I_0(\mu\delta)}{\dfrac{I_1(\mu\delta)}{\sqrt{1-\dfrac{4\Omega^2}{\omega^2}}}} - \frac{1}{We}\left[-\frac{1}{\delta^2} + k^2\right] \tag{6.94}$$

where the Weber number is defined as $We = \dfrac{\rho_l^* (W_{in}^*)^2 R_n^*}{\sigma^*}$.

According to these changes, let us rewrite the implicit expressions (6.15), (6.16), and (6.35), which we needed to determine $k_{he}$, $k_v$, and $k_n$.

- Wave number at the head end, $z = 0$:

$$\frac{\omega}{k_{he}} = \sqrt{\frac{1}{k_{he}} \frac{-I_1(k_{he}r_{he}) + \dfrac{I_1(k_{he}R_v)}{K_1(k_{he}R_v)} K_1(k_{he}r_{he})}{I_0(k_{he}r_{he}) + \dfrac{I_1(k_{he}R_v)}{K_1(k_{he}R_v)} K_0(k_{he}r_{he})} \left( \frac{C^2}{r_{he}^3} - K_{\rho\sigma.he} \right)} \tag{6.95}$$

where

$$K_{\rho\sigma.he} = \rho_g \frac{\omega^2}{k_{he}} \frac{I_0(\mu_{he}r_{he})}{\dfrac{I_1(\mu_{he}r_{he})}{\sqrt{1 - \dfrac{4\Omega^2}{\omega^2}}}} - \frac{1}{We} \left[ -\frac{1}{r_{he}^2} + k_{he}^2 \right]$$

$$\mu_{he} = k_{he} \sqrt{1 - \frac{4\Omega^2}{\omega^2}}$$

- Wave number at the end of the head end region, $z = 2R_t$:

$$\frac{\omega}{k_v} = \bar{u}_{zv} + \sqrt{\frac{1}{k_v} \frac{-I_1(k_v r_v) + \dfrac{I_1(k_v R_v)}{K_1(k_v R_v)} K_1(k_v r_v)}{I_0(k_v r_v) + \dfrac{I_1(k_v R_v)}{K_1(k_v R_v)} K_0(k_v r_v)} \left( \frac{C^2}{r_v^3} - K_{\rho\sigma.v} \right)} \tag{6.96}$$

where

$$K_{\rho\sigma.v} = \rho_g \frac{\omega^2}{k_v} \frac{I_0(\mu_v r_v)}{\dfrac{I_1(\mu_v r_v)}{\sqrt{1 - \dfrac{4\Omega^2}{\omega^2}}}} - \frac{1}{We} \left[ -\frac{1}{r_v^2} + k_v^2 \right]$$

$$\mu_v = k_v \sqrt{1 - \frac{4\Omega^2}{\omega^2}}$$

- Wave number at the nozzle exit, $z = L_v + L_c + L_n$:

$$\frac{\omega}{k_n} = \bar{u}_{zn} + \sqrt{\frac{1}{k_n} \frac{-I_1(k_n r_n) + \dfrac{I_1(k_n R_n)}{K_1(k_n R_n)} K_1(k_n r_n)}{I_0(k_n r_n) + \dfrac{I_1(k_n R_n)}{K_1(k_n R_n)} K_0(k_n r_n)} \left( \frac{C^2}{r_n^3} - K_{\rho\sigma.n} \right)} \tag{6.97}$$

where

$$K_{\rho\sigma.n} = \rho_g \frac{\omega^2}{k_n} \frac{I_0(\mu_n r_n)}{I_1(\mu_n r_n)} \sqrt{1 - \frac{4\Omega^2}{\omega^2}} - \frac{1}{We}\left[-\frac{1}{r_n^2} + k_n^2\right]$$

$$\mu_n = k_n \sqrt{1 - \frac{4\Omega^2}{\omega^2}}$$

## 6.4 Results

Let us apply the equations derived in this chapter to the injector whose response in shown in Bazarov [1, Fig. 23] and in Fig. 2.7 of this dissertation, and parameters are given in Table 2.4 in Chapter 2.

To start, we will compare the injector response which follows from our Kelvin's wave model and its long wave limit, derived in Section 6.2, with the injector response following from Bazarov's theory, which we have investigated in depth in Chapter 2 and Appendix A. This comparison is shown in Fig. 6.5.

Notice that we are showing two results for Bazarov's response: with and without wave reflections. Bazarov's response without reflections can be calculated, if in the response functions $\Pi_{v2}$ and $\Pi_{vn}$ in Chapter 2, we set the number of reflections to be equal to zero. The response due to Bazarov calculated without reflections is of more interest for us in this particular comparison, since we do not have the reflections either in this chapter. Nevertheless, it is of instructive interest to see the original Bazarov's response calculated with wave reflections. We can immediately see that the absence of reflections has "flattened" the original Bazarov's response with reflections, which is expected, since the presence of reflections makes the amplitude of free surface fluctuation in the vortex chamber of the injector larger.

Also in Fig. 6.5, we can see that our responses which account only for downstream traveling waves, both in Kelvin's wave form and its long wave limit, lie lower than the response (without reflections) predicted by Bazarov's theory. This may be directly attributed to the fact that Bazarov's response still includes the response functions due

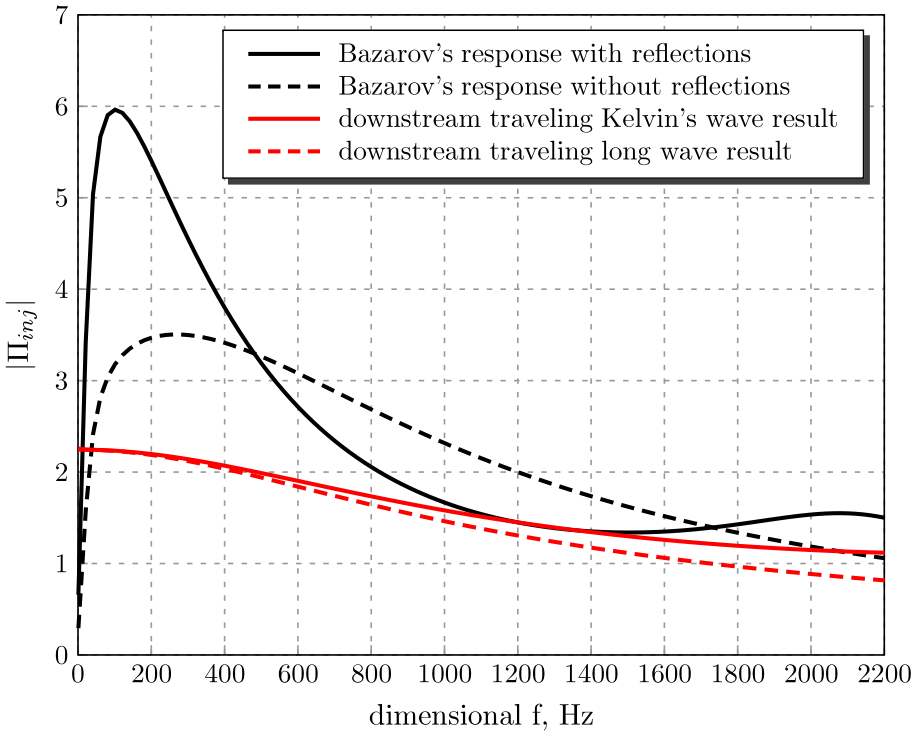


Figure 6.5.: Comparison between injector responses following from Section 6.2 and Bazarov's theory (injector parameters described in Table 2.4)

to vorticity waves, or to the "incorrect" choice of the artificial viscosity coefficient on our side. Finally, note that, at the long wave limit, we are getting lower response than the response which follows from the general Kelvin's waves. This may be seen from the perspective that, when we have long disturbance waves traveling on the core of the injector, the flow is less excited in the radial direction than when we have general Kelvin's waves, which, in turn, causes less nozzle mass flow rate oscillation in the first case compared to the second.

Next, we take the injector response result due to downstream Kelvin's waves, shown as a solid red line in Fig. 6.5, and investigate its sensitivity to the gas density and surface tension variation due to the correction factor, $K_{\rho\sigma}$, derived in Section 6.3, Fig. 6.6 and 6.7.

The gas density is varied from 0.1% to 75% of the liquid desnity. Note that the 0.1% case represents approximately an air-water case at sea level and $20°C$, and high pressure combustors may have values as high as 10%. In Fig. 6.6, we can see that the 0.1% case (black line) overlaps with the 1% case (blue line), and so, we do not see any significant changes in the injector response up to the case when the gas density becomes 10% of the liquid density.

To put this conclusion into perspective, let us consider an example of equilibrium combustion of liquid oxygen (LOX) and gaseous hydrogen (GH2) in a hypothetical injector, which consists of two types of injector elements: the swirl elements that inject the LOX, and the plain orifice elements that inject the GH2. For simplicity, take the injection temperatures to be $90.19°K$ for LOX and $25°C$ for GH2, and the injection pressures to be 1 $atm$ for both of them. Further, let the oxidizer to fuel

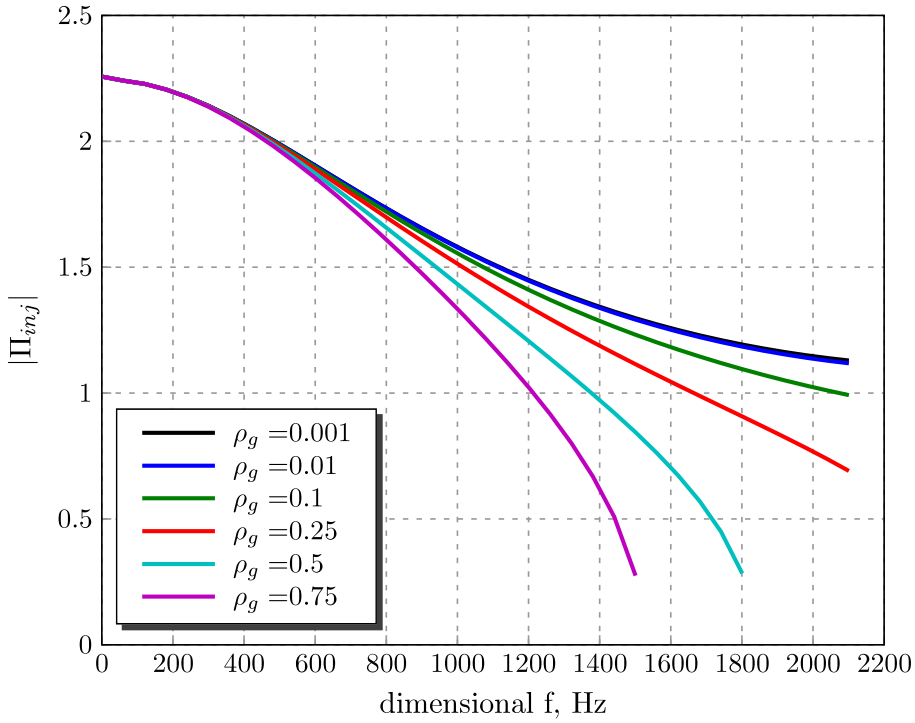


Figure 6.6.: Injector response sensitivity to gas density variation due to Section 6.3 (injector parameters described in Table 2.4)

ratio be 3.9. For these conditions, if we consider the equilibrium combustion at a chamber pressure of 3000 $psia$, the Air Force Chemical Equilibrium Specific Impulse Code gives the adiabatic chamber temperature of $3102.7°K$ and the molecular weight of products equal to 9.807 $kg/kmol$. These products are assumed to fill the gaseous cores of the swirl elements. Applying the ideal gas law, this results in the combustion products' density equal to 7.863 $kg/m^3$. Now, at its injection conditions, the LOX has the density of 1141 $kg/m^3$, which gives for the products to LOX density ratio of 0.7%. Then, considering the above result, we can say that for this propellant combination, the injector response can be calculated without accounting for inertial effects of the gaseous core.

The surface tension coefficient, $\sigma^*$, is varied from $1 \cdot \sigma_0^*$ to $10^4 \cdot \sigma_0^*$, where $\sigma_0^* = 0.0728\ N/m$ is the baseline surface tension coefficient, which is taken equal to that between air and water at sea level and $20°C$. For the injector described in Table 2.4, this gives the baseline Weber number of 2991.4. In Fig. 6.7, we can observe that the response is not affected by the surface tension up to the very last case (all lines from black to red overlap), when it becomes $10^4$ times larger than the baseline. This tells us that, in general, we can feel confident to omit the consideration of the capillary effects in the injector response calculations altogether.

## 6.5 Conclusions and Discussion

In this chapter, we have considered a hypothetical problem, when we assume that the disturbance waves in the swirl injector travel only downstream and do not experience the reflections as they propagate from the point of initiation to the nozzle exit. The form of waves was taken to be of the general Kelvin's type with the intention to obtain a mathematical description of this problem valid in the entire range of the wave lengths.

By neglecting the reflected waves, we could use the results of Chapter 4 to derive the expressions for the unsteady fluctuation of the injector pressure drop and nozzle

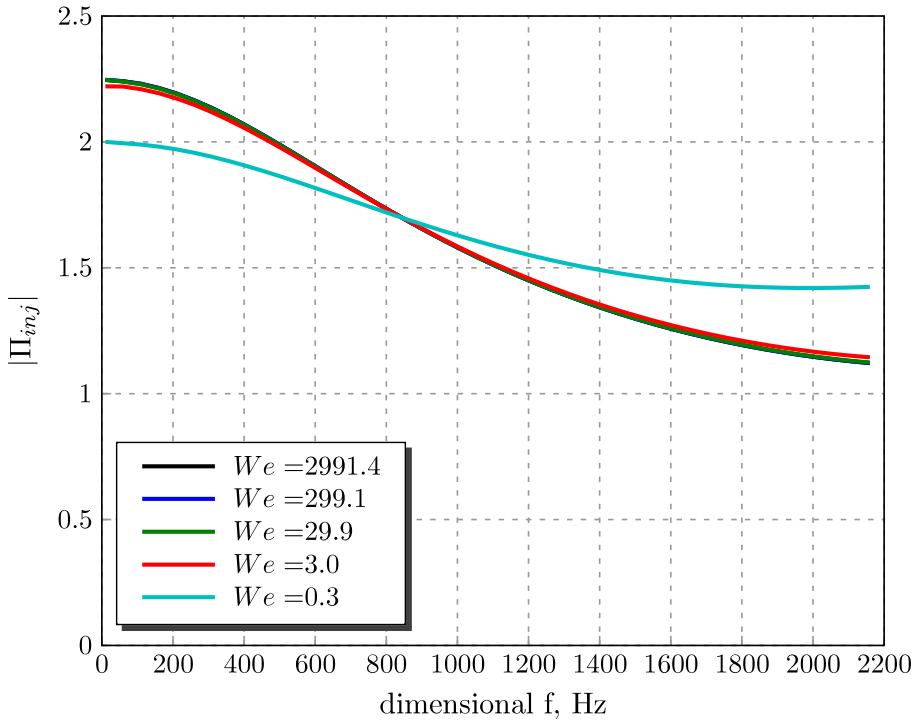


Figure 6.7.: Injector response sensitivity to surface tension coefficient variation due to Section 6.3 (injector parameters described in Table 2.4)

exit mass flow rate, which are directly involved in the calculation of the injector response. In these expressions, we have considered the head end region and the nozzle region of the injector to be cylindrical, and thus we were able to use the simplified dispersion equation that does not include the refractive terms.

Within this setup, as a first task, we have derived the injector response that does account for the presence of the gaseous core, and then made an assessment of that response at the long wave limit, Section 6.2. In the second task, we have questioned what would be the influence of the inertial and capillary effects of the gaseous core, if it would be taken into account, Section 6.3. This resulted in a conclusion that we can use the equations that we have derived in the first task for the injector response calculation, with the only difference that a correction coefficient has to be included in the dispersion equation when determining the wave numbers. This

correction coefficient explicitly includes the gas-liquid density ratio and the surface tension coefficient at the gas-liquid interface.

The results have shown that the produced injector response is overall smaller than predicted by Bazarov's theory. Also, the response at the long wave limit is not drastically different from the response computed with the Kelvin's waves, with the former being smaller than the latter. The density variation study has shown that we should worry about the inertial effects of the core only after its density becomes larger than 10% of the liquid's. And the surface tension variation has shown that the surface tension coefficient has to grow on the order of $10^4$ larger than it normally is at the ambient temperature, which indicates that the surface tension correction can be eliminated in the injector response calculations.

To conclude, we have to point out that the overall goal of this chapter was to have an assessment of the Kelvin's waves on the injector response, because the existing dynamic theory by Bazarov did not provide any information on this subject. Of course, this analysis is not complete without the consideration of the reflected waves. However, it may serve as a good starting point from where the reflected waves may be added. Based on Chapter 5, to do that, one has to know the reflective properties of Kelvin's waves as they propagate downstream the core of the injector. Eventually, it might be possible that the whole added notion of wave reflection could be lumped into some type of correction coefficient similar to the one that included the density ratio and the surface tension above. As a result of this analysis, the calculated response shown as the solid red line in Fig. 6.5 could grow to form a "hump" region at the intermediate frequencies, as does the original response curve with reflections due to Bazarov.

# 7. COMPUTATIONAL SIMULATIONS OF SWIRL INJECTOR DYNAMICS BASED ON BOUNDARY ELEMENT METHOD

## 7.1 Introduction

The Boundary Element Method (BEM) is a computational tool which can be effectively used for computations of the problems that require an accurate resolution of the free surface. This capability of BEM stems from the fact that, unlike traditional finite difference or finite element methods, this technique solves the governing differential equation in the considered domain exactly, and all computational efforts to satisfy approximately the boundary conditions are performed only at the domain boundary. This allows one to reduce the dimension of the problem by one [112]. For example, the axisymmetric 3D problem of the flow in a swirl injector considered in this study is reduced to a solution of a surface integral instead of a volume integral, as would be the case in the finite element approach. In turn, this greatly decreases the required computational time and data storage.

There are also disadvantages of the BEM inherent to its mathematical setup. For example, in the axisymmetric problem considered here, there may be singularities in the solution that arise when the field point of the solution is close to the base point, or, it is difficult to compute the solution itself, due to the fact that it involves numerous elliptic integrals (Liggett and Liu [39, pp. 161,162]), and finally, at sharp corner nodes, because of the non-uniqueness of the solution, one has to use the auxiliary equations in order to make its approximation [112, Sec. 12.2].

There are many books and papers written on this subject. Jaswon [113] provides a good historical review of the BEM, where he also cites the major applications of the method to the structural mechanics and electrostatics problems. The often cited

books that review the mathematics behind the method are Brebbia [38], Gipson [114] and the above mentioned Liggett and Liu [39]. BEM has been also successfully applied to the unsteady free surface flow problems. Longuet-Higgins and Cokelet [115] , [116], for example, have demonstrated how the sea water waves tip over and break by using this technique. BEM has been also successfully applied to study high speed jets and their atomization at Purdue University: Hilbing [117], [118], Heister [119], Park [120]. And, as was mentioned in Chapter 1, there are BEM models now, due to Park [37] and Richardson [43], capable of computing the steady and unsteady flows in swirl injectors.

In this study, we will continue using BEM based on the models by Park [37] and Richardson [43], with the correction of the inflow boundary conditions, which we will discuss below. They have used the BEM to obtain the injector response and compare it to the theoretical response by Bazarov [1]. And, as we have mentioned in Chapter 1, the results by Richardson have shown that there is a considerable disagreement between the computational and theoretical responses, Fig. 1.2. From Chapter 2 we know that, due to the shortcomings of Bazarov's theory, this comparison may be not appropriate, because the theoretical response results may behave differently after fixing its shortcomings. Having this in mind, in this dissertation, we will also use the BEM to compute the injector response, as we sweep through an array of disturbance frequencies, but the focus will be to compare the frequencies, at which the BEM response peaks out, with the resonant frequencies, which we have calculated in Chapter 5. It is believed for now that this comparison will reveal more significant information about the dynamic behavior of the injector than the information about the matching of computational and theoretical responses above, since the resonant modes are truly the most noticeable phenomena that show up in cold flow or hot fire tests of the injector. And, at the same time, if the resonant peaks do show consistency with those predicted analytically, this will validate both the BEM code and the analytical models presented in Chapters 4 and 5 of this thesis against each other.

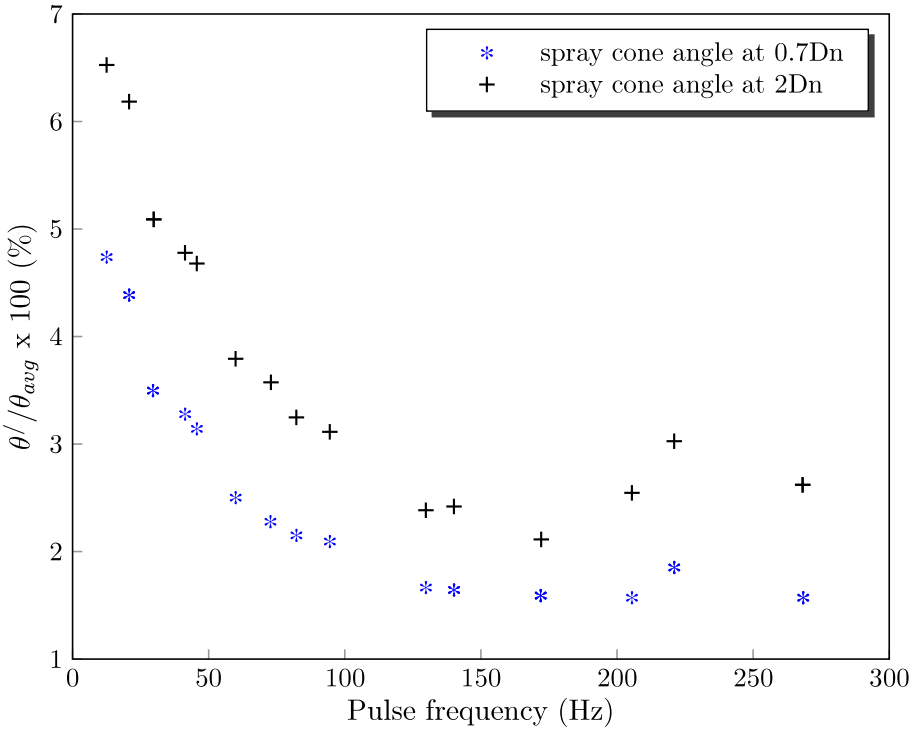


Figure 7.1.: Experimental data due to Ahn [55, Fig. 6.15] on spray cone angle fluctuation at distances of 0.7 and 2 nozzle diameters from the nozzle exit, peak observed at 221 Hz

As was mentioned in Chapter 1, there is an experiment at Purdue University, Ahn [55], [56], where the aim is precisely to test the response of the injector to the different pulsation frequencies of the flow in the manifold. This injector is the baseline injector investigated in this thesis, whose parameters are shown in Tables 2.2 and 2.3. Let us take a look at the experimental result showing the spray cone angle fluctuation versus the flow pulsing frequency [55, Fig. 6.15], which we present here as Fig. 7.1. Notice that the data makes a peak at the frequency of about 221 Hz. We may attribute this peak to the first mode of injector resonance, which follows from ACRM's in Chapter 5 to be 226 Hz (see Table 5.2). Let us remember this number and look for it when we present the computational results for the injector response further on.

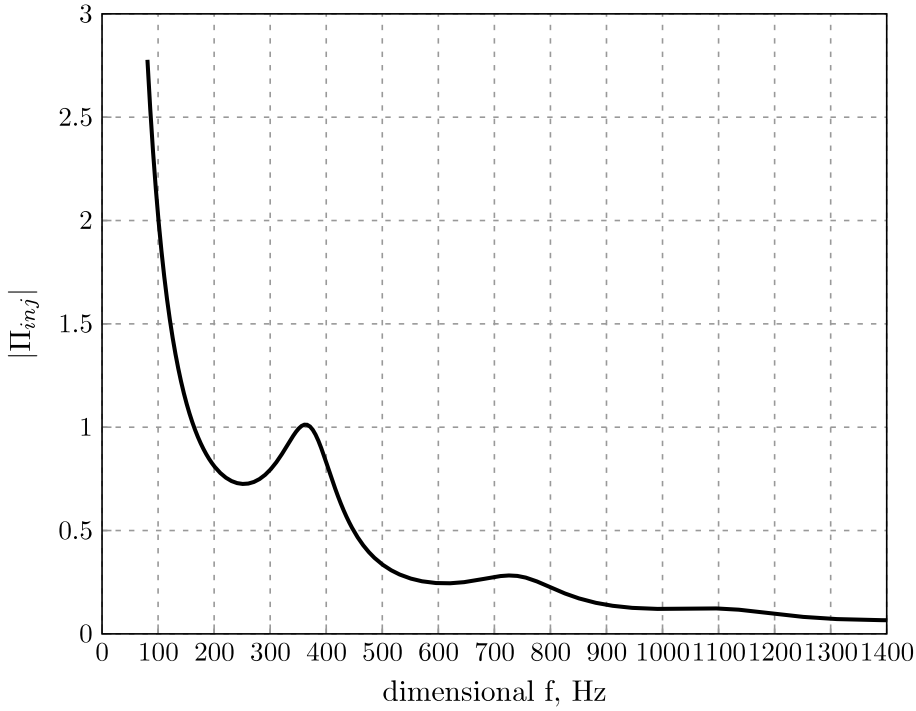


Figure 7.2.: Response of baseline injector calculated using Bazarov's [1] linear theory, first peak observed at 361 Hz, second peak observed at 726 Hz (artificial viscosity coefficient $\nu = 0.1$)

Continuing the discussion on that experimental peak, one would wonder what would the existing Bazarov's [1] theory give in its vicinity. Figure 7.2 shows the answer. There is no peak around 221 Hz, and the closest peak in this area is at 361 Hz, then comes the second peak located further in the higher frequencies, at 726 Hz. Is this due to the shortcomings that we have outlined in Chapter 2? Or, on the contrary, is the linear theory correct, and the experimental peak has been merely incorrectly captured? These are rather the core questions which we pursue to answer in this chapter. If we can prove that the experimental peak is indeed a resonance peak, then this may serve as a significant input for future dynamic studies of the swirl injectors.

## 7.2 Brief Review of Mathematics Behind Boundary Element Method

For the completeness of this report, let us briefly go through the mathematics on which the BEM is based. In doing this, we will closely follow the notation and the equations used in Gipson [114], which will be different from the notation that we have used so far throughout this thesis. A particular case, when the Laplace's equation is the governing differential equation in the flow domain, will be considered here.

Consider a domain $\Omega$ bounded by the revolving surface $\Gamma$ in the cylindrical coordinate system $r, z$, Fig. 7.3, where by $\vec{r}_l$ we denote a base point, and by $\vec{r}$ an arbitrary field point. Suppose that the boundary $\Gamma$ can be divided into two parts, $\Gamma_1$ and $\Gamma_2$, on which we know either the velocity potential, $\phi$, or the velocity itself, $q = \partial\phi/\partial n$, which is taken in the direction of the unit normal vector $\hat{n}$. Let us denote the known

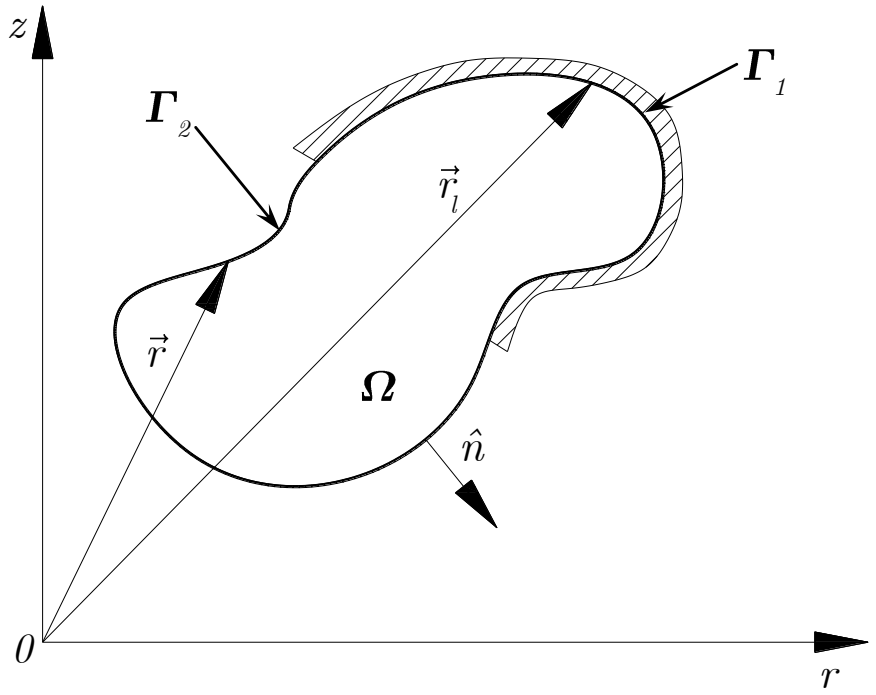


Figure 7.3.: Elementary domain schematic considered for BEM computation

parameters by bar, and the approximate values of parameters by hat further on. Then, the problem statement can be written as:

$$\nabla^2\phi = 0 \quad \text{in } \Omega \tag{7.1}$$

$$\phi = \begin{cases} \bar{\phi} & \text{on } \Gamma_1 \\ \hat{\phi} & \text{on } \Gamma_2 \end{cases} \tag{7.2}$$

$$q = \frac{\partial\phi}{\partial n} = \begin{cases} \hat{q} & \text{on } \Gamma_1 \\ \bar{q} & \text{on } \Gamma_2 \end{cases} \tag{7.3}$$

We can attempt to solve this problem approximately, if we deal with its weighted residual form

$$\int_\Omega \left(\nabla^2\hat{\phi}\right) W_l d\Omega + \int_{\Gamma_1} \left(\hat{\phi} - \bar{\phi}\right) \bar{W}_l d\Gamma + \int_{\Gamma_2} \left(\hat{q} - \bar{q}\right) \bar{\bar{W}}_l d\Gamma = 0 \tag{7.4}$$

where $W_l$, $\bar{W}_l$, and $\bar{\bar{W}}_l$ are the weighting functions approximating the respective integrand functions $\nabla^2\hat{\phi}$, $\hat{\phi} - \bar{\phi}$, and $\hat{q} - \bar{q}$. Also, the integration is performed over the whole domain in the first integral, and over the $\Gamma_1$ and $\Gamma_2$ parts of the boundary in the next two integrals.

This equation is hard to solve directly because of the second order of differentiation caused by the Laplacian under the integral sign. We can eliminate the Laplacian from this equation, if we assume the following equalities for the weighting functions

$$\bar{W}_l = \frac{\partial W_l}{\partial n} \text{ on } \Gamma_1 \qquad \text{and} \qquad \bar{\bar{W}}_l = -W_l \text{ on } \Gamma_2$$

With this, we can rewrite Eq. (7.4) as

$$\int_\Omega \left(\nabla^2 W_l\right)\hat{\phi} d\Omega + \int_{\Gamma_1} \left(\frac{\partial\hat{\phi}}{\partial n} W_l - \bar{\phi}\frac{\partial W_l}{\partial n}\right) d\Gamma + \int_{\Gamma_2} \left(\bar{q} W_l - \frac{\partial W_l}{\partial n}\hat{\phi}\right) d\Gamma = 0 \tag{7.5}$$

where the Laplacian is not present anymore. This equation is a starting point for the BEM formulation. We can further modify it in such way that the domain integral will disappear leaving us only with the boundary integrals. This is achieved by assuming that the weighting function is equal to the Green's function, $G$, in the three dimensional space, or

$$W_l = -\frac{1}{4\pi\left|\vec{r} - \vec{r}_l\right|} = G$$

With this, we can rewrite Eq. (7.5) as

$$c_l\phi\left(\vec{r}_l\right) - \int_\Gamma \phi \frac{\partial G}{\partial n} d\Gamma = -\int_\Gamma qG d\Gamma$$
$$c_l\phi\left(\vec{r}_l\right) + \frac{1}{4\pi}\int_\Gamma \phi \frac{\partial}{\partial n}\left(\frac{1}{|\vec{r}-\vec{r}_l|}\right) d\Gamma = \frac{1}{4\pi}\int_\Gamma q \cdot \frac{1}{|\vec{r}-\vec{r}_l|} d\Gamma \tag{7.6}$$

where $c_l$ is the correction factor that accounts for a situation when the field point $\vec{r}$ in consideration is at the same location as the base point $\vec{r}_l$.

Next, to put this equation into a computational form, a discretization has to be performed. Consider now our case of axisymmetric flow in the swirl injector, Fig. 7.4. Suppose that we divide the whole boundary of the flow, $\Gamma$, into $j = 1 \ldots E$ small elements, $\Gamma_e$, shown as red in this figure. And lastly, let us assume that on each

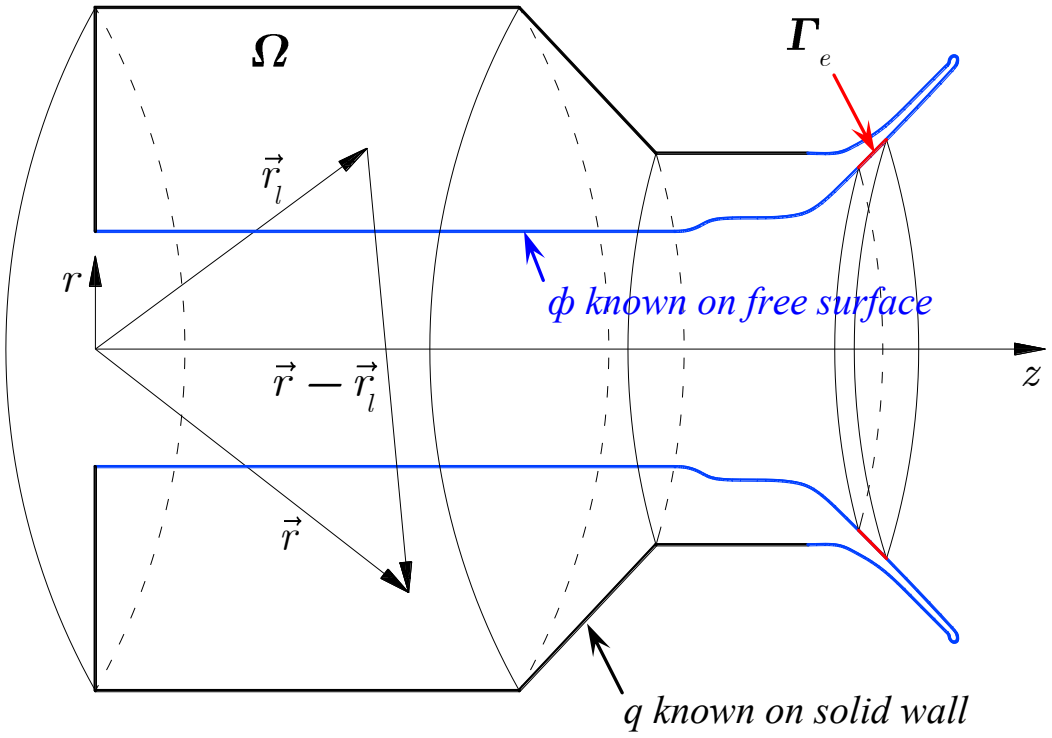


Figure 7.4.: Axisymmetric domain schematic of swirl injector flow considered for BEM computation

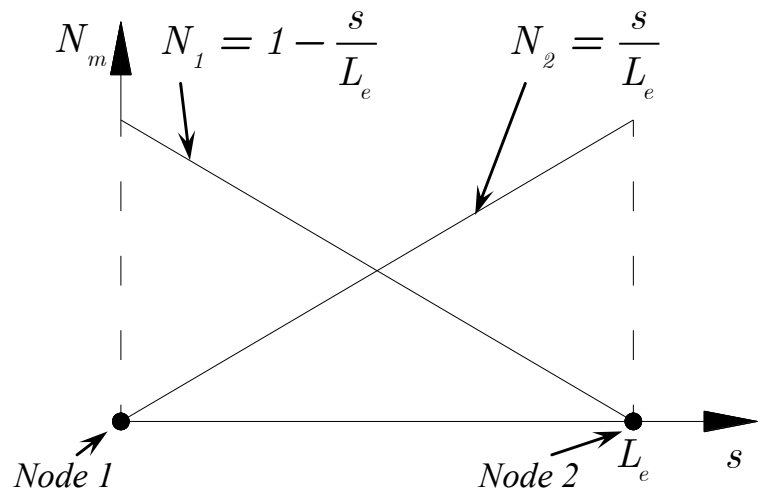


Figure 7.5.: Schematic of weighting functions for linear element in BEM

element we can make a linear approximation of $\phi$ and $q$ given by

$$\hat{\phi} = \hat{\phi}_1^j \left(1 - \frac{s}{L}\right) + \hat{\phi}_2^j \frac{s}{L} = \hat{\phi}_1^j N_1 + \hat{\phi}_2^j N_2$$
$$\hat{q} = \hat{q}_1^j \left(1 - \frac{s}{L}\right) + \hat{q}_2^j \frac{s}{L} = \hat{q}_1^j N_1 + \hat{q}_2^j N_2$$

where $\hat{\phi}_1^j$, $\hat{\phi}_2^j$, $\hat{q}_1^j$, and $\hat{q}_2^j$ are the approximations of $\phi$ and $q$ on both ends of an element, and $N_1$, $N_2$ are the chosen linear functions, see Fig. 7.5. With this, we can rewrite Eq. (7.6) as

$$c_l \phi\left(\vec{r}_l\right) - \frac{1}{4\pi} \sum_{j=1}^{E} \sum_{m=1}^{2} \hat{\phi}_m^j \int_{\Gamma_e} r N_m A\left(p, \vec{r}, \vec{r}_l\right) d\Gamma =$$
$$= \sum_{j=1}^{E} \sum_{m=1}^{2} \hat{q}_m^j \int_{\Gamma_e} \frac{r N_m K\left(p\right)}{\left[\left(r + r_l\right)^2 + \left(z - z_l\right)^2\right]^{\frac{1}{2}}} d\Gamma \qquad (7.7)$$

where

$$p^2 = \frac{4 r r_l}{\left(r + r_l\right)^2 + \left(z - z_l\right)^2}$$

$$A\left(k, \vec{r}, \vec{r}_l\right) = -\frac{4}{\left[\left(r + r_l\right)^2 + \left(z - z_l\right)^2\right]^{\frac{1}{2}}} \times$$
$$\times \left( \frac{1}{2r} \left[ K\left(p\right) + \frac{r^2 - r_l^2 - \left(z - z_l\right)^2}{\left(r - r_l\right)^2 + \left(z - z_l\right)^2} E\left(p\right) \right] n_r + \frac{\left(z - z_l\right) E\left(p\right)}{\left(r - r_l\right)^2 + \left(z - z_l\right)^2} n_z \right)$$

where $n_r$ and $n_z$ are the components of the unit normal vector, and

$$K(p) = \int_0^{\frac{\pi}{2}} \frac{d\psi}{\sqrt{1 - p^2 \sin^2 \psi}} \qquad E(p) = \int_0^{\frac{\pi}{2}} \sqrt{1 - p^2 \sin^2 \psi} d\psi$$

are the elliptic integrals of the first and the second types.

Next, let us define the integrals in Eq. (7.7) as $D$ and $S$ kernels. Further, let us put the base point $\vec{r}_l$ at the end of an element, so that $\vec{r}_l = \vec{r}_j$, and then, sweep through all other elements of the boundary to compute the values of $\phi$ and $q$ at the base point. Then we can cast that equation in a more convenient matrix form as

$$c_j \phi(\vec{r}_j) - \sum_{j=1}^{E} \sum_{m=1}^{2} \hat{\phi}_m^j D_m^j = \sum_{e=1}^{E} \sum_{m=1}^{2} \hat{q}_m^j S_m^j \tag{7.8}$$

or

$$[c_j I - D][\phi] = [S][q] \tag{7.9}$$

To conclude, the solution of the BEM problem at some particular time step in this study proceeds as follows:

1. Based on the given coordinates of all points on the boundary, the normal components, $n_r$, $n_z$, the lengths of the boundary elements, $\Gamma_e$, are computed, and the elliptic integrals $K(p)$, $E(p)$ are approximated by the curve fits provided in Abramowitz and Stegun [121, Chap. 17].

2. The integrals in Eq. (7.7) are evaluated based on the approximation by Gaussian quadratures [122, Chap. 8], and then, the $D$ and $S$ matrices are constructed in accord with Eq. (7.8). They are further modified so that the known flow parameters are placed on the RHS of Eq. (7.9), and the unknown ones – on its LHS.

3. The solution for $\phi$ and $q$ is found by matrix inversion, where successive over relaxation, or LU decomposition techniques may be used [122, Chap. 2]. This step requires the largest computational time. In this study, this step is accelerated by using the ScaLAPACK matrix inversion routines [123] incorporated into the solution due to Park [124], [125], [126].

## 7.3 Boundary Conditions

As we have discussed above, on each point of the flow boundary we know either $\phi$ or $q$, which we set from the known or assumed boundary conditions. With regard to the inflow boundary and the solid wall boundary, we can set the normal velocities, $q$, exactly. At the inflow boundary, they may be set to their prescribed values as a function of time, and on the solid boundary, they must be zero at all times. Accordingly, the velocity potentials, $\phi$, are the unknowns on these boundaries. On the free surface, however, we do not have any information about the normal velocities, $q$, but, we know that the velocity potentials of its points are governed by the unsteady Bernoulli's equation [71, p. 71]. Figure 7.4 summarizes this and shows schematically where we know which parameter. In what follows, we will review these boundary conditions in more detail and point out the differences with the previous models of Park [37] and Richardson [43], which we have implemented to make the code as close as possible in its boundary conditions to the analysis in Chapter 5, in order to validate the injector resonance.

### 7.3.1 Inflow Boundary Condition

In the previous models by Park [37] and Richardson [43], the tangential inflow was modeled as a cylindrical slot, where the flow enters through its upper cylindrical surface and proceeds radially towards the axis of the injector, and it was assumed that the two straight sides of the cylinder are not letting any fluid in or out, or $q = 0$ there, Fig. 7.6. The swirl was imposed on this radially entering flow only at the free surface, through the first couple of nodes closest to the head end wall, by the swirling term in the Bernoulli's equation. *Let us note here that, in the real three dimensional inflow case, because the swirl acts throughout the entire body of the fluid, the circumferential component of the velocity would start to appear right at the upper boundary of that inflow cylindrical slot, and be present all the way down to the free surface, which would probably reduce the strong radial component of the*

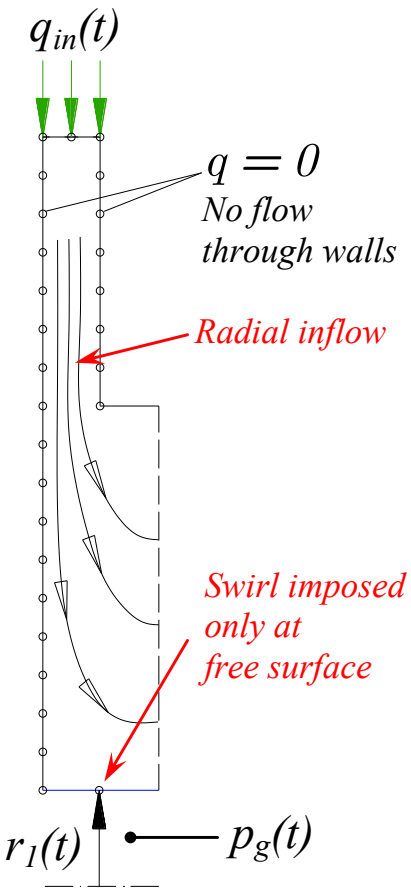


Figure 7.6.: Schematic of inflow setup in previous BEM models by Park [37] and Richardson [43]

*velocity created by this setup. Because of that, the cylindrical slot does not accurately represent the physical inflow.*

Next, let us briefly review the way the inflow velocity was computed in Richardson's [43] model. It was assumed that it is valid to use the steady state formulation of the Bernoulli's equation to relate the fluctuating pressure drop to the instantaneous circumferential velocity at the head end radius,

$$u_{\theta he}(t) = \sqrt{\frac{2\Delta p_{inj}(t)}{\rho}} = \sqrt{\frac{2\left[\Delta \bar{p}_{inj} + p_g(t)\right]}{\rho}} \tag{7.10}$$

where the fluctuating gas pressure $p_g$ (see Fig. 7.6) was set to zero in the steady state computations, and to a sinusoidal function of small amplitude in the unsteady computations. *On the other hand, it follows from the unsteady Bernoulli's equation derived by Park [37, Eq. 4.14] and Richardson [43, Eq. 4.12], which governs the free surface movement in general, that the instantaneous circumferential velocity at the head end radius is given by*

$$u_{\theta he}(t) = \sqrt{\frac{1}{Ro^2 (r_1(t))^2}} \tag{7.11}$$

*where the Rossby number, Ro, is constant, and $r_1$ is the radius of the first node adjacent to the head end wall (see Fig. 7.6). By comparing Eqs. (7.10) and (7.11), it becomes clear that, to be consistent with the rest of the flow beyond the head end, the circumferential velocity at the head would have been computed more properly with Eq. (7.11).*

Proceeding further, Richardson [43, Eq. 4.12] has computed the inflow velocity at the entrance to the cylindrical slot as

$$q_{in}(t) = -\sqrt{2\Delta p_{inj}(t)} \cdot \frac{r_1(t)}{R_{in}} \tag{7.12}$$

*Note however, that this expression is valid only for the inflow at the exit of the real tangential inlet, $W_{in}$ (see Fig. 1.1), and the velocity $q_{in}$ has to be recomputed from it based on the mass flow conservation.*

To diminish the inaccuracies in these previous models, it is proposed now to focus on the flow region that is located downstream of the head end region of the injector, i.e. the region where we can assume that flow has developed into an overall axial, and all of the flow turning has ended. Accordingly, let us cut off the head end region of the injector at the edge of the tangential inlet, $z = 2R_t$, and set the inflow boundary just downstream of this edge, as shown in Fig. 7.7. Finally, let us distribute the inflow velocity, $q_{in}$, equally (in the radial direction) at this new inflow boundary.

At the steady state, after the initial transient, the inflow velocity, $q_{in}$, should be equal to the fairly well known theoretical axial velocity in the uniform vortex chamber

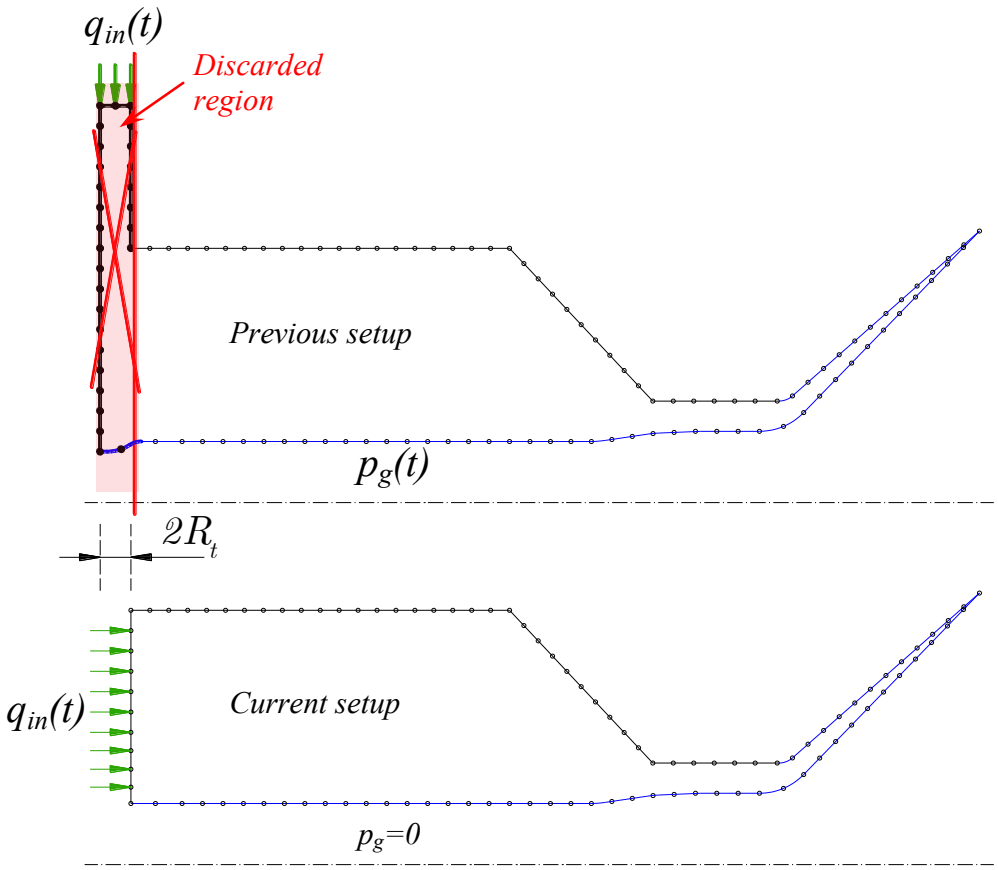


Figure 7.7.: Schematic of current BEM flow setup compared to prior models by Park [37] and Richardson [43]

region, $\bar{u}_{zv}$ (see Table 2.3). Downstream of the head end, the uniform inflow should produce the flow with a practically constant and small axial velocity up to the nozzle entrance transition.

On the other hand, to set the unsteady flow disturbances, we can simply add a sinusoidal fluctuation to that stabilized inflow velocity. Note that the resulting unsteady flow is equivalent to the flow which would be disturbed acoustically from the downstream combustion chamber end. That is, the oscillating nozzle mass flow rate caused by the downstream end would cause the disturbances in the vortex chamber through the nozzle entrance transition region, which then eventually would reach the head end, in form of the upstream traveling waves (see Chapter 4 for more discussion).

Also note that the current BEM setup is close in its velocity field to all three reflection/resonance models that we have considered in Chapter 5. Recall that the first two of them, ACRM-1 and ACRM-2, assumed a uniform zero bulk flow velocity in the vortex chamber, $\bar{u}_{zv} = 0$. In the BEM case, this velocity will be very small and not zero, but nevertheless uniform. Also recall that, in the CCRM, we have divided the vortex chamber into two distinct regions: the head end region with zero bulk flow velocity and the uniform vortex chamber region with the small bulk flow velocity equal to $\bar{u}_{zv}$. This is again similar to our current BEM setup, with the difference that we are starting right from the uniform vortex chamber region.

With regard to the gaseous pressure in the core, we know from Chapter 6 that its action may be noticeable only if the gas-to-liquid density ratio is on the order of 10%, in the non-reflective flow setup. Recall also the example of LOX-GH2 combustion at the end of Chapter 6, in which case, at the chamber pressure of 3000 psia, we have reached the value of only 0.7% for this ratio. Lastly, we have learned that the overall effect of the surface tension presence is quite weak. Let us generalize these conclusions and assume that we can completely ignore the inertial and capillary effects of the core further on in this study, which allows us to set the gas pressure in the core to zero, $p_g = 0$.

### 7.3.2 Free Surface Boundary Condition

To track the movement of the points on the free surface, we need to have its Lagrangian description in terms of the unsteady Bernoulli's equation. In our BEM setup, we are dealing with an axisymmetric flow, and hence, we can track the point movement only in a 2D plane, which crosses the axis of the injector. We cannot "see" the swirling component of the flow, which is perpendicular to this plane. Therefore, the Bernoulli's equation describing the free surface movement in the BEM code has to represent the flow field, which is the result of a subtraction of the swirling flow field component from the total flow field.

For this purpose, in the series of the previous BEM codes, Yoon [42, Sec. 3.2], Park [37, Sec. 4.1], Richardson [43, Sec. 4.3], computing the injector flows and their atomization, the total potential field, has been introduced, and thereafter represented as being consistent of two parts: the first, which describes the movement only in the radial and the axial directions, and the second, which describes the movement only in the circumferential direction. The resulting Bernoulli's equation of these authors has included the Rossby number.

In this subsection, let us show an alternative derivation of the unsteady Bernoulli's equation, which will clearly show the presence of the angular momentum term, $C$, in its final expression, instead of the Rossby number.

For an axisymmetric ideal flow, we can write the angular momentum equation in the form

$$\frac{D}{Dt}\left(ru_\theta\right) = \frac{DC}{Dt} = 0 \tag{7.13}$$

where $D/Dt$ is the material derivative, and, as was the case throughout this dissertation, we have used the definition of the angular momentum constant, $C = ru_\theta$. We are dealing with an overall potential flow, whose velocity field is given by

$$\nabla\phi = [u_r, u_\theta, u_z] = \left[\frac{\partial\phi}{\partial r}, \frac{1}{r}\frac{\partial\phi}{\partial\theta}, \frac{\partial\phi}{\partial z}\right] = \left[\frac{\partial\phi}{\partial r}, \frac{C}{r}, \frac{\partial\phi}{\partial z}\right] \tag{7.14}$$

where we have used the fact that the circumferential flow component is given by the potential free vortex.

Next, the Lagrangian derivative for the whole flow field may be written as

$$\frac{D\phi}{Dt} = \frac{\partial\phi}{\partial t} + \nabla\phi\cdot\nabla\phi \tag{7.15}$$

In this equation, we know that the Eulerian time derivative is given by the usual unsteady Bernoulli's equation (see Section 4.3), which, since we neglect the gaseous core presence, can be written as

$$\frac{\partial\phi}{\partial t} + \frac{1}{2}\nabla\phi\cdot\nabla\phi = A \tag{7.16}$$

where $A$ represents the steady state terms. Without the loss of generality, we can set $A = 0$ by incorporating the steady terms into $\phi$. With this, we can rearrange Eq. (7.16) to

$$\frac{\partial \phi}{\partial t} = -\frac{1}{2}\nabla\phi \cdot \nabla\phi \tag{7.17}$$

The second term in Eq. (7.15) can be obtained from Eq. (7.14) as

$$\nabla\phi \cdot \nabla\phi = \left(\frac{\partial \phi}{\partial r}\right)^2 + \left(\frac{\partial \phi}{\partial z}\right)^2 + \frac{C^2}{r^2} \tag{7.18}$$

Combining Eqs. (7.15), (7.17), and (7.18), we have

$$\frac{D\phi}{Dt} = -\frac{1}{2}\nabla\phi \cdot \nabla\phi + \nabla\phi \cdot \nabla\phi = \frac{1}{2}\nabla\phi \cdot \nabla\phi = \frac{1}{2}\left[\left(\frac{\partial \phi}{\partial r}\right)^2 + \left(\frac{\partial \phi}{\partial z}\right)^2 + \frac{C^2}{r^2}\right] \tag{7.19}$$

To get the Lagrangian derivative for the points moving in the 2D BEM plane, which say are represented by the velocity potential $\phi_{BEM}$, we can subtract the Lagrangian derivative of the swirling component of the flow from the Lagrangian derivative of the total field,

$$\frac{D\phi_{BEM}}{Dt} = \frac{D\phi}{Dt} - \frac{D\left(C\theta\right)}{Dt} \tag{7.20}$$

The Lagrangian derivative of the swirling component of the flow can be written as

$$\frac{D\left(C\theta\right)}{Dt} = \frac{DC}{Dt}\theta + C\frac{D\theta}{Dt} \tag{7.21}$$

In this expression we know that the first term is zero due to Eq. (7.13), and for the second term we have

$$\frac{D\theta}{Dt} = \frac{\partial \theta}{\partial t} + \left[u_r, \frac{C}{r}, u_z\right] \cdot \left[\frac{\partial \theta}{\partial r}, \frac{1}{r}\frac{\partial \theta}{\partial \theta}, \frac{\partial \theta}{\partial z}\right] = \frac{C}{r^2}$$

Then we can rewrite Eq. (7.21) as

$$\frac{D\left(C\theta\right)}{Dt} = \frac{C^2}{r^2} \tag{7.22}$$

Substituting Eqs. (7.19) and (7.22) into Eq. (7.20) we obtain

$$\frac{D\phi_{BEM}}{Dt} = \frac{1}{2}\left[\left(\frac{\partial \phi}{\partial r}\right)^2 + \left(\frac{\partial \phi}{\partial z}\right)^2 + \frac{C^2}{r^2}\right] - \frac{C^2}{r^2} = \frac{1}{2}\left[\left(\frac{\partial \phi}{\partial r}\right)^2 + \left(\frac{\partial \phi}{\partial z}\right)^2 - \frac{C^2}{r^2}\right] \tag{7.23}$$

To be consistent with the $\phi$-$q$ notation for the BEM parameters which we have been using in this chapter, we can rewrite the last equation with omitting the "BEM" index,

$$\frac{D\phi}{Dt} = \frac{1}{2}\left[\left(\frac{\partial\phi}{\partial r}\right)^2 + \left(\frac{\partial\phi}{\partial z}\right)^2 - \frac{C^2}{r^2}\right] \tag{7.24}$$

but we have to keep in mind that this equation describes only the 2D motion of the points on the free surface and not the whole potential field movement. Also note that the dimensional and nondimensional forms of this equation look the same, and the Rossby number does not appear in the former.

## 7.4 Grid Setup

Most of the time, in BEM computations, the nodes on the free surface move in such fashion, that the distance between them becomes irregular. In this study, the grid is set up in such way, that the distance between the nodes on the free surface remains approximately constant at all times, both in steady and unsteady simulations. In order to preserve equal distances, when the coordinates are updated, we construct a spline curve that goes through each point, then divide this curve into equal intervals, $ds_{grid}$, Fig 7.8, and then redefine the coordinates of the points so that they are located at the ends of those intervals. For the free surface node located at the inflow boundary, $z = 0$, we assume that its radius is equal to the radius of the next free surface node adjacent from the right, so that the free surface makes a 90° angle with the inflow boundary. By doing this, we can avoid ambiguity in setting the velocities at this corner of the flow.

On the inflow and the solid boundaries, we try to reduce the number of nodes to minimize the computational time. On these boundaries, only the nodes that are located close to the moving free surface nodes do strongly affect the resulting solution for the overall free surface movement at each time step. And hence, the distance between the nodes, at the locations where the free surface connects to the rest of the boundary, has to be approximately equal to $ds_{grid}$. For the nodes that are far from

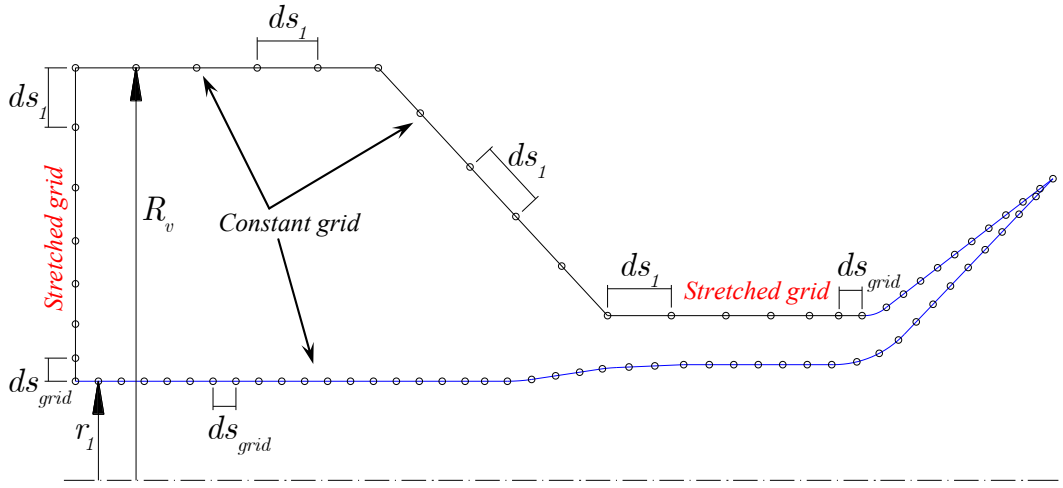


Figure 7.8.: Grid schematic in BEM simulations

the free surface, however, we can choose larger distances, since their influence on the solution is weaker. Conclusively, we can stretch the grid at these nodes as shown in Fig. 7.8. Starting from the lower left corner, the grid interval is initially equal to $ds_{grid}$, then it stretches to $ds_1$ at the upper left corner. On the straight cylindrical boundary and on the conical convergence boundary, we keep the intervals approximately equal to $ds_1$. Lastly, on the nozzle boundary, the grid interval decreases from $ds_1$ to $ds_{grid}$ again.

The stretching is accomplished as follows. First, we choose a desired number of intervals on the inflow boundary, $N_h$. Next, we suppose that the intervals between the nodes, $ds$, increase as a power of some coefficient, $K_h$, which is greater than 1, or

$$ds_j = ds_{grid} \cdot K_h^j \text{ where } j = 1 \ldots N_h$$

We can find the coefficient of this geometric progression from the fact that the sum of all intervals on the inflow boundary should be equal to $R_v - r_1$, or

$$\sum_{j=1}^{N_h} ds_j = ds_{grid} \sum_{j=1}^{N_h} K_h^j = ds_{grid} \left( K_h^1 + K_h^2 + K_h^3 + \ldots \right) = R_v - r_1$$

When the flow is unsteady, the radius $r_1$ is varying in time, and the free surface node at the inflow boundary, $r_0$, tracks this variation exactly, since they are set to be

equal at all times, Fig. 7.9. If we would leave all other nodes on the inflow boundary intact, this could create a situation when the distances between the nodes at the lower left corner of the flow are too uneven, which could in turn lead to the singularity in the solution. To overcome this problem, we need to compress and expand the grid according to $r_1$ time variation. For this purpose, we can still use the geometric progression algorithm above to compute the intervals between the nodes, where the number of intervals on the inflow boundary, $N_h$, is kept as it was, but the coefficient of the geometric progression, $K_h$, is recomputed at each computational time step based on the new $r_1$. This will result in variable grid spacing as shown in Fig. 7.9. For clarity, we have indicated the last interval on the inflow boundary, which is now unsteady, as $ds'$, to distinguish from $ds_1$ above in Fig. 7.8.

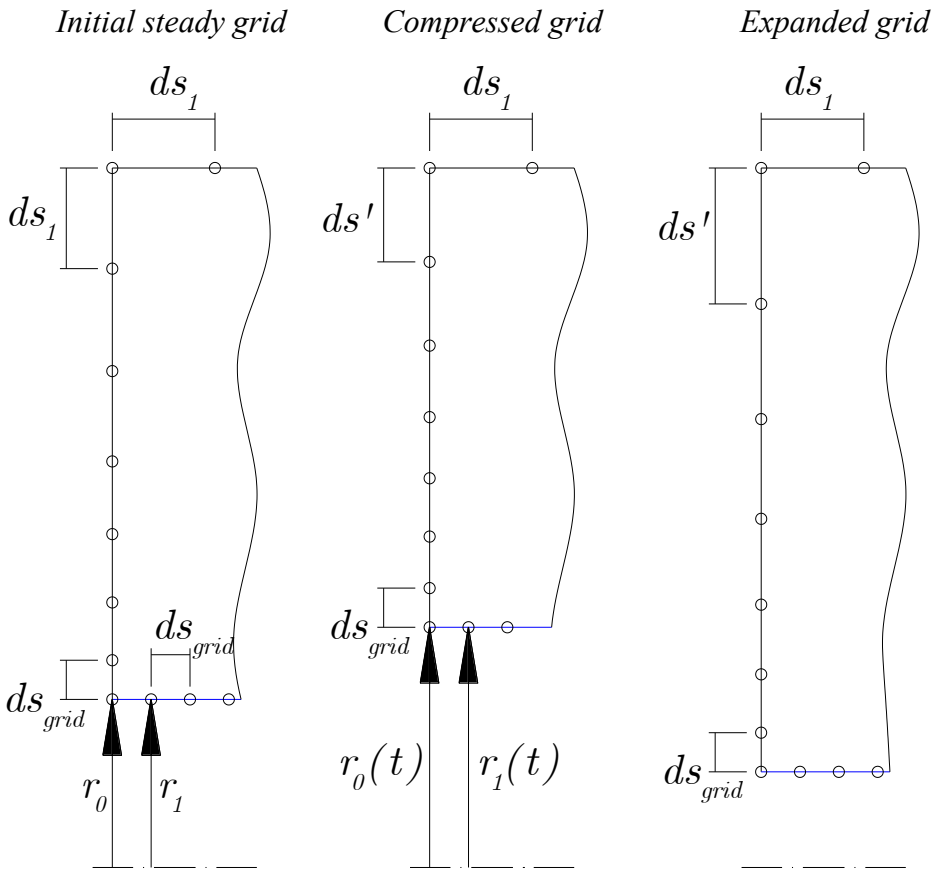


Figure 7.9.: Schematic of grid compression and expansion at inflow boundary

## 7.5 Time Stepping Procedure

Suppose that we are at the beginning of a new computational time step, and we know the coordinates of all points, and the values of $\phi$ and $q$ at each point.

The updating of the velocities, $q$, is easy, because, on the solid wall boundary, they are zero at all times, and, at the inflow boundary they follow the prescribed law of variation as follows. In the steady state runs, we compute the inflow velocity as

$$q_{in} = \frac{N_{in} R_t^2 \bar{W}_{in}^2}{R_v^2 - \left(r_1\left(t\right)\right)^2}$$

where, in the numerator, we have the constant inflow mass flow rate of a "real" injector having $N_{in}$ number of tangential inlets and the steady inflow velocity $\bar{W}_{in} = 1$ (see Sec. 2.3), and the denominator is the cross-sectional flow area at the first node right after the inflow boundary (see Figs. 7.8 and 7.9). After the initial transient, the radius $r_1$ attains an almost constant value (more discussion to follow below), which accordingly causes $q_{in}$ to stabilize. Let us say that the stabilized value of $q_{in}$ is $\bar{q}_{in}$. Then, at some point in time in this steady state, we start to pulse the flow by letting the inflow velocity to follow the sinusoidal law

$$q_{in}\left(t\right) = \bar{q}_{in} + q'_{in}\left(t\right) = \bar{q}_{in}\left(1 + q_{osc}\right)\sin\left(\omega t\right)$$

where $q_{osc}$ is the amplitude of oscillation.

The updating of the velocity potentials at the free surface points of the flow is accomplished by using Eq. (7.24). For that, first, the derivatives $\dfrac{\partial\phi}{\partial z}$ and $\dfrac{\partial\phi}{\partial r}$, and the swirl term $C^2/r^2$ are evaluated at all points. The derivatives here are computed based on five point finite differences for non-uniform grids, which are provided in Hilbing [41, App. A]. These derivatives are also used to update the $r$ and $z$ coordinates of the free surface points.

The final step in this procedure is to compute the unknown $q$'s on the free surface, and the unknown $\phi$'s on the solid and inflow boundaries. This is accomplished by inverting the matrix equation (7.9), where we use the known updated $q$'s and $\phi$'s, and $r$'s and $z$'s as an input information.

There are a couple of computational details that should be pointed out to complete the description of the BEM time stepping:

- All of the free surface updating above is accomplished by using the fourth order Runge-Kutta scheme.

- If the distance between any two points at their updated locations becomes less than some prescribed radius of tolerance, then this signals the BEM code that the fluid body next to these points is ready to pinch off as a droplet (see [42, Fig. 7.5]). When such pinching event is performed, the numbers of the points are redefined to reflect the loss of nodes that disappeared out of the computation with the drop.

- When $q$'s and $\phi$'s are updated, their distribution along the free surface may not be smooth from time to time. This may result in non-physically large movements of some points on the free surface compared to the others. To overcome this problem, numerical smoothing filter due to Longuet-Higgins and Cokelet [115] is used, which modifies $q$'s and $\phi$'s as

$$\phi_j = \frac{-\phi_{j+2} + 4\phi_{j+1} + 10\phi_j + 4\phi_{j-1} - \phi_{j-2}}{16}$$

For more detailed description of the subroutines involved in the BEM code and its flow chart the reader is referred to Hilbing [41, App. A,B] and Yoon [42, App. B,C,E].

## 7.6 Injector Response Extraction from BEM Results

In this section, let us discuss how we can post process the BEM output to calculate the injector response, whose definition we rewrite here for convenience:

$$\Pi_{inj} = \frac{\dfrac{\dot{m}'_n}{\bar{\dot{m}}_n}}{\dfrac{\Delta p'_{inj}}{\Delta \bar{p}_{inj}}}$$

Let us link the output to the equations that we have derived for the long wave limit injector response in Chapter 6. The long wave limit is considered, because we set the velocities on the inflow boundary to be invariable in radial direction. Note that, for the general Kelvin's waves, this would not be the case, because the profile of the instantaneous axial velocity at the inflow boundary would be curved due to the presence of the Bessel functions. We will start first with the pressure drop, $\Delta p_{inj}$, and then proceed to the nozzle mass flow rate, $\dot{m}_n$, formulation.

### 7.6.1 Injector Pressure Drop

Because in our current BEM model we are analyzing the flow starting from the left end of the uniform vortex chamber region, or from $z = 2R_t$ of the actual injector, and the tangential inlets are out of our consideration (see Fig. 7.7), then the total pressure drop of the BEM injector is equal to the pressure drop through the liquid body at the inflow boundary. Recall now the equations that we wrote for the actual injector to describe the steady and unsteady components of the pressure drop through the liquid body from Chapter 6:

$$\Delta \bar{p}_{he} = \rho \frac{C^2}{2} \left[ \frac{1}{r_{he}^2} - \frac{1}{R_v^2} \right]$$

$$\Delta p'_{he} = \rho \frac{C^2}{r_{he}^3} \eta|_{z=0}$$

If we follow the derivation of these equations, we may notice that we can adapt them to our BEM injector by making the following replacements: the steady radius

of the free surface at the head end, $r_{he}$, with the average, or steady, value of $r_1(t)$, and the free surface fluctuation at the head end, $\eta|_{z=0}$, with the fluctuation of $r_1(t)$ (see Fig. 7.9). Denoting the average value and the fluctuation of $r_1$ by $\bar{r}_1$ and $r_1'$ respectively, we obtain the following equations for the BEM injector pressure drop:

$$\Delta\bar{p}_{inj} = \rho\frac{C^2}{2}\left[\frac{1}{\bar{r}_1^2} - \frac{1}{R_v^2}\right]$$
$$\Delta p'_{inj} = \rho\frac{C^2}{\bar{r}_1^3}r_1'$$

where $\bar{r}_1$ and $r_1'$ can be computed from the array of instantaneous values of $r_1$ generated by the BEM code as

$$\bar{r}_1 = \frac{\max\left(r_1\left(t\right)\right) + \min\left(r_1\left(t\right)\right)}{2}$$
$$r_1' = \frac{\max\left(r_1\left(t\right)\right) - \min\left(r_1\left(t\right)\right)}{2}$$

### 7.6.2 Nozzle Mass Flow Rate

When we derived the equations for injector resonance in Chapter 5, and the equations for the long wave fluctuations of the nozzle mass flow rate in Chapter 6, we were assuming that the steady free surface stops transitioning and becomes cylindrical after the distance of $0.5R_n$ from the nozzle start (see Section 3.3 and Table 3.1 for more discussion). And we based that conclusion on the matching of the analytical free surface shape with the steady state BEM free surface shape (see Fig. 3.9(c)). However, it has to be pointed out that this matching was only approximate. When we run the steady state BEM cases, we usually see that the free surface in the nozzle continues to vary all the way from the nozzle start to the point where it starts to curve significantly to transition into the spray. Figure 7.10 illustrates this in an exaggerated manner, where we can see in sequence proceeding downstream: an initial "hump" region, then a secondary smaller "valley" region, then a relatively constant flow section, then the region where the free surface exhibits a relatively uniform slope, and finally the transition to a conical sheet.

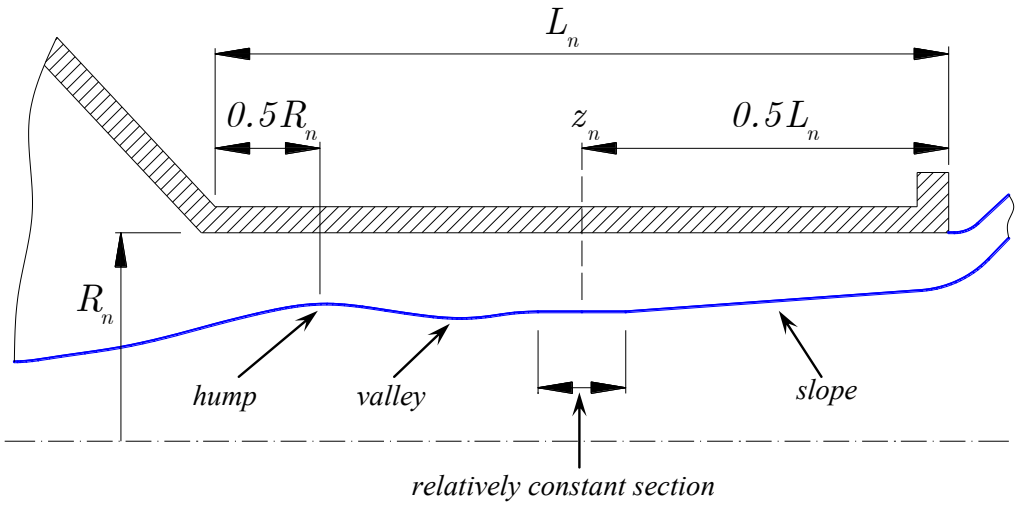


Figure 7.10.: Schematic of steady free surface in BEM injector nozzle and choice of flow section where nozzle mass flow rate measurements are taken

In order to have a valid comparison of the unsteady BEM results to the analytic resonance results in Chapter 5, we need to choose the location in the nozzle of the BEM injector, where we can assume that the steady free surface radius can be considered constant. This is an important choice, because if the free surface radius still changes, it becomes difficult to discern the disturbance waves traveling on such curved surface from the free surface itself. For now, it seems that, right at the middle of the nozzle, the steady free surface radius is almost constant. This will be the location where the measurements of the nozzle mass flow rate will be taken in this computational study. Further on, we will designate this location as $z_n$ (see Fig. 7.10).

It is important to point out how the disturbance wave time lag between the center of the nozzle and the nozzle exit compares with the period of oscillation at high frequencies. Let us denote the time lag by $\Delta t$, and the period by $\tau$. Then, the time lag is given by $\Delta t = 0.5L_n/c_n = 0.5 \cdot 4/5.7525 = 0.3477$, where $c_n$ is the long wave speed in the nozzle (independent of the disturbance frequency) from Table B.1 in Appendix B. To calculate the period of oscillation, let us take the highest frequency of 1300 Hz, which we will consider further in the BEM simulations of this chapter.

According to Section 2.3, this converts to dimensionless $\omega = 13.7960$, which, in turn, gives for the period $\tau = 2\pi/\omega = 0.4554$. Thus, we can conclude from the ratio $\Delta t/\tau = 0.3477/0.4554 = 0.7806$ that the time lag and the period of oscillation at the highest considered frequency are of the same order. Which means that, in order to deduce the injector response right at the nozzle exit from the injector response computed at the center of the nozzle, one would need to take the disturbance wave time lag into account. With regard to the amplitude of the response, however, we can say that the location in the nozzle where the response is measured is not important, based on the fact that the injector response is generally very weakly dependent on the nozzle length, which we will see later on.

To compute the mass flow rate, in general, one has to know the profile of the axial velocity at the chosen $z$ location, and subsequently integrate this profile over the flow cross-section. It is possible to compute the velocities at interior nodes of the flow in BEM (see Gipson [114, Sec. 3.11] and Richardson [43, Sec. 4.5]), where the increasing of the amount of the interior nodes leads to the better estimation of the mass flow integral. However, the additional computational time required to compute the mass flow rate due to this method is quite significant, on the order of 30% of the normal computational time, when the mass flow rate is not required. In addition to that, from the previous study of Richardson [43], we know that the axial velocity profile can be approximately described as being flat.

In this study, we need to run a large number of cases, on the order of 1000, to have the injector response at a variety of inflow disturbance frequencies. Each case takes from 30 to 60 hours to run on a single processor (there will be more discussion on this later). Therefore, to save computational time, in this study we have chosen a different, less precise, method of mass flow rate estimation, which may be described as follows:

1. On the solid and free surface boundaries of the nozzle, we find the points that are closest from the left side to the section $z = z_n$, and designate their numbers by the indices $jup$ and $jlo$ respectively, Fig. 7.11.

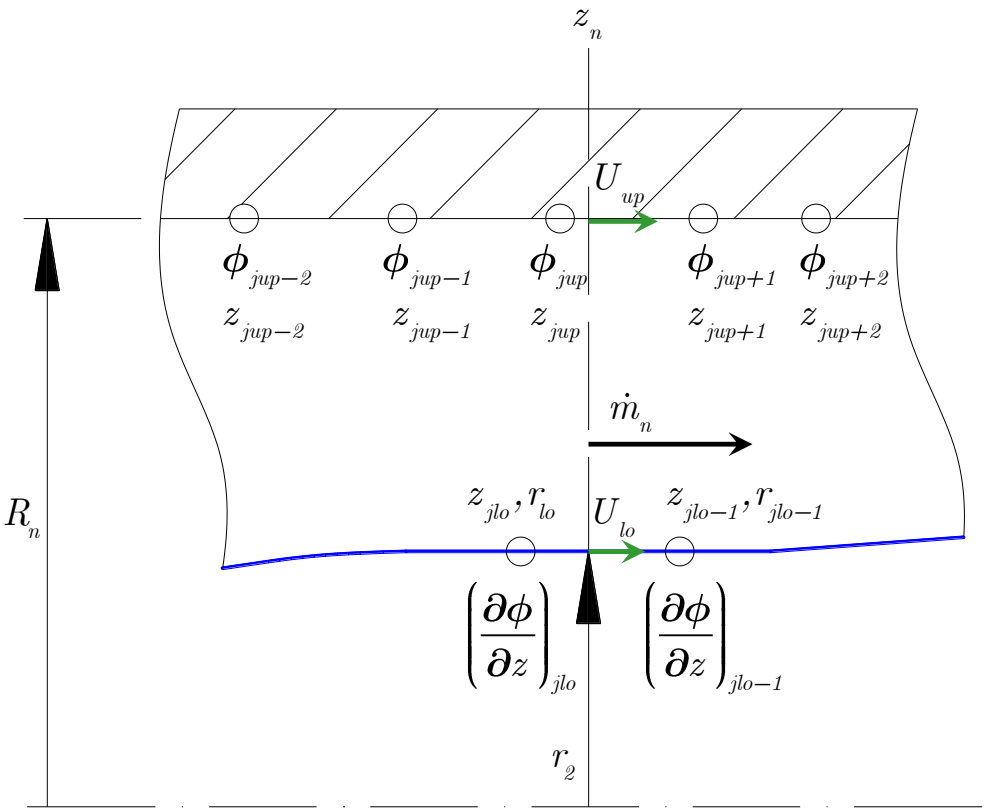


Figure 7.11.: Schematic of flow parameters needed for nozzle mass flow rate estimation in BEM

2. On the upper (solid) boundary, we estimate the axial flow velocity $U_{up}$ by the fourth-order constant-grid central difference formula [127, Tab. 5.1] given by

$$U_{up} = \frac{\phi_{jup-2} - 8\phi_{jup-1} + 8\phi_{jup+1} - \phi_{jup+2}}{3\left(z_{jup+2} - z_{jup-2}\right)}$$

Note that, even though our grid on the nozzle boundary is non-uniform due to stretching, we presume here roughly that, at the center of the nozzle and its vicinity, the distances between the nodes are not much different. On the lower (free surface) boundary, the axial velocity $U_{lo}$ is estimated by a linear interpolation given by

$$U_{lo} = \left(\left(\frac{\partial\phi}{\partial z}\right)_{jlo-1} - \left(\frac{\partial\phi}{\partial z}\right)_{jlo}\right)\frac{z_n - z_{jlo}}{z_{jlo-1} - z_{jlo}} + \left(\frac{\partial\phi}{\partial z}\right)_{jlo}$$

Note that the counting of the nodes is arranged in the clockwise direction.

3. The radius of the free surface is estimated by the similar linear interpolation from the radii of two neighboring points

$$r_2 = (r_{jlo-1} - r_{jlo}) \frac{z_n - z_{jlo}}{z_{jlo-1} - z_{jlo}} + r_{jlo}$$

4. The velocity profile between the velocitis $U_{lo}$ and $U_{up}$ is assumed to be linear and is represented as

$$U(r) = (U_{up} - U_{lo}) \frac{r - r_2}{R_n - r_2} + U_{lo}$$

5. Integrating these velocities over the cross-section $R_n - r_2$ we obtain the nozzle mass flow rate:

$$\begin{aligned} \dot{m}_n &= \int_{r_2}^{R_n} U(r) 2\pi r dr = \int_{r_2}^{R_n} \left[ (U_{up} - U_{lo}) \frac{r - r_2}{R_n - r_2} + U_{lo} \right] 2\pi r dr \\ &= \pi \left[ U_{lo} \left( R_n^2 - r_2^2 \right) + 2 \frac{U_{up} - U_{lo}}{R_n - r_2} \left( \frac{R_n^3 - r_2^3}{3} - r_2 \frac{R_n^2 - r_2^2}{2} \right) \right] \end{aligned}$$

Finally, when we post-process the nozzle mass flow rate data array of all computational time steps, we can say that its average (or steady state) value and its fluctuation are given by

$$\begin{aligned} \bar{\dot{m}}_n &= \frac{\max(\dot{m}_n(t)) + \min(\dot{m}_n(t))}{2} \\ \dot{m}'_n &= \frac{\max(\dot{m}_n(t)) - \min(\dot{m}_n(t))}{2} \end{aligned}$$

## 7.7 Grid Convergence Study of Baseline Case

The baseline case injector considered in this chapter has the same nondimensional characteristics as described in Tables 2.2 and 2.3, with the exception for the vortex chamber length, which is now shorter by $2R_t$, or $L_v = 19$.

In the parametric studies of the injector resonance coming later, we will be investigating the flow fluctuation in the injector at frequencies from close to zero up to approximately 1300 Hz. If we go back to Table 5.2, this means that we will cover the expected resonant modes roughly from the first to the fifth, whose values are

respectively $f_0^* = 226.2$ Hz and $f_0^* = 1131.1$ Hz. To choose the time step, $dt$, for the BEM simulations in this chapter, let us convert the last covered resonant mode into its corresponding nondimensional period:

$$T_0 = \frac{1}{f_0^*}\frac{\bar{W}_{in}^*}{R_n^*} = \frac{1}{1131.1 \text{ Hz}}\frac{3.7596 \text{ m/s}}{0.25 \text{ in} \cdot 0.0254 \text{ m/in}} = 0.5234$$

In accord with that, let us choose a time step which is 3 orders of magnitude smaller than that resonant period, or $dt = 0.0005$. It is assumed that this time step is small enough to capture all wave disturbance processes occurring in the injector.

From Section 7.4, it follows that the main parameters that set the grid size are: $ds_{grid}$, which is the length of an element on the free surface boundary, and $N_h$, which is the number of the stretched intervals on the inflow boundary.

In all cases, we choose the number of intervals on the inflow boundary to be $N_h = 20$, because the author believes that, on the solid boundary, this produces a large enough grid to reduce the number of nodes, and, at the same time, a small enough grid to produce the expected steady free surface shape that matches well with the theoretical steady state predictions of Bazarov [1].

To choose a particular grid size, $ds_{grid}$, appropriate for this study, initially, at $t = 0$, we deflect the free surface from its normal steady state shape by setting the following initial conditions:

- The core radius is set to be uniform in $z$ direction starting from the inflow boundary, $z = 0$, until the nozzle end, $z = L_v + L_c + L_n$, Fig. 7.12. Its value is set to be equal to $r_v/1.5 = 0.7177/1.5 = 0.4785$, where $r_v$ is the theoretical steady nondimensional core radius in the uniform vortex chamber region (see Table 2.3).

- At the nozzle end, an additional cylindrical section ending with a toroidal cap is added to represent the initial shape of the spray cone, Fig. 7.12.

- The velocity potentials on the free surface are set to be distributed as

$$\phi_j = \frac{\bar{\dot{m}}_{in}}{\pi\left(R_v^2 - (r_v/1.5)^2\right)} z_j$$

where, from Tables 2.2 and 2.3, the steady state incoming mass flow rate is given by $\bar{\dot{m}}_{in} = N_{in}\pi R_t^2 \bar{W}_{in} = 4 \cdot \pi \cdot 0.5^2 \cdot 1 = \pi$

- The inflow velocity is set based on that incoming mass flow rate as well,

$$q_{in} = \frac{\bar{\dot{m}}_{in}}{\pi \left(R_v^2 - (r_v/1.5)^2\right)}$$

After that, we let the flow to adjust and reshape due to its tendency to achieve the maximum flow rate in the nozzle (Chinn [4, Subsec. 3.3.1], Binnie [128, Chap. 4]) and observe how its characteristics converge to constant values, Fig. 7.12. This process is governed largely by the time stepping procedure outlined in Section 7.5. We will observe the convergence of the free surface radii $r_1$ (see Fig. 7.9) and $r_2$ (see Fig. 7.11), which shall tend to the respective theoretical steady radii $r_v$ and $r_n$ (see Fig. 2.1). When the code converges, we shall make a choice of $ds_{grid}$, based on which converged solution best matches the steady theoretical predictions of Bazarov [1].

For the baseline injector, which is a rather long injector, the preliminary investigation shows immediately that we are bounded by the following range of the grid sizes: $ds_{grid} = 0.06 \ldots 0.09$. The lower limit of this range follows from the consideration that we want to keep the size of the solution matrices at each time step smaller than 1000x1000, and the grid size smaller than 0.06 generates larger matrices. The upper limit follows from the fact that, beyond the grid size of 0.09, we are running into a situation when the distances the nodes cover during their motion at each time step become larger than the spray film thickness, which consequently results in the overlapping of some of the nodes over the others on the spray boundary, which, eventually produces singularities in the solution. Conclusively, the grid sizes that we have chosen to test are: $ds_{grid} = 0.06,\ 0.07,\ 0.08,\ 0.09$.

In the following two subsections, we will investigate the influence of these grid sizes on the free surface behavior at both the steady and the unsteady states. When considering the unsteady state, we will also show the sensitivity of the injector response to the grid size.

### 7.7.1 Steady State Convergence

Figure 7.13 shows the time history of the radii $r_1$ and $r_2$ as the the flow converges from its initial state to the steady state. The resulting final value of $r_1$ and $r_2$ and the corresponding theoretical values for $r_v$ and $r_n$ from Table 2.2 are summarized in Table 7.1. Also shown are the computational times it took to run each grid size case. Each case in this section and further on in this chapter has been computed using a single 2.4 GHz processor.

We can see that the results for the grid sizes of 0.06 and 0.07 are the most satisfactory. On the one hand, the grid size of 0.07 produces the closest results for $r_1$ and $r_2$ relative to their corresponding theoretical values $r_v$ and $r_n$. On the other hand, the values of $r_1$ at different grid sizes suggest that the the grid size of 0.06 is the one where we achieve convergence. We shall note that, even if there is a 16 hour compute time difference between the 0.06 and 0.07 cases, we are interested in having a smaller grid size, with the idea that it may capture the free surface disturbance waves (ideally infinitesimally small) better than the larger grid size. Later on, we will have a more extended discussion on this subject.

Table 7.1: Grid convergence results for $r_1$ and $r_2$ (baseline injector)

| Grid size, $ds_{grid}$ | $r_1$ | $r_v$ | $r_2$ | $r_n$ | Time, hours |
|---|---|---|---|---|---|
| 0.06 | 0.7200 | 0.7177 | 0.8122 | 0.8077 | 59.3 |
| 0.07 | 0.7193 | 0.7177 | 0.8087 | 0.8077 | 43.8 |
| 0.08 | 0.7186 | 0.7177 | 0.8204 | 0.8077 | 34.3 |
| 0.09 | 0.7175 | 0.7177 | 0.8242 | 0.8077 | 28.5 |

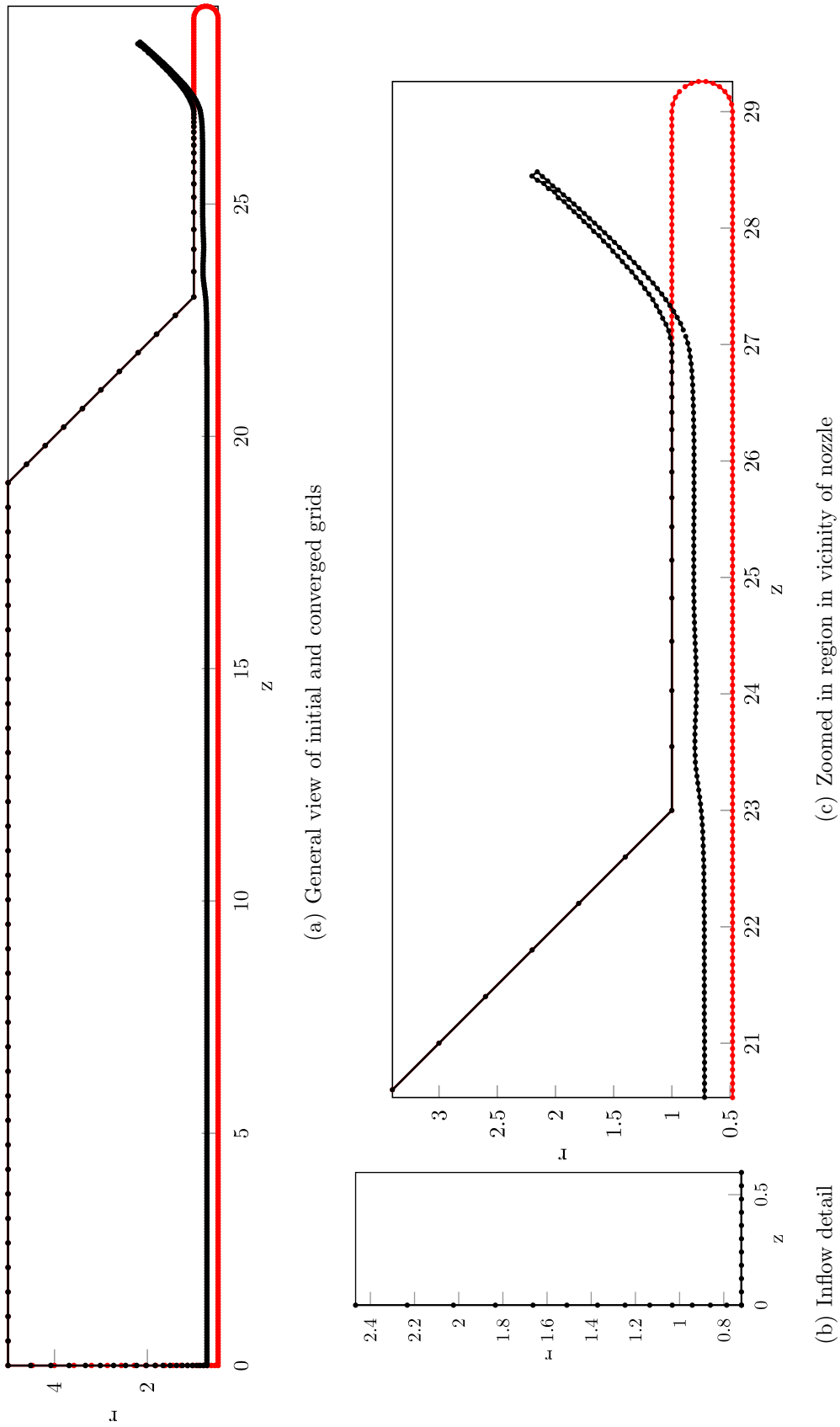


(a) General view of initial and converged grids

(b) Inflow detail

(c) Zoomed in region in vicinity of nozzle

Figure 7.12.: Transition of free surface from initial to steady state shape with illustration of node locations for $ds_{grid} = 0.06$ (initial shape shown in red)

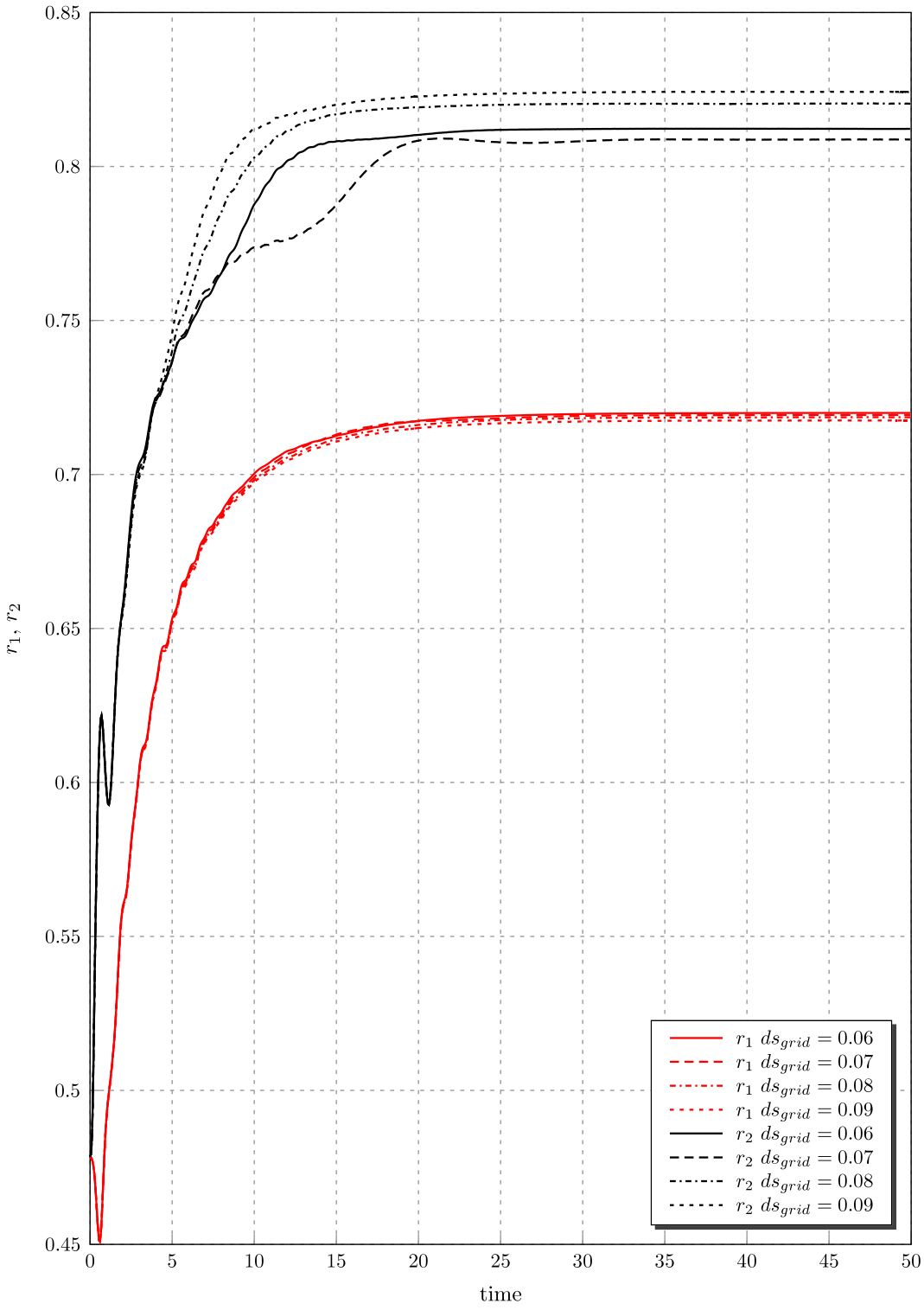


Figure 7.13.: Convergence of transient free surface radii $r_1$ and $r_2$ from initial to steady state values as a function of grid size, $ds_{grid}$

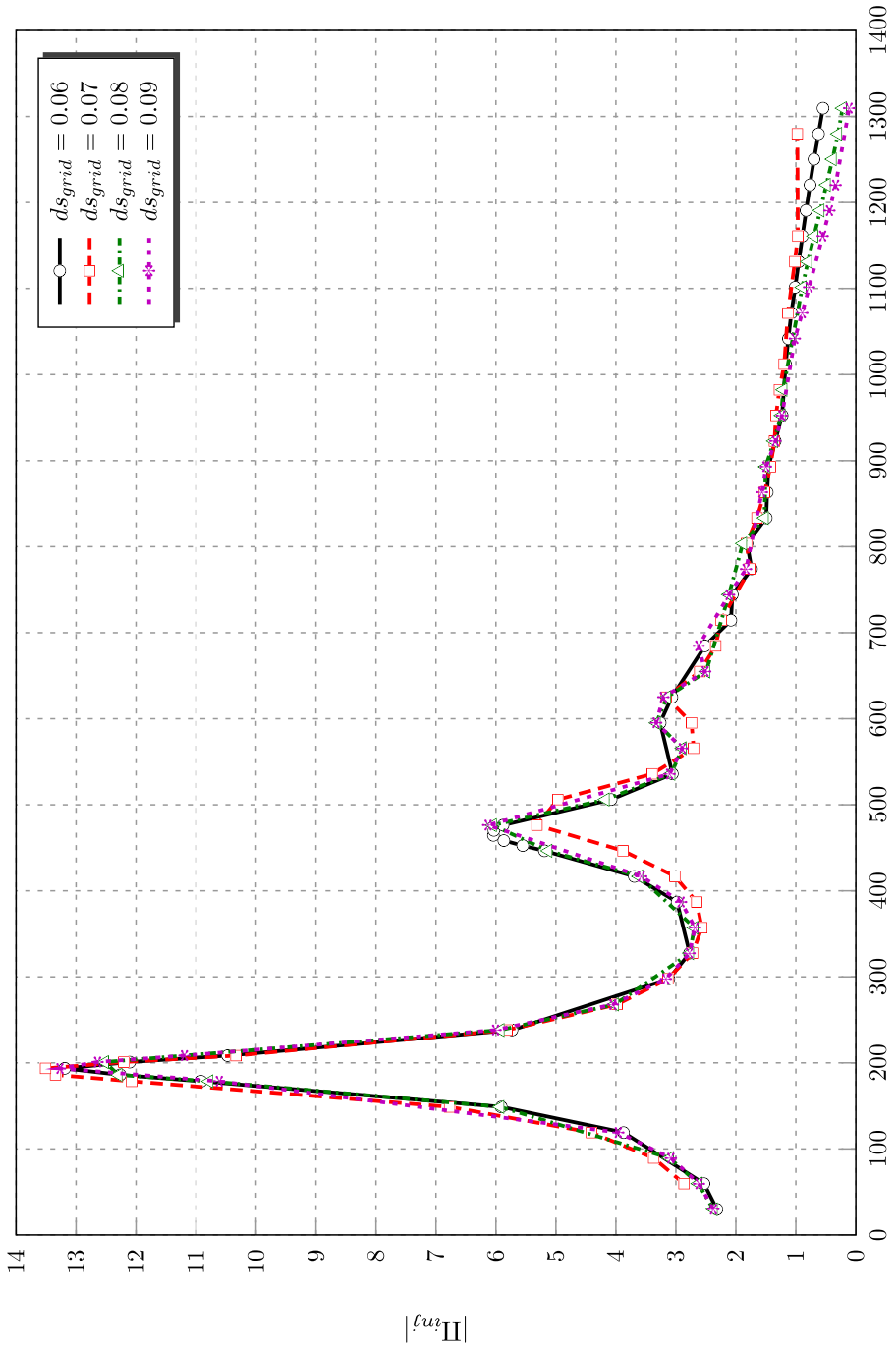


Figure 7.14.: BEM injector response sensitivity to grid size variation (baseline injector)

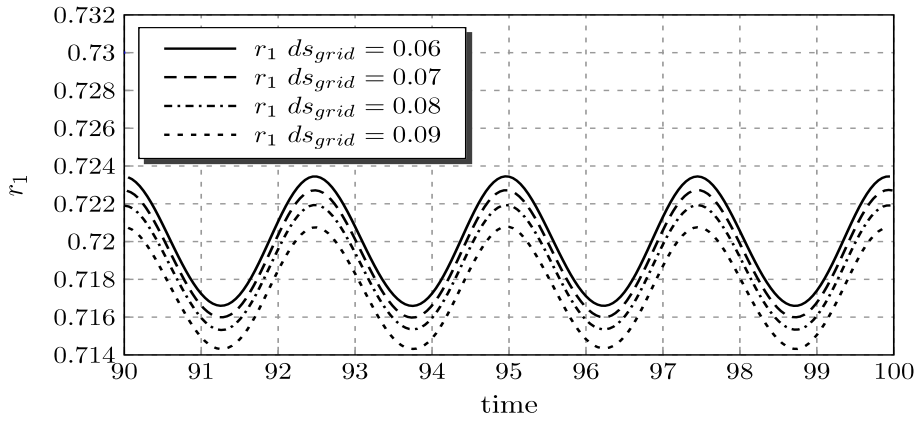


(a) Fluctuation of free surface radius at inflow boundary

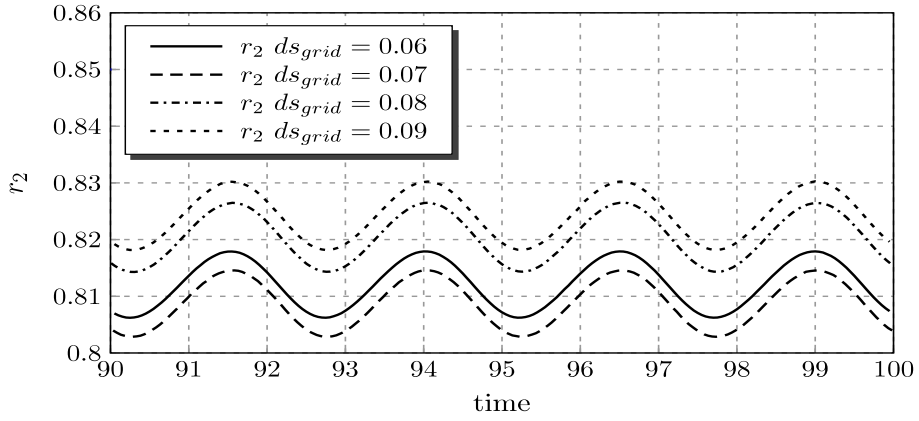


(b) Fluctuation of free surface radius at nozzle center

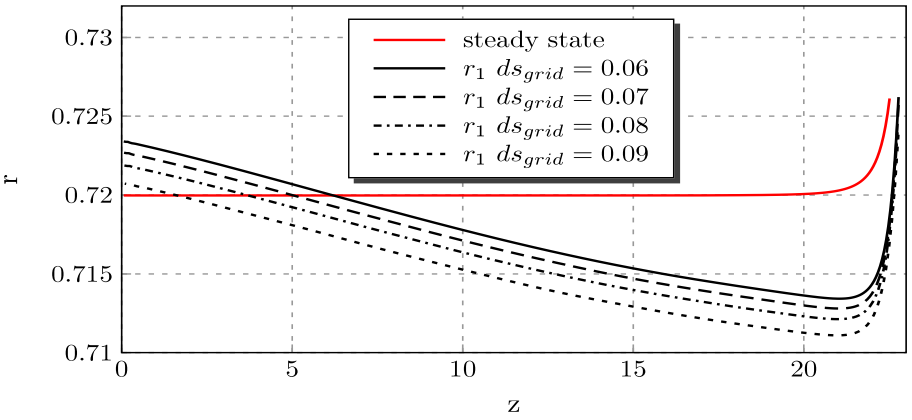


(c) Corresponding wave shapes in vortex chamber at time $t = 100$

Figure 7.15.: Convergence of unsteady free surface radii and corresponding wave shapes as a function of grid size, $ds_{grid}$ (baseline injector, $f^* = 238.1$ Hz, pulsation magnitude $q_{osc} = 30\%$, pulsation started at time $t = 50$)

### 7.7.2 Unsteady State Convergence

We can also run the grid convergence study of the unsteady pulsed flow to have an additional information about the solution sensitivity to the grid size. As was mentioned above, we will start running the pulsed cases from the point where we had the converged solution in the steady runs, and the inflow velocity will be governed by the sinusoidal law (see Section 7.5). In all unsteady cases in this chapter, as well as in this subsection, we let the steady flow to continue for a little while after $t = 50$, then, start the pulsations at $t = 50.0100$, and finish them at $t = 100$, with the pulsation magnitude $q_{osc} = 30\%$, which is baseline pulsation level. In the next section, there will be more discussion with regard to the choice of this magnitude. Note that it takes about the same time to compute the unsteady cases from $t = 50$ to $t = 100$ as to compute the steady cases from $t = 0$ to $t = 50$ (see Table 7.1).

First, let us compute the injector response for the considered grid sizes in the range of frequencies from $f^* = 0 \ldots 1300$ Hz. Note that, in order to do that, at each frequency, we choose a time interval $t = 70 \ldots 99.5$, where we can consider that the disturbances are stabilized. In Fig. 7.14, we can observe that the response curves for all grid sizes are roughly identical, which does not leave us with a definite choice of the grid size.

To resolve this ambiguity, let us now consider the frequency of 238.1 Hz, which is close to the first peak, and where we can observe that the values of the BEM injector responses do not differ much. At the frequency of 238.1 Hz, the stabilized pulsations of $r_1$ and $r_2$ are shown in Fig. 7.15, together with the wave shapes corresponding to them at the final time $t = 100$. In Fig. 7.15(a), we can see that the convergence for the free surface radius at the inflow boundary, $r_1$, is achieved at $ds_{grid} = 0.06$. On the other hand, in Fig. 7.15(b), we can see that the free surface radius at the center of the nozzle, $r_2$, converges at $ds_{grid} = 0.07$. However, from Fig. 7.15(c), which shows the converged wave shapes, we can conclude that we achieve convergence, when the grid size $ds_{grid} = 0.06$ is used.

Then, gathering together the conclusions with regard to the steady state convergence in the previous subsection with the conclusions with regard to the unsteady state convergence in this subsection, we conclude that $ds_{grid} = 0.06$ is the grid size where we achieve convergence, and use that size for further investigations in this chapter.

## 7.8 Assessment of Nonlinearity and Choice of Pulsation Magnitude

In this section, we wish to assess the effect of pulsation magnitude on the injector response and the free surface fluctuation. By performing this assessment, we can figure out if the nonlinearity effects start to appear, and if they do – at what pulsation magnitude? To do that, let us consider the pulsation of the baseline injector with magnitudes $q_{osc}$ equal to 5%, 10%, 30%, and 50%, at the frequency of 476.3 Hz (which is the frequency close to the second peak in Fig. 7.14), at $ds_{grid} = 0.06$.

Figure 7.16 shows the injector responses at various pulsation magnitudes. We can see that all responses line up quite well. On the other hand, Fig. 7.17 and Table 7.2 show the time histories, and the average and fluctuation values of the free surface radii $r_1$ and $r_2$ (where the latter were computed as shown above in Subsection 7.6.1). From Table 7.2, we can conclude that free surface fluctuation increases roughly linearly with the increase of pulsation magnitude. Notice that, at pulsation magnitudes of 5% and 10%, the unsteady free surface in the nozzle deviates from its steady state by only 0.16% and 0.31%. This may be better visulized if we take a look at Fig. 7.18, which shows the wave shapes developing in the vortex chamber and the nozzle at different pulsation magnitudes, at time $t = 100$. In Fig. 7.18(b), we can see that at 30% pulsation we get a much more distinctive wave shape in the nozzle than at 5% and 10%.

At the same time, by looking at the time histories of $r_1$ and $r_2$ in Fig. 7.17, we can conclude that the pulsation can be well described as linear at all considered magnitudes. A question may arise now: why do we get a linear sinusoidal fluctuation

Table 7.2: Response of free surface radii $r_1$ and $r_2$ to various pulsation magnitudes (baseline injector, $f^* = 476.3$ Hz)

| $q_{osc}$ | $\bar{r}_1$ | $r_1'$ | $r_1'/\bar{r}_1$ | $\bar{r}_2$ | $r_2'$ | $r_2'/\bar{r}_2$ |
|---|---|---|---|---|---|---|
| 5% | 0.7200 | 0.0007 | 0.0981% | 0.8121 | 0.0013 | 0.1579% |
| 10% | 0.7200 | 0.0014 | 0.1961% | 0.8121 | 0.0025 | 0.3135% |
| 30% | 0.7199 | 0.0042 | 0.5868% | 0.8120 | 0.0076 | 0.9360% |
| 50% | 0.7199 | 0.0070 | 0.9772% | 0.8119 | 0.0127 | 1.5588% |

of the free surface at pulsation magnitudes as strong as 30% or 50%? These numbers seem large, however, bear in mind that the bulk flow velocity in the vortex chamber is quite small. From Table 2.3, it is $\bar{u}_{zv} = 0.0408$, compare that to the expected long wave speed in the vortex chamber from Table B.1, $c_v = 30.6089$. Thus, the resulting bulk flow pulsation may be considered as quite weak, which accordingly results in the linear fluctuation of the free surface.

To make a final selection of the pulsation magnitude, we discard the 5% and 10% magnitudes, as they do not deform the free surface sufficiently from the steady state, and 50% magnitude, as we do not want to move away from the linear theory too much, which leaves us with the 30% magnitude. This will be the pulsation magnitude which we will further use in the parametric studies coming later on in this chapter.

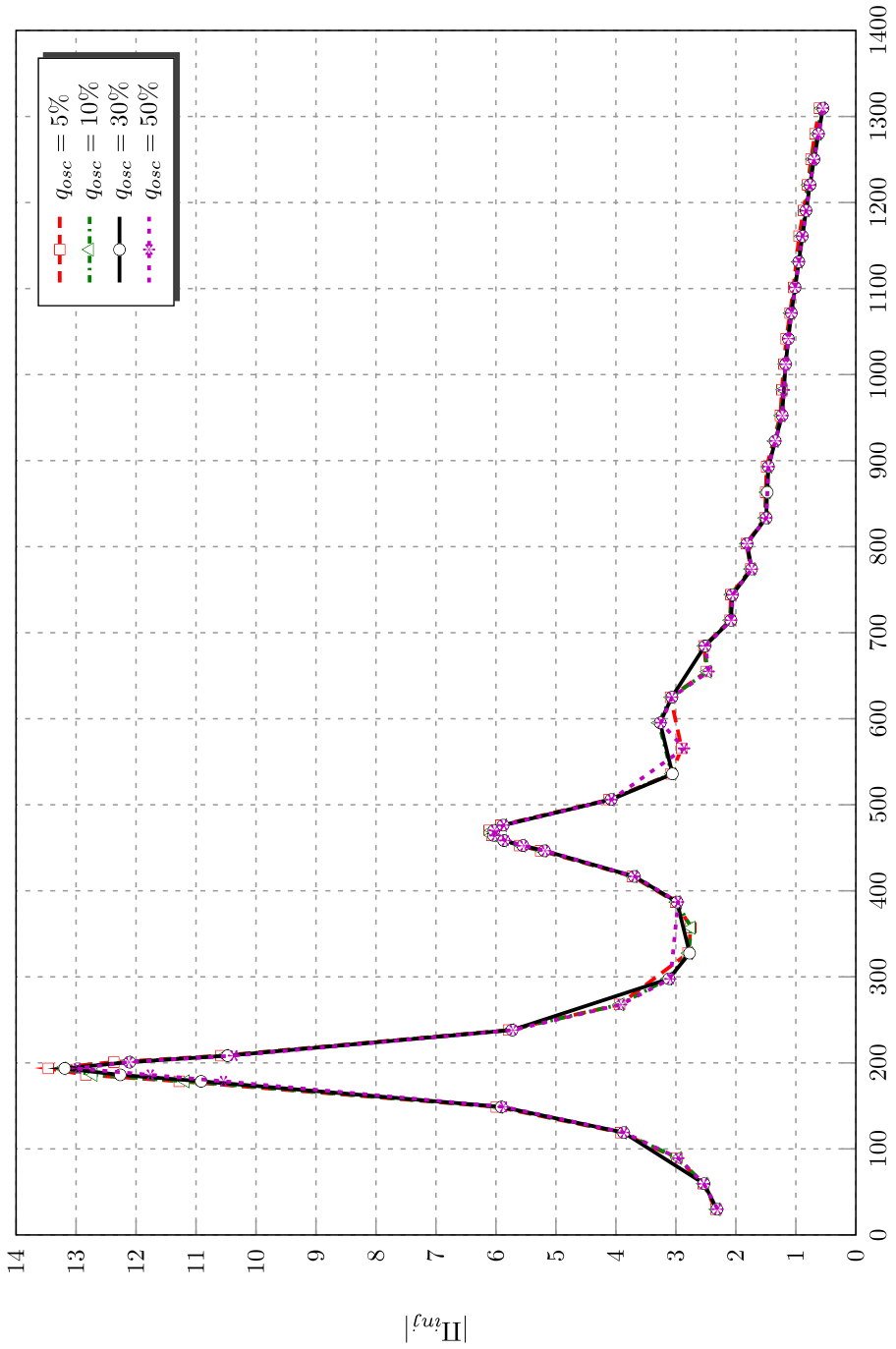


Figure 7.16.: BEM injector response sensitivity to pulsation magnitude variation (baseline injector)

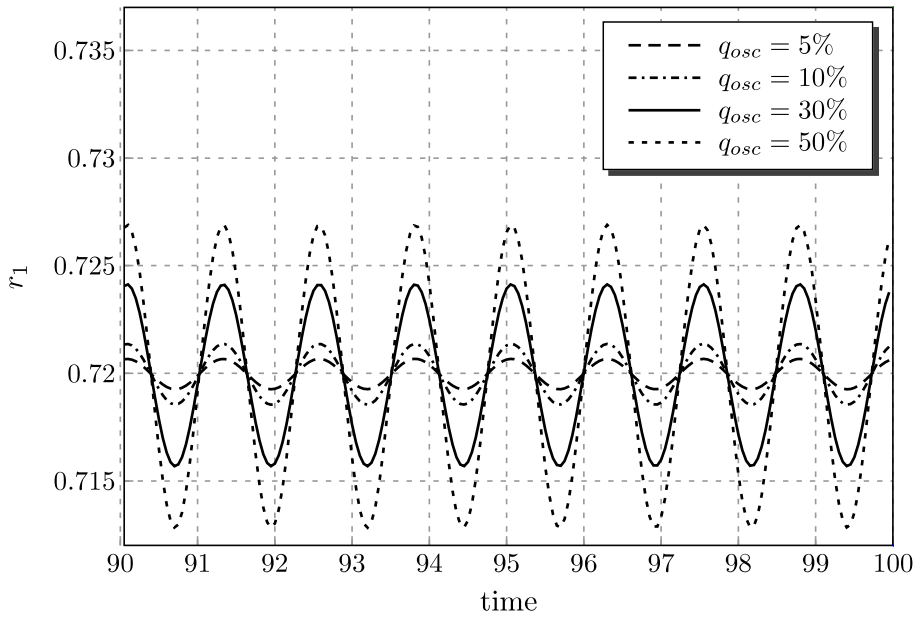


(a) Fluctuation of free surface radius at inflow boundary

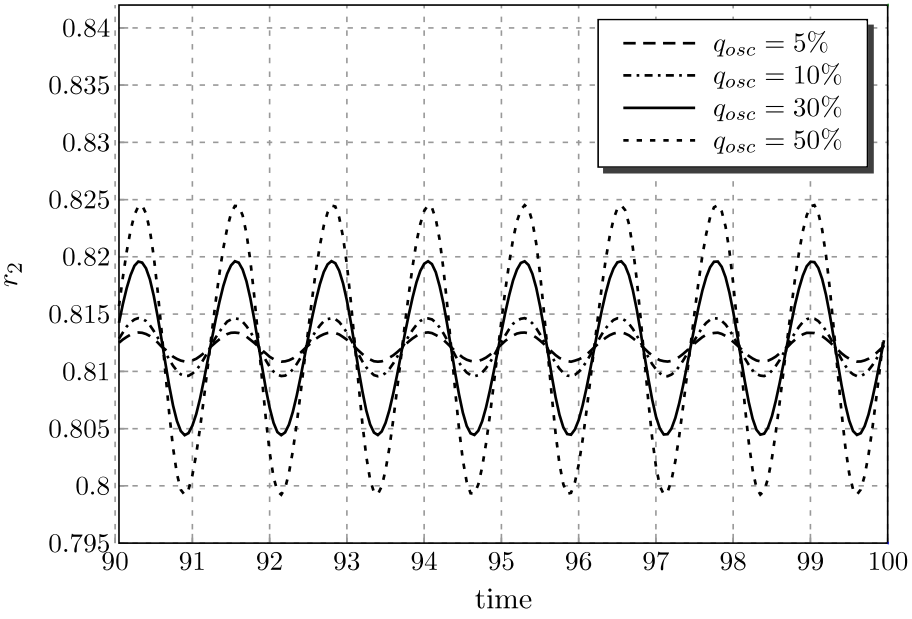


(b) Fluctuation of free surface radius at nozzle center

Figure 7.17.: Stabilized fluctuation of unsteady free surface radii as a function of pulsation magnitude, $q_{osc}$ (baseline injector, $f^* = 476.3$ Hz, pulsation started at time $t = 50$)

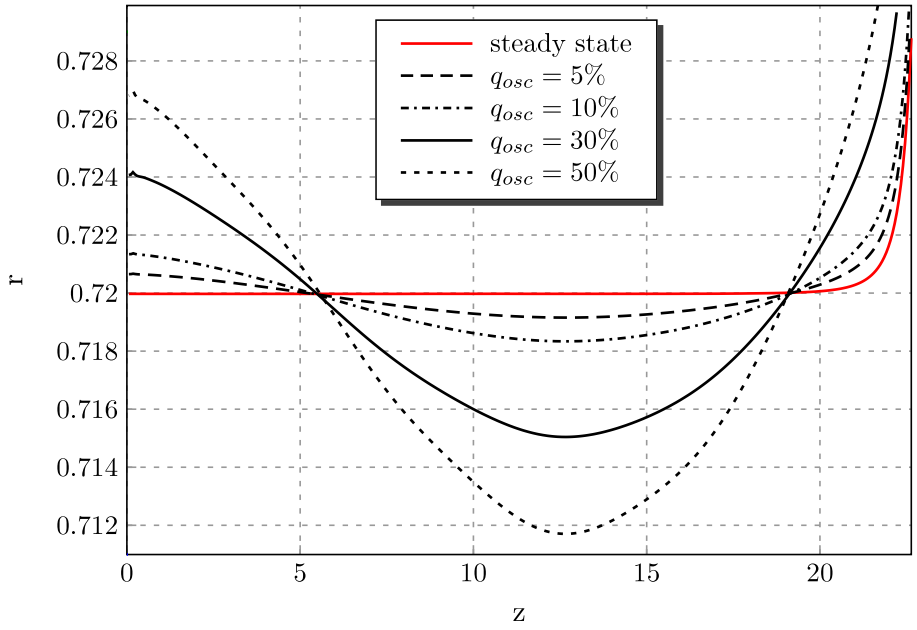


(a) Wave shapes in vortex chamber upon uniform steady free surface

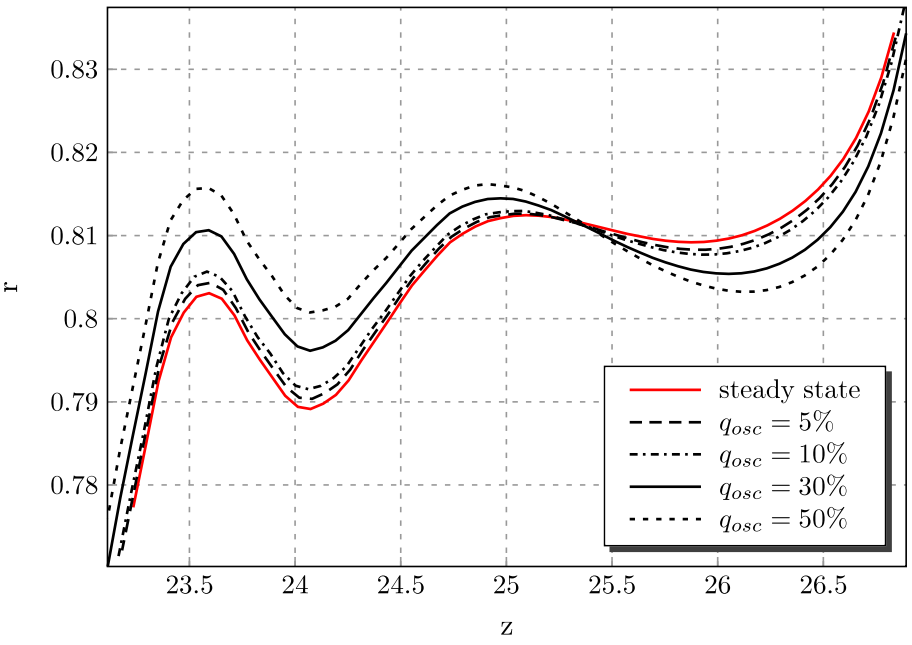


(b) Wave shapes in nozzle upon nonuniform steady free surface

Figure 7.18.: Wave shapes in vortex chamber and nozzle as a function of pulsation magnitude, $q_{osc}$, at time $t = 100$ (baseline injector, $f^* = 476.3$ Hz, pulsation started at time $t = 50$)

## 7.9 Parametric Studies of Unsteady Flow, Validation of Resonant Modes

In this section, we will obtain the injector response as a function of disturbance frequency, $\omega$, by the sinusoidal variation of the inflow velocity, $q_{in}$, with the amplitude of 30% of its steady state value, and the grid size of $ds_{grid} = 0.06$ (see discussion in Sections 7.7 and 7.8 on their choices), and assess its sensitivity to the following charactersitics of the BEM injector:

- conical convergence angle, $\alpha$,
- vortex chamber length, $L_v$,
- nozzle length, $L_n$,
- vortex chamber radius, $R_v$,
- steady tangential inlet inflow velocity, $\bar{W}_{in}$.

In each parametric study, in addition to the computational BEM injector response results, we will also present the following two sets of results:

- The images of the converged steady state flow boundaries in the vicinity of the conical convergence and the nozzle sections in order to have a visual understanding of how the free surface shape has changed with regard to the change in a particular parameter. By doing this, we will observe whether or not the way how the free surface transitions from the vortex chamber to the nozzle is similar to the way we have described it in Chapter 3. This is important to know, because this transitional shape was one of the input parameters in the conical convergence resonance model in Chapter 5.
- The analytical results for the first two resonant modes of the "real" injector following from the resonance models in Chapter 5. Note that, in all cases below, the vortex chamber of the "real" injector will be by one nondimensional length unit longer than that of the BEM injector.

In each study, we will make a conclusion of how well the frequencies, where the computational response peaks out, match the analytical resonant frequencies. The resonant peaks will be summarized in the tables for convenience. As before in Chapter 5, we will have the following abbreviations:

- ACRM's = Abrupt Convergence Resonance Models, which include ACRM-1 and ACRM-2, and

- CCRM = Conical Convergence Resonance Model, where we preserve 8 cylindrical sections in nozzle entrance transition in all studied cases.

We will conclude the parametric studies with the illustration of the wave patterns from the BEM simulations, which occur respectively when the injector is at resonance, and when it is not.

### 7.9.1 Conical Convergence Angle Variation

For this parametric study, we have already seen the converged shapes of steady free surfaces in the nozzle entrance transition region in Chapter 3. There, we have concluded that the free surface is almost insensitive to the conical convergence angle, $\alpha$, and that it can be assumed that the transition starts at the distance of $-0.5R_n$ and ends at $+0.5R_n$ relative to the point where the conical section of the injector ends and the nozzle starts (see Section 3.4).

From the compound image of the BEM injector responses in Figs. 7.19 and 7.20, whose peaks are summarized in Table 7.3, we can overall see that the response peaks shift to higher frequencies, as the convergence angle becomes steeper. This behavior to shift to the higher frequencies can be explained as follows: (a) the steeper the convergence, the shorter the total distance, over which the disturbances may travel back and forth in the vortex chamber and the conical convergence section; (b) due to (a), the shorter standing waves in the vortex chamber are naturally selected (see Chapter 5 for more discussion); (c) but the shorter standing wave selection, or generation, means higher disturbance frequencies are involved.

With regard to the BEM peak magnitudes in Fig. 7.19, we can not see any pronounced tendency to grow larger or smaller, neither around the first peak, nor around the second peak. We can attribute this to the following facts: (a) the amplitude of oscillation is closely related to the mass of the swirling liquid body upstream of the nozzle, which we will clearly see in the next parametric study when we vary the vortex chamber length; (b) when we vary the convergence angle, the total volume of that liquid body does not change drastically, since the dominant vortex chamber length is kept constant. Also note that, from the practical standpoint, we can not guess the peaks exactly, since that would require a much larger number of computational points around each of them.

From the way the ACRM's were setup in Chapter 5, we know that they are by definition insensitive to the conical convergence angle, $\alpha$, because it is assumed that the abrupt step discontinuity is placed right at the point where the conical convergence section begins. Therefore, in Fig. 7.21(a) and in Table 7.3, we have shown only the results for the baseline injector, which we have already seen in Chapter 5. On the other hand, in Fig. 7.21(b), we can observe that the CCRM does react to the $\alpha$ variation in the same manner as the BEM has shown, the peaks have the overall tendency to shift to the higher frequencies, and the intensity of the outgoing waves, $a_2$, does not exhibit any visible trend, except in the steep angle case of 80°, where it has grown much larger. The latter feature may be expected, because the upstream traveling waves would grow to larger magnitudes in steeper convergence geometries, which overall would lead to larger magnitudes of the outgoing wave (see Section 4.4).

In Table 7.3, we have indicated by the red color the peak frequencies where the ACRM's best match those of BEM, and by the blue color – the peaks best matching using the CCRM, with the accuracy within 10%. Further on, we will do the same in the next subsections.

From Table 7.3, we can conclude that the ACRM's have reproduced the first BEM peak relatively well only at convergence angles steeper than 60°. On the other hand, there is an excellent matching of the second peak frequencies of BEM with the

Table 7.3: Summary of resonant peaks for conical convergence angle variation cases (based on Figs. 7.19–7.22)

| $\alpha$ | Peaks, Hz | BEM | ACRM's | $K_{cor}$ | Corrected ACRM's | CCRM |
|---|---|---|---|---|---|---|
| 30° | Peak 1 | 178.6 | 226.2 | 0.7904 | 178.8 | 116 |
| | Peak 2 | 416.7 | 678.7 | n/a | n/a | 448 |
| 45° | Peak 1 | 193.5 | 226.2 | 0.8508 | 192.5 | 118 |
| | Peak 2 | 464.4 | 678.7 | n/a | n/a | 470 |
| 52.5° | Peak 1 | 196.5 | 226.2 | 0.8810 | 199.3 | 120 |
| | Peak 2 | 488.2 | 678.7 | n/a | n/a | 476 |
| 60° | Peak 1 | 208.4 | 226.2 | 0.9112 | 206.2 | 120 |
| | Peak 2 | 494.1 | 678.7 | n/a | n/a | 471 |
| 70° | Peak 1 | 214.3 | 226.2 | 0.9515 | 215.2 | 122 |
| | Peak 2 | 506.0 | 678.7 | n/a | n/a | 479 |
| 80° | Peak 1 | 226.2 | 226.2 | 0.9918 | 224.4 | 147 |
| | Peak 2 | 523.9 | 678.7 | n/a | n/a | 520 |
| 90° | Peak 1 | 232.2 | 226.2 | 1.0321 | 233.5 | n/a |
| | Peak 2 | 529.8 | 678.7 | n/a | n/a | n/a |

CCRM. This indicates, that we can be fairly sure in calculating analytically the second resonant peak by using the third resonance model at all convergence angles, if there would be no access to expensive BEM computations. The analytical calculation of the first peak however leaves us certain only with the steeper convergence angles, starting largely from 60° as the results show. Note that this can be expected from the way the ACRM's were arranged. Overall, we see here that none of the analytic resonance models provides a single best answer, and that they should rather be used together,

where we would use the ACRM's for the first resonant peak and the CCRM for the second resonant peak. We will see below that this is the case in other parametric variations as well.

We may wonder now, if it is possible to introduce a correction coefficient that accounts for the difference between the first peaks produced by ACRM's and BEM, at the convergence angles $\alpha$ less than 60°. For this purpose, we have plotted the first peak frequencies following from ACRM's and BEM versus all considered angles in Figure 7.22(a). This figure shows that the first resonant peak of BEM depends approximately linearly on $\alpha$. Then, in Fig. 7.22(b), we have plotted the ratio of the first peak frequencies from BEM to the theoretical first resonant frequency. Now, we can fit a straight line through the corresponding data points in Fig. 7.22(b) and define this line as the correction coefficient, $K_{cor}$. The values of $K_{cor}$ at different convergence angles are shown in Table 7.3. Accordingly, if we multiply $K_{cor}$ with the theoretical value of the first peak following from the ACRM's, we can obtain its corrected value at the angles $\alpha < 60°$, which is shown in Table 7.3 under the column named "Corrected ACRM's". Similarly, we will include the corrected values of the first peak in the following parametric studies as well.

In conclusion, we shall take a moment to recognize that the analytical ACRM and BEM values of the first peak for $\alpha = 45°$ in Table 7.3, 226.2 Hz and 193.5 Hz, fall in the ballpark of the experimental peak of 221 Hz in Fig. 7.1, from which we started the whole discussion in this chapter. This supports the vision that this experimental peak is not merely an error in the experimental data processing, but rather a distinct resonant peak. Ideally, we should have had a second experimental peak, whose analytical and computational values we already have in Table 7.3, to be completely certain in this conclusion. But for now, we have three sources of the evidence pointing to the first resonant mode of the swirl injector: the analytical models in Chapter 5, the BEM results in this chapter, and one experimental data point. Let us go on and see if we will be getting other matching peaks predicted by analytics and computations. If they exist, then we will have an even stronger argument.

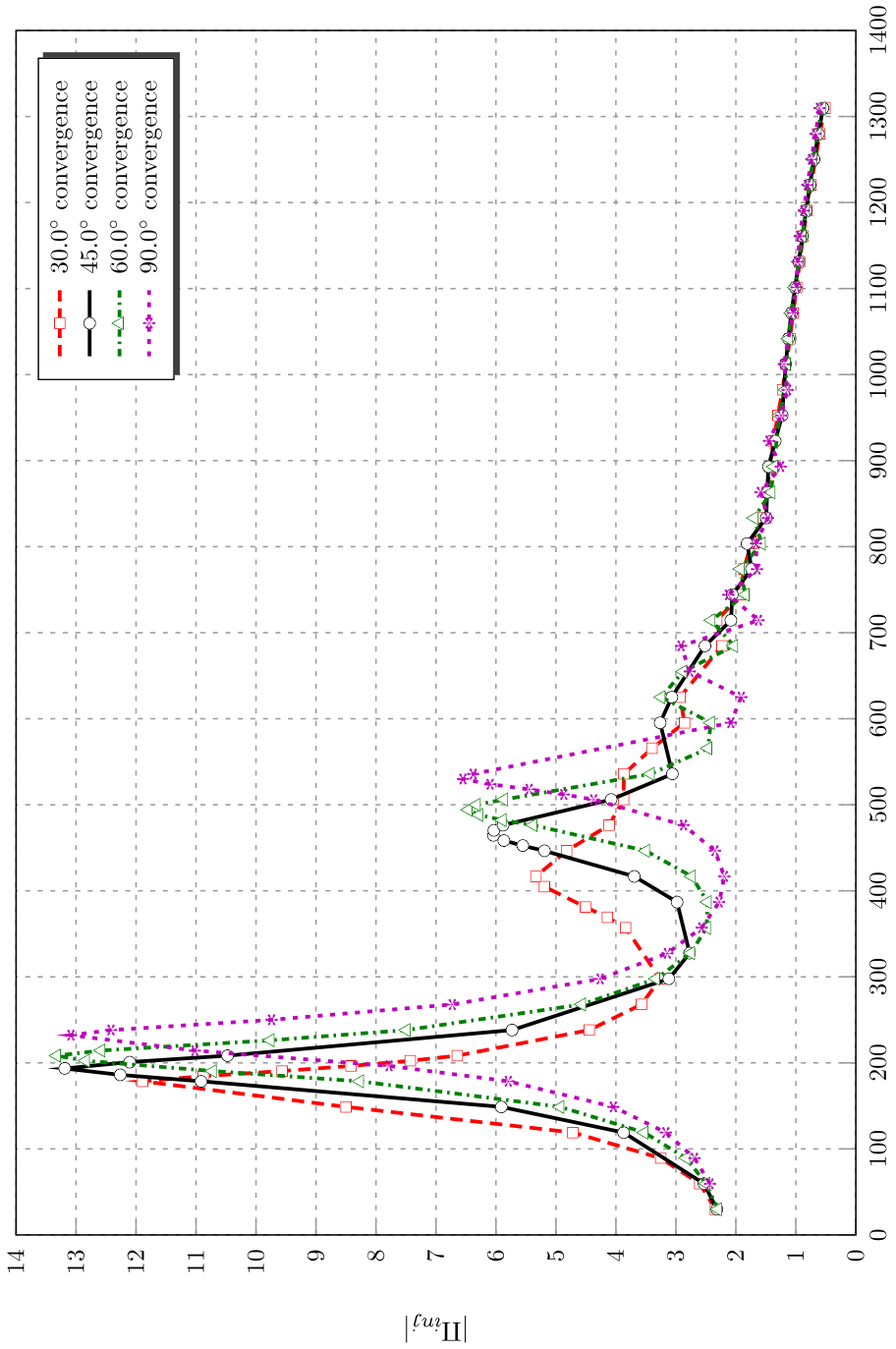


Figure 7.19.: BEM injector response sensitivity to conical convergence angle variation

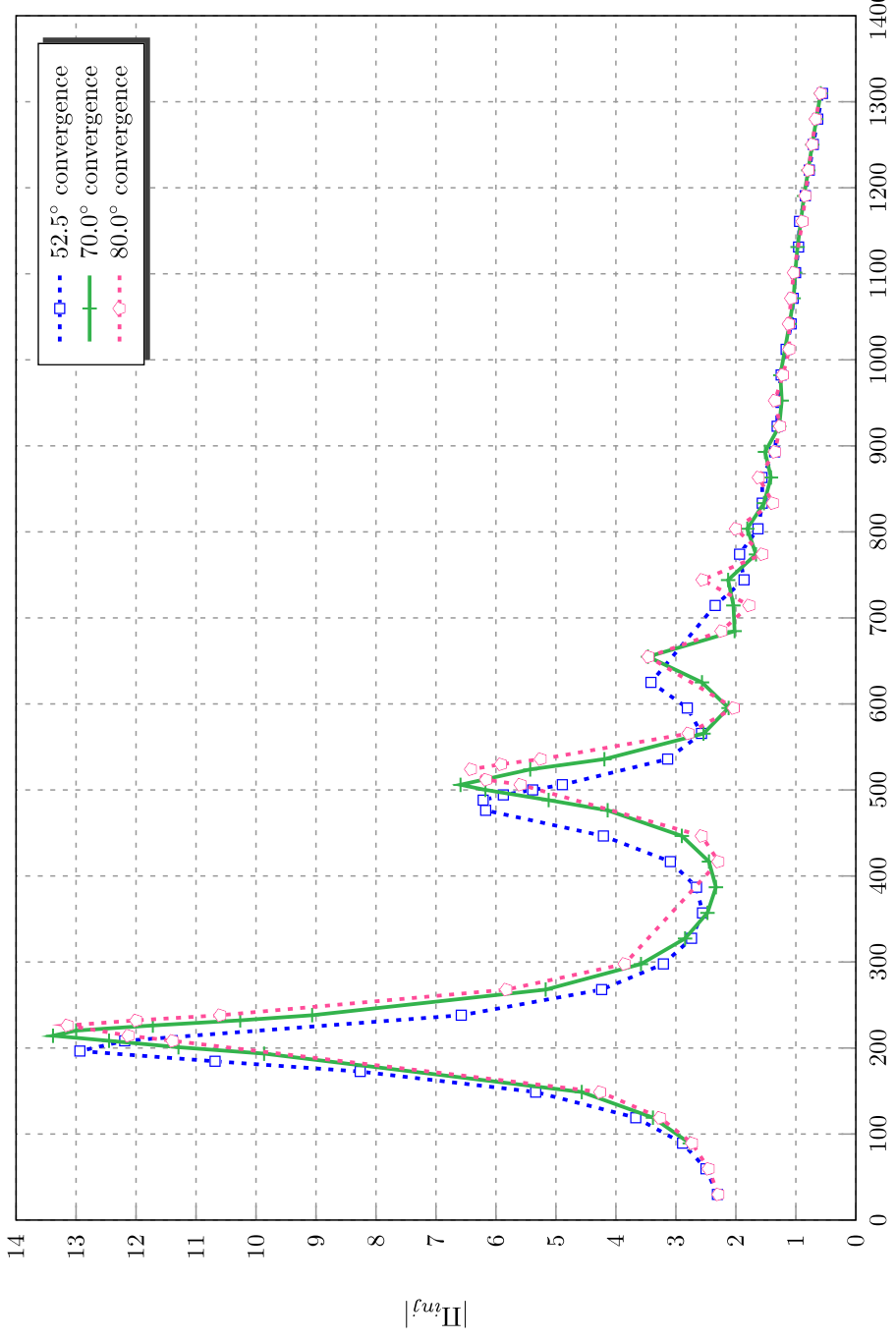


Figure 7.20.: BEM injector response sensitivity to conical convergence angle variation (additional angles)

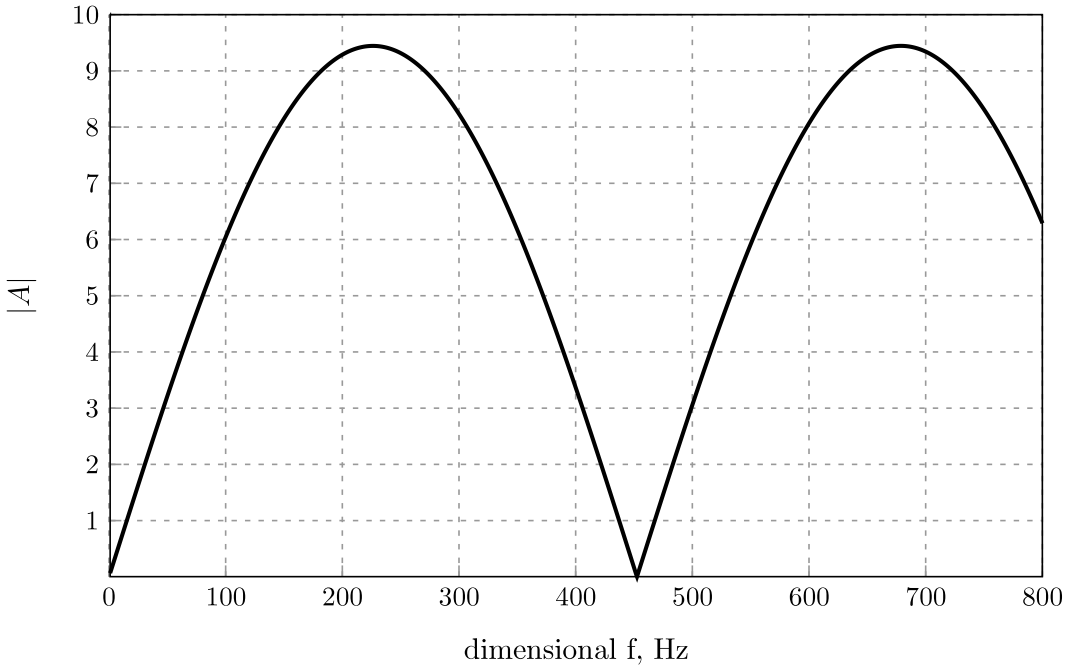


(a) Resonant peaks due to ACRM-2 (same curve for all convergence angles)

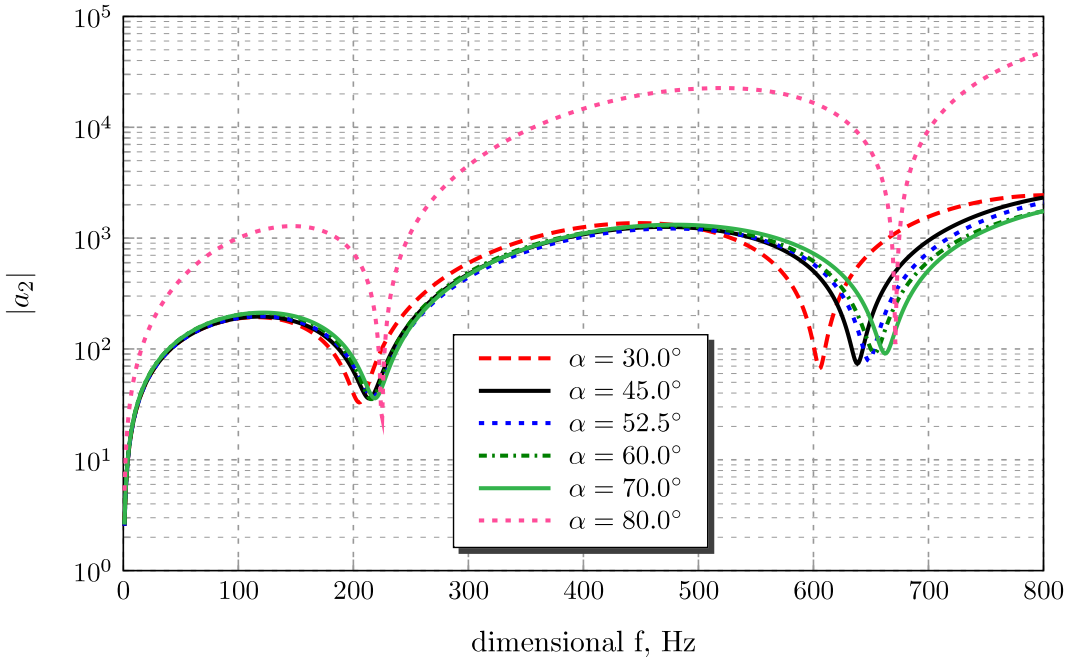


(b) Resonant peaks due to CCRM

Figure 7.21.: Sensitivity of resonant peaks predicted by ACRM's and CCRM to conical convergence angle variation

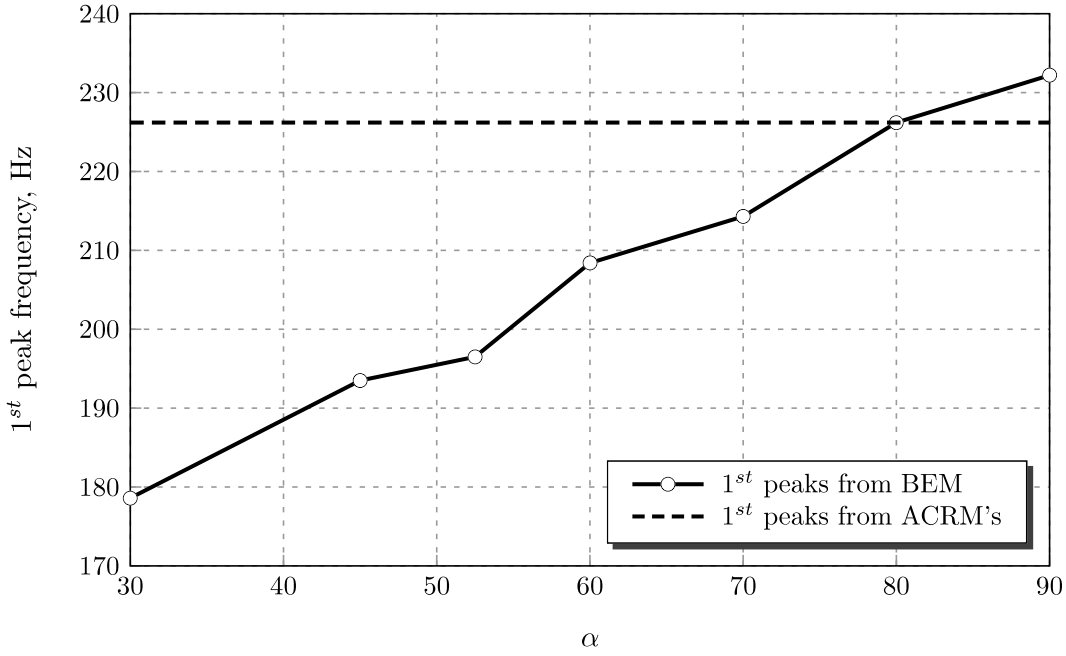


(a) First resonant peaks from BEM and ACRM's (see Figs. 7.19, 7.20, and 7.21(a))

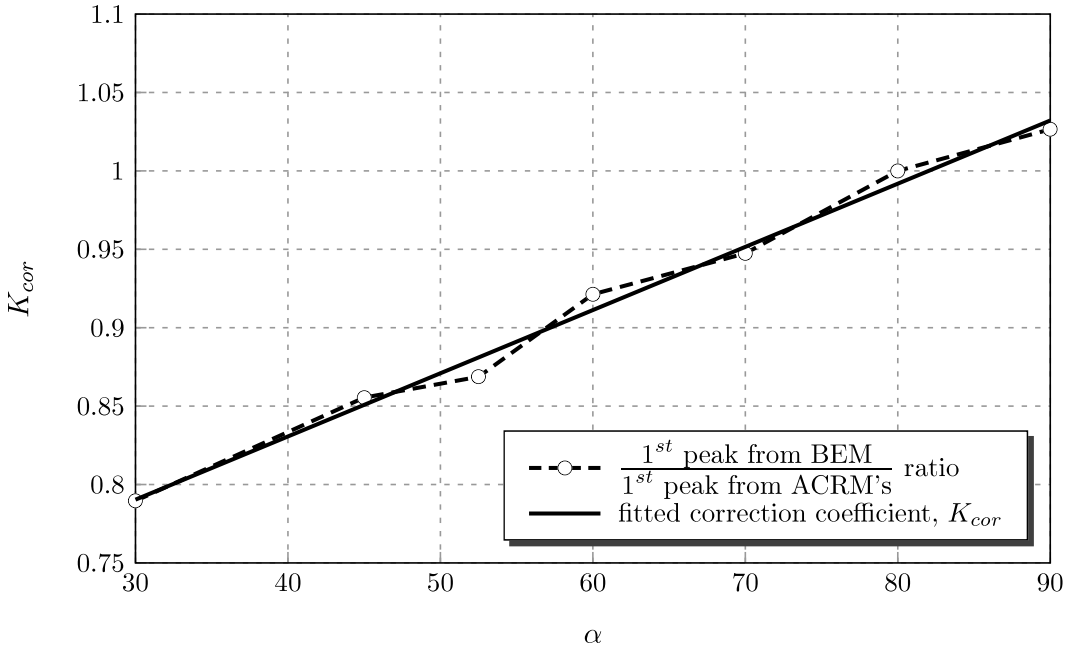


(b) Correction coefficient for first resonant peak in ACRM's

Figure 7.22.: Correction of first resonant peak in ACRM's from comparison with BEM

### 7.9.2 Vortex Chamber Length Variation ($90^\circ$ convergence angle)

In this subsection, we have decided to play on the above learned fact that the ACRM's exhibit a good agreement with BEM at steep convergence angles, and conduct the resonance study of the injectors with different vortex chamber lengths, $L_v$, all having an $\alpha = 90^\circ$ of conical convergence. The CCRM would not apply in this case because it would result in the solution singularity. Based on the above observations, we should be expecting an excellent matching of the first resonant peak between BEM and ACRM's.

Let us first digress briefly to the steady free surfaces resulting when we vary $L_v$, Fig. 7.23. In Fig. 7.23(c), we can see that the free surfaces in $L_v = 5$, 10, and 19 cases coincide, and they exhibit a similar behavior as we described in Chapter 3: the transition starts $-0.5R_n$ and ends at $+0.5R_n$. There is some fluctuation of the free surface after $+0.5R_n$, but it is bounded within about 15% variation, which, in this study, we consider as insignificant and model as a straight line. Regarding the $L_v = 15$ case, we can see that its transition ends further downstream, at approximately $+1.0R_n$, and the free surface fluctuation after this point is very slight. Hence, this case comes out of the $\pm 0.5R_n$ rule, which we have used in Chapter 3. The nature of this deviation is unclear as of now and needs further investigation.

Figure 7.24 and Table 7.4 show respectively the computational BEM results, and the frequencies where the BEM response curves for each $L_v$ peak out. We can see that the peaks shift to the left, or to lower frequencies, as the vortex chamber length is increased. An analogy here may be drawn with the string musical instruments. Smaller size instruments, like the violin, produce higher pitch sounds than the bigger size instruments, like the guitar, or contrabass. As in the above subsection, this is attributed to the fact that the longer vortex chamber naturally selects/generates longer standing waves that are the result of the lower pulsation frequency, and vice

versa. We can look at this from the mathematical point of view as well, if we rewrite the equation for the resonant modes from Section 5.2,

$$\omega_0 = n\frac{\pi}{2L_v}\sqrt{C^2\frac{R_v^2 - r_v^2}{2r_v^4}}, \qquad n = 1, 3, 5, \ldots \tag{7.25}$$

with which the ACRM peaks are calculated in Table 7.4. From this equation, it becomes clear that the values of the resonant frequencies will decrease, as the vortex chamber length is increased. Note, however, that this equation does not provide any information about the amplitude of the oscillation when the injector is at resonance.

Continuing the discussion on the oscillation amplitudes, in Fig. 7.24, we can also see that the amplitudes of the peak responses grow larger, as the vortex chamber becomes longer. The explanation of physics here may be cast in terms of the spring-damper oscillator, whose vibration energy is conserved at all times and is given by $E = 0.5m\omega^2A^2$, where $m$ is the mass of the oscillating body, $\omega$ is the oscillation frequency, and $A$ is the oscillation amplitude (see discussion in Kinsler [100, Sec. 1.7]). Notice that the mass has the power of 1, whereas the frequency has the power of 2. Then, we can write the following: (a) the increase in $L_v$ causes proportional linear increase in the mass of the liquid body in the injector's vortex chamber; (b) we also know from above, that the increase in $L_v$ decreases the peak frequency; (c) in all $L_v$ cases, we excite that liquid mass with the same energy, which is the kinetic energy of excitation $0.5q_{in}^2$ at the inflow boundary; (d) but, if we have a linear mass increase from (a) and a quadratic frequency decrease from (b), then, to conserve the energy of oscillation, the amplitude $A$ should grow in the above formula for the energy.

With regard to the analytical predictions of ACRM-2 (where the peaks can be calculated by using ACRM-1) in Fig. 7.25, we can see a similar trending of the peaks to the left, as we increase $L_v$. It is not possible however to capture the trend for peak amplitudes, as we did in BEM results, because, in all cases here, we set one single amplitude of the incident wave, $D = 1$, and there is the same abrupt step discontinuity causing the reflection and transmission, which can produce only one peak amplitude of the outgoing wave, $A$ (see Section 5.4 for more discussion).

Table 7.4: Summary of resonant peaks for vortex chamber length variation cases (based on Figs. 7.24 and 7.25)

| $L_v$ | Peaks, Hz | BEM | ACRM's |
|---|---|---|---|
| 5 | Peak 1 | 622.1 | 754.1 |
| | Peak 2 | no data | 2262.3 |
| 10 | Peak 1 | 395.9 | 411.3 |
| | Peak 2 | no peak | 1234.0 |
| 15 | Peak 1 | 287.5 | 282.8 |
| | Peak 2 | 610.8 | 848.4 |
| 19 | Peak 1 | 232.2 | 226.2 |
| | Peak 2 | 529.8 | 678.7 |

Now, let us compare the frequencies where the peaks are located in the BEM responses and their analytic counterparts. In Table 7.4, we can see that they match very well for the first resonant peak beginning from the vortex chamber length of $L_v = 10$. Investigation shows that, for vortex chambers shorter than $L_v = 10$, the wave pattern in the vortex chamber of the injector cannot be described as a standing wave anymore. Also, it is clear that the second resonant peak is far from agreement, which follows the conclusion in the previous subsection that the ACRM's cannot capture it.

The matching of the first resonant peak strengthens the conclusion we have made in the prior subsection, where we said that the ACRM's may be successfully used to calculate the first resonant peak in steep angle geometries. The precaution should be taken, though, as to from what vortex chamber length to start to be sure in their results. Ideally then, one would need either experimental or computational input to have the information about that "safe" minimal length.

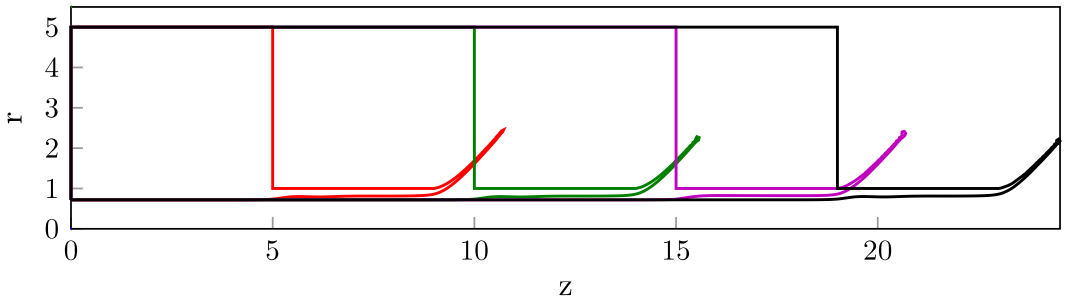


(a) General view of considered cases (legend below)

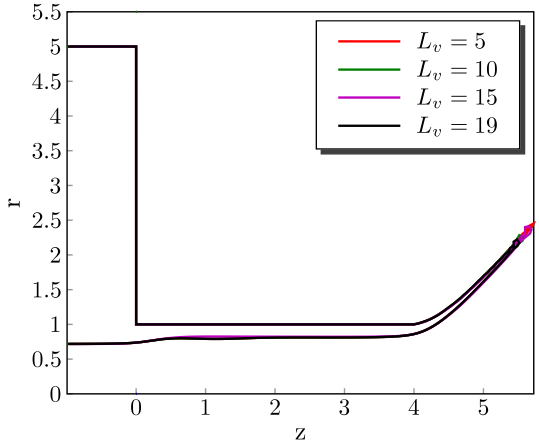


(b) Collapsed view of considered cases

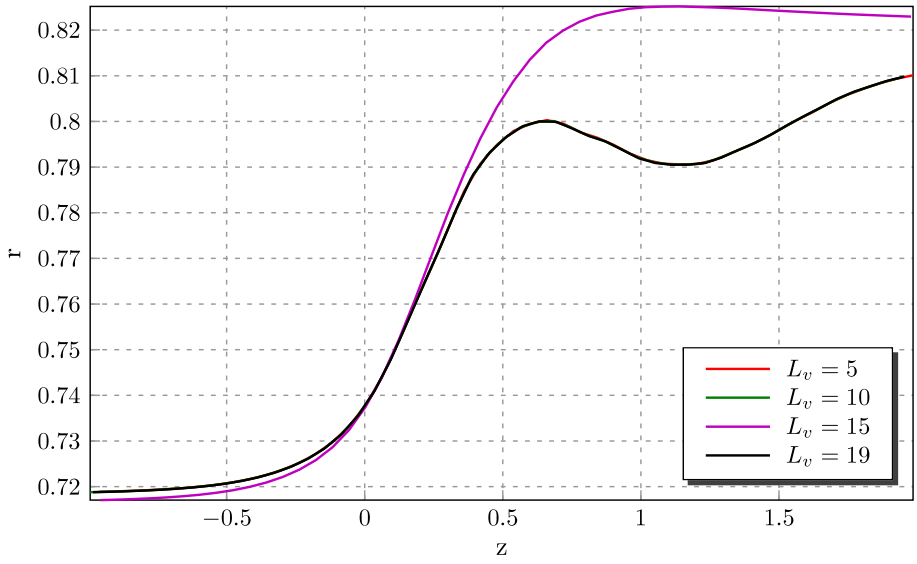


(c) Zoomed in view of free surfaces in nozzle entrance transition region

Figure 7.23.: Steady state BEM flow boundaries at various vortex chamber lengths (90° convergence angle)

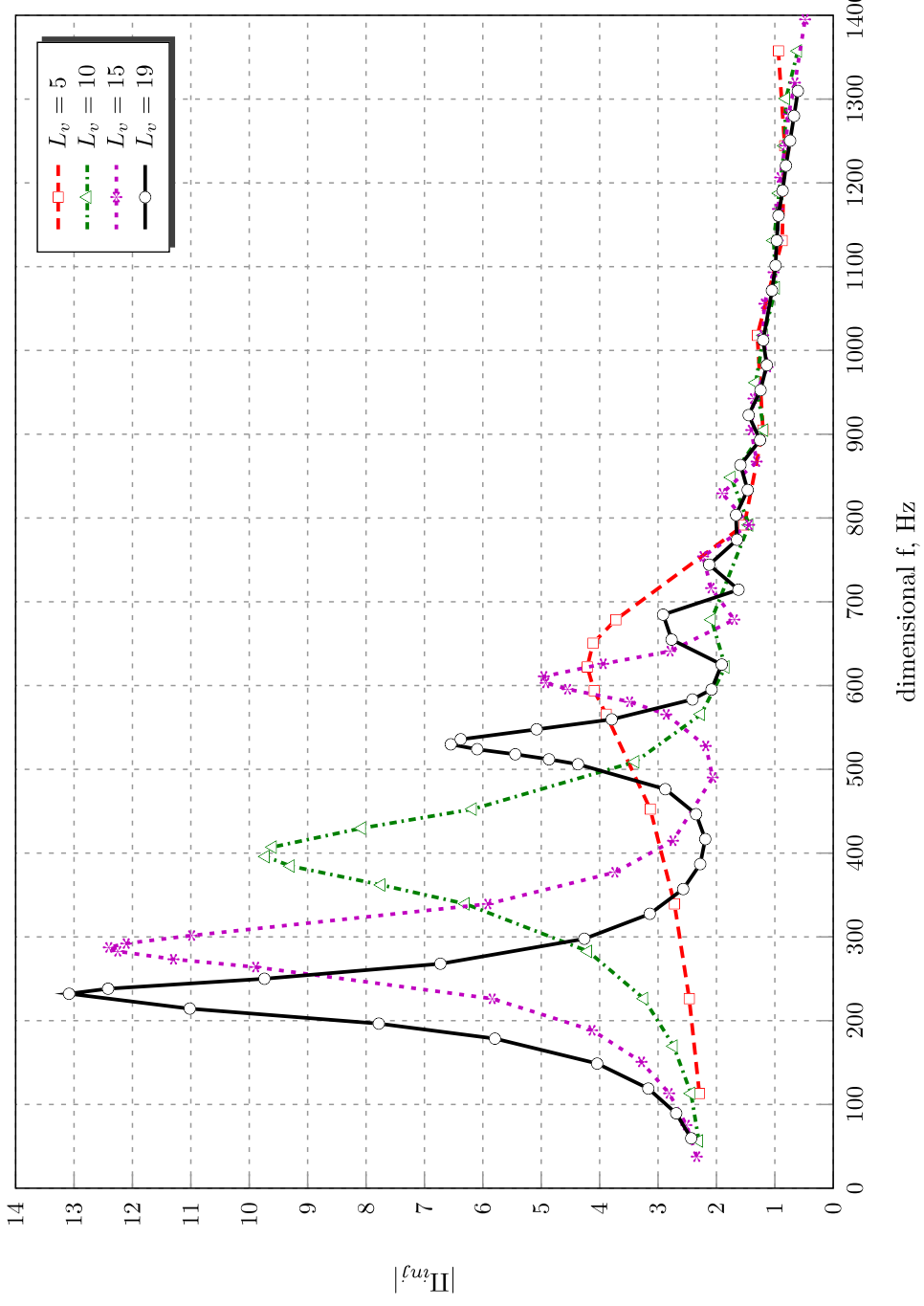


Figure 7.24.: BEM injector response sensitivity to vortex chamber length variation (90° convergence angle)

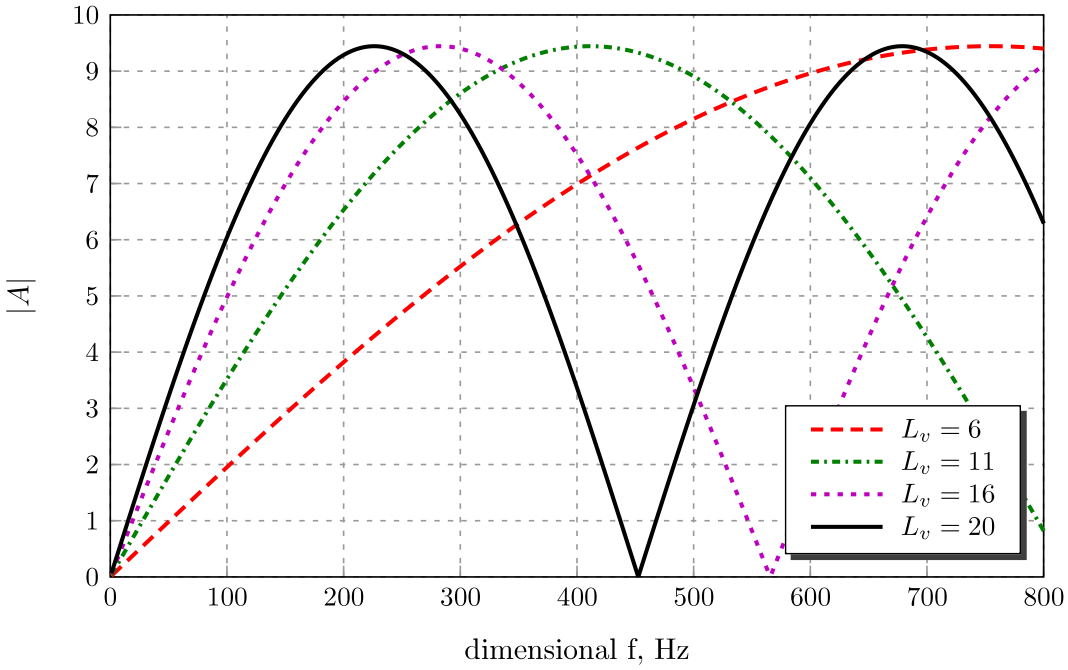


Figure 7.25.: Sensitivity of resonant peaks predicted by ACRM-2 to vortex chamber length variation (90° convergence angle)

### 7.9.3 Nozzle Length Variation ($45^\circ$ convergence angle)

Figure 7.26 shows the steady free surface when the injector has different nozzle lengths. They all fit well together in the $\pm 0.5R_n$ rule, except the free surface for the $L_n = 2$ case. The free surface there ends its transition in the nozzle entrance region later downstream, at roughly $+0.8R_n$, and begins to transition to spray much earlier, roughly at $1.5R_n$. These features of the $L_n = 2$ case may be attributed simply to the fact that the nozzle is very short, and the fluid almost immediately starts transitioning into the conical sheet, giving a very different pattern than in the longer nozzle cases (see similar results in Park [37, Fig. 4.12]).

The BEM injector responses shown in Fig. 7.27 and their peaks summarized in Table 7.5 reveal that the response is overall insensitive to the nozzle length. Notice that the $L_n = 2$ response curve looks same as the others. Which tells us that, even if the free surface in the nozzle entrance transition region was different in this case, it did not affect the wave reflection/transmission characteristics much.

Theoretically, the deviation of the steady free surface in the $L_n = 2$ case from the rest should affect us in terms of the CCRM, where the point where the transition ends is one of its inputs. Nonetheless, based on the knowledge of response constancy at various nozzle lengths, which have learned from BEM simulations, and for simplicity, we will assume that it ends at the same $+0.5R_n$ location with the same radius equal to $r_n$ as the other free surfaces. This allows us to use the same baseline injector results for the analytical peaks in all $L_n$ cases.

Let us now compare the analytical and the BEM peaks with each other. In Table 7.5, we can see that the ACRM's have not shown a good agreement for the first peak. But one has to bear in mind the following facts: (a) this study has been conducted for the injector with a $45^\circ$ convergence angle, (b) it was shown previously, that the ACRM's are accurate for the convergence angles greater than $60^\circ$. To conlude, we can say that the 226.2 Hz and 193.5 Hz mismatch in this case study merely illustrates these facts. And this is supported by the fact that the second peak in Table 7.5 is

Table 7.5: Summary of resonant peaks for nozzle length variation cases (based on Fig. 7.27 and Section 5.6)

| $L_n$ | Peaks, Hz | BEM | ACRM's | Corrected ACRM's | CCRM |
|---|---|---|---|---|---|
| 2 | Peak 1 | 193.5 | 226.2 | 192.5 | 118 |
| | Peak 2 | 464.4 | 678.7 | n/a | 470 |
| 4 | Peak 1 | 193.5 | 226.2 | 192.5 | 118 |
| | Peak 2 | 464.4 | 678.7 | n/a | 470 |
| 6 | Peak 1 | 193.5 | 226.2 | 192.5 | 118 |
| | Peak 2 | 470.3 | 678.7 | n/a | 470 |
| 8 | Peak 1 | 193.5 | 226.2 | 192.5 | 118 |
| | Peak 2 | 470.3 | 678.7 | n/a | 470 |

very well predicted by the third model, as was the case in the conical convergence angle variation study. Notice that the values of corrected ACRM's calculated with the correction coefficient $K_{cor} = 0.8508$ (see Table 7.3 at $\alpha = 45°$) agree will with the BEM results for the first peak.

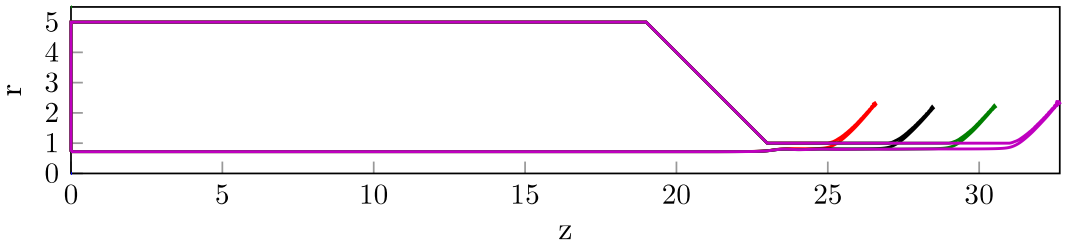


(a) General view of considered cases (legend below)

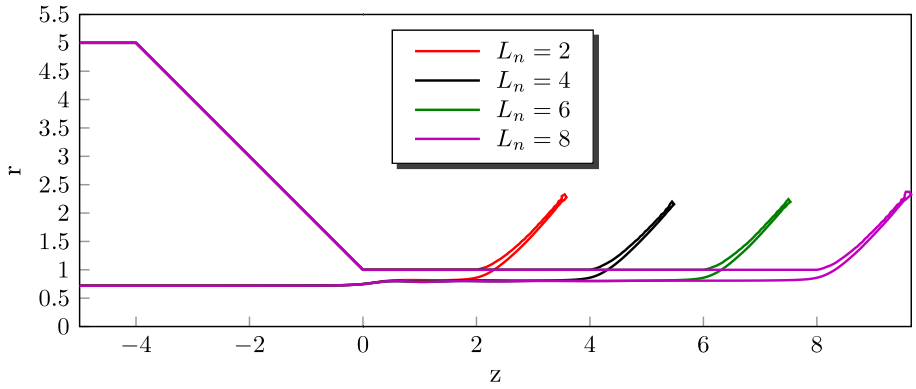


(b) Collapsed view of considered cases at nozzle start

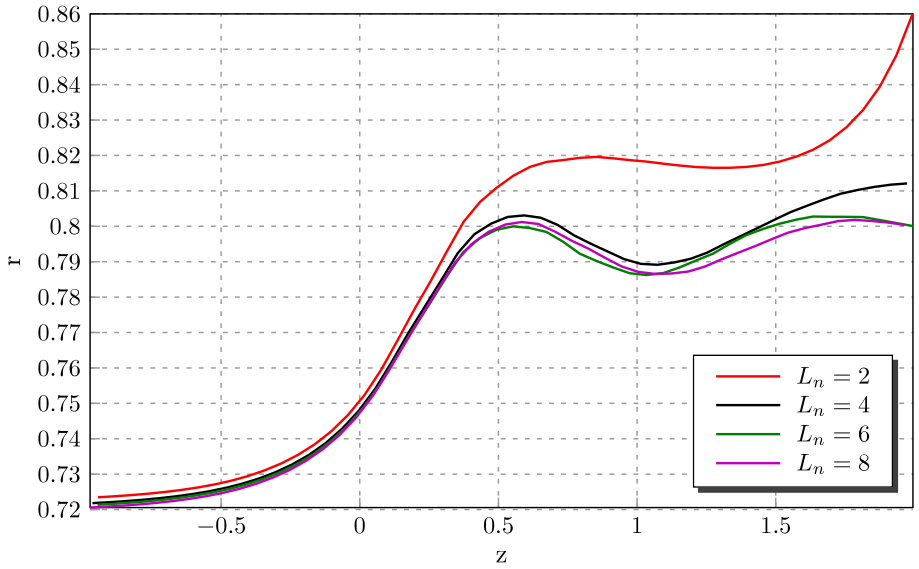


(c) Zoomed in view of free surfaces in nozzle entrance transition region

Figure 7.26.: Steady state BEM flow boundaries at various nozzle lengths (45° convergence angle)

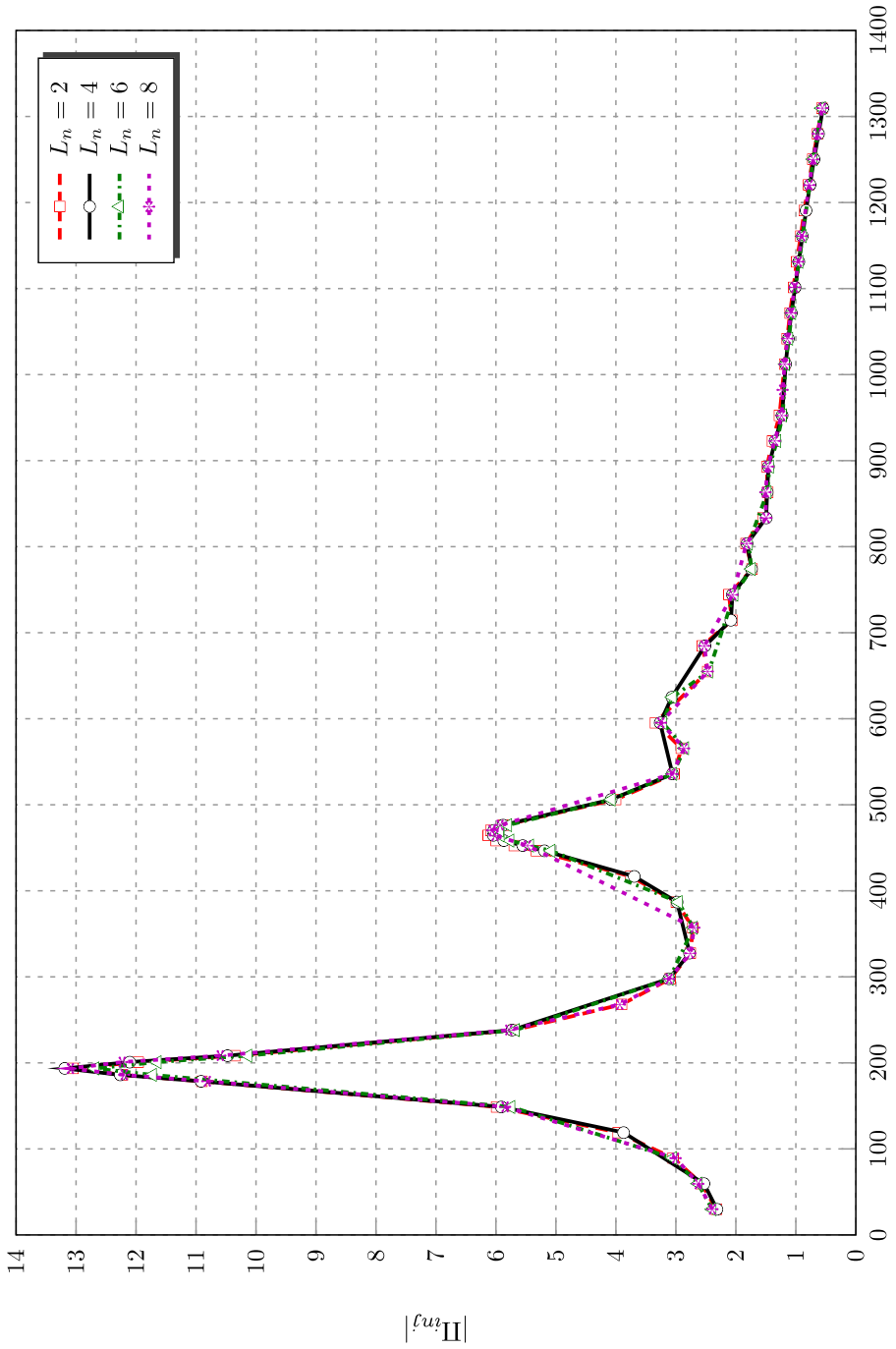


Figure 7.27.: BEM injector response sensitivity to nozzle length variation (45° convergence angle)

### 7.9.4 Vortex Chamber Radius Variation ($45^\circ$ convergence angle)

In this study, we have considered a hypothetical case when we vary the vortex chamber radius, leaving everything else the same, including the steady dimensional tangential inlet inflow velocity, which from Table 2.3 is equal to $\bar{W}_{in}^{*} = 3.7596$ m/s. Note that, if an experimentalist would wish to set up an analogous experiment, he/she would be required to vary the pressure drop accordingly to keep the same value of the inflow velocity.

Figure 7.28 shows the respective flow geometries. Notice that decreasing the vortex chamber radius leads to decrease in the core radius, and reduction in the angle of the conical sheet exiting the nozzle. This is due to the fact that the angular momentum, or the swirl strength, respectively becomes smaller. In turn, this allows the swirling fluid to descend to to a lower core radius. And, because of the greater inertia in the axial direction relative to the baseline case, the fluid is able to discharge further (see similar results in Park [37, Fig. 4.15]).

We are more interested in the behavior of the free surface in the transition region. In Fig. 7.28(c), we can clearly see that the transition in the smaller $R_v$ cases starts more upstream and ends more downstream of the baseline case. In this study, we consider the following approximations: for $R_v = 3.75$ case, the transition starts at $-1.0R_n$ and ends at $+1.0R_n$, for $R_v = 2.50$ case, the transition starts at $-1.5R_n$ and ends at $+1.5R_n$. Accordingly, the corresponding corrections are made in the inputs for CCRM.

With regard to the computational BEM injector responses, we can see in Fig. 7.29 and Table 7.6 that, as we decrease the vortex chamber radius, the peaks shifts to the left, or to the lower frequencies. Moreover, in the $R_v = 3.75$ case, we start to see the third harmonic mode. In the $R_v = 2.50$ case, the third mode is very apparent, and the fourth starts to appear. Mathematically, the shifting of the peaks to the left can be clearly attributed to the decrease in the swirl strength, if we look at Eq. (7.25), which shows a proportional dependence between the resonant frequency,

$\omega_0$, and the angular momentum constant, $C$. From the physical point of view, we can say that, as we decrease $R_v$, the relative increase of the flow momentum in the axial direction, which we mentioned above, leads to natural elongation of the disturbance waves, which in turn causes the oscillating flow system in the injector to "choose" the lower resonant frequencies. In the same Fig. 7.29, we can also observe the decrease in the peak intensities. This is again due to this effect of the stronger flow motion in the axial direction, which causes damping of the disturbances in the radial direction, which, in turn, leads to overall weaker free surface distortions, and hence weaker mass flow oscillations in the nozzle.

Let us now take a look at the results of the analytic resonance models in Fig. 7.30 and Table 7.6. We can see that both the ACRM-2 and the CCRM have captured the above BEM trends as we decrease $R_v$ – shifting of the peaks to the lower frequencies and decreasing of their magnitudes. In terms of the actual values of the peaks, however, we can see in Table 7.6 that the ACRM's performed better and located the first two peaks in $R_v = 2.50$ and $R_v = 3.75$ cases. Also, for the first time in this study

Table 7.6: Summary of resonant peaks for vortex chamber radius variation cases (based on Figs. 7.29 and 7.30)

| $R_v$ | Peaks, Hz | BEM | ACRM's | Corrected ACRM's | CCRM |
|---|---|---|---|---|---|
| 2.50 | Peak 1 | 70.2 | 76.2 | 64.8 | no peak |
| | Peak 2 | 220.5 | 228.6 | n/a | 162 |
| 3.75 | Peak 1 | 134.2 | 141.7 | 120.6 | no peak |
| | Peak 2 | 350.5 | 425.1 | n/a | 274 |
| 5.00 | Peak 1 | 193.5 | 226.2 | 192.5 | 118 |
| | Peak 2 | 464.4 | 678.7 | n/a | 470 |

so far, the second BEM peak of 220.5 Hz, in the $R_v = 2.50$ case, has been accurately predicted. With regard to the $R_v = 5.00$ case, we can say again that, because the 45° injectors are considered here, there is a discrepancy between the ACRM's and the BEM. The respective corrected ACRM's, on the other hand, agree well with the BEM results.

Lastly, with regard to the CCRM, we have already discussed the baseline case matching of the BEM peak of 464.4 Hz with the analytic peak of 470 Hz, when $R_v = 5.00$. At the other vortex chamber radii, however, the CCRM does not perform well. This may be related to the wrong choice of the locations where we have assumed that the free surface starts and ends its transitioning, or to the fact, that in the smaller $R_v$ geometries, the equations of the long wave fluctuations of the mass flow rate and momentum, which we derived in Section 5.3, are not accurately representing the flow disturbances.

Overall, from this study, we can once again take a note that the ACRM's are adequate for the first resonant peak when $R_v$ is varied. The CCRM, however, should not be used for small vortex chamber radii, and further improvement of it is required.

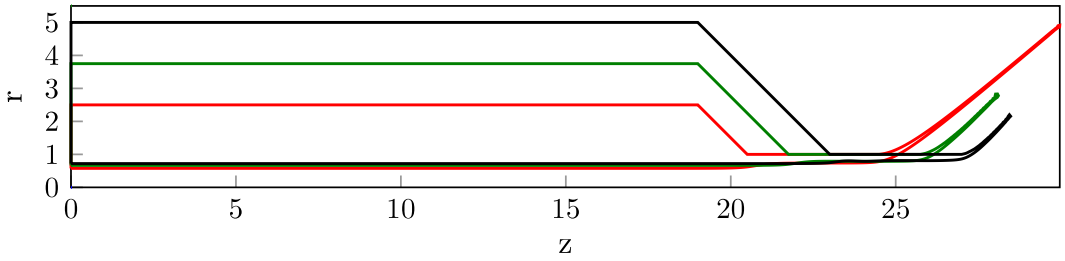


(a) General view of considered cases (legend below)

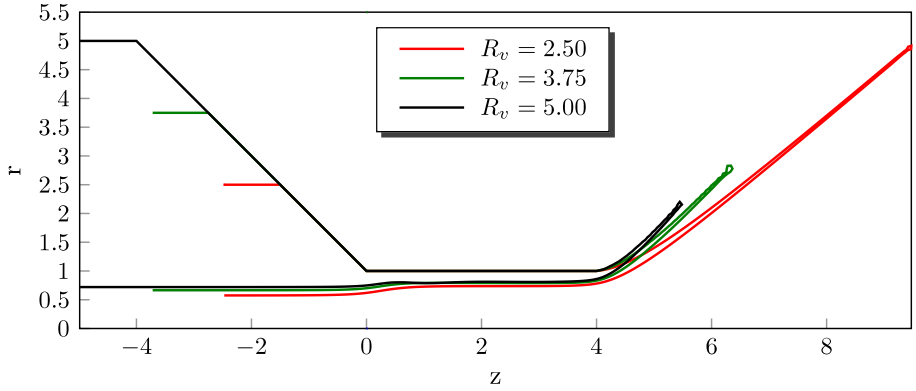


(b) Collapsed view of considered cases at nozzle start

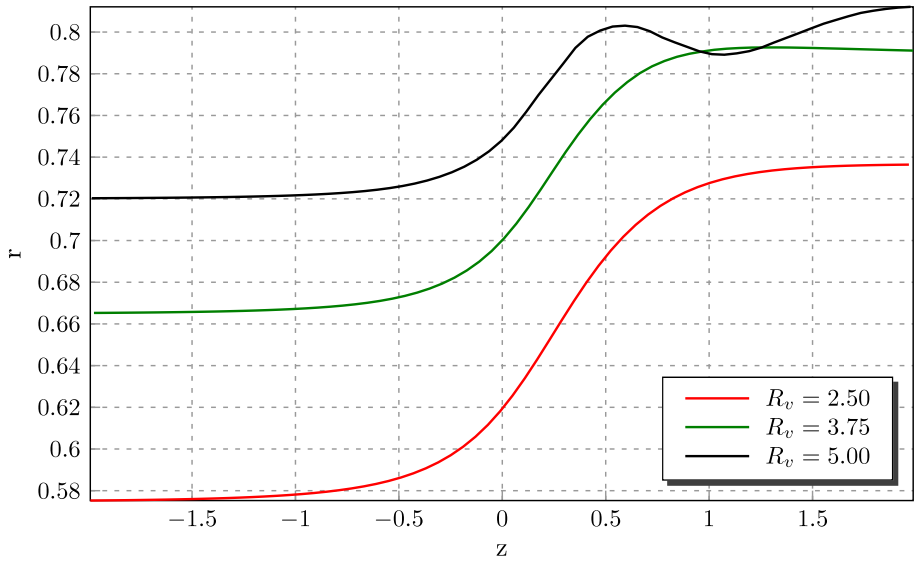


(c) Zoomed in view of free surfaces in nozzle entrance transition region

Figure 7.28.: Steady state BEM flow boundaries at various vortex chamber radii (45° convergence angle)

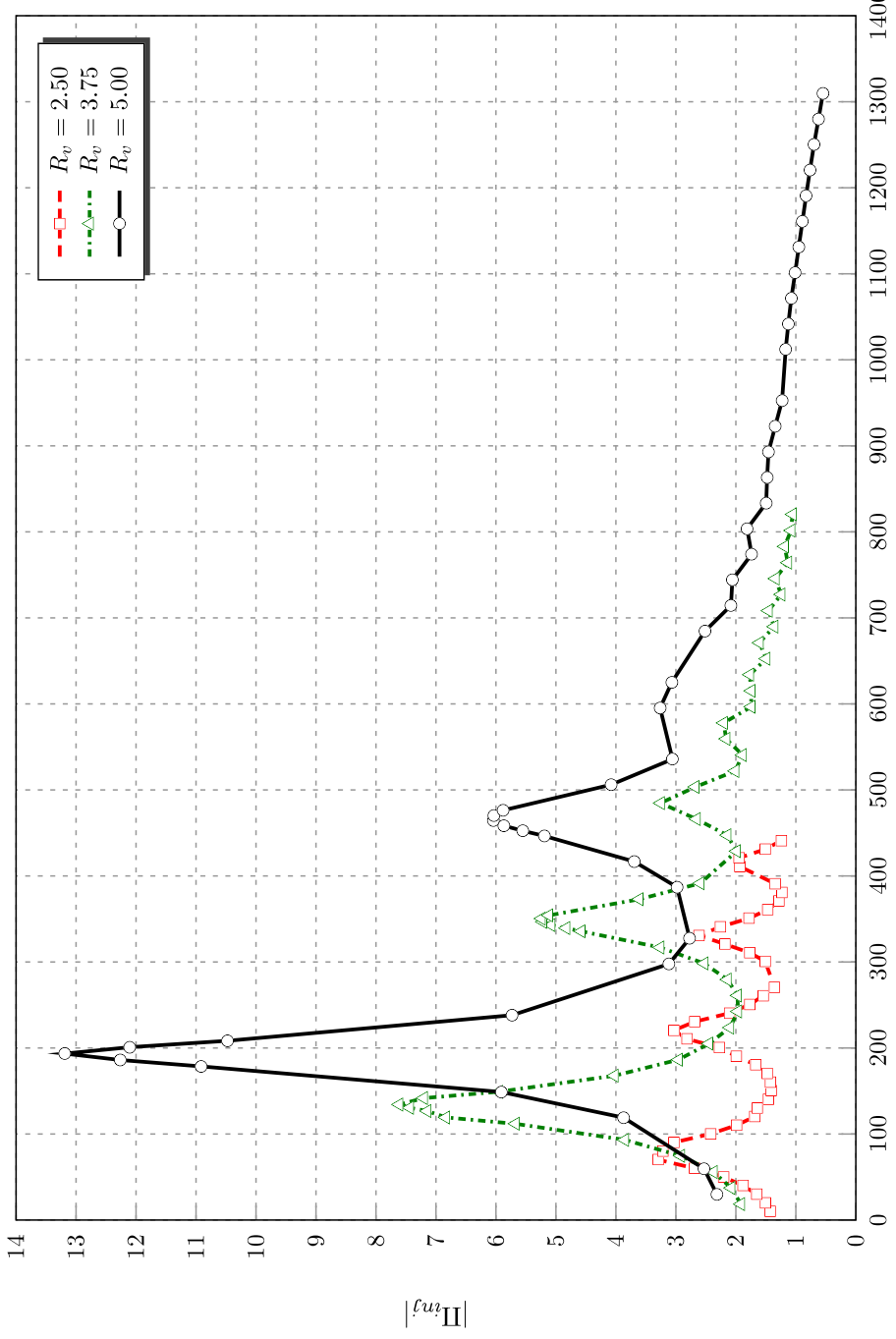


Figure 7.29.: BEM injector response sensitivity to vortex chamber radius variation (45° convergence angle)

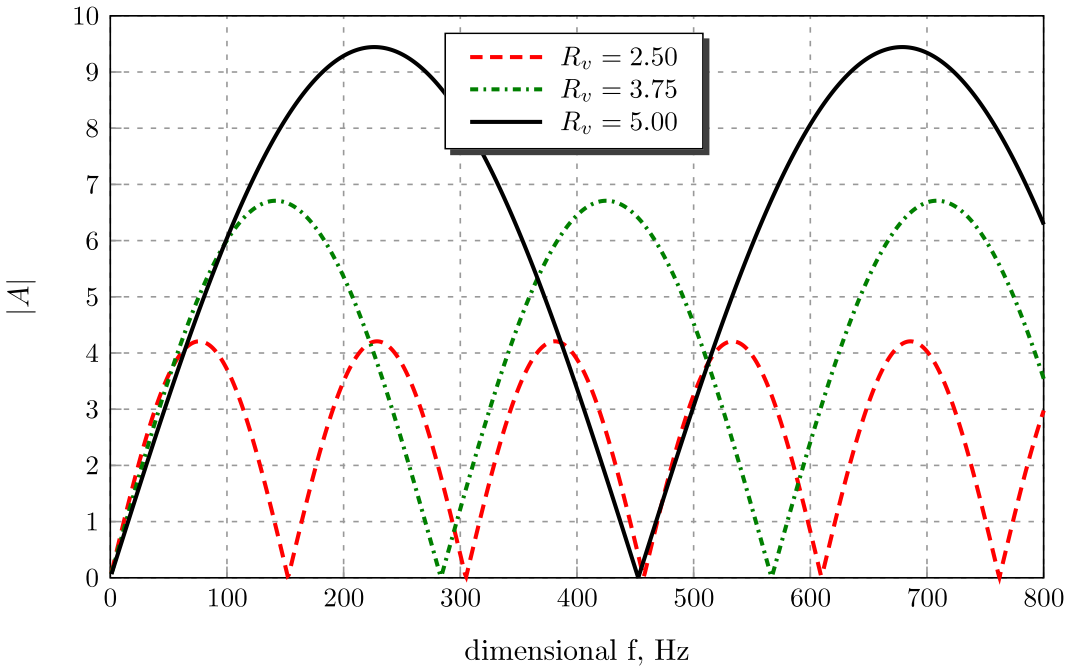


(a) Resonant peaks due to ACRM-2

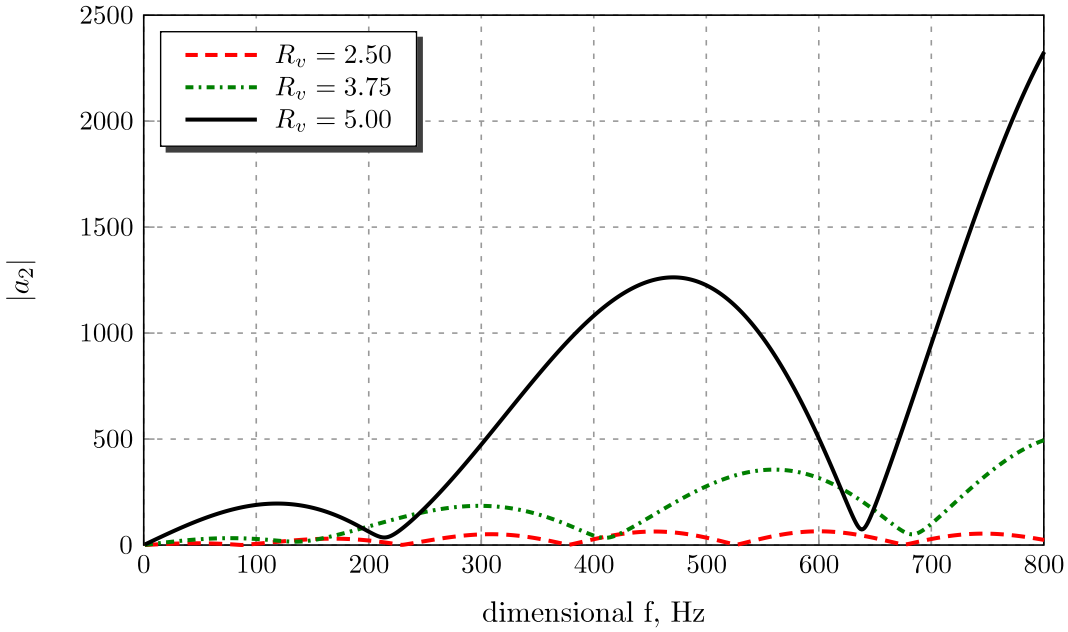


(b) Resonant peaks due to CCRM

Figure 7.30.: Sensitivity of resonant peaks predicted by ACRM's and CCRM to vortex chamber radius variation (45° convergence angle)

### 7.9.5 Steady Tangential Inlet Inflow Velocity Variation ($45^\circ$ convergence angle)

In this study, we have been varying the steady inflow velocity $\bar{W}_{in}$, which, one should note, automatically causes changes in the incoming mass flow rate, through $\bar{\dot{m}}_{in} = N_{in}\pi R_t^2 \bar{W}_{in}$, and changes in the swirl intensity, through $C = \bar{W}_{in} R_{in}$.

Let us first look through the steady free surface images in Fig. 7.31. We can see that all free surfaces, except the one in the $\bar{W}_{in} = 0.25$ case, are approximately the same and can be represented by the methodology described in Chapter 3. The free surface in the $\bar{W}_{in} = 0.25$ case starts to transition earlier and finishes later. Also, after the end of its transition, it is more deformed than the other free surfaces. The nature of this fact remains unclear as of now, and further investigation into the subject is needed. More importantly, this causes an uncertainty, if it is still possible to assume a constant radius of the steady free surface in the nozzle, as we did in Chapter 3. But, for now, let us simply make an assumption that the steady free surface in the $\bar{W}_{in} = 0.25$ case is the same as in the other cases.

The BEM injector responses for these cases in Fig. 7.32 show the following trends: the resonant peaks shift to the left as we decrease the inflow inflow velocity, the "envelopes" around them squeeze in to the narrower ranges, and the amplitudes of the peaks decline in their values. Now, since in this study, two parameters – the mass flow rate and the swirl strength – change simultaneously, it becomes harder to explain these trends from one single point of view. A good starting point to do that is the previous study, where we were varying the swirl strength only by changing $R_v$. There, we have seen exactly the same trends, but the peaks were not as narrow as here. This tells us that the narrowing of the peaks may be attributed to the slower motion in the axial direction, which is the result of the smaller mass flow rate. And this idea may be strengthened if we follow the long wave discussion in Appendix B. From it, we can conclude that the slower moving bulk flow generates longer waves,

given the disturbance frequency stays the same. Hence, the slower moving flow will naturally select longer waves and lower frequencies, when it is at resonance.

The analytic resonance models in Fig. 7.33 show similar tendency for the peaks to shift to the left. However, the effect of the diminishing peak amplitude is captured by the CCRM only. The ACRM-2 cannot do that because, in analogy with the cases when we varied $L_v$, the step change from the vortex chamber to the nozzle remains the same.

The comparison of the peaks in Table 7.7 reveals that the CCRM has an accurate estimation of the second resonant peaks. Note that the value of $R_v$ in this study was favorable for the third model to apply. On the other hand, the ACRM's have not captured the first resonant peak as good. However, with the correction for 45°, as in the above studies, the agreement between them becomes satisfactory.

Table 7.7: Summary of resonant peaks for steady tangential inlet inflow velocity variation cases (based on Figs. 7.32 and 7.33)

| $\bar{W}_{in}$ | Peaks, Hz | BEM | ACRM's | Corrected ACRM's | CCRM |
|---|---|---|---|---|---|
| 0.25 | Peak 1 | 12.1 | 14.1 | 12.0 | 7 |
| | Peak 2 | 27.9 | 42.4 | n/a | 29 |
| 0.50 | Peak 1 | 48.4 | 56.6 | 48.2 | 30 |
| | Peak 2 | 119.1 | 169.7 | n/a | 118 |
| 0.75 | Peak 1 | 108.8 | 127.3 | 108.3 | 67 |
| | Peak 2 | 267.9 | 381.8 | n/a | 265 |
| 1.00 | Peak 1 | 193.5 | 226.2 | 192.5 | 118 |
| | Peak 2 | 464.4 | 678.7 | n/a | 470 |

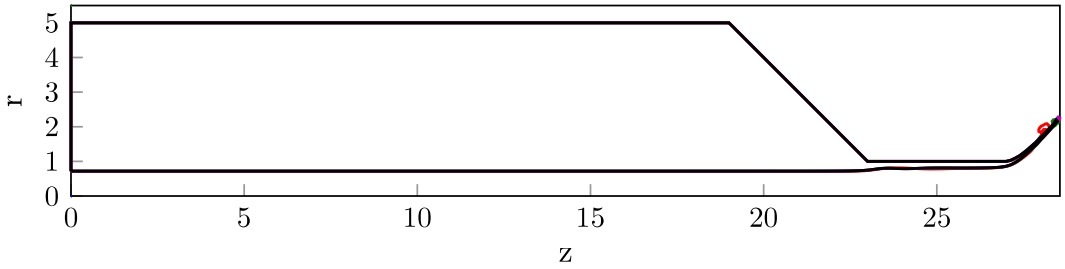


(a) General view of considered cases (legend below)

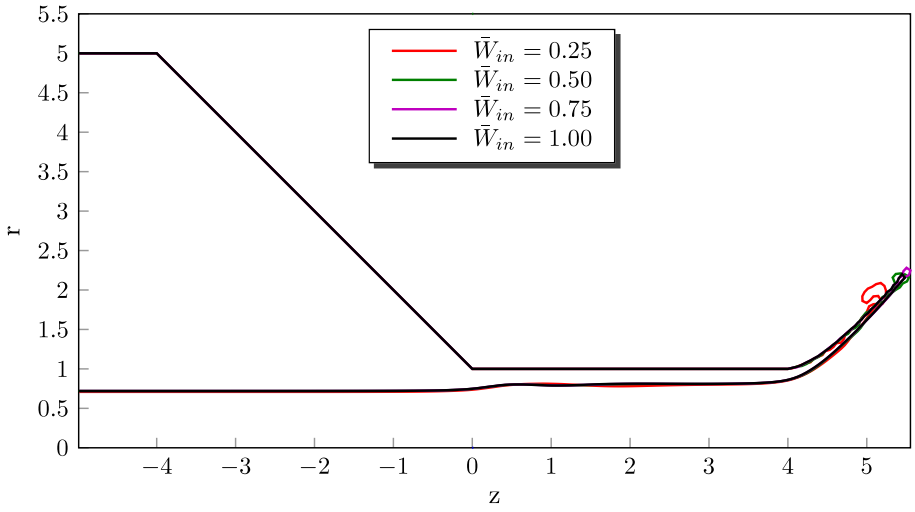


(b) Collapsed view of considered cases at nozzle start

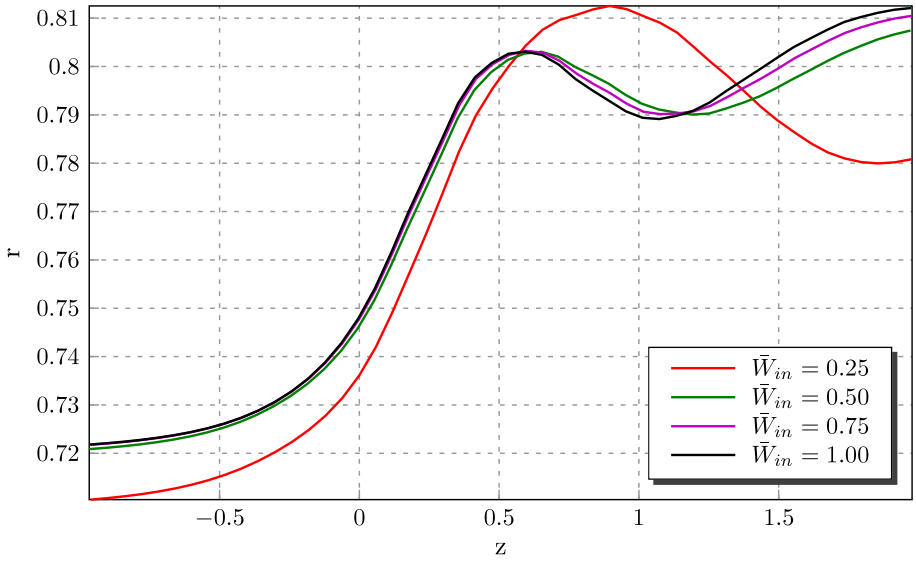


(c) Zoomed in view of free surfaces in nozzle entrance transition region

Figure 7.31.: Steady state BEM flow boundaries at various steady tangential inlet inflow velocities (45° convergence angle)

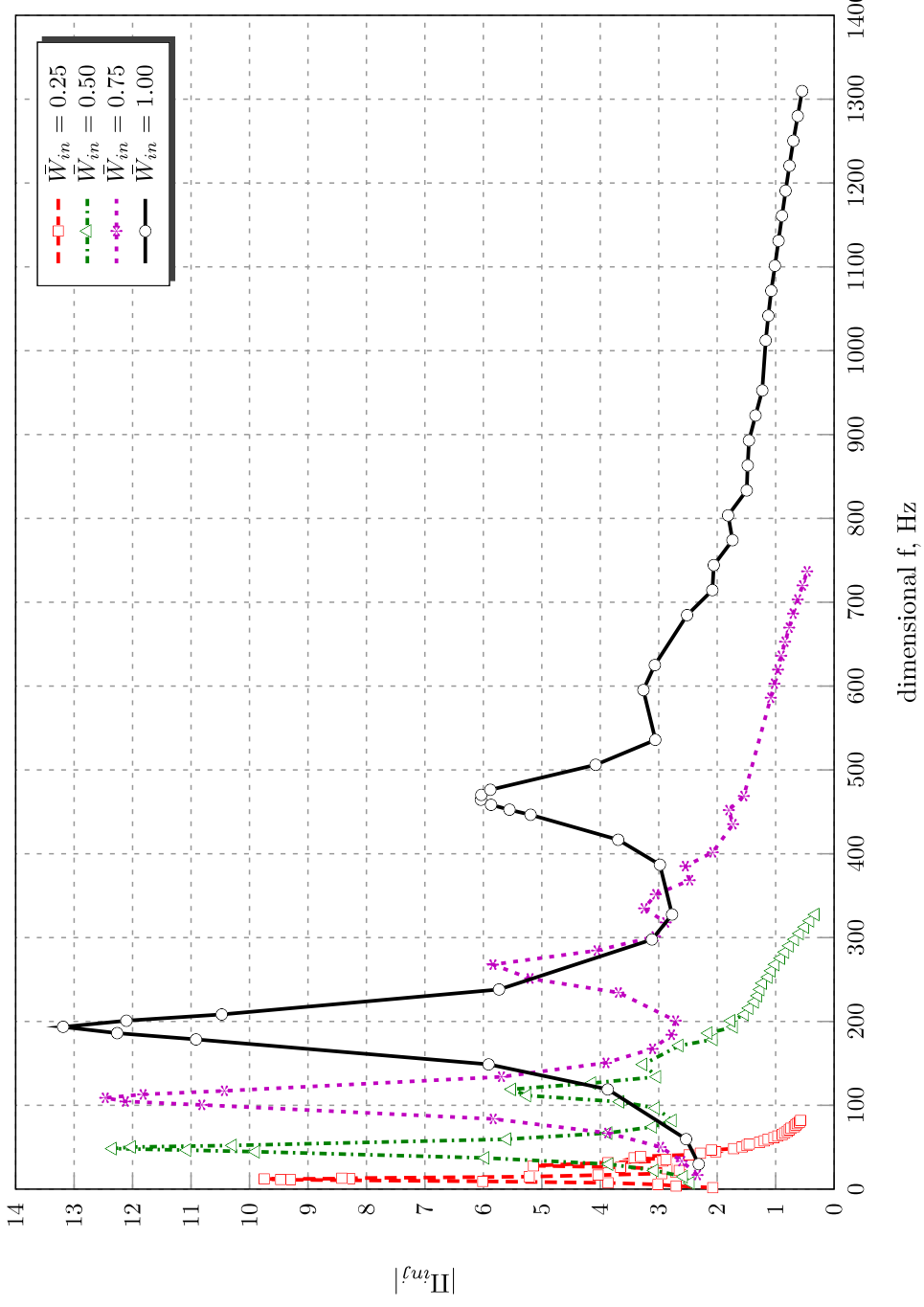


Figure 7.32.: BEM injector response sensitivity to steady tangential inlet inflow velocity variation (45° convergence angle)

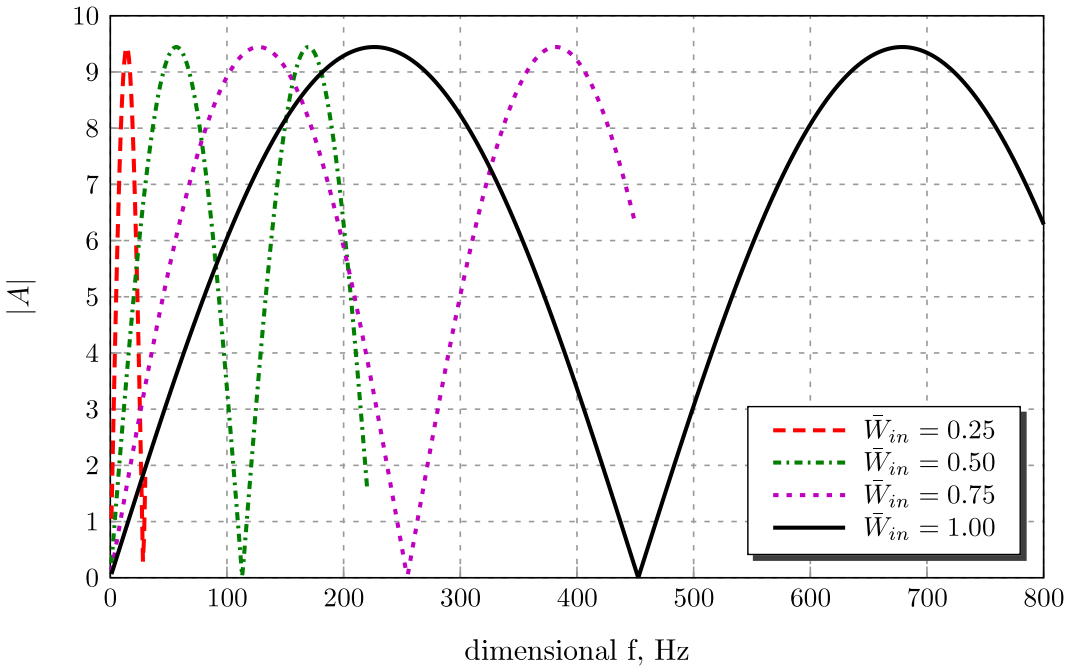


(a) Resonant peaks due to ACRM-2

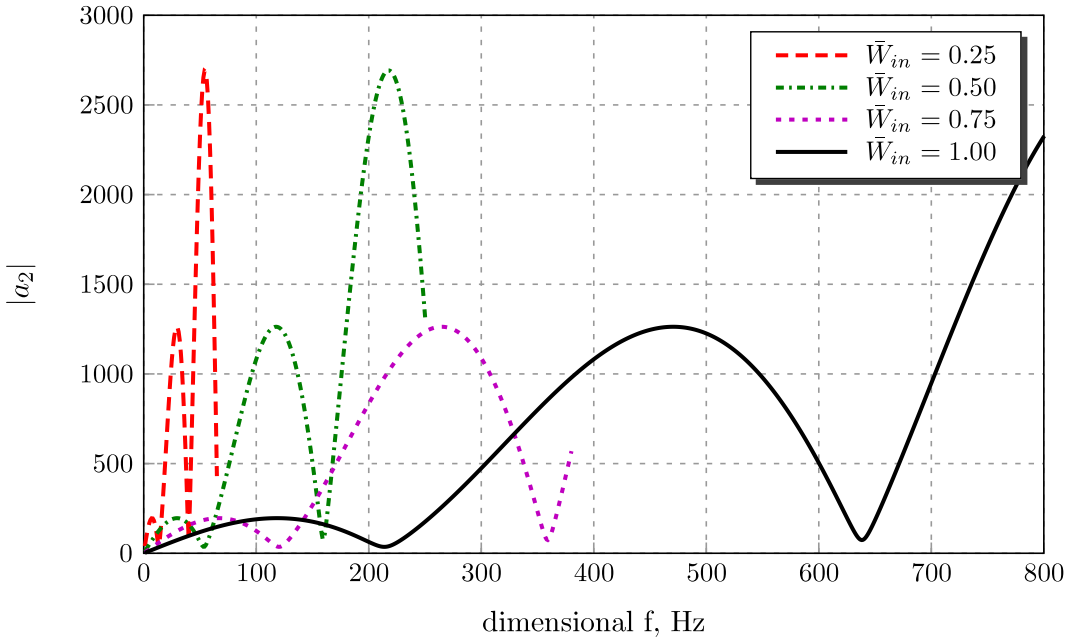


(b) Resonant peaks due to CCRM

Figure 7.33.: Sensitivity of resonant peaks predicted by ACRM's and CCRM to steady tangential inlet inflow velocity variation (45° convergence angle)

### 7.9.6 Comparison of Resonant and Non-Resonant Wave Shapes

In Section 7.9.2, where we have considered the 90° injector with different vortex chamber lengths, we have seen in Table 7.4 that the ACRM's predict the first resonant peak very accurately. This was due to the fact that a 90° injector has exactly the same form of abrupt change from the vortex chamber to the nozzle like we were assuming in the ACRM's. The question arises now: if the analytic and the BEM peaks for the first resonant mode match so well, then can the wave pattern in the vortex chamber be really described as a standing wave pattern, which we considered in Section 5.2, or not?

It is of instructional interest to show that this is indeed so, which we do in this subsection. For this purpose, we choose a 90° injector with the vortex chamber length of $L_v = 19$ (see Fig. 7.23(a)), and consider the free surface motion in the thin region around the mean free surface radius in the vortex chamber, which is equal to $r_v = 0.7177$ (see Table 2.2). Next, we select a short time period of flow pulsation, $t = 67.6950 \ldots 70.3950$ during which we have a stable flow pulsation, and that allows us to see the entire period of the resonant wave development. During this time interval, we will first present the results for the first resonant frequency of 232.2 Hz (see Table 7.4), and then the results at a non-resonant frequency, which, in this investigation, we have chosen to be 357.2 Hz.

Figures 7.34 and 7.35 show the development of the resonant wave pattern. Notice that the free surface moves much weaker at the head end, $z = 0$, than at the entrance to the nozzle, $z = 18$. But this is very similar to the standing wave pattern which we deduced in Section 5.2, where the node was located at the head end, and the antinode – at the nozzle entrance. This clearly proves that, when the injector is at its first resonant mode, the disturbance wave pattern in its vortex chamber should be very close to a standing wave.

Now, let us take a look at the non-resonant wave pattern in Figs. 7.36 and 7.37. The situation is now completely different. We do not have a distinct node or an

antinode anymore. The node that is apparent travels back and forth around the center of the vortex chamber. This reinforces our idea in Section 5.2 that, when the injector is not at its first resonant mode, the wave pattern in its vortex chamber cannot be described as a standing wave.

To conclude, we have to mention that, in cases when the analytically predicted first peak matches that of BEM, we observe similar standing wave patterns in other parametric simulations as well, i.e. when we vary $\alpha$, $L_v$, $L_n$, $R_v$, and $\bar{W}_{in}$. At the second resonant frequency, however, the standing wave pattern does not seem to apply. We may attribute that directly to the fact that the partially standing waves become predominant. And, in support of this conclusion, we have seen it in the above studies, that the ACRM's, which operate with a standing wave presumption, generally are not capable of capturing the second resonant peak, and that the CCRM is a more appropriate tool for its analytic prediction.

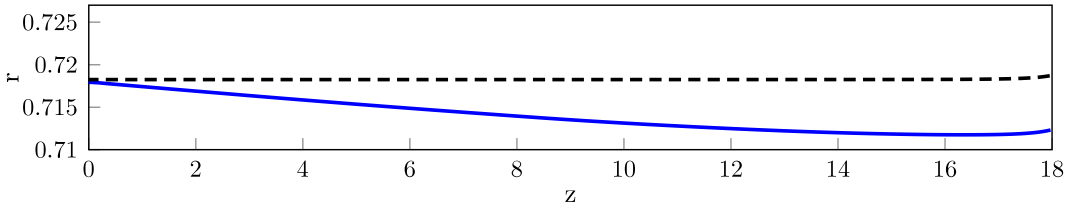


(a) $t = 67.6950$

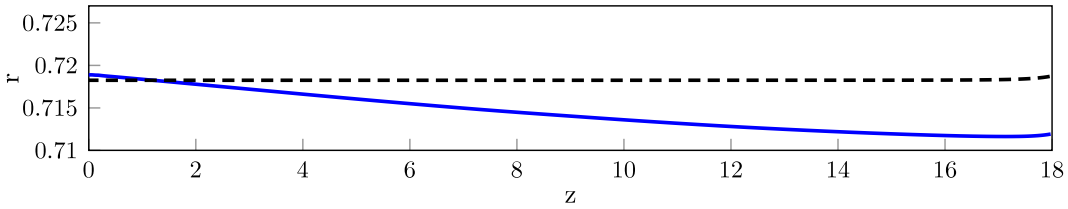


(b) $t = 67.9950$

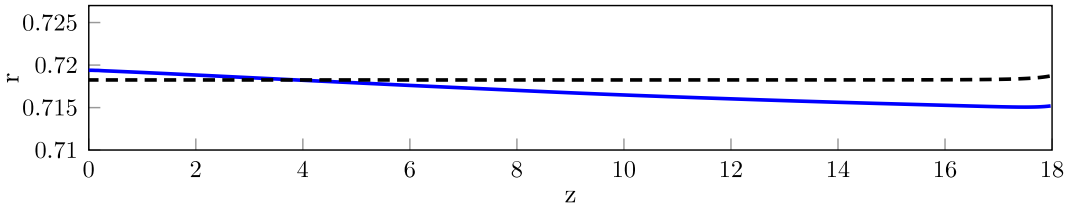


(c) $t = 68.2950$

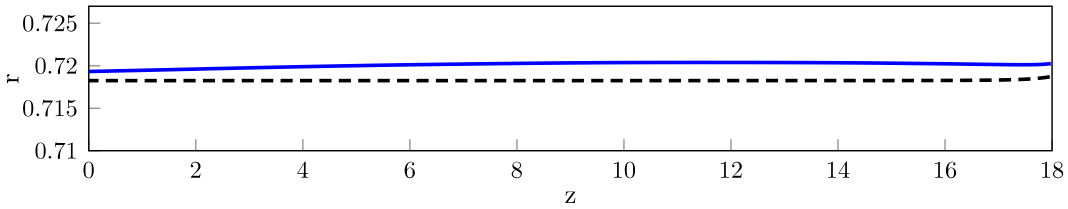


(d) $t = 68.5950$

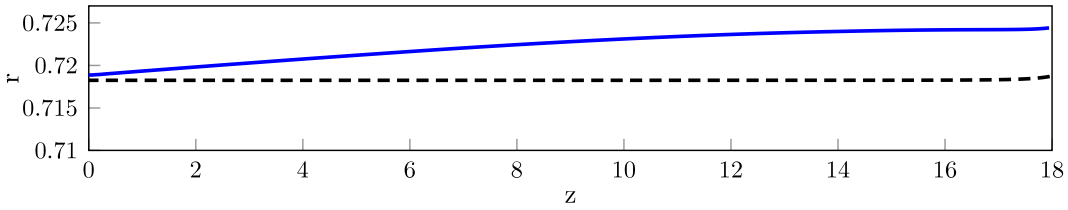


(e) $t = 68.8950$

Figure 7.34.: Time development of first mode free surface resonant wave pattern in swirl injector's vortex chamber, motion in positive radial direction (90° convergence angle, $L_v = 19$, $f^* = 232.2$ Hz)

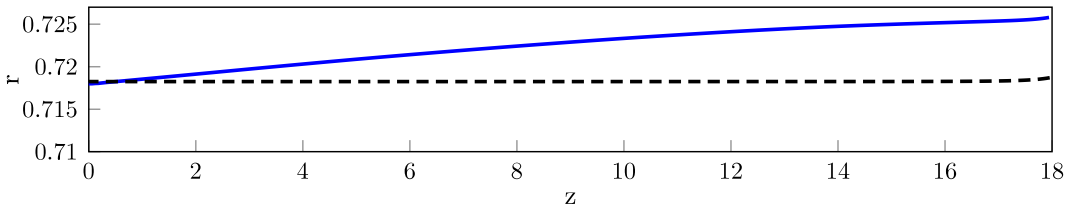


(a) $t = 69.1950$

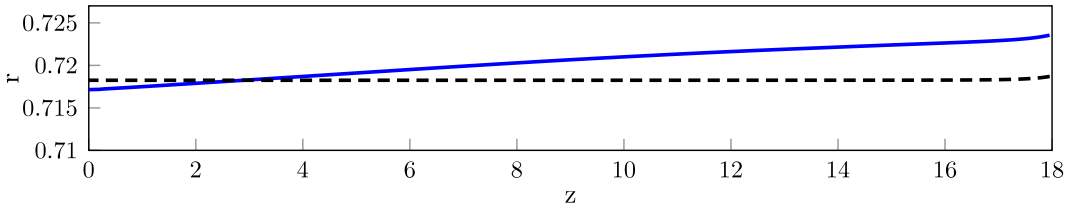


(b) $t = 69.4950$

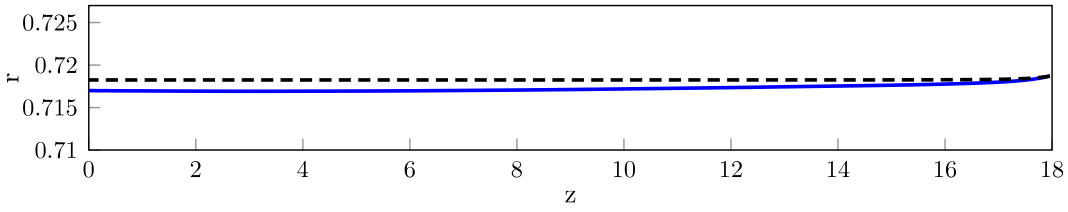


(c) $t = 69.7950$

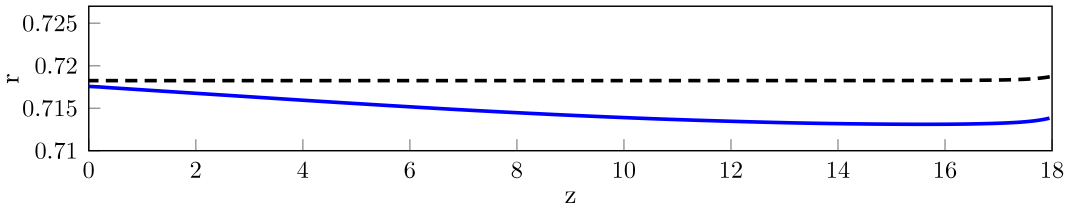


(d) $t = 70.0950$

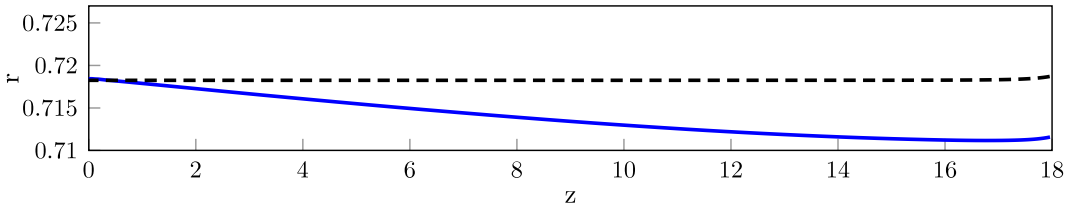


(e) $t = 70.3950$

Figure 7.35.: Continuation from $t = 68.8950$ of time development of first mode free surface resonant wave pattern shown in Fig. 7.34, motion in negative radial direction

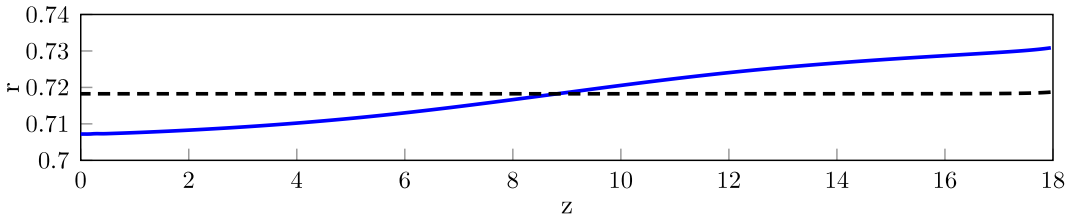


(a) $t = 67.6950$

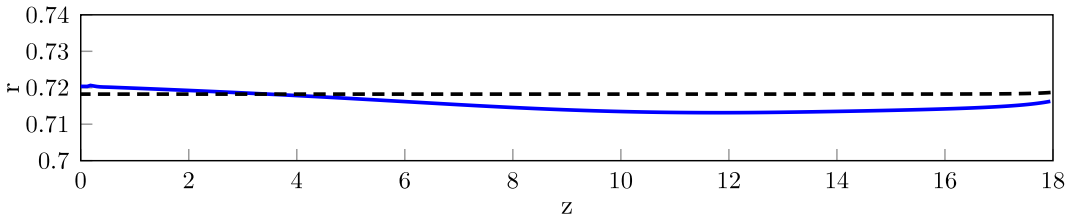


(b) $t = 67.9950$

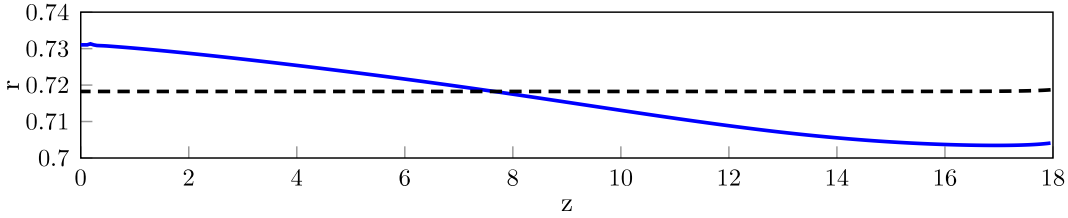


(c) $t = 68.2950$

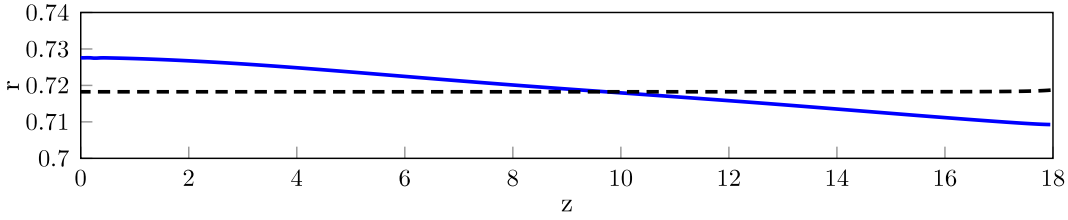


(d) $t = 68.5950$

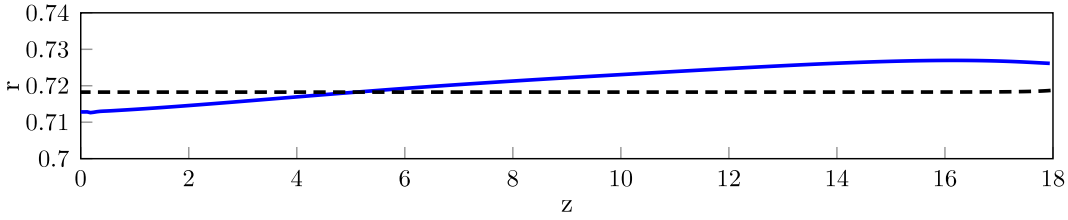


(e) $t = 68.8950$

Figure 7.36.: Time development of free surface non-resonant wave pattern in swirl injector's vortex chamber (90° convergence angle, $L_v = 19$, $f^* = 357.2$ Hz)

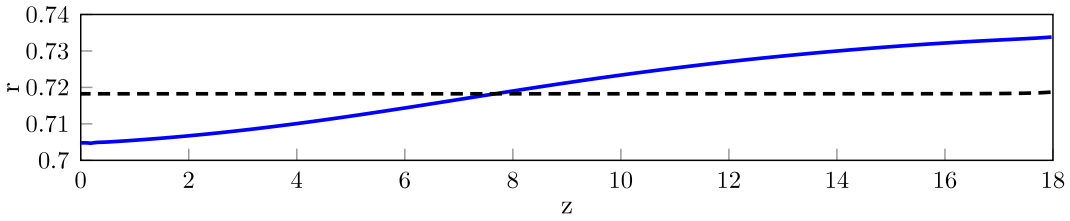


(a) $t = 69.1950$

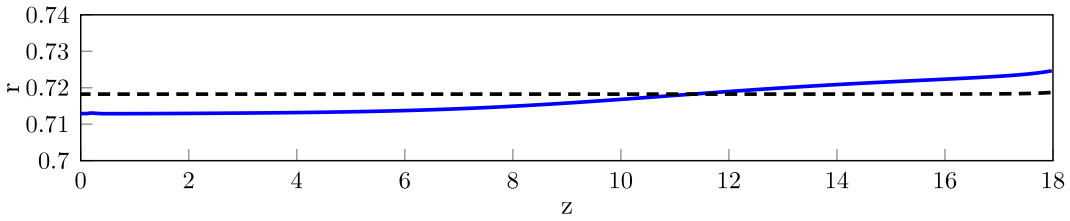


(b) $t = 69.4950$

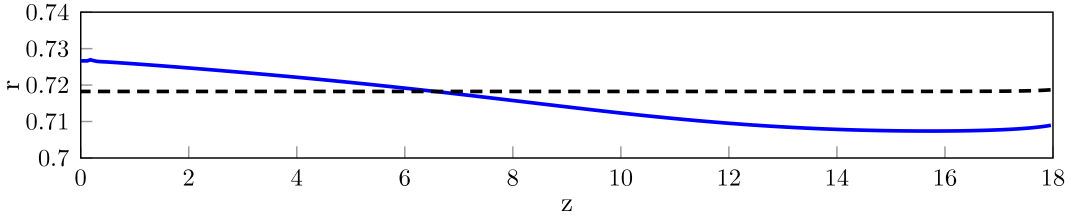


(c) $t = 69.7950$

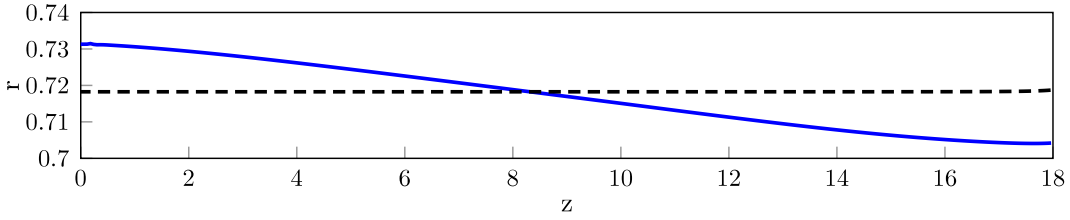


(d) $t = 70.0950$

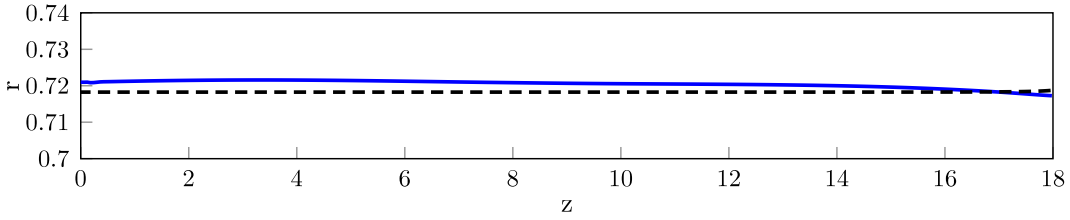


(e) $t = 70.3950$

Figure 7.37.: Continuation from $t = 68.8950$ of time development of free surface non-resonant wave pattern shown in Fig. 7.36

## 7.10 Conclusions and Discussion

We have started this chapter with the notion that, for the baseline injector, we have one experimental data point for spray cone fluctuation at the pulsation frequency of 221 Hz. We also know from Chapter 5 that the ACRM's predict the first resonant frequency of 226.2 Hz. On the other hand, Bazarov's [1] response curve does not show any extremum in the area of those frequencies. This naturally raised a question whether or not the similarity between the analytic 226.2 Hz and the experimental 221 Hz peaks was a coincidence. To have the third input, and in general, to link together the analytics, the experiment, and the computations, we have conducted the parametric studies of the same injector by using the BEM technique.

We have started with briefly reviewing the mathematics behind the BEM and the advantages of its usage for this particular problem. Then, we have shown how to change the boundary conditions of the existing BEM code, so that the flow setup becomes very similar to that in Chapter 5, where we have studied the injector resonance. Next, we discussed how we can extract the injector response from the output data produced by the BEM code. And finally, we have explained our choices for the grid size and time steps which we have applied in the BEM simulations.

To answer the above raised question, we have then conducted an extensive parametric study of the BEM injector, where we have varied the conical convergence angle, $\alpha$, the vortex chamber length, $L_v$, the nozzle length, $L_n$, the vortex chamber radius, $R_v$, and the steady tangential inlet inflow velocity, $\bar{W}_{in}$. In each study, we have commented, both from mathematical and physical points of view, on the shifting of the response peaks to either lower or higher frequencies, and on the decrease or the increase in their amplitudes.

More importantly, we have compared the frequencies where the BEM responses peak out with the resonant frequencies, which we can predict analytically by using the resonance models in Chapter 5. In some of the cases, the matching of the peaks was very satisfactory, in other cases, it was not. But the overall conclusion, which we

can carry out from the parametric studies, is that the ACRM's give accurate results for the first resonant peak, with the condition that the conical convergence angles have to be steeper than 60°. On the other hand, the CCRM predicts very reasonably the second resonant peak, with the limitation that the radius of the vortex chamber cannot be small.

Overall then, since we see a relatively consistent matching of the resonant peaks predicted analytically and by BEM, then, we can conclude that the experimental peak point was not a coincidence, but a first resonant mode of this particular injector. Moreover, if we bear in mind the conditions, with which each of the analytic resonance models can be applied, then we can declare that, now, we have an analytic tool, at least in its nascent state, which we can use to obtain the preliminary estimates of the resonant frequencies of the injector, prior to conducting expensive computational or experimental studies. Furthermore, an injector designer can now have an idea, where to expect an amplification or damping of the flow pulsations. Or, if there is some consistent pitch frequency in the hot fire tests, one can have an idea whether or not it may be attributed to the resonance. We can also say that the modified BEM model which we have setup in this study, provides itself as an adequate computational tool, which reveals all important physics of the injector resonance, and clearly shows the resonant modes.

It is clear that there are areas that need to be improved both in the analysis, and the BEM model. In the analysis, one can immediately wonder: why does not the CCRM, which seems to be more complete, capture the first peak? Or, why do not the ACRM's capture the second resonant peak? To fill these gaps, one obviously has to add more features to the analysis. Probably, it would be best to work with the CCRM, and precisely speaking, on deriving the higher order equations of the long wave fluctuations of the mass flow rate and the momentum. Speaking of the long waves, another more complex feature to add would be the Kelvin's waves.

With regard to BEM, from the notes about the inflow boundary, one can instantly see that the inflow modeling remains a rather big problem as of now. Probably, the

avenue to take here would be to attempt a complete three-dimensional modeling of it. Then, the inflow solution may be connected through additional boundary conditions to the "main" flow in the vortex chamber. Or, from the start, it could be best to model the entire injector flow in 3D. A BEM technique extended to 3D flows already exists in Chao [129]. And this reference may serve as a starting point in this improvement. Another apparent limitation of the existing code is that it handles only the irrotational flow. In reality, as we have discussed in Section 2.1, at the unsteady state, we should have an unsteady angular momentum, which gives rise to non-zero and variable vorticity. The code could become more realistic if the vorticity–stream function approach instead of velocity–velocity potential would be taken. This type of approach is well described analytically, where the references to start are Batchelor [79] and Golubev [130], [62].

# 8. CONCLUSIONS AND RECOMMENDATIONS FOR FUTURE WORK

Recall from Chapter 1 that we have started the whole discussion in this thesis from the two following facts: (a) there is one well published linear theory by Bazarov [1] that describes the dynamics of the swirl injectors, and (b) there are the computational results by Richardson [43], where the injector response does not match that predicted by Bazarov' theory (see Fig. 1.2). This mismatch left us wondering what might be the cause of it: is it the linear theory, or is it the computational flow setup? It seemed easier to address the theory first, and then the computational code.

We have reviewed the linear theory by Bazarov in Chapter 2 and concluded that there are a number of simplifying flow assumptions that potentially could represent the unsteady flow dynamics in the swirl injector in an inaccurate way. The major ones were the following:

1. The flow representation at the nozzle entrance of the injector in form of an abrupt step discontinuity, which leads to the ignorance of the wave refractions.

2. The long wave presumption for the flow disturbances, which leads to imprecise wave speeds at high disturbance frequencies.

3. The independence of the reflection coefficient from the disturbance frequency, which leads to inability to capture the injector resonance phenomenon.

To illustrate the first concept in this list, we have started with analyzing both analytically and numerically the steady free surface in the transition region of the injector in Chapter 3, which yielded an analytic model that can predict it with a reasonable accuracy. This model may be improved if one finds a way to describe the boundary conditions more precisely, such as the points where the steady free

surface starts and ends to transition, and the flow velocities at these points. Also, more functions, such as logarithmic, and Bessel's $J_0$ and $Y_0$, could be added to the solution, to make it more complete.

Then, using that predicted profile of the steady free surface in the transition, in Chapter 4, we have conducted a small disturbance analysis to understand more completely the refractive properties of the long waves as they propagate through the transition. To address the second item in the list above, and have a valid analytic prediction for the wave characteristics in the broader frequency range, we have extended the wave refraction analysis to be based on the Kelvin's waves. Overall, from this refraction analysis we have learned that the disturbance waves may grow and decay, and change their length as they travel through the transition. Also, an important information has been revealed that, in the long wave limit, the same expressions for the wave speed may be used as in the simple cylindrical swirling flows. From the results that are produced by both long and Kelvin's wave refraction descriptions, we have seen that the discontinuities are generated at the points in the flow where there are abrupt changes in the steady axial bulk flow velocity or the cross-sectional area. These discontinuities could be diminished and smoothed out, if one would develop the linear analyses in both long and Kelvin's wave models further, so that they include the higher order terms.

To tackle the third item in the list above, we have performed a wave reflection analysis in Chapter 5. Only the long waves were considered in this analysis, while its extension to the Kelvin's waves has presented itself as a difficult and non-feasible option. The wave reflections naturally cause the injector to resonate at some frequencies, just like in Helmholtz resonators. We have considered three different models of wave reflections/injector resonance:

- ACRM-1, which is based on the intuitive guess of where the nodes and antinodes may be located, if the injector happens to be at resonance.

- ACRM-2, which is based on the more formal description of wave reflection and transmission in the transition region, but where the latter is simplified to being a sudden step discontinuity.

- CCRM, which is the analogue of ACRM-2, but more complete in the sense that the transition region is acknowledged to have its distinct conical and free surface boundaries. In this model, we have discretized the flow in the transition region into small cylindrical sections and have used the long wave speeds valid in the cylindrical flows, which we have shown is possible to do, based on the refraction analysis in Chapter 4.

Overall, the wave reflection analysis has shown that the reflective properties of the transition region do depend on the disturbance frequency, and uncovered the ways to calculate the resonant frequencies of the swirl injector. Later, in Chapter 7, we have concluded that the first two resonance models, ACRM-1 and ACRM-2, predict reasonably well the first resonant frequency, but, only in the injector geometries having the conical convergence angle, $\alpha$, steeper than 60°. Whereas, the third model, CCRM, locates quite accurately the second resonant frequency, but with the condition that the vortex chamber radius, $R_v$, cannot be small (smaller than 5 in this particular study), which is very closely related to the way the steady free surface transition is modeled in Chapter 3 and the improvements required there.

The future work could be undertaken to improve the CCRM in such way that it captures the first resonant peak as successfully as the ACRM's, without having the limitation for the vortex chamber radius. This could be accomplished, if one would advance the wave reflection/transmission analysis to the order higher than one. In order to do that, one would need to revisit the equations describing the long wave fluctuations of the mass flow rate and momentum in Section 5.3. Another possible improvement would be to include the evanescent wave modes, which fade away far from the reflective boundaries, but add more realism to the description of the reflection/transmission wave dynamics.

In Chapter 6, we have used the analysis of Chapter 4 to discuss the question of how would the gaseous core density and the surface tension at the gas-liquid interface affect the injector response. The simplifying presumption here was that we neglected the wave reflections completely and were dealing with the wave refractions only. From this chapter, we have learned that the injector response decays as the gas density grows, and that we can notice it only after the gas-to-liquid density ratio becomes greater that 10%. The surface tension, however, has a minimal effect, such that it can be considered negligible overall. Obviously, the omittance of wave reflections renders this analysis to be only partial. At the same time, the inclusion of the wave reflections presents itself as a topic where the model could be further improved.

Chapter 7 was meant to address the discrepancy between Bazarov's theory and Richardson's computational points in a numerical sense. But, based on the knowledge that we have gathered from Chapters 2–5, we have decided to switch the emphasis from proving whose result was more correct to the question if the numerical code can reproduce the resonant frequencies that we have predicted in Chapter 5. Another important question we have raised in this chapter was: do those resonant frequencies match the experimental peak response for the spray cone fluctuation of Ahn [55]? For computations, we have used the code based on the Boundary Element Method. This particular technique has allowed us to resolve the fluctuating free surface with a higher precision than the other finite element codes would provide. In the code description, we have illustrated how to:

- change the inflow boundary condition so that the overall flow dynamics becomes similar to that in Chapter 5,
- arrange the movement of the points on the inflow boundary so that the distances at the lower left corner of the flow remain even,
- extract the injector response information from the code output.

The results have shown that, indeed, the numerical injector response does have extrema at the frequencies that we have expected theoretically, and the first resonant

peak is located close to the experimental, especially when the conical convergence angle in the computational runs is steeper than 60°. Which validates the free surface and the refraction/reflection models described in Chapters 3–5 and the computational code against each other.

Of course, the BEM code leaves many areas for improvement. The first one, that is easily seen, is the tangential inflow. It seems that, in order to model the inflow in a truly realistic sense, one has to switch to the 3D code (see Chao [129]), instead of the axisymmetric 2D that we have employed. After doing that, one could still try to use the present normal velocity – velocity potential approach, with the extension to 3D, to conserve the overall irrotational setup for the whole flow domain. The second area of improvement would be to abandon this irrotational flow approach, since it does not allow us to have a nonuniform angular momentum that is able to change in space and time, and switch to the vorticity–stream function approach, which naturally allows to track those changes. A simplest analytical description of the latter approach can be found in Batchelor [79].

To conclude, we can say that we have implicitly answered the question of matching of Bazarov's theoretical and Richardson's computational results: the matching was simply not possible due to the shortcomings in Bazarov's linear theory, and due to the way the dynamic flow was arranged in the computational code. Nonetheless, the results of this dissertation are valuable in the sense that they point out the important aspects of the swirl injector dynamics that have to be accounted for in the future research studies, such as the free surface transition and the refractions of the disturbance waves that it causes. More importantly, they reveal the important notion of the swirl injector injector resonance, which future investigators/designers may use to tune the injector to the resonant peak, or out of the resonant peak, in order to respectively amplify or damp the overall flow pulsations.

# LIST OF REFERENCES

# LIST OF REFERENCES


[1] V. G. Bazarov. *Liquid Injector Dynamics*. Mashinostroenie, 1979. In Russian with English Translation.

[2] A. H. Lefebvre. Fifty years of gas turbine injection. *Atomization and Sprays*, 10(3–5), 2000.

[3] M. R Long, V. G. Bazarov, and W. E. Anderson. Main chamber injectors for advanced hydrocarbon booster engines. Number AIAA 2003-4599, Washington, DC, July 2003. 39th AIAA/ASME/SAE/ASEE Joint Propulsion Conference and Exhibit, American Institute of Aeronautics and Astronautics.

[4] J. J. Chinn. *The Internal Flow Physics of Swirl Atomizer Nozzles*. PhD thesis, University of Manchester, Institute of Science and Technology, 1996.

[5] S. Kim, D. Kim, and Y. Yoon. Effect of geometry on the liquid film thickness and formation of air core in a swirl injector. Number AIAA-2007-5460, Washington, DC, July 2007. 43rd AIAA/ASME/SAE/ASEE Joint Propulsion Conference and Exhibit, American Institute of Aeronautics and Astronautics.

[6] G. I. Taylor. The mechanics of swirl atomizers. In *Seventh International Congress on Applied Mechanics*, volume 2, pages 280–285, 1948.

[7] E. Giffen and A. Muraszew. *The Atomisation of Liquid Fuels*, chapter 4. John Wiley and Sons, New York, 1953.

[8] I. Bayvel and Z. Orzechowski. *Liquid Atomization*, chapter 5-2. Taylor and Francis, 1993.

[9] J. B. Kennedy. High weber number smd correlations for pressure atomizers. *Journal of Engineering for Gas Turbines and Power*, 108:191–195, 1986.

[10] N. K. Rizk and A. H. Lefebvre. Internal flow characteristics of simplex swirl atomizers. *Journal of Propulsion and Power*, 1(3):193–199, 1985.

[11] A. H. Lefebvre. *Atomization and Sprays*, chapter 5. Taylor and Francis, 1989.

[12] Y. Khavkin. *The Theory and Practice of Swirl Atomizers*, chapter 7. Taylor and Francis, 2004.

[13] D. Mondal, A. Datta, and A. Sarkar. Droplet size and velocity distributions in a spray from a pressure swirl atomizer: Application of maximum entropy formalism. In *Proceedings of the Institution of Mechanical Engineers, Part C: Journal of Mechanical Engineering Science*, volume 218, pages 737–749. Professional Engineering Publishing, 2004.

[14] C.-C. Chu, S.-F. Chou, and H.-I. Lin. Theoretical analysis of heat and mass transfer in swirl atomizers. *Journal of Heat and Mass Transfer*, 43:1213–1224, 2007.

[15] M. Doumas and R. Laster. Liquid-film properties for centrifugal spray nozzles. *Chemical Engineering Progress*, 49(10), 1953.

[16] V. Yang, M. Habiballah, J. Hulka, and M. Popp. *Liquid Rocket Thrust Chambers: Aspects of Modeling, Analysis, and Design*, chapter 2, pages 56–66. American Institute of Aeronautics and Astronautics, Washington, DC, 2004.

[17] J. Xue. *Computational Simulation of Flow Inside Pressure-Swirl Atomizers*. PhD thesis, University of Cincinnati, 2004.

[18] J. N. Hinckel, H. F. V. Nova, and V. G. Bazarov. Cfd analysis of swirl atomizers. Number AIAA 2008-5229, Washington, DC, July 2008. 44th AIAA/ASME/SAE/ASEE Joint Propulsion Conference and Exhibit, American Institute of Aeronautics and Astronautics.

[19] M. S. Balasubramanyam and C. P. Chen. Numerical design studies on internal flow characteristics of lox/ch4 swirl injector. Number AIAA 2009-5040, Washington, DC, August 2009. 45th AIAA/ASME/SAE/ASEE Joint Propulsion Conference and Exhibit, American Institute of Aeronautics and Astronautics.

[20] N. Dombrowski and D. Hasson. The flow characteristics of swirl (centrifugal) spray pressure nozzles with low viscosity liquids. *Journal of American Institute of Chemical Engineering*, 15(4), 1969.

[21] A. J. Yule and I. R. Widger. Swirl atomizers operating at high water pressure. *International Journal of Mechanical Sciences*, 38(8–9):981–999, 1996.

[22] D. Cooper, J. J. Chinn, and A. J. Yule. Experimental measurements and computational predictions of the internal flow field in a pressure swirl atomizer. ILASS-Europe, 1999.

[23] C.-C. Chu, S.-F. Chou, H.-I. Lin, and Y.-H. Liann. An experimental investigation of swirl atomizer sprays. *Journal of Heat and Mass Transfer*, 45(1):11–22, 2008.

[24] W. Thomson, Baron Kelvin. Vibrations of a columnar vortex. In *Proceedinds of the Royal Society of Edinburgh*, pages 155–168, March 1880. Case II.

[25] Lord Rayleigh. On the dynamics of revolving fluids. In *Proceedings of the Royal Society of London*, volume 93 of *Series A, Mathematical and Physical Sciences*, pages 148–154, March 1917.

[26] A. M. Binnie. The theory of waves travelling on the core in a swirling liquid. In *Proceedings of the Royal Society of London*, volume 205 of *Series A, Mathematical and Physical Sciences*, pages 530–540, March 1951.

[27] T. Maxworthy. Waves on vortex cores. *Fluid Dynamic Research*, 3:52–62, 1988.

[28] D. Feikema. Liquid film characteristics inside a pressure-swirl atomizer. Number AIAA-1998-3692, Washington, DC, July 1998. 34th AIAA/ASME/SAE/ASEE Joint Propulsion Conference and Exhibit, American Institute of Aeronautics and Astronautics.

[29] V. G. Bazarov. Influence of propellant injector stationary and dynamic parameters on high frequency combustion stability. Number AIAA 1996-3119, Washington, DC, July 1996. 32nd AIAA/ASME/SAE/ASEE Joint Propulsion Conference and Exhibit, American Institute of Aeronautics and Astronautics.

[30] K. J. Miller. Experimental study of longitudinal instabilities in a single element rocket combustor. Master's thesis, Purdue University, 2005. Appendix B.2.

[31] K. Miller, J. Sisco, and W. Anderson. Combustion instability with a single-element swirl injector. *Journal of Propulsion and Power*, 23(5), 2007.

[32] W. O. Criminale, T. L. Jackson, and R. D. Joslin. *Theory and Computation of Hydrodynamic Stability*, chapter 4.1. Cambridge University Press, Cambridge, 2003.

[33] C. Wu, S. Farokhi, and R. Taghavi. Spatial instability of a swirling jet - theory and experiment. *AIAA Journal*, 30(6):1545–1552, 1992.

[34] V. Bazarov, E. Lee, D. Lineberry, B. Swanner, and R. A. Frederick. Pulsator designs for liquid rocket injector research. Number AIAA 2007-5156, Washington, DC, July 2007. 43rd AIAA/ASME/SAE/ASEE Joint Propulsion Conference and Exhibit, American Institute of Aeronautics and Astronautics.

[35] V. G. Bazarov and V. Yang. Liquid-propellant rocket engine injector dynamics. *Journal of Propulsion and Power*, 14(5), 1998.

[36] M. Ismailov and S. D. Heister. Nonlinear modeling of classical swirl injector dynamics. Number AIAA 2009-5402, Washington, DC, August 2009. 45th AIAA/ASME/SAE/ASEE Joint Propulsion Conference and Exhibit, American Institute of Aeronautics and Astronautics.

[37] H. Park. *Flow Characteristics of Viscous High-Speed Jets in Axial/Swirl Injectors*. PhD thesis, Purdue University, 2005. Chapter 4.

[38] C. A. Brebbia. *The Boundary Element Method for Engineers*. John Wiley and Sons, 1978.

[39] J. A. Liggett and P. L-F. Liu. *The Boundary Integral Equation Method for Porous Media Flow*. George Allen and Unwin (Publishers), 1983.

[40] D. J. Cartwright. *Underlying Principles of the Boundary Element Method*. WIT Press, 2001.

[41] J. H. Hilbing. *Nonlinear Modeling of Atomization Processes*. PhD thesis, Purdue University, 1996.

[42] S. G. Yoon. *A Fully Nonlinear Model for Atomization of High-Speed Jets*. PhD thesis, Purdue University, 2002.

[43] R. Richardson. *Linear and Nonlinear Dynamics of Swirl Injectors*. PhD thesis, Purdue University, 2007.

[44] R. Richardson, H. Park, J. V. Canino, and S. D. Heister. Nonlinear dynamic response modeling of a swirl injector. AIAA 2007-5454, Washington, DC, July 2007. 43rd AIAA/ASME/SAE/ASEE Joint Propulsion Conference and Exhibit, American Institute of Aeronautics and Astronautics.

[45] R. W. Fox and A. T. McDonald. *Introduction to Fluid Mechanics*. John Wiley and Sons, 5 edition, 1998.

[46] Q.-F. Fu, L.-J. Yang, and X.-D. Wang. Theoretical and experimental study of the dynamics of a liquid swirl injector. *Journal of Propulsion and Power*, 26(1):94–101, January-February 2010.

[47] L.-J. Yang and Q.-F. Fu. Theoretical study of dynamics of open-end liquid swirl injector. Number IAC-06-C4.P.3.09. 57th International Astronautical Congress, October 2006.

[48] H. Huo, N. Zong, and V. Yang. Cryogenic fluid dynamic response of swirl injector to external forcing at. Number AIAA 2009-233, Washington, DC, January 2009. 47th AIAA Aerospace Sciences Meeting Including The New Horizons Forum and Aerospace Exposition, American Institute of Aeronautics and Astronautics.

[49] P. G. Drazin and W. H. Reid. *Hydrodynamic Stability*, chapter 1. Cambridge University Press, 1981.

[50] M. S. Balasubramanyam, C. P. Chen, and V. G. Bazarov. Numerical design investigation of a hydro-mechanical pulsator for liquid rocket injector research. Number AIAA 2008-5230, Washington, DC, July 2008. 44th AIAA/ASME/SAE/ASEE Joint Propulsion Conference and Exhibit, American Institute of Aeronautics and Astronautics.

[51] M. S. Balasubramanyam, C. P. Chen, and V. G. Bazarov. Numerical design investigation of a hydro-mechanical pulsator for liquid rocket injector research. Number AIAA 2009-4956, Washington, DC, July 2009. 45th AIAA/ASME/SAE/ASEE Joint Propulsion Conference and Exhibit, American Institute of Aeronautics and Astronautics.

[52] T. Khil, S. Kim, S. Cho, and Y. Yoon. Quantifying the variation of mass flow rate in a simplex swirl injector by the pressure fluctuation for the injector dynamic research. Number B1-1. Asian Joint Conference on Propulsion and Power, March 2008.

[53] T. Khil, S. Kim, S. Cho, and Y. Yoon. Quantifying the variation of mass flow rate generated in a simplex swirl injector by the pressure fluctuation. Number AIAA 2008-4849, Washington, DC, July 2008. 44th AIAA/ASME/SAE/ASEE Joint Propulsion Conference and Exhibit, American Institute of Aeronautics and Astronautics.

[54] M. Wilson, D. M. Lineberry, and M. D. Moser. Experimental pulsator characterization for liquid injector research. Number AIAA 2009-5941, Washington, DC, July 2009. 45th AIAA/ASME/SAE/ASEE Joint Propulsion Conference and Exhibit, American Institute of Aeronautics and Astronautics.

[55] B. Ahn. Forced excitation of swirl injectors using a hydro-mechanical pulsator. Master's thesis, Purdue University, 2009.

[56] B. Ahn, M. Ismailov, and S. D. Heister. Forced excitation of swirl injectors using a hydro-mechanical pulsator. Number AIAA 2009-5043, Washington, DC, August 2009. 45th AIAA/ASME/SAE/ASEE Joint Propulsion Conference and Exhibit, American Institute of Aeronautics and Astronautics.

[57] D. Kim, J.-H. Im, H. Koh, and Y. Yoon. Effect of ambient gas density on spray characteristics of swirling liquid sheets. *Journal of Propulsion and Power*, 23(3), May-June 2007.

[58] R. J. Kenny, J. R. Hulka, M. D. Moser, and N. O. Rhys. Effect of chamber back-pressure on swirl injector fluid mechanics. *Journal of Propulsion and Power*, 25(4), July-August 2009.

[59] S. Chandrasekhar. *Hydrodynamic and Hydromagnetic Stability*, chapter 1. Oxford University Press, 1961.

[60] W. C. Niewkamp. Flow analysis of a hollow cone nozzle with potential flow theory. 3rd International Conference on Liquid Atomisation and Spray Systems, The Institute of Energy, July 1985.

[61] C. R. Wylie and L. C. Barrett. *Advanced Engineering Mathematics*. McGraw-Hill, 6 edition, 1995.

[62] V. V. Golubev and H. M. Atassi. Acoustic-vorticity waves in swirling flows. *Journal of Sound and Vibration*, 209(2):203–222, 1998.

[63] V. G. Bazarov. Lectures on liquid propellant rocket engine injectors. AAE 690A Lecture Notes at Purdue University, 2003.

[64] D. L. Darmofal, R. Khan, E. M. Greitzer, and C. S. Tan. Vortex core behaviour in confined and unconfined geometries: a quasi-one-dimensional model. *Journal of Fluid Mechanics*, 449:61–84, 2001.

[65] C. A. Coulson. *Waves. A Mathematical Account of the Common Types of Wave Motion*. Oliver and Boyd, 7 edition, 1955.

[66] C. C. Mei. *Theory and Applications of Ocean Surface Waves. Part 1: Linear Aspects*. World Scientific, 2005.

[67] J. W. Miles. Surface-wave scattering matrix for a shelf. *Journal of Fluid Mechanics*, 28(4):755–767, 1967.

[68] K. Kajiura. On the partial reflection of water waves passing over a bottom of variable depth. In *Proceedings of the tsunami meetings associated with the tenth Pacific Science Congress*, volume 24, pages 206–234. Pacific Science Congress, September 1961.

[69] D. H. Peregrine. Interaction of water waves and currents. In C.-S. Yih, editor, *Advances in Applied Mechanics*, volume 16. Academic Press, 1976.

[70] Z. Nehari. *Conformal Mapping*. McGraw-Hill Book Company, 1 edition, 1952.

[71] I. G. Currie. *Fundamental Mechanics of Fluids*. Marcel Dekker, 3 edition, 1993.

[72] A. Gray and G. B. Mathews. *A Treatise on Bessel Functions and Their Applications to Physics*, chapter 8. McMillan and Co, London, 1931. Paragraph 1.

[73] S. A. Bostandzhiyan. Uniform helical fluid motion in a cone with a diaphragm. *Fluid Dynamics*, 1(1):29–33, 1966.

[74] T. Miloh. Conical potential flow about bodies of revolution. *Quarterly Journal of Mechanics and Applied Mathematics*, 29(1):35–60, 1976.

[75] A. Dillmann. Linear potential theory of steady internal supersonic flow with quasi-cylindrical geometry. part 1. flow in ducts. *Journal of Fluid Mechanics*, 281:159–191, 1994.

[76] W. S. Lewellen. A review of confined vortex flows. CR 1772, National Aeronautics and Space Administration, Washington, D.C., 1971. Chapter 2.2.

[77] S. N. Barua. A source in a rotating fluid. *The Quarterly Journal of Applied Mathematics*, 8(1):22–29, 1954.

[78] R. R. Long. Source and sinks at the axis of a rotating liquid. *The Quarterly Journal of Applied Mathematics*, 9(4):385–393, 1956.

[79] G. K. Batchelor. *An Introduction to Fluid Dynamics*, chapter 7.5. Cambridge University Press, Cambridge, 1967.

[80] F. Bowman. *Introduction to Bessel Functions*, chapter 3. Dover Publications, 1958.

[81] R. Haberman. *Elementary Applied Partial Differential Equations with Fourier Series and Boundary Value Problems*, chapter 7. Prentice-Hall, 1983.

[82] W. D. McKee. The reflection of water waves by shear currents. *Pure and Applied Geophysics*, 115(4):937–949, 1977.

[83] J. Billingham and A. C. King. *Wave Motion*, chapter 4. Cambridge University Press, 2000.

[84] S. Arendt, D. C. Fritts, and O. Andreassen. The initial value problem for kelvin vortex waves. *Journal of Fluid Mechanics*, 344:181–212, 1997.

[85] R. Khan. A quasi-one-dimensional analysis for confined vortex cores. Master's thesis, Massachusetts Institute of Technology, 1992. Chapter 2.

[86] J. M. Brookfield. Vortical flows in an adverse pressure gradient. Master's thesis, Massachusetts Institute of Technology, 1993. Chapter 2.

[87] M. W. Dingemans. Advanced series on ocean engineering. In P. L.-F. Liu, editor, *Water Wave Propagation Over Uneven Bottoms. Part 1 – Linear Wave Propagation*, volume 13. World Scientific, 1997.

[88] C.-Y. Chow. Swirling flow in tubes of non-uniform cross-sections. *Journal of Fluid Mechanics*, 38(4):843–854, 1969.

[89] X. Nan and Y. Xieyuan. Stability analysis of slowly divergent swirling flow (i) - theory. *Applied Mathematics and Mechanics*, 16(11):1047–1054, 1993.

[90] I. Didenkulova, E. Pelinovsky, and T. Soomere. Long wave dynamics along a convex bottom. *Journal of Geophysical Research*, 114, 2009.

[91] E. Kreyszig. *Advanced Engineering Mathematics*. John Wiley and Sons, 9 edition, 2006.

[92] M. S. Longuet-Higgins and R. W. Stewart. The changes in amplitude of short gravity waves on steady non-uniform currents. *Journal of Fluid Mechanics*, 10(4):529–549, 1961.

[93] J. W. Miles and W. Munk. Harbor paradox. *Journal of the Waterways and Harbors Division*, 87:111–130, 1961.

[94] J. W. Miles. Harbor seiching. *Annual Review of Fluid Mechanics*, 6:17–33, 1974.

[95] J. W. Miles and Y. K. Lee. Helmholtz resonance of harbours. *Journal of Fluid Mechanics*, 67(3):445–464, 1975.

[96] J. W. Miles. The coupling of a cylindrical tube to a half-infinite space. *The Journal of the Acoustical Society of America*, 20(5):652–664, 1948.

[97] U. Ingard. On the theory and design of acoustic resonators. *The Journal of the Acoustical Society of America*, 25(6):1037–1061, 1953.

[98] R. C. Chanaud. Effects of geometry on the resonance frequency of helmholtz resonators. *Journal of Sound and Vibration*, 178(3):337–348, 1994.

[99] S. K. Tang. On helmholtz resonators with tapered necks. *Journal of Sound and Vibration*, 279(3):1085–1096, 2005.

[100] L. E. Kinsler and A. R. Frey. *Fundamentals of Acoustics*. John Wiley and Sons, 2 edition, 1962.

[101] A. K. Gupta, D. G. Lilley, and N. Syred. *Swirl Flows*. Abacus Press, 1984.

[102] R. M. Sorensen. *Basic Coastal Engineering*, chapter 4. John Wyley and Sons, 1978.

[103] G. F. Carrier, R. P. Shaw, and M. Miyata. Channel effects in harbor resonance. In *Proceedings of the American Society of Civil Engineers*, volume 97 of *Journal of the Engineering Mechanics Division*, pages 1703–1716, 1971.

[104] M. R. Spiegel. *Schaum's Outline of Mathematical Handbook of Formulas and Tables*. McGraw-Hill, 2 edition, 1968.

[105] R. G. Dean and R. A. Dalrymple. *Water Wave Mechanics for Engineers and Scientists*. Prentice-Hall, 1984.

[106] T. J. O'Hare and A. G. Davies. A new model for surface wave propagation over undulating topography. *Coastal Engineering*, 18:251–266, 1992.

[107] J. Ponstein. Instability of rotating cylindrical jets. *Applied Scientific Research*, 8(A):450–456, 1959. Paragraph 5.

[108] A. M. Binnie. Annular hydraulic jumps. In *Proceedings of the Royal Society of London*, volume 282 of *Series A, Mathematical and Physical Sciences*, pages 155–165, November 1964.

[109] M. Lessen, N. V. Deshpande, and B. Hadji-Ohanes. Stability of a potential vortex with a non-rotating and rigid-body rotating top-hat jet core. *Journal of Fluid Mechanics*, 60(3):459–466, 1973.

[110] V. I. Smirnov. *A Course of Higher Mathematics*, volume 2 of *Adiwes International Series in Mathematics*, chapter 5. Pergamon Press, 1964.

[111] S. D. Heister. Stability of free surfaces. AAE630 Lecture Notes, Purdue University, School of Aeronautics and Astronautics (unpublished), 2006.

[112] G. Beer, I. Smith, and C. Duenser. *The Boundary Element Method with Programming*. Springer Verlag, 2008.

[113] M. A. Jaswon. A review of the theory. In C. A. Brebbia, editor, *Basic Principles and Applications*, volume 1 of *Topics in Boundary Element Research*, chapter 1. Springer Verlag, 1984.

[114] G. S. Gipson. In C. A. Brebbia and J. J. Connor, editors, *Boundary Element Fundamentals – Basic Concepts and Recent Developments in the Poisson Equation*, volume 2 of *Topics in Engineering*. Computational Mechanics Publications, 1987.

[115] M. S. Longuet-Higgins and E. D. Cokelet. The deformation of steep surface waves on water. i. a numerical method of computation. In *Proceedings of the Royal Society of London*, volume 350 of *Series A, Mathematical and Physical Sciences*, pages 1–26, July 1976.

[116] M. S. Longuet-Higgins and E. D. Cokelet. The deformation of steep surface waves on water. ii. growth of normal-mode instabilities. In *Proceedings of the Royal Society of London*, volume 364 of *Series A, Mathematical and Physical Sciences*, pages 1–28, July 1978.

[117] J. H. Hilbing, S. D. Heister, and C. A. Spangler. A boundary-element method for atomization of a finite liquid jet. *Atomization and Sprays*, 5:621–638, 1995.

[118] J. H. Hilbing and S. D. Heister. Droplet size control in liquid jet breakup. *Physics of Fluids*, 8(6):1574–1581, 1996.

[119] S. D. Heister. Boundary element methods for two-fluid free surface flows. *Engineering Analysis with Boundary Elements*, 19(4):309–317, 1997.

[120] H. Park, S. S. Yoon, and S. D. Heister. A nonlinear atomization model for computation of drop size distributions and spray simulations. *International Journal for Numerical Methods in Fluids*, 48:1219–1240, 2005.

[121] M. Abramowitz and I. A. Stegun. *Handbook of Mathematical Functions: with Formulas, Graphs, and Mathematical Tables*. Dover, 1965.

[122] M. T. Heath. *Scientific Computing An Introductory Survey*. McGraw Hill, 2 edition, 1965.

[123] L. S. Blackford, J. Choy, A. Cleary, D'Avezedo E., I. Dhillon, J. Dongarra, S. Hammarling, G. Henry, A. Petitet, K. Stanley, D. Walker, and R.C. Whaley. *ScaLAPACK Users' Guide*. Society for Industrial and Applied Mathematics Press, 1997.

[124] K. S. Park. Modeling dense sprays produced by pressure-swirl atomizers. Master's thesis, Purdue University, 2008.

[125] K. S. Park and S. D. Heister. On the parallelization of unsteady bem problems with variable mesh size. *Engineering Analysis with Boundary Elements*, 34:289–296, 2009.

[126] K. S. Park and S. D. Heister. Nonlinear modeling of drop size distributions produced by pressure-swirl atomizers. *International Journal of Multiphase Flow*, 36:1–12, 2010.

[127] J. D. Hoffman. *Numerical Methods for Engineers and Scientists*. McGraw-Hill, 2 edition, 1992.

[128] A. M. Binnie. The passage of a perfect fluid through a critical cross-section or "throat". In *Proceedings of the Royal Society of London*, volume 197 of *Series A, Mathematical and Physical Sciences*, pages 545–555, July 1949.

[129] C. Chao. *3 Dimensional Boundary Element Method*. PhD thesis, Purdue University, 1998.

[130] V. V. Golubev and H. M. Atassi. Sound propagation in an annular duct with mean potential swirling flow. *Journal of Sound and Vibration*, 198(5):601–616, 1996.

# APPENDICES

# A. MatLab Code Listing for Calculation of Steady Flow Parameters and Injector Response due to Bazarov

```
% This script calculates injector response for injector shown in Fig. 23, p. 67 of
% V. G. Bazarov. Liquid Injector Dynamics. Mashinostroenie, 1979.
% Injector parameters are given in second paragraph, at p. 67.
%
% Functions used:
% steady_injector, Bazarov_response
%-------------------------------------------------------------------------%

global Rv Rt Rn Nin Win Lt Lv Lc Ln Ageom phi rhe rv uthhe uzv

%---Given dimensional parameters-----------------------------------------%
Ln_d  =  8E-3;      % m, nozzle length
Rin_d =  7E-3;      % m, inflow radius
Lv_d  = 25E-3;      % m, length of vortex chamber (90 degree convergence)
Lt_d  =  2E-3;      % m, tangential inlet length

rho   = 1000;       % kg/m^3, water density
dpinj = 0.6E6;      % Pa, injector pressure drop

%---Given nondimensional injector parameters-----------------------------%
Rv  = 3;                  % vortex chamber radius
Rn  = 1;                  % nozzle radius
Win = 1;                  % inflow velocity
Nin = 4;                  % number of tangential inlets
Ageom = 3;                % geometric characteristic
alpha = 89.99*pi/180;     % angle of conical convergence
Rt = (-Rn + sqrt(Rn^2 + 4*Ageom*Nin*Rv))/(2*Ageom*Nin);
                          % tangential inlet radius
Rn_d = Rin_d/(Rv-Rt);     % m, dimensional nozzle radius
Lv = Lv_d/Rn_d;           % vortex chamber length
Ln = Ln_d/Rn_d;           % nozzle length
Lt = Lt_d/Rn_d;           % tangential inlet length
Lc = (Rv-Rn)/tan(alpha);  % length of conical section

nu = 0.1;                 % artificial viscosity coefficient
```

```
%---Calculation of nondimensional steady core radii and flow velocities---%
steady_injector;

%---Calculation of wave speed in uniform regions-------------------------%
% wave speed in uniform vortex chamber region
cv = sqrt((uthhe*rhe)^2*(Rv^2-rv^2)/(2*rv^4)) + uzv;
% wave speed in uniform nozzle region
cn = uthhe*2*sqrt(phi/(2-phi));

%---Calculation of dimensional steady velocities-------------------------%
uthhe_d = sqrt(2*dpinj/rho); % m/s, circumferential velocity at rhe
Win_d   = uthhe_d/uthhe;     % m/s, inflow velocity

%---Calculation of injector response-------------------------------------%

%~~~Frequeuncies considered~~~~~~~~~~~~~~~~~~~~~~%
f_d     = 5:5:2200;             % Hz
omega_d = 2*pi*f_d;             % radians/sec
omega   = omega_d*Rn_d/Win_d;   % nondimensional
%~~~~~~~~~~~~~~~~~~~~~~~~~~~~~~~~~~~~~~~~~~~~~~~~~%

PIinj = Bazarov_response(cv,cn,nu,omega);

%=========================================================================%
function steady_injector                                                  %
% This function computes steady core radii and flow velocities            %
% at injector head end and in uniform vortex chamber and nozzle regions   %
%=========================================================================%

global Rv Rt Rn Nin Win Ageom phi rhe rv rn uthhe uzv uzn

Rin = Rv-Rt;    % inflow radius
C   = Win*Rin;  % angular momentum

Ageom = Rin*Rn/(Nin*Rt^2);              % geometric characteristic
syms phis; phis = solve('Ageom-(1-phis)*sqrt(2)/(phis*sqrt(phis))',phis);
phi = subs(phis,Ageom); phi = phi(1,1); % coefficient of flow area
a   = 2*(1-phi)^2/(2-phi);              % (rhe/Rn)^2
mu  = sqrt(a)/Ageom;                    % discharge coefficient

rhe = Rn*sqrt(a);       % core radius at head end
rn  = Rn*sqrt(1-phi);   % core radius in uniform nozzle region

% Introduce K = rhe/rv, find K by using bisection method
```

```
check = 0; Klo = 0.5; Khi = 1-10^-10;
while check == 0

    Kme = (Klo+Khi)/2;

    flo = sqrt(1-Klo^2)*((Rv/Rn)^2 - (rhe/Rn)^2/Klo^2) - mu;
    fme = sqrt(1-Kme^2)*((Rv/Rn)^2 - (rhe/Rn)^2/Kme^2) - mu;
    fhi = sqrt(1-Khi^2)*((Rv/Rn)^2 - (rhe/Rn)^2/Khi^2) - mu;

    if flo*fme > 0        Klo = Kme;
    elseif fhi*fme > 0    Khi = Kme;
    end

    if abs(Khi-Klo)<=10^-8
        check = 1;  K = Kme;
    end
end
rv = rhe/K; % core radius in uniform vortex chamber region

% circumferential velocity at rhe, at head end (z=0)
uthhe = C/rhe;
% axial velocity in uniform vortex chamber region
uzv   = uthhe*mu/(Rv^2-rv^2);
% axial velocity in uniform nozzle region
uzn   = sqrt(uzv^2 + C^2*(1/rv^2 - 1/rn^2));

%=========================================================================%
function[PIinj] = Bazarov_response(cv,cn,nu,omega)
% This function computes injector response due to Chapter 4,
% V. G. Bazarov. Liquid Injector Dynamics. Mashinostroenie, 1979.
%=========================================================================%

global Rv Win Lt Lv Lc Ln rhe Ageom phi uzv

%----Auxilliary parameters for injector response calculation-----------%
xbarlim = 1-10^-10;     % integral upper limit
ni = 1000;              % number of intervals
dxbar = xbarlim/ni;     % integration step
Cint  = 1 - 1/(Rv/rhe); % constant in vorticity wave integration
PIrefl = 1-2*sqrt(phi)/sqrt(Rv^2-rhe^2); % nozzle reflection coefficient
%-------------------------------------------------------------------%
```

```
for q = 1 : length(omega)

    %~~~Tangential channel response~~~~~~~~~~~~~~~~~~~~~~~~~~~~~~~~~~~~~~~~~~~~~~~~~~~~~~~~~~~~%
    Sht = omega(q)*Lt/Win;                  % inlet Strouhal number
    PIt(q,1) = 1/2*(1-i*Sht)/(1+Sht^2);     % transfer function of tangential channel

    %~~~Vortex chamber response to surface waves~~~~~~~~~~~~~~~~~~~~~~~~~~~~~~~~~~~~~~~~~~~~~~%
    PHIv = omega(q)*(Lv+Lc)/cv;             % vortex chamber phase shift

    Nsum = 1000; % number of members in infinite series
    sumhe = 0; sumvn = 0;
    for n = 0 : Nsum
        sumhe = sumhe + PIrefl^n*exp(-i*(2*n+0)*PHIv)*exp(-(2*n+0)*nu*PHIv);
        sumvn = sumvn + PIrefl^n*exp(-i*(2*n+1)*PHIv)*exp(-(2*n+1)*nu*PHIv);
    end;
    % transfer function of vortex chamber due to surface waves
    PIv2(q,1) = sumhe/(Ageom * sqrt(2*(Rv^2-rhe^2)) );
    % transfer function of nozzle entrance due to surface waves
    PIvn(q,1) = sumvn;

    %~~~Vortex chamber response to vorticity waves~~~~~~~~~~~~~~~~~~~~~~~~~~~~~~~~~~~~~~~~~~~~~%
    Shv = omega(q)*Rv/uzv;   % vortex chamber Strouhal number

    %---Trapezoidal integration---%
    CosInt=0; SinInt=0;
    xbar(1) = 0;
    for k = 2 : ni+1
        xbar(k) = xbar(k-1) + dxbar;

        % Function fxbar
        fxbar_l = Shv * xbar(k-1) * tan(pi/2*xbar(k-1));
        fxbar_r = Shv * xbar(k)   * tan(pi/2*xbar(k));

        % cos integrand function
        fcos_l = cos(fxbar_l) / (1 - Cint*xbar(k-1))^3 * exp(-nu*fxbar_l);
        fcos_r = cos(fxbar_r) / (1 - Cint*xbar(k))^3   * exp(-nu*fxbar_r);
        fcos_av = (fcos_l + fcos_r)/2;

        % sin integrand function
        fsin_l = sin(fxbar_l) / (1 - Cint*xbar(k-1))^3 * exp(-nu*fxbar_l);
        fsin_r = sin(fxbar_r) / (1 - Cint*xbar(k))^3   * exp(-nu*fxbar_r);
        fsin_av = (fsin_l + fsin_r)/2;
```

```
        % Cos and Sin integrals
        CosInt = CosInt + Cint*fcos_av*dxbar;
        SinInt = SinInt + Cint*fsin_av*dxbar;
    end

    RePIv3 = 2*CosInt;  ImPIv3 = -2*SinInt;

    % Transfer function of vortex chamber due to vorticity waves
    PIv3(q,1) = RePIv3 + i*ImPIv3;

    %~~~Nozzle response~~~~~~~~~~~~~~~~~~~~~~~~~~~~~~~~~~~~~~~~~~~~~~~~~~~~~%
    PHIn = omega(q)*Ln/cn;                    % nozzle phase shift
    PIn(q,1) = (1 - PIrefl)*exp(-i*PHIn);     % nozzle transfer function

    %~~~Total injector response~~~~~~~~~~~~~~~~~~~~~~~~~~~~~~~~~~~~~~~~~~~~%
    PIinj(q,1)  = Rv^2/rhe^2 * PIt(q,1) * PIvn(q,1) * PIn(q,1) / ...
                  (1 + 2*PIt(q,1)*(PIv2(q,1) + PIv3(q,1)));

end
```

# B. Determination of Wave Speeds in Swirling Cylinder-Bounded Flows

In this section, the author shows example calculations for cylindrical regions of the flow where the bulk stream velocity and the radii of flow boundaries do not change, which permits one to ignore refraction phenomenon. The chosen cylindrical flow sections are: the uniform vortex chamber region and the uniform nozzle region (Fig. 2.1) of the baseline injector (Tables 2.2 and 2.3). The example nondimensional frequency in these calculations is $\omega = 10$, which converts to $f = 942.3$ Hz as shown in Section 2.3.

For long waves, the solution of the wave equation (Chinn [4, Subsec. 3.4.1], Bazarov [1, Sec. 3.3]) may be written in the form

$$\omega - k\bar{u}_z = \pm k\sqrt{C^2\frac{R^2-\delta^2}{2\delta^4}} \tag{B.1}$$

For the wave speeds valid in the *entire* frequency range, there exists a classical 1880 work by Kelvin [24], who has studied the propagation of small disturbances in the infinite irrotational cylindrical flows. Based on Kelvin's dispersion [24, Eq. (33)], the solution of the wave equation (for axisymmetric waves) is

$$\omega - k\bar{u}_z = \pm\sqrt{k\frac{-I_1(kr_0)+\dfrac{I_1(kR_0)}{K_1(kR_0)}K_1(kr_0)}{I_0(kr_0)+\dfrac{I_1(kR_0)}{K_1(kR_0)}K_0(kr_0)}\frac{C^2}{r_0^3}} \tag{B.2}$$

Notice that in the low frequency limit, this dispersion includes the long wave solution above. From these equations it is easy to obtain the solutions for the wave number, $k$, and the wave speed, $c = \omega/k$, numerically, they are summarized in Table B.1. We can see that Kelvin's dispersion gives larger wave numbers, or shorter wave lengths, as expected. Notice that, in the nozzle, we have solutions only for waves that are propagating downstream. We can explain this, and consider all other possible solutions,

if we follow the standard methodology outlined in Peregrine [69, Chap. B] for finding the wave numbers for disturbances that propagate on a bulk stream or current. This is presented in the sections below.

Table B.1: Wave characteristics in uniform vortex chamber and nozzle regions (baseline injector, $\omega = 10$)

| **Uniform Region** | **Wave Type** | $k$ | $c$ | **Propagation Direction** |
|---|---|---|---|---|
| Vortex chamber | Long wave | –0.3276 | –30.5273 | upstream |
| | | +0.3267 | +30.6089 | downstream |
| | Kelvin's result | –1.2524 | –7.9849 | upstream |
| | | +1.2174 | +8.2145 | downstream |
| Nozzle | Long wave | +1.7384 | +5.7525 | downstream |
| | Kelvin's result | +1.7563 | +5.6938 | downstream |

## B.1 Long Wave Solutions

### B.1.1 Uniform Vortex Chamber Region

In the vortex chamber, if we introduce functions

$$g_{1v} = \omega - k\bar{u}_{zv} \qquad g_{2v} = +k\sqrt{C^2\frac{R_v^2 - r_v^2}{2r_v^4}} \qquad g_{3v} = -k\sqrt{C^2\frac{R_v^2 - r_v^2}{2r_v^4}}$$

the solutions for the wave numbers may be found as points where $g_{1v}$ intersects with $g_{2v}$ or $g_{3v}$, indicated by circles on Fig. B.1 (circles will indicate solutions in next cases further on as well). Correspondingly, the point, at which the wave number is negative, represents a wave traveling upstream, and the point, at which the wave number is positive, represents a wave traveling downstream. Notice that the roots are almost symmetrical, however not exactly equal, because $\bar{u}_{zv}$ is small, but finite.

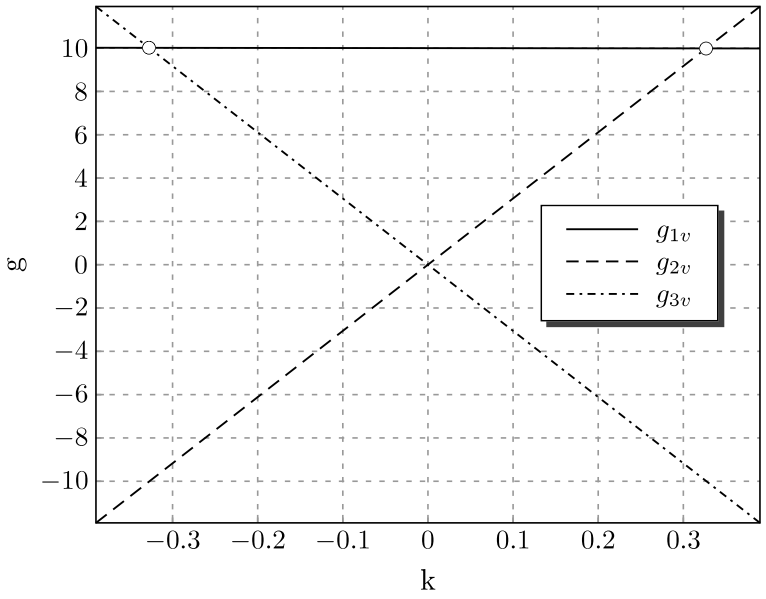


Figure B.1.: Long wave solutions for wave number in uniform vortex chamber region ($C = 4.5$, $\bar{u}_{zv} = 0.0408$, $R_v = 5$, $r_v = 0.7177$)

### B.1.2 Uniform Nozzle Region

In the nozzle, we can introduce similar functions

$$g_{1n} = \omega - k\bar{u}_{zn} \qquad g_{2n} = +k\sqrt{C^2\frac{R_n^2 - r_n^2}{2r_n^4}} \qquad g_{3n} = -k\sqrt{C^2\frac{R_n^2 - r_n^2}{2r_n^4}}$$

In contrast with the vortex chamber, in the nozzle, there will be only one intersection, between $g_{2n}$ and $g_{1n}$, because the function $g_{3n}$ is parallel to $g_{1n}$, Fig. B.2. It is easy to explain the existence of a single positive root if we consider the derivatives

$$\frac{dg_{1n}}{dk} = \frac{d\omega}{dk} - \bar{u}_{zn} = -\bar{u}_{zn}$$
$$\frac{dg_{3n}}{dk} = -\sqrt{C^2\frac{R_n^2 - r_n^2}{2r_n^4}} = -\bar{u}_{zn}$$

where we note that $\dfrac{d\omega}{dk} = 0$ because the $\omega$ is a constant number as follows from Peregrine [69, p. 26], and that $+\sqrt{C^2\dfrac{R_n^2 - r_n^2}{2r_n^4}} = \bar{u}_{zn}$ from the established fact that the disturbance phase speed is equal to the bulk stream axial velocity in the nozzle

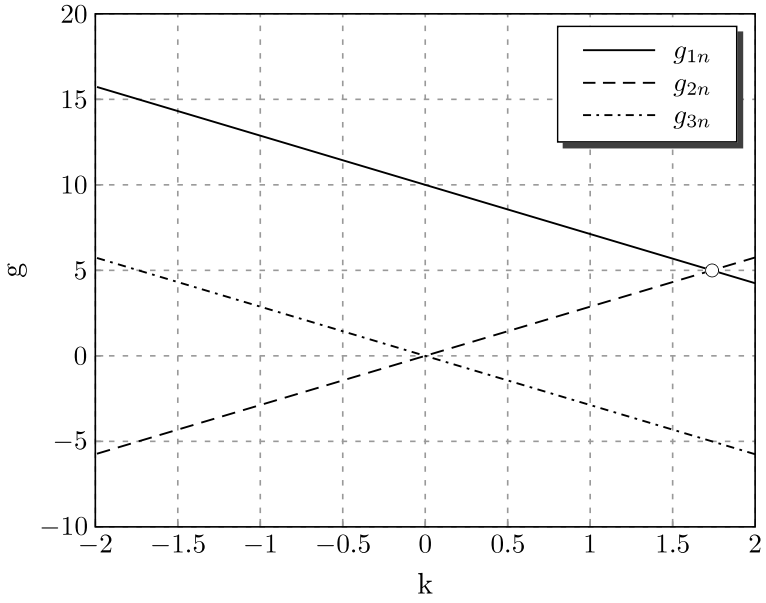


Figure B.2.: Long wave solutions for wave number in uniform nozzle region ($C = 4.5$, $\bar{u}_{zn} = 2.8762$, $R_n = 1$, $r_n = 0.8077$)

(Chinn [4, Subsec. 3.4.1]). The fact that the upstream traveling waves are absent in the nozzle is very similar to the situation in a supersonic compressible flow through which the disturbances may not propagate upstream.

## B.2 Kelvin's Wave Solutions

For waves valid in the whole frequency range, we will leave functions $g_{1v}$ and $g_{1n}$ same as above, however the corresponding functions $g_{2v}$, $g_{3v}$, $g_{2n}$, and $g_{3n}$ will now follow from the dispersion Eq. (B.2), which creates curvature in their shapes as opposed to the straight lines above.

### B.2.1 Uniform Vortex Chamber Region

After introducing functions

$$g_{2v} = + \sqrt{k \frac{-I_1(kr_v) + \frac{I_1(kR_v)}{K_1(kR_v)} K_1(kr_v)}{I_0(kr_v) + \frac{I_1(kR_v)}{K_1(kR_v)} K_0(kr_v)} \frac{C^2}{r_v^3}}$$

$$g_{3v} = - \sqrt{k \frac{-I_1(kr_v) + \frac{I_1(kR_v)}{K_1(kR_v)} K_1(kr_v)}{I_0(kr_v) + \frac{I_1(kR_v)}{K_1(kR_v)} K_0(kr_v)} \frac{C^2}{r_v^3}}$$

the solutions for wave number are given by their intersections with $g_{1v}$ shown on Fig. B.3. As in the long wave case, they are almost symmetrical.

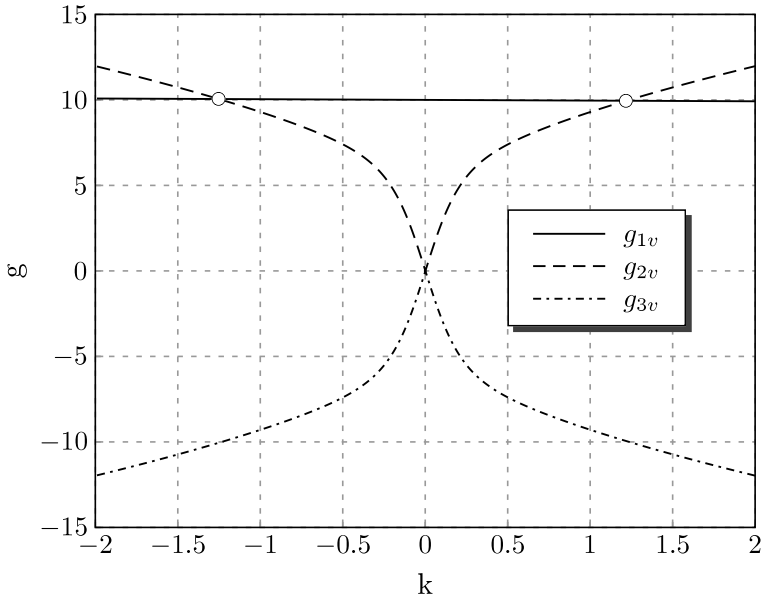


Figure B.3.: Kelvin's wave solutions for wave number in uniform vortex chamber region ($C = 4.5$, $\bar{u}_{zv} = 0.0408$, $R_v = 5$, $r_v = 0.7177$)

### B.2.2 Uniform Nozzle Region

Similarly to above, after introducing functions

$$g_{2n} = + \sqrt{k \frac{-I_1(kr_n) + \frac{I_1(kR_n)}{K_1(kR_n)} K_1(kr_n)}{I_0(kr_n) + \frac{I_1(kR_n)}{K_1(kR_n)} K_0(kr_n)} \frac{C^2}{r_n^3}}$$

$$g_{3n} = - \sqrt{k \frac{-I_1(kr_n) + \frac{I_1(kR_n)}{K_1(kR_n)} K_1(kr_n)}{I_0(kr_n) + \frac{I_1(kR_n)}{K_1(kR_n)} K_0(kr_n)} \frac{C^2}{r_n^3}}$$

the solutions for wave number are shown in Fig. B.4. Notice the point of intersection lying in the negative $g$ area. At this point, $k > 0$, which stands for disturbance waves propagating downstream, and $g_{1n} = \omega - k\bar{u}_{zn} < 0$, so that $\frac{\omega}{k} < \bar{u}_{zn}$. But this indicates that these disturbance waves are *swept away by current* in stream wise direction. Therefore, this solution is not physical and we do not consider it in further calculations.

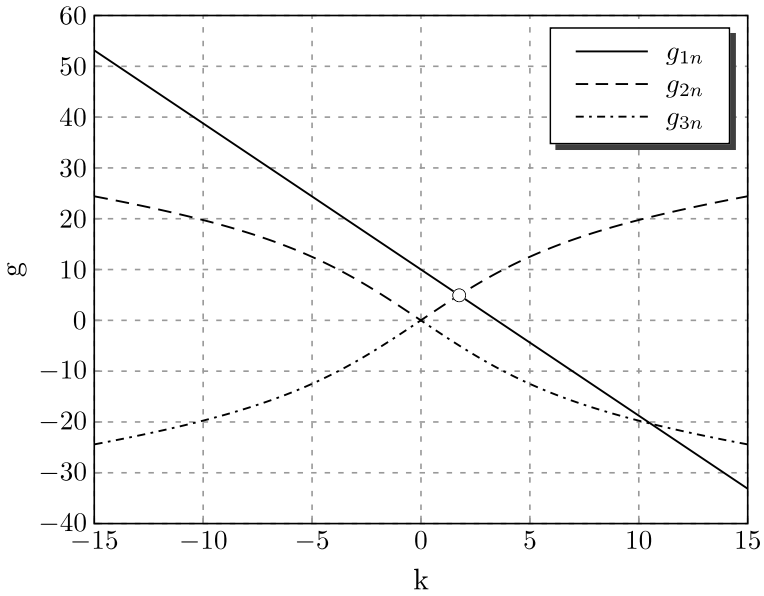


Figure B.4.: Kelvin's wave solutions for wave number in uniform nozzle region ($C = 4.5$, $\bar{u}_{zn} = 2.8762$, $R_n = 1$, $r_n = 0.8077$)

Finally, we have to mention the absence of a solution in the large negative $k$ area. In the uniform nozzle region, the steady axial velocity $\bar{u}_{zn}$ is so large, that $g_{1n}$ is quite steep. But at the same time, it is so steep that, no matter what value $\omega$ has, it will not intersect with the negative wing of $g_{2n}$.

VITA

# VITA

Maksud Ismailov was born on November 8, 1982, in the former Soviet Union, to the family of an aerospace engineer and a pediatric doctor. Due to the travel assignments of his father, during his childhood, he lived and went to schools in multiple cities and countries around the world, among which the Marie-Therese Gymnasium in Erlangen, Germany (1994-1996), and Nishi Junior High School in Kiryu, Japan (1997-1998).

In 1999 he got accepted at the Department of Liquid Rocket Engines of Moscow State Technical University named after N. E. Bauman, Moscow, Russia, where he has studied for the next six years. In the years 2003–2005 he was a graduate research assistant there, with the focus on the engine cycle design and optimization. After completing his study in 2005 with a Master of Science in Aeronautics and Astronautics, he moved to the United States.

In the United States, after working in 2006 briefly as a mechanical engineer for General Vortex Energy, Missouri City, Texas, he entered the doctoral program at the School of Aeronautics and Astronautics at Purdue University, in August 2006. In the years 2007-2010, he was a graduate research assistant there, with the research focused on the dynamics of the swirl injectors, the results of which were presented in this dissertation. In 2008, he met his wife Masuda, who was a marketing coordinator at Atkins Global, London, United Kingdom, at that time. In September 2009 he became a father, when his daughter Sabeena was born. After receiving his Ph.D. in Aeronautics and Astronautics from Purdue, he was employed by Blue Origin in Kent, Washington, in June of 2010.